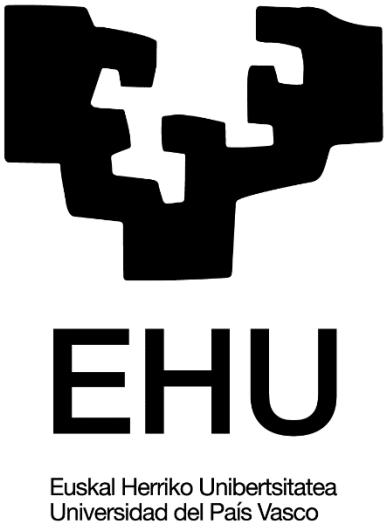
Universidad del País Vasco / Euskal Herriko Unibertsitatea



Doctoral Thesis

Cement-Based Thermoelectric and Photothermoelectric Materials for Low-Grade Heat and Solar Energy Harvesting

Author

Mohamad Barzegar

Thesis Director

Dr. Jorge Sánchez Dolado

2026

Abstract

Urban infrastructure absorbs and dissipates substantial low-grade heat, particularly under solar irradiation, yet this energy remains largely unused. Cementitious materials offer a scalable, low-cost, and structurally compatible platform for distributed energy harvesting, but their thermoelectric application is limited by low output, environmental sensitivity, and incomplete understanding of charge-transport mechanisms. This thesis investigates cement-based thermoelectric (TE) and photothermoelectric (PTE) systems from material-level transport to device-level solar energy harvesting and environmental performance.

The work first clarifies the role of ionic thermoelectricity in alkali-activated cementitious materials. Geopolymer-based hybrid cement, copper-slag-modified composites, kaolin-clay geopolymers, and GGBFS-based systems were studied to determine how binder chemistry, pore structure, moisture state, intrinsic voltage, and ionic mobility govern the Seebeck response. A significant intrinsic voltage was identified as a critical source of measurement bias, leading to a refined protocol that separates true thermally induced voltage from pre-existing electrochemical potential. The kaolin- and slag-based systems further showed that TE polarity and magnitude are controlled by the balance between dominant ionic species, pore connectivity, activator content, and thermal conductivity rather than by ionic concentration alone.

Building on this mechanistic understanding, a chessboard-like PTE cement cell was developed by combining a high-absorbance geopolymer/copper-slag segment with a high-reflectance white-cement segment. This architecture generates a lateral temperature gradient under illumination, coupling photothermal heating with ionic TE voltage generation. Outdoor testing of two series-connected cells produced a Seebeck coefficient of 9.9 mV K^{-1}, confirming effective solar-driven operation under real conditions. Further optimization increased the harvested energy to 1.81×10^6 μJ m^{-2} over one hour, demonstrating competitive performance while retaining the advantages of low cost, processability, and large-area scalability.

The environmental response of the PTE system was then evaluated under static and dynamic climatic conditions. Controlled chamber tests showed that relative humidity and temperature directly regulate output by controlling ionic pathway stability and thermodiffusive mobility. Dynamic simulations revealed that voltage generation depends on the coupled evolution of irradiation, moisture availability, and thermal gradients, rather than solar intensity alone. The ability of humid conditions to restore performance after drying highlights the moisture-rechargeable nature of cementitious ionic TEs.

Overall, this thesis establishes cement-based thermoelectricity as an environmentally responsive energy-harvesting mechanism and advances it toward scalable PTE materials. Its main contributions are the clarification of ionic transport as the governing mechanism, the identification and correction of intrinsic-voltage effects, the use of industrial geopolymers and aggregates for functional cement design, and the demonstration of a

solar-driven cement cell operating under realistic environmental conditions. These findings provide a foundation for multifunctional cementitious materials capable of harvesting low-grade heat and solar energy directly from the built environment.

Resumen

La infraestructura urbana absorbe y disipa una cantidad considerable de calor de baja calidad, especialmente bajo irradiación solar, aunque esta energía permanece en gran medida desaprovechada. Los materiales cementicios ofrecen una plataforma escalable, de bajo coste y estructuralmente compatible para la recolección distribuida de energía, pero su aplicación termoeléctrica está limitada por su baja potencia de salida, sensibilidad ambiental y una comprensión incompleta de los mecanismos de transporte de carga. Esta tesis investiga sistemas termoeléctricos (TE) y fototermoeléctricos (PTE) basados en cemento, desde el transporte a escala de material hasta la recolección de energía solar a escala de dispositivo y su comportamiento ambiental.

El trabajo clarifica primero el papel de la termoelectricidad iónica en materiales cementicios activados alcalinamente. Se estudiaron cementos híbridos basados en geopolímeros, compuestos modificados con escoria de cobre, geopolímeros de arcilla caolinítica y sistemas basados en GGBFS para determinar cómo la química del ligante, la estructura porosa, el estado de humedad, el voltaje intrínseco y la movilidad iónica gobiernan la respuesta Seebeck. Se identificó un voltaje intrínseco significativo como una fuente crítica de sesgo en la medición, lo que condujo a un protocolo refinado que separa el voltaje realmente inducido térmicamente del potencial electroquímico preexistente. Los sistemas basados en caolín y escoria mostraron además que la polaridad y magnitud TE están controladas por el equilibrio entre las especies iónicas dominantes, la conectividad porosa, el contenido de activador y la conductividad térmica, más que por la concentración iónica por sí sola.

A partir de esta comprensión mecanística, se desarrolló una celda de cemento PTE con arquitectura tipo tablero de ajedrez, combinando un segmento de geopolímero/escoria de cobre de alta absorbancia con un segmento de cemento blanco de alta reflectancia. Esta arquitectura genera un gradiente lateral de temperatura bajo iluminación, acoplando el calentamiento fototérmico con la generación de voltaje TE iónico. Los ensayos al aire libre de dos celdas conectadas en serie produjeron un coeficiente Seebeck de 9,9 mV K^{-1}, confirmando una operación solar efectiva bajo condiciones reales. Una optimización posterior aumentó la energía recolectada hasta $1{,}81 \times 10^{6}$ μJ m^{-2} durante una hora, demostrando un rendimiento competitivo mientras se conservan las ventajas de bajo coste, procesabilidad y escalabilidad a grandes áreas.

La respuesta ambiental del sistema PTE se evaluó posteriormente bajo condiciones climáticas estáticas y dinámicas. Los ensayos en cámara climática controlada mostraron que la humedad relativa y la temperatura regulan directamente la salida al controlar la estabilidad de las vías iónicas y la movilidad termodifusiva. Las simulaciones dinámicas revelaron que la generación de voltaje depende de la evolución acoplada de la irradiación, la disponibilidad de humedad y los gradientes térmicos, más que de la intensidad solar por sí sola. La capacidad de las condiciones húmedas para restaurar el rendimiento tras el secado resalta la naturaleza recargable por humedad de los TE iónicos cementicios.

En conjunto, esta tesis establece la termoelectricidad basada en cemento como un mecanismo de recolección de energía ambientalmente sensible y la aproxima al desarrollo de materiales PTE escalables. Sus principales contribuciones son la clarificación del transporte iónico como mecanismo gobernante, la identificación y corrección de los efectos del voltaje intrínseco, el uso de geopolímeros industriales y áridos para el diseño de cementos funcionales, y la demostración de una celda de cemento accionada por energía solar bajo condiciones ambientales realistas. Estos resultados proporcionan una base para el desarrollo de materiales cementicios multifuncionales capaces de recolectar calor de baja calidad y energía solar directamente del entorno construido.

To my parents, family, and friends, and to everyone whose encouragement and kindness supported me along the way. With special gratitude to Dr. Jorge Sánchez-Dolado and Dr. Guido Goracci, whose invaluable guidance, support, and knowledge profoundly shaped this journey.

Related dissemination and publications

The research presented in this thesis has been disseminated through a series of peer-reviewed publications and ongoing manuscripts focused on cement-based thermoelectric and photothermoelectric materials for energy harvesting. The work first addressed the thermoelectric behavior of sustainable geopolymer concrete incorporating recycled copper slag aggregates, where the role of intrinsic voltage and ionic transport in cementitious matrices was clarified. This study demonstrated the potential of industrially scalable geopolymer-based concrete for thermoelectric energy harvesting and proposed a refined measurement protocol to separate the true thermally induced voltage from pre-existing intrinsic voltage contributions.

The research was then extended to different geopolymer systems, including kaolin clay-based and GGBF slag-based geopolymers, to investigate how precursor chemistry, activator content, ionic mobility, and thermal transport govern the thermoelectric response. Building on these material-level studies, a chessboard-like photothermoelectric cement cell was developed by combining cementitious segments with contrasting optical properties. This design enabled the generation of a horizontal temperature gradient under solar irradiation and demonstrated the feasibility of scalable solar energy harvesting using cement-based materials.

Further work, currently under preparation, investigates the influence of environmental conditions on cement-based photothermoelectric performance. This study focuses on the coupled effects of temperature, relative humidity, moisture history, and realistic climatic cycles on ionic transport and voltage generation. By combining static environmental measurements with dynamic climate simulations, this work aims to bridge the gap between controlled laboratory demonstrations and real-world operation of cement-based PTE systems.

In addition, the introductory chapter of this thesis is being developed into a review article on energy harvesting using cement-based materials. This review will place cementitious thermoelectric and photothermoelectric systems within the broader context of multifunctional construction materials, low-grade heat recovery, solar energy harvesting, ionic transport, functional fillers, and smart infrastructure applications.

Publications

[1] **Sustainable geopolymer concrete for thermoelectric energy harvesting** M. Barzegar, G. Goracci, P. Martauz, J. S. Dolado, *Construction and Building Materials* 411 (2024) 134398.

https://doi.org/10.1016/j.conbuildmat.2023.134398

[2] **Kaolin Clay-Based Geopolymer for Ionic Thermoelectric Energy Harvesting** G. Goracci, M. B. Ogundiran, M. Barzegar, A. Iturrospe, A. Arbe, J. S. Dolado, *ACS Omega* 9 (2024) 13728–13737.

https://doi.org/10.1021/acsomega.3c08257

[3] **GGBF slag-based geopolymer for ionic thermoelectric energy harvesting**
G. Moutaoukil, M. Barzegar, G. Goracci, J. S. Dolado, *Developments in the Built Environment* 26 (2026) 100890.
https://doi.org/10.1016/j.dibe.2026.100890

[4] **A chessboard-like photothermoelectric cement cell: a new design for scalable and high-efficiency solar energy conversion**
M. Barzegar, G. Goracci, P. Martauz, J. S. Dolado, *Materials Horizons* 12 (2025) 10760–10769.
https://doi.org/10.1039/d5mh01248a

[5] **Interplay of Ionic Transport and Environmental Conditions in Cement-Based Photothermoelectric Materials**
M. Barzegar, G. Goracci, P. Martauz, J. S. Dolado, Under preparation.

[6] **Energy Harvesting Using Cement-Based Materials: From Thermoelectric Transport to Smart Infrastructure Applications**
M. Barzegar, G. Goracci, J. S. Dolado, Review article under preparation.

Related Conferences, Workshops, and Academic Presentations

[1] **High-Resolution TGA: A New Tool for Investigating the Effect of Water on Electrical Conductivity of Concrete**

M. Barzegar, G. Goracci, J. S. Dolado

Workshop of Sustainable Materials for Energy Storage Solutions, Centro de Física de Materiales, Spain, 2022.

[2] **Thermoelectric Properties Enhancement of Hybrid-Cement-Based Concrete Using Industrial Aggregates**

M. Barzegar, G. Goracci, P. Martauz, J. S. Dolado

Sixth International Symposium on Innovative Materials and Processes in Energy Systems, IMPRES Symposium, 2022.

[3] **Sustainable Geopolymer Concrete for Thermoelectric Energy Harvesting**

M. Barzegar, G. Goracci, P. Martauz, J. S. Dolado

16th International Congress on the Chemistry of Cement, ICCC 2023, 2023.

[4] **Sustainable Geopolymer Cementitious Composite for Thermoelectric Energy Harvesting**

M. Barzegar, G. Goracci, P. Martauz, J. S. Dolado

RILEM Week 2024: Final Conference of RILEM, Toulouse, France, 2024.

[5] **High-Resolution TGA Combined with BDS: A New Tool to Investigate the Effect of Water on the Electrical Conductivity of Concrete**

M. Barzegar, G. Goracci, P. Martauz, J. S. Dolado

12th Conference on Broadband Dielectric Spectroscopy and its Applications, Lisbon, Portugal, 2024.

[6] **Scalable Cement-Based Thermoelectric Systems for Sustainable Energy Harvesting in Outdoor Environments**

M. Barzegar, G. Goracci, P. Martauz, J. S. Dolado

18th European Congress and Exhibition on Advanced Materials and Processes, FEMS EuroMat 2025, Granada, Spain, 2025.

[7] **Scalable Cement-Based Thermoelectric Systems for Sustainable Energy Harvesting in Outdoor Environments**

M. Barzegar, G. Goracci, P. Martauz, J. S. Dolado

Week of Excellence, Engaged Lecture & Dialogue Series, Department of Engineering, University of Perugia, Italy, 2025.

[8] **Interplay of Ionic Transport and Environmental Conditions in Cement-Based Photo-Thermoelectric Materials**

Table of Content

1. Research Background 1
1.1. Introduction 1
1.1.1. Urban Energy Challenges 1
1.1.2. Opportunity for Energy Harvesting from Urban Low-Grade Heat 1
1.1.3. Multifunctional Cementitious Materials 2
1.2. Fundamentals of Thermoelectric Energy Conversion 2
1.2.1. Thermoelectric Effects 2
1.2.2. Thermoelectric Performance Metrics 4
1.2.3. Device-Level Considerations 5
1.3. Types of Thermoelectric Transport Mechanisms 5
1.4. Thermoelectric Behavior of Cementitious Materials 7
1.4.1. Transport Mechanisms in Thermoelectric Cementitious Materials 7
1.4.2. Thermal Transport and Figure of Merit 13
1.4.3. Optimization of Thermoelectric Performance 13
1.5. Binder Chemistry and Phase Composition 13
1.5.1. Portland Cement Systems 14
1.5.2. Alkali-Activated Materials and Geopolymers 15
1.6. Functional Additions for Thermoelectric Cementitious Composites 22
1.6.1. Carbon-Based Fillers 23
1.6.2. Metallic Fillers 26
1.6.3. Metal-Oxide Thermoelectric 26
1.6.4. Hybrid Carbon–Oxide Systems 28
1.6.5. Inorganic and Dielectric Functional Fillers 28
1.6.6. Section Summary 28
1.7. Microstructure and Pore-Structure Engineering 30
1.7.1. Porosity, Water Distribution, and Ionic Transport 30
1.7.2. Nanopores and Electric Double-Layer Effects 31
1.7.3. Interfacial Water Layers and Electrode Coupling 31
1.7.4. Section Summary 33
1.8. Photothermoelectric Cement-Based Materials 33

1.9. Stability and Environmental Response 34
1.9.1. Influence of Humidity and Moisture Cycling 35
1.9.2. Thermal Cycling Stability 35
1.9.3. Section Summary 36
1.10. Challenges and Research Outlook 36
1.10.1. Remaining Scientific Challenges 36
1.10.2. Motivation for the Present Thesis 37
2. Experimental Methods 39
2.1. Materials Characterization 39
2.1.1. Structural and Chemical Characterization 39
2.1.2. Thermal and Microstructural Analysis 40
2.1.3. Spectroscopic and Optical Characterization 41
2.2. Thermoelectric Measurements 42
2.2.1. Thermal Conductivity Measurements 42
2.2.2. Electrical Transport Measurements 43
2.2.3. Seebeck Measurements 44
2.3. Device-Level and Photothermoelectric Measurements 45
2.3.1. Surface Wettability and Moisture Interaction 45
2.3.2. Indoor Photothermoelectric Measurements under Controlled Irradiation 45
2.3.3. Outdoor Photothermoelectric Measurements 46
2.3.4. Controlled Environmental Chamber Measurements 47
3. Sustainable Geopolymer Concrete for Thermoelectric Energy Harvesting 50
3.1. Experimental 50
3.1.1. Materials and Sample Preparation 50
3.1.2. Material Characterization 52
3.2. Results and Discussion 52
3.2.1. Material Characterization 52
3.2.2. Thermoelectric Properties 57
3.3. Conclusion 67
4. Kaolin Clay-Based Geopolymer for Ionic Thermoelectric Energy Harvesting 68
4.1. Experimental 68
4.1.1. Materials and Sample Preparation 68
4.1.2. Material Characterization 69

4.2. Results and Discussion 70
4.2.1. Material Characterization 70
4.2.2. Thermoelectric Properties 75
4.3. Conclusions 81
5. GGBF slag-based geopolymer for ionic thermoelectric energy harvesting 83
5.1. Experimental 83
5.1.1. Materials and Sample Preparation 83
5.1.2. Material Characterization 84
5.2. Results and Discussion 85
5.2.1. Material Characterization 85
5.2.2. Thermoelectric Properties 91
5.3. Conclusion 97
6. A Chessboard-Like Photothermoelectric Cement Cell: A New Design for Scalable and High-Efficiency Solar Energy Conversion 98
6.1. Experimental 99
6.1.1. Materials and Sample Preparation 99
6.1.2. Material Characterization 100
6.2. Results and Discussion 100
6.2.1. Thermoelectric Properties of the PTE Components 100
6.2.2. Proof of Concept of the PTE Cell Design and Performance 102
6.2.3. Temperature and Light Power Dependence of the PTE Cell Performance 104
6.2.4. Rechargeability of PTE Cells (effect of relative humidity) 105
6.2.5. Connection of PTE Cells (chessboard concept) 108
6.2.6. Outdoor Measurements (connected samples) 110
6.2.7. PTE Cells for Solar Energy Harvesting 113
6.3. Conclusion 120
7. Interplay of Ionic Transport and Environmental Conditions in Cement-Based Photo-Thermoelectric Materials 121
7.1. Experimental 122
7.1.1. Materials and Sample Preparation 122
7.1.2. Material Characterization 122
7.2. Results and Discussion 123
7.2.1. Effect of Environmental Parameters on the PTE Response (static condition) 123

7.2.2. Performance Under Dynamic Climatic Conditions 128
7.3. Conclusion 133
8. Conclusion: Summary, Implications, and Future Work 135
8.1. Summary of the Thesis 135
8.2. Scientific and Practical Implications 137
8.3. Limitations of the Present Work 138
8.4. Future Work 139
8.5. Final Remarks 140
9. References 142

List of Tables

Table 3-1 Chemical composition of the Geopolymer-based hybrid cement GHC and CS aggregates. 51
Table 4-1 Oxide composition of IKW clay (wt. %)..... 70
Table 5-1 Chemical composition of GGBF slag 84
Table 5-2 Chemical composition of the prepared samples per weight..... 84
Table 5-3 TE Voltage characteristics of the samples at three applied temperatures. 94
Table 6-1 Chemical compositions of the different parts of the PTE cell..... 99
Table 6-2 Summarized result of PTE measurement for different irradiation powers... 105
Table 6-3 The total resistance and the electrical conductivity of different PTE cells for solar energy harvesting 116
Table 6-4 Dissipated/Harvested energy over different external loads for different sample modifications 118

List of Figures

Figure 1.1 Schematic exploded representation of a thermoelectric module, showing the legs, electrodes, insulating layers, and heat spreaders/heat exchangers. 5
Figure 1.2 Schematic diagram of (a) electronic thermoelectric effect and (b) ionic thermoelectric effect [15]. 9
Figure 1.3 (a) Thermoelectric voltage evolution with temperature after leaching for 0.05%~0.15%rGO/C; (b) variation of temperature difference versus time [12]. 12
Figure 1.4 Schematic representation of cement hydration products showing the C–S–H network and portlandite plates together with indicative electronic band-gap characteristics. 14
Figure 1.5 Comparison of nano-structure of C-S-H and geopolymer [24] 16
Figure 1.6 (a) XRD pattern of metakaolin [24]. (b) TE response of geopolymer with insulated and reconnected interface [18]. 18
Figure 1.7 Na+ and OH- leaching concentration variation curve, (b) the XRD patterns, and (c) the SEM photos of AAF, AAFS, and AAS [8]. 20
Figure 1.8 (a) Seebeck voltage versus temperature difference for geopolymers with different alkali concentrations (b) with different curing temperatures 22
Figure 1.9 Schematic and photographs of a cement-based thermoelectric generator (TEG) module, including thermal distribution (IR image), electrical characterization, and output performance for (a) OPC/SWCNT [39] and (b) Alkali-Activated/SWCNT [40]..... 24
Figure 1.10 Published results on the effect of using functional additions on the TE performance of cement-based materials 29
Figure 1.11 Interfacial mechanisms of geopolymer-based ionic thermoelectric materials: influence of interfacial electric fields [18]. 32
Figure 1.12 (a) experimental setup for photothermoelectric energy harvesting of cement composite (b) calculated harvested energy over time [61]. 34
Figure 2.1 The schematic experimental setup of the Seebeck measurement. 44
Figure 2.2 (a) Setup for the indoor PTE test. (b) Schematic of the Seebeck measurement setup 46
Figure 2.3 The PTE setup for the outdoor measurements. 47
Figure 2.4 (a) the climatic chamber and the data logging system for temperature and voltage, (b) the samples configuration inside the climatic chamber 48
Figure 3.1 (a) Experimental setup for sample preparation, (b). cement paste, (c). curing samples in water. 51
Figure 3.2 XRD pattern of (a) industrially prepared CS aggregate. And (b) X-ray diffraction of GHC and GHC-75CS after curing. 53
Figure 3.3 Thermogravimetric analysis (TG and DTA) (a) GHC and (b) GHC-75CS. . 54
Figure 3.4 (a) Incremental intrusion vs. pore size diameter. (b) log differential intrusion vs. pore size diameter 55

Figure 3.5 The elastic modulus of the GHC and GHC 75CS as a function of increasing temperature 56
Figure 3.6 Intrinsic voltage between two electrodes before applying temperature differences (a) cement paste and (b) cement paste with 75% CS aggregates..... 56
Figure 3.7 (a) Evolution of the intrinsic voltage over time for two GHC75CS from the same batch (b) open circuit voltage measurement over 100h 57
Figure 3.8 Thermal conductivity of pure cement paste and cement concretes at different temperatures..... 58
Figure 3.9 The heating ramp's effect on the electrical conductivity of the samples..... 59
Figure 3.10 Thermoelectric voltage of GHC-75CS as a function of different temperature differences (ΔT) with the linear fit of y = 4.392x-25.725 60
Figure 3.11 (a) Voltage profile of GHC and (b) GHC-75CS at the applied temperature of 90 °C, (c) the temperature difference between two electrodes of GHC, and (d) GHC-75CS. 61
Figure 3.12 (a), (b), and (c) evolution of thermoelectric voltage with three applied temperatures for GHC, and (d), (e), and (f) for GHC-75CS. 62
Figure 3.13 The variation of the open circuit voltage of dried GHC-75CS at applied 70 °C (a) dried at 60 °C overnight, and (b) dried at 105 °C overnight..... 63
Figure 3.14 Schematic view of (a) ions in the initial stage before applying ΔT, (b) diffusion of ions during different stages of the voltage profile, (c) the role of different ions diffusion on voltage profile 64
Figure 3.15. Seebeck coefficient of cement paste and concrete at the measured temperature. 66
Figure 3.16 The calculated figure of merit (ZT) of GHC and GHC-75CS. 67
Figure 4.1 Pictures of raw (IKWRC) and calcined (IKWCC) IKW clay 68
Figure 4.2 TGA/DTG curves of the three IKW raw clay (a) and IKW geopolymer (b) 70
Figure 4.3 XRD patterns of (a) IKW raw clay (IKWRC), (b) calcined clay (IKWCC), and (c) geopolymer (IKWG). In (b) and (c), the estimated amorphous contribution (dashed lines) has been subtracted, yielding the crystalline contribution (black lines). From comparison 72
Figure 4.4 ATR-FTIR spectra of (a) IKW raw clay (IKWRC), (b) calcined clay (IKWCC), and (c) geopolymer (IKWG). 72
Figure 4.5 Curves of heat flow (a) and total quantity of heat released (b) of IKW calcined clay. 74
Figure 4.6 (a) Specific heat capacity, and (b) thermal conductivity as a function of temperature of IKW-geopolymer. 75
Figure 4.7 Real part of complex conductive function measured by Impedance Spectroscopy as a function on frequency at 300K 76
Figure 4.8 Fitting results of electrical conductivity 77
Figure 4.9 Seebeck voltage profile as a function of time 78
Figure 4.10 Seebeck Voltage measured for different applied temperatures 79
Figure 4.11 Seebeck Coefficient of IKW-geopolymer 80
Figure 4.12 The calculated figure of merit (ZT) of IKW-geopolymer. 81

Figure 5.1 XRD pattern of GGBF slag 84
Figure 5.2(a) The normalized heat flow and (b) the total heat of the prepared sample as a function of time 86
Figure 5.3 XRD patterns of S0.3, S0.4, and S0.45 (Ca: calcite, Ak: akermanite, Gp: gypsum, An: anorthite, M: mullite) 87
Figure 5.4 Development of the ultrasonic pulse velocity over time of the samples S0.3, S0.4, and S0.45 88
Figure 5.5 The elastic modulus of the samples S0.3, S0.4 and S0.45 after 1day, 7days and 28days 89
Figure 5.6 Thermogravimetric analysis of the samples S0.3, S0.4 and S0.45 (a) TGA, (b) DTGA 90
Figure 5.7 The thermal conductivity of the samples prepared with different AS/S ratios 91
Figure 5.8 The electrical conductivity of the samples with different alkali activator concentrations as a function of temperature 92
Figure 5.9 The thermovoltage generated under different applied temperatures for samples prepared using different AS/S ratios, (a) 0.3, (b) 0.4, (c) 0.45 93
Figure 5.10 The Seebeck coefficient of the samples prepared with three alkali concentrations under different applied temperatures 95
Figure 5.11 The thermoelectric figure of merit for samples with different AS/S ratios. 96
Figure 6.1 The voltage profile and temperature gradient of (a,b.) geopolymer hybrid cement with 75 wt.% copper slag aggregate (black) (c,d). white cement (white)..... 102
Figure 6.2 Digital photograph of the PTE cell prepared using two types of cement composites, (b) Light reflectance of the two parts of the PTE cell (black and white) and their difference in solar window (SW) obtained via FTIR spectroscopy, (c) Temperature distribution throughout the PTE cell under exposure to light at 850 W m^{-2} obtained by thermal camera after 30 minutes of illumination, (d) Temperature gradient induced in the PTE cell under 850 W m^{-2} irradiation monitored by thermocouples and the induced PTE voltage, (e) Schematic of the mechanism of the PTE cell. 103
Figure 6.3 PTE measurement of a single cell at different irradiation powers, (b) temperature differences created under different irradiation. 105
Figure 6.4 Contact angle measurement of two segments of PTE cell at time 0s and 4s, (a) and (c) black component, (b) and (d) white component, (e) map of the major cities of the representative climate zone 107
Figure 6.5The PTE voltage of the sample, under 950 W m^{-2} light illumination. Before each cycle the sample was dried and stored in humidity chamber at RH 50% 108
Figure 6.6 Voltage profile of two PTE cells connected in series under 850 W m^{-2}. (b) The temperature gradient induced in the connected system, and the digital photograph of the connected cells 109
Figure 6.7 The open circuit voltage of (a) four PTE cells connected in series (b) six PTE cells connected in series. 109
Figure 6.8 (a) relative humidity, (b) air temperature, and (c) wind and gust speed during outdoor measurement. 111

Figure 6.9 The PTE voltage generated under solar radiation on the first day of outdoor measurement.....111
Figure 6.10 (a) PTE voltage and solar irradiance during the second day of measurement. (b) Temperature induced in each electrode. (c) PTE voltage and solar irradiance during the third day of measurement. (d) PTE voltage vs. temperature difference and fit to the data for extraction of the Seebeck coefficient 112
Figure 6.11 Working principle of an iTEC in the charging stage 114
Figure 6.12 The voltage output of the as-produced sample connected to different external loads.....115
Figure 6.13The Nyquist plot of the Geopolymer hybrid cement with 75% copper slag aggregates 115
Figure 6.14 Voltage output of samples prepared based on different strategies (Table 6.3) connected to a 72 kΩ external load. 117
Figure 6.15 The voltage output of the samples connected to different external loads under 850 W m^{-2} lamp irradiation, after different modifications of (a) BWB2 as-received sample, doped with seawater, (b) BWS1 as-received sample, reduced size, (c) BWS2 sample with reduced size and Ag electrodes, (d) BWS3 sample after decreasing the size utilizing Ag electrodes and doping with standard seawater 118
Figure 6.16 (a) Maximum power obtained for the different samples. (b) Energy harvested over a period of 5 minutes for each sample connected to a 72 kΩ external load. (c) Voltage profile of the BWS3 sample connected to a 3.3 kΩ load for more than 1 h. (d) The comparison of the max power of the cement-based PTE cell with the state-of-the-art PTE materials [109,115,116]. 119
Figure 7.1 The PTE voltage response of the sample under different RH and temperatures, (a) 10 ºC, (b) 25 ºC, (c) 40 ºC..... 125
Figure 7.2 Absolute maximum voltage (|V|max) vs. relative humidity at 10, 25, and 40 °C under 900 W m^{-2} irradiation. 126
Figure 7.3 Influence of night-time RH (10%, 30%, 60%, 90%) on the subsequent PTE performance measured at 25 °C, 60% RH, and 900 W m^{-2}..... 128
Figure 7.4 The PTE response vs solar irradiance under Cairo summer condition (X axis demonstrates local time), (b) the RH before and during the illumination, (c) the ambient temperature before and during illumination. The time format is D:hh:mm 130
Figure 7.5 The PTE response vs solar irradiance under Madrid summer condition (X axis demonstrates local time), (b) the RH before and during the illumination, (c) the ambient temperature before and during illumination, (e) The time format is D:hh:mm..... 131
Figure 7.6 (a) The PTE response vs solar irradiance under Singapore summer condition (X axis demonstrates local time), (b) the RH before and during the illumination, (c) the ambient temperature before and during illumination. The time format is D:hh:mm ... 133

Nomenclature

Symbols

Symbol	Definition	Typical unit
A	Cross-sectional area of the sample/cell used in resistance calculations	m^2
C_p	Specific heat capacity	J kg^{-1} K^{-1}
E	Elastic modulus or harvested energy, depending on context	GPa or J
E_{harv}	Harvested electrical energy, commonly normalized by area	J, μJ m^{-2}
f	Frequency in impedance or dielectric measurements	Hz
I	Electrical current	A
J	Current density	A m^{-2}
k, κ	Thermal conductivity	W m^{-1} K^{-1}
k_e	Electronic contribution to thermal conductivity	W m^{-1} K^{-1}
k_l	Lattice/phonon contribution to thermal conductivity	W m^{-1} K^{-1}
L	Distance between electrodes or effective transport length	m
m	Mass	g, kg
N	Number of thermoelectric legs, cells, or thermocouples	dimensionless
n	Charge-carrier concentration	m^{-3}
P	Electrical output power	W
P_{max}	Maximum electrical output power	W
PF	Power factor, defined as $S^2\sigma$	W m^{-1} K^{-2} or μW m^{-1} K^{-2}
$\dot{q}$	Heat-transfer rate	W
R	Electrical resistance	Ω
R_{int}	Internal resistance of the material/device	Ω
R_L	External load resistance	Ω
S	Seebeck coefficient	V K^{-1}, mV K^{-1}, or μV K^{-1}
t	Time	s, min, h
T	Temperature or absolute temperature	°C or K
T_{amb}	Ambient temperature	°C
T_c	Cold-side temperature	°C or K
T_h	Hot-side temperature	°C or K
V	Electrical voltage or terminal voltage	V or mV
V_c	Electrical potential measured at the cold electrode	V or mV
V_h	Electrical potential measured at the hot electrode	V or mV
V_{oc}	Open-circuit voltage	V or mV
$\lvert V\rvert_{max}$	Absolute maximum voltage generated during a test	V or mV
Z	Electrical impedance	Ω
Z′	Real component of impedance	Ω
Z″	Imaginary component of impedance	Ω

ZT	Dimensionless thermoelectric figure of merit	dimensionless
ΔT	Temperature difference between hot and cold sides/electrodes	K
ΔV	Thermally induced voltage difference, commonly $V_c - V_h$	V or mV
η	Thermoelectric conversion efficiency	% or dimensionless
λ	Wavelength, e.g., Cu Kα radiation in XRD	Å or nm
μ	Charge-carrier mobility	$m^2\ V^{-1}\ s^{-1}$
Π	Peltier coefficient	V or $W\ A^{-1}$
ρ	Density or electrical resistivity, depending on context	$kg\ m^{-3}$ or Ω m
σ	Electrical conductivity	$S\ m^{-1}$
τ	Thomson coefficient	$V\ K^{-1}$
θ	Diffraction angle in XRD; 2θ is the measured diffraction angle	degree
ε	Emissivity or strain, depending on context	dimensionless
α	Absorptance/absorption coefficient, when used for optical response	dimensionless

Abbreviations and acronyms

Abbreviation	Meaning
AAM	Alkali-activated material
AAF	Alkali-activated fly ash
AAFS	Alkali-activated fly ash–slag binder
AAS	Alkali-activated slag
AC	Alternating current
Ag	Silver; used in silver-paint electrodes
AS/S	Alkaline solution-to-slag ratio
ATR-FTIR	Attenuated total reflectance Fourier-transform infrared spectroscopy
BDS	Broadband dielectric spectroscopy
CB / nCB	Carbon black/nanocarbon black
CF	Carbon fiber
CNF	Carbon nanofiber
CNT	Carbon nanotube
CS	Copper slag
C–A–S–H	Calcium–aluminosilicate–hydrate gel
C–S–H	Calcium–silicate–hydrate gel
DC	Direct current
DTG / DTGA	Derivative thermogravimetry / derivative thermogravimetric analysis
DTA	Differential thermal analysis
EDL	Electric double layer
EG	Expanded graphite
e-TE	Electronic thermoelectricity
FA	Fly ash
FTIR	Fourier-transform infrared spectroscopy
GGBF / GGBFS	Ground granulated blast-furnace slag
GHC	Geopolymer-based hybrid cement
GNP	Graphene nanoplatelet
HLF-NMR	High/low-field nuclear magnetic resonance, where referenced
ICDD	International Centre for Diffraction Data
IR	Infrared
i-TE	Ionic thermoelectricity
iTEC	Ionic thermoelectric cell/capacitor, depending on context
LOI	Loss on ignition
MCT	Mercury–cadmium–telluride detector
MDSC	Modulated differential scanning calorimetry
MIP	Mercury intrusion porosimetry
MK	Metakaolin
M-TECC	Mixed ionic–electronic thermoelectric cementitious composite
N–A–S–H	Sodium–aluminosilicate–hydrate gel
NIR	Near-infrared

OPC	Ordinary Portland cement
PC	Portland cement
PCM	Phase-change material
PDF-2	Powder Diffraction File database
PTE	Photothermoelectric
rGO	Reduced graphene oxide
RH	Relative humidity
SEM	Scanning electron microscopy
SF	Steel fiber
Si–O–T	Silicon–oxygen–tetrahedral bond, where T = Si or Al
SW	Solar window
SWCNT / SWNT	Single-walled carbon nanotube
TE	Thermoelectric
TEG	Thermoelectric generator
TG	Thermogravimetry
TGA	Thermogravimetric analysis
UHI	Urban heat island
UPV	Ultrasonic pulse velocity
WC / BLWC	White cement / BL white cement
XRD	X-ray diffraction
XRF	X-ray fluorescence

Material and sample codes

Code	Definition
GHC	Reference geopolymer-based hybrid cement paste/composite
GHC-75CS	Geopolymer-based hybrid cement containing 75 wt.% copper slag aggregate
CS	Copper slag aggregate used as the dark/high-absorbance component
BLWC	White cement used as the reflective/white component of the PTE cell
IKW	Kaolin clay system investigated in Chapter 4
IKWRC	Raw IKW clay
IKWCC	Calcined IKW clay
IKWG	IKW-based geopolymer
GGBF / GGBFS	Ground granulated blast-furnace slag precursor used in Chapter 5
S0.3	GGBFS-based geopolymer prepared with AS/S = 0.30
S0.4	GGBFS-based geopolymer prepared with AS/S = 0.40
S0.45	GGBFS-based geopolymer prepared with AS/S = 0.45
BWB1	As-received full-size PTE cell; 2 × 0.7 × 8 cm; copper-tape electrodes; conditioned at RH 75%
BWB2	Full-size PTE cell; 2 × 0.7 × 8 cm; soldered-wire configuration; doped with 3.5 wt.% NaCl solution
BWS1	Reduced-size PTE cell; 2 × 0.7 × 4 cm; copper-tape electrodes; conditioned at RH 75%
BWS2	Reduced-size PTE cell; 2 × 0.7 × 4 cm; soldered-wire/silver-paint electrodes; conditioned at RH 75%
BWS3	Optimized reduced-size PTE cell; 2 × 0.7 × 4 cm; soldered-wire/silver-paint electrodes; doped with 3.5 wt.% NaCl solution

Chemical species and phase labels

Label/species	Meaning
Ak	Akermanite
An	Anorthite
Ca	Calcite
CH	Portlandite/calcium hydroxide, $Ca(OH)_2$
Et	Ettringite
F	Fayalite
Gp	Gypsum
M	Mullite
Q	Quartz
si	Pyroxene-type silicate phase used in copper slag XRD interpretation
spinel ss	Spinel-type solid solution phase
T	Tobermorite or C–S–H-like crystalline analogue, depending on XRD context
Na^+	Sodium ion
K^+	Potassium ion
Ca^{2+}	Calcium ion
OH^-	Hydroxide ion
NaCl	Sodium chloride; used as 3.5 wt.% solution to enhance ionic conductivity
FeO	Ferrous oxide
Fe_2O_3	Ferric oxide
SiO_2	Silicon dioxide/quartz

Chapter I

Research Background

1.1. Introduction

1.1.1. Urban Energy Challenges

Urban areas face a dual energy challenge: rising consumption and intensifying environmental pressures. Rapid urbanization and industrialization have historically driven increases in fossil fuel use and CO_2 emissions, as cities expand and demand for energy-intensive infrastructure grows. This dynamic is particularly pronounced in developing regions, where energy consumption surges with urban growth, while high-income regions show opportunities for energy-saving through cleaner technologies and improved urban planning.

One critical phenomenon intensifying urban energy demand is the Urban Heat Island (UHI) effect. UHI arises from the absorption and retention of heat by urban materials, leading to higher ambient temperatures compared to rural surroundings. This local warming significantly elevates cooling energy requirements, with studies reporting up to a 19% median increase in cooling demand and up to 120% in extreme cases, while marginally reducing heating energy needs. These impacts vary across and within cities, intensifying in dense urban cores.

Mitigation strategies often involve passive surface technologies—such as reflective "cool" roofs, green facades, and phase-change material (PCM)-based coatings—that reduce heat absorption and regulate thermal loads. These solutions not only lower building cooling energy consumption but also moderate UHI intensity, offering systemic benefits at the urban scale. For instance, PCM-integrated roofs have demonstrated notable reductions in peak cooling loads, supporting more sustainable energy profiles.

The integration of renewable energy and smart grids complements passive building-surface technologies by enabling buildings to participate in distributed energy generation and storage. Smart grids enhance efficiency by enabling two-way power flows, demand-side management, and incorporation of distributed energy generation.

Together, urban heat mitigation strategies, passive surface technologies, and smart energy systems create a pathway for buildings to contribute to distributed clean-energy generation, a concept that aligns with the objectives of this thesis on thermoelectric and photothermoelectric cement-based composites.

1.1.2. Opportunity for Energy Harvesting from Urban Low-Grade Heat

Despite ongoing efforts to reduce urban heat accumulation, large quantities of thermal energy remain dissipated across the built environment. Urban infrastructure—including roads, pavements, bridges, and building envelopes—continuously absorbs solar radiation and releases heat generated by transportation systems, industrial processes, and building operations. Much of this energy exists as low-grade heat, typically below 100 °C, which is widely distributed across urban surfaces.

Although the temperature gradients associated with these sources are modest, their spatial extent and persistence offer a significant opportunity for distributed energy harvesting. Converting even a small fraction of this thermal energy into electricity could contribute to powering sensors, monitoring systems, and low-power devices integrated into infrastructure. Realizing such capabilities requires materials capable of operating passively across large surface areas while maintaining long-term durability under environmental exposure [1,2].

1.1.3. Multifunctional Cementitious Materials

Concrete is the most widely used man-made material and is pervasive in buildings, transportation networks, and urban surfaces, making cementitious materials an attractive platform for multifunctional infrastructure.

Recent research has explored the development of multifunctional cementitious materials that integrate mechanical performance with additional functional capabilities. These materials can respond to environmental stimuli such as stress, temperature, moisture, or light, enabling applications including self-sensing structural health monitoring, self-healing crack repair, thermal regulation, and environmental remediation through photocatalytic surfaces.

Among these emerging functionalities, energy harvesting represents one of the most transformative opportunities. Cementitious materials capable of converting ambient mechanical, thermal, or solar energy into electrical power could enable infrastructure systems that actively participate in energy generation. By integrating energy-harvesting capabilities directly into structural materials, urban surfaces may evolve from passive energy consumers into active contributors to sustainable energy systems.

In this context, thermoelectric and photothermoelectric cement-based composites have recently emerged as promising candidates for harvesting low-grade heat from the built environment. These materials offer the potential to convert temperature gradients present in urban infrastructure into electrical energy, opening new possibilities for self-powered sensing, distributed energy generation, and multifunctional infrastructure systems.

1.2. Fundamentals of Thermoelectric Energy Conversion

Thermoelectric (TE) energy conversion is a solid-state process that directly transforms heat into electricity by exploiting the motion of charge carriers under a temperature gradient. Unlike conventional power-generation technologies, thermoelectric systems operate without moving parts or working fluids and do not produce greenhouse gas emissions during operation. These characteristics provide important advantages, including low maintenance requirements, long operational lifetimes, and high reliability. As a result, thermoelectric materials have attracted increasing interest for harvesting low-grade heat in applications where conventional energy-conversion technologies are impractical.

1.2.1. Thermoelectric Effects

The thermoelectric phenomenon arises from the coupling between thermal and electrical transport in conductive materials. Three closely related effects describe this coupling: the

Seebeck effect, the Peltier effect, and the Thomson effect. These effects govern the conversion of temperature gradients into electrical energy and vice versa [2–4].

1.2.1.1 Seebeck Effect

The Seebeck effect describes the generation of an electrical potential difference when a temperature gradient is applied across a conductor or semiconductor. When one side of a material is heated, charge carriers diffuse from the hot region toward the colder region due to the higher carrier energy and mobility at elevated temperatures. This diffusion leads to a redistribution of charge carriers until an internal electric field is established that opposes further carrier movement [1,2,4]. The resulting voltage difference is referred to as the thermoelectric voltage.

The magnitude of the voltage generated is proportional to the temperature difference applied across the material and is characterized by the Seebeck coefficient S, defined as

$$V = S\,\Delta T \qquad \textit{Equation 1.1}$$

Where ΔV is the open-circuit voltage, and ΔT is the temperature difference across the material. The sign of the Seebeck coefficient indicates the dominant charge carriers within the material: positive values correspond to hole-dominated (p-type) transport, while negative values correspond to electron-dominated (n-type) transport.

In practical devices operating under electrical load, the measured voltage is typically lower than the open-circuit voltage because electrical current flowing through the material introduces Joule heating and modifies the internal temperature distribution.

1.2.1.2 Peltier Effect

The inverse process: when an electric current Icrosses a junction between two dissimilar materials $a$and b, heat is absorbed at one side and released at the other at a rate

$$\dot{Q} = (\pi_a - \pi_b)\, I \qquad \textit{Equation 1.2}$$

Where $\pi$is the Peltier coefficient with units $[\mathrm{W\,A^{-1}}] = [\mathrm{V}]$ [2–4]. The direction of heat flow flips with current direction. At the device level, Peltier heating/cooling occurs at every metal/leg interface and must be considered alongside parasitic Joule heating and Fourier heat conduction to predict net performance [4].

1.2.1.3 Thomson Effect

In a single homogeneous conductor carrying current in the presence of a temperature gradient, there is continuous reversible heating or cooling along the leg with a volumetric rate

$$\dot{q}_T = \tau\, J \cdot \nabla T \qquad \textit{Equation 1.3}$$

where $\tau$is the Thomson coefficient $[\mathrm{V\,K^{-1}}]$ and J is the current density [3,4]. This term modifies the internal temperature profile and, together with Joule heating $\dot{q}_J = \mathbf{J}^2/\sigma$, affects the achievable ΔTunder operating conditions [4].

1.2.1.4 Kelvin Relations

The Seebeck, Peltier, and Thomson effects are not independent phenomena. In thermodynamic equilibrium they are connected through the Kelvin relations, which establish a fundamental link between the coefficients describing each effect.

$$\pi = S\,T, \tau = T\,\frac{dS}{dT} \qquad \textit{Equation 1.4}$$

These relations demonstrate that the Peltier coefficient and Thomson coefficient are directly related to the Seebeck coefficient. Consequently, although the Seebeck effect provides the basis for thermoelectric energy generation, the Peltier and Thomson effects must be considered when analyzing heat flow and energy conversion efficiency in practical thermoelectric devices.

1.2.2. Thermoelectric Performance Metrics

The performance of thermoelectric materials is governed by the coupled transport of charge carriers and heat [2,3]. Three material properties are particularly important: the Seebeck coefficient S, the electrical conductivity σ, and the thermal conductivity k.

1.2.2.1 Power Factor

The electrical contribution to thermoelectric performance is commonly expressed through the power factor (PF), defined as

$$PF = S^2\sigma \qquad \textit{Equation 1.5}$$

Where S is the Seebeck coefficient and σ is the electrical conductivity. The Seebeck coefficient quantifies the voltage generated per unit temperature difference, whereas electrical conductivity describes the ability of the material to transport electrical current. Their product $S^2\sigma$ therefore reflects the effectiveness with which a material converts a temperature gradient into usable electrical power.

For a thermoelectric element with fixed geometry, the maximum electrical power output scales approximately with the power factor [1,2]. Consequently, increasing the power factor is a central objective in thermoelectric material design.

1.2.2.2 Figure of Merit

The overall efficiency of thermoelectric materials is described by the dimensionless figure of merit ZT:

$$ZT = \frac{S^2\sigma T}{k} \qquad \textit{Equation 1.6}$$

Where T is the absolute temperature and k is the total thermal conductivity of the material, including both lattice and electronic contributions [1–4].

Optimizing ZT requires simultaneously achieving a high Seebeck coefficient, high electrical conductivity, and low thermal conductivity. However, these properties are strongly interdependent. Increasing carrier concentration n boosts $\sigma = ne\mu$ (with mobility μ) but tends to decrease S; meanwhile, increasing σ also raises the electronic thermal conductivity via the Wiedemann–Franz law ($k_e = L\sigma T$), tightening the coupling among all three quantities [2,3]. In practice, PF exhibits an optimum at intermediate n where the trade-off between $S$and $\sigma$is most favorable [2].

Conventional semiconductors (e.g., Bi_2Te_3) commonly achieve $ZT \approx 1$near room temperature; advanced low-dimensional systems can reach $ZT \sim 2$ in optimized regimes, yet widespread deployment is constrained by cost, scarcity, and stability considerations [3]. Cementitious composites, while typically exhibiting lower $ZT(\approx 10^{-3}–10^{-2})$, offer scalability, cost advantages, and direct compatibility with infrastructure, motivating their investigation for distributed harvesting of low-grade heat [1].

1.2.3. Device-Level Considerations

Cement-based TE devices mirror classical module architecture: thermoelectric legs/units, electrodes, electrical insulation, heat exchangers, mechanical supports/encapsulation, and sensing/control for monitoring and optimization (Figure 1.1) [1,2,4]. The legs are connected thermally in parallel and electrically in series to build voltage while maintaining heat flow. For a device with internal resistance (R), current (I), and terminal voltage (V), the output power obeys

$$P=IV=I^2R \qquad \textit{Equation 1.7}$$

and achieves a maximum when the load resistance matches the internal resistance [1,2]. For a thermoelectric generator (TEG), the maximum power scales with the number of thermocouples (N), the Seebeck coefficient, and the applied ΔT [2]:

$$Pmax \propto \frac{(NS\Delta T)^2}{4R} \qquad \textit{Equation 1.8}$$

Device conversion efficiency η is bounded by the Carnot limit and improves with increasing average ZT across the operating temperature window [1,2]. In typical modules with practical ZT ~ 1, η is often below 10%, whereas higher ZT would asymptotically approach Carnot behavior [1].

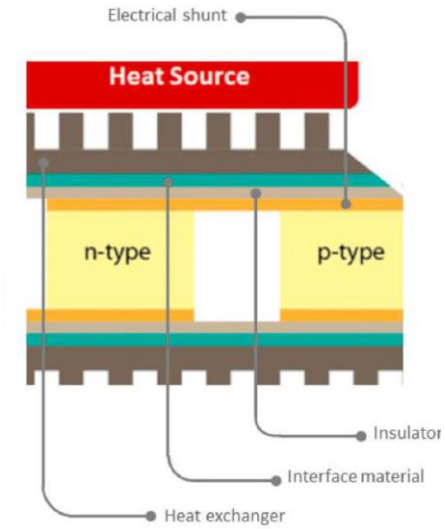


Figure 1.1 Schematic exploded representation of a thermoelectric module, showing the legs, electrodes, insulating layers, and heat spreaders/heat exchangers.

1.3. Types of Thermoelectric Transport Mechanisms

Thermoelectric energy conversion can arise from different charge transport mechanisms depending on the nature of the charge carriers and the medium through which they

migrate. Broadly, thermoelectric systems can be classified into three principal categories: electronic thermoelectric (e-TE) systems, ionic thermoelectric (i-TE) systems, and mixed ionic–electronic thermoelectric systems. This classification provides a fundamental framework for understanding thermoelectric behavior across material classes and is particularly relevant for cementitious materials, where multiple transport mechanisms often coexist.

In conventional thermoelectric materials, charge transport is governed by electrons or holes moving through a solid-state lattice. In these electronic thermoelectric systems, a temperature gradient induces carrier diffusion from the hot region to the cold region due to the higher energy and mobility of carriers at elevated temperatures, resulting in a measurable voltage difference as described by the Seebeck effect [1–3]. The magnitude and sign of the Seebeck coefficient are determined by the electronic structure of the material, including carrier concentration and the density of states near the Fermi level [4,5].

Electronic thermoelectric performance is governed by the interdependent parameters of Seebeck coefficient (S), electrical conductivity (σ), and thermal conductivity (k), which together define the power factor and the dimensionless figure of merit (ZT) [4,6]. Optimization in these systems requires balancing carrier concentration and mobility, as increasing electrical conductivity often reduces the Seebeck coefficient and increases thermal conductivity through electronic contributions described by the Wiedemann–Franz law [7]. Typical electronic thermoelectric materials, such as bismuth telluride–based compounds, exhibit Seebeck coefficients on the order of tens to hundreds of microvolts per kelvin and rely on band-structure engineering and carrier scattering mechanisms to achieve high efficiency [4,6].

In contrast, ionic thermoelectric systems operate through the thermally driven migration of ions within an electrolyte. This process is governed by the Soret effect, in which different ionic species exhibit distinct thermodiffusion behaviors under a temperature gradient, leading to charge separation and the generation of an electrochemical potential difference known as the ionic Seebeck effect [8–10]. Unlike electronic systems, ionic thermoelectricity requires the presence of a fluid or quasi-fluid medium that enables ion mobility [9].

A defining feature of ionic thermoelectric systems is their ability to generate very large Seebeck coefficients, often reaching the millivolt-per-kelvin range, significantly exceeding those of conventional electronic materials [8,9]. This enhanced thermopower arises from strong coupling between ion transport, solvation dynamics, and entropy flow [11]. Such high Seebeck responses make i-TE an attractive route for enhancing the thermoelectric efficiency of these systems. However, ionic systems typically exhibit lower electrical conductivity and are highly sensitive to environmental conditions such as temperature, humidity, and solvent content. Their performance is strongly influenced by factors including ion concentration, mobility, and interfacial electrochemical phenomena such as electric double-layer formation [8].

Between these two limiting cases lies a third class of materials: mixed ionic–electronic thermoelectric systems, in which both ions and electrons (or holes) contribute

simultaneously to charge transport. In such systems, ionic carriers migrate through electrolyte phases while electronic carriers are transported through conductive solid networks. The resulting thermoelectric response reflects the combined contributions of both carrier types and is often more complex than in purely electronic or ionic systems [12].

Depending on the relative magnitude and direction of ionic and electronic fluxes, these contributions may reinforce or oppose each other, leading to nonlinear voltage–temperature relationships or even polarity inversion [6,13]. Importantly, mixed conduction offers a pathway to partially overcome the intrinsic trade-off between Seebeck coefficient and electrical conductivity. Ionic transport can provide large thermopower, while electronic pathways enhance conductivity. When these mechanisms are properly aligned and engineered, they can contribute constructively, enabling simultaneous improvement of both parameters and thus enhancing the power factor [3,12,14].

Microstructure, interfacial properties, and carrier mobility strongly influence the interaction between ionic and electronic carriers. For example, the accumulation of ions under a temperature gradient can generate internal electric fields that modulate electronic transport, leading to transient or time-dependent thermoelectric responses [12]. Such coupling effects are particularly significant in heterogeneous or porous systems, where distinct transport pathways coexist and interact across multiple length scales [3].

1.4. Thermoelectric Behavior of Cementitious Materials

The macroscopic thermoelectric (TE) behavior of cementitious materials arises from the coupled evolution of electrical conductivity (σ), Seebeck coefficient (S), and thermal conductivity (κ), which are governed by the chemistry of the binder, the microstructural characteristics of the matrix, and the presence of functional fillers. Achieving useful thermoelectric performance in cement-based systems requires balancing these interdependent transport properties. Increasing electrical conductivity through conductive networks often reduces the Seebeck coefficient, while strategies aimed at lowering thermal conductivity may alter pore connectivity and influence ionic transport. Consequently, the thermoelectric response of cementitious materials reflects a complex interplay between material composition, microstructure, and charge-transport mechanisms.

1.4.1. Transport Mechanisms in Thermoelectric Cementitious Materials

Cementitious materials represent a unique class of thermoelectric systems in which multiple charge-transport mechanisms coexist and interact within the binder matrix. The thermoelectric response of these materials arises from the combined contribution of three principal pathways—ionic conduction, electronic conduction, and mixed ionic–electronic transport—whose relative importance depends on binder composition, moisture content, pore structure, and the presence of conductive additions. In intrinsically hydrated systems such as Portland cement paste and geopolymers, interconnected pore-solution networks enable ionic thermoelectricity, as widely reported in recent studies [8,10,12,15]. Concurrently, the incorporation of conductive fillers such as carbon fibers, carbon nanotubes, or graphene introduces electronically conductive pathways, enabling hybrid

transport behavior and further enhancing thermoelectric performance [3,4]. Moreover, most thermoelectric cement-based composites can operate as mixed ionic–electronic systems, where both carrier types contribute to the overall response.

1.4.1.1 Ionic Conduction

Despite the fact that ionic conduction constitutes the primary charge-transport mechanism in cementitious matrices lacking conductive fillers, the thermoelectric response of these materials has historically been interpreted predominantly in terms of electronic transport. Consequently, most early research efforts focused on enhancing thermoelectric performance through the incorporation of conductive additions such as carbon-based fillers, aiming to establish percolated electronic pathways within the matrix. This perspective persisted until very recently, when Wei et al. [15] systematically demonstrated that cement-based materials can exhibit a pronounced intrinsic ionic thermoelectric effect governed by pore-solution ion migration. The role of ionic mobility is most clearly evidenced by drying experiments, in which removal of pore solution suppresses ion transport and reduces the thermoelectric response to negligible values. This work marked a critical paradigm shift, establishing ionic thermodiffusion as the dominant mechanism in unmodified systems, and thereby opening a new research direction centered on chemically tunable, filler-free thermoelectric cementitious materials.

The fundamental mechanism of ionic thermoelectricity (i-TE) is schematically illustrated in Figure 1.2b. Under an applied temperature gradient ($\Delta T \neq 0$), mobile ionic species within the pore solution migrate from the hot side toward the cold side driven by thermodiffusion. Unlike electrons (Figure 1.2a), ions cannot enter the external circuit; instead, they accumulate at the electrode–electrolyte interface, forming localized charge regions. This ionic accumulation induces an internal electric field, which is balanced by electron flow in the external circuit, thereby generating a measurable voltage.

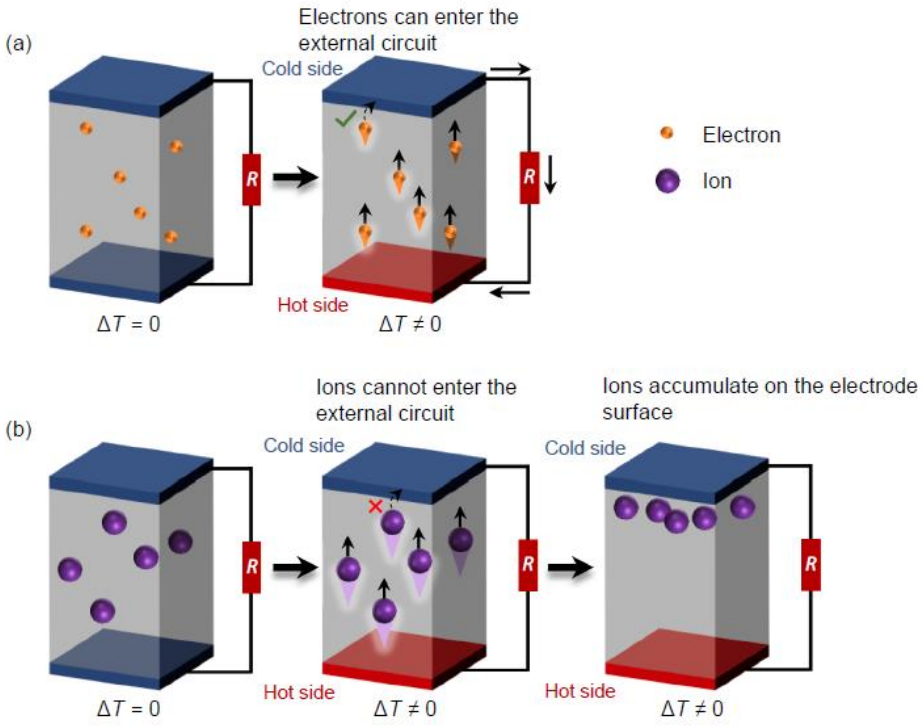


Figure 1.2 Schematic representation of (a) the electronic thermoelectric effect and (b) the ionic thermoelectric effect [15].

Growing evidence shows that ionic conduction represents the dominant mechanism responsible for thermoelectric voltage generation in alkali-activated materials [8,16–19]. Beyond this general description, Wang et al. [18] further clarified that the governing mechanism is long-range ionic migration through the bulk matrix rather than mere interfacial charge accumulation. In this framework, the geopolymer behaves as a multiphase ionic conductor consisting of a negatively charged aluminosilicate gel network intertwined with liquid-filled pore channels. Ionic transport occurs predominantly through the liquid phase, while the gel phase modulates ion mobility through electrostatic interactions and hydrogen bonding. Due to their higher mobility, Na^+ cations preferentially migrate and accumulate at the cold side, whereas OH^- anions lag behind and concentrate toward the hot side, resulting in internal charge separation that is ultimately converted into a measurable electrical signal through charge exchange processes at the electrode interfaces.

A similar mechanism is also reported in ordinary Portland cement, where thermoelectric behavior is likewise governed by pore-solution ion transport [15]. In sealed and well-hydrated systems, hydroxide ions (OH^-) dominate conduction, resulting in n-type thermoelectric behavior. However, this response is not intrinsic and can be tuned through pore-solution chemistry. Under controlled leaching, depletion of OH^- shifts the dominant carriers toward alkali and alkaline-earth cations (K^+, Na^+, Ca^{2+}), reversing the Seebeck polarity to p-type. After ~72 h of leaching, Seebeck coefficients as high as $S \approx 1.06$ mV K^{-1} and power factors of ≈ 0.060 μW m^{-1} K^{-2} have been reported in filler-free cement pastes, rivaling values obtained in composites with conductive additions [15]. This transition is governed by the relative contribution of ionic species, rather than moisture

content alone, reflecting shifts in dominant ionic species within the pore solution. Leveraging this mechanism, multi-element ionic thermoelectric devices based on conditioned OPC have achieved $S \approx 3.98$ mV K^{-1} under $\Delta T \approx 45$ °C. These findings revise earlier interpretations that linked thermopower primarily to moisture content [20,21], demonstrating instead that thermoelectric behavior in OPC is governed by ionic composition and conditioning history. These findings challenge the conventional view that thermoelectric behavior in Portland cement is negligible or purely electronic, demonstrating instead that OPC can function as a chemically tunable ionic thermoelectric material.

In addition to pore-mediated ionic transport in cementitious systems, ionic conduction can also originate from intrinsic lattice defects within the solid phase. A representative example is mayenite ($Ca_{12}Al_{14}O_{33}$), which exhibits ionic conductivity through oxygen species confined within its cage-like crystal structure. As reported by Rudradawong et al. [22], the introduction of nano-carbon induces the formation of oxygen vacancies, enabling ion hopping between adjacent cages and resulting in positive ionic conduction, as confirmed by a positive Seebeck coefficient. This mechanism represents a distinct solid-state pathway that complements pore-solution-based ionic transport, indicating that multiple ionic conduction modes may coexist depending on composition and microstructure.

- **Intrinsic Voltage and Electret Behavior in Cement-Based Materials**

In addition to thermally induced voltage generation, cementitious materials can exhibit an intrinsic electrical potential even in the absence of an applied temperature gradient. This inherent voltage is characteristic of electret materials and has been reported in both Portland cement [23] and metakaolin-based geopolymers [24]. Its presence indicates that cement-based systems can sustain internal charge separation arising from their physicochemical structure and ionic distribution.

The origin of intrinsic voltage is generally attributed to slight spatial inhomogeneity in pore-solution ion distribution. Despite thorough mixing, local variations in ionic concentration persist, leading to internal polarization. As described by Huang and Chung [23], this polarization separates positive and negative charge centers, which relax into a stable configuration that induces surface charges of opposite polarity. This behavior is analogous to classical electrets, where quasi-permanent internal electric fields arise from trapped or redistributed charges.

Experimental observations confirm that this voltage is non-negligible. In Portland cement, the intrinsic voltage varies in both magnitude and polarity and evolves during curing, stabilizing as ion mobility decreases [23]. In the metakaolin system, Li et al. [24] observed a ~10 mV voltage at zero temperature difference ($\Delta T = 0$), confirming the existence of an intrinsic component. It should be noted that the intrinsic voltage is approximately one order of magnitude higher than the TE response in these materials.

From a thermoelectric standpoint, intrinsic voltage has important implications. It shifts the thermoelectric voltage–temperature (ΔV–ΔT) relationship away from the origin, introducing an offset unrelated to the Seebeck effect. If not accounted for, this can lead to systematic errors in evaluating thermoelectric parameters, particularly in ionic systems

where internal charge distributions are sensitive to moisture, curing history, and pore-solution chemistry.

Overall, intrinsic voltage is an inherent electrochemical feature of cementitious materials, closely linked to ionic transport and microstructural heterogeneity. Its presence confirms the electret-like nature of these systems and highlights the need for careful interpretation of thermoelectric measurements.

1.4.1.2 Electronic Conduction

Electronic transport becomes significant when conductive or semiconductive fillers are incorporated into the cementitious matrix. In these systems, electrons or holes serve as the primary charge carriers, and the thermoelectric behavior is largely controlled by the dispersion, connectivity, and interfacial interaction of the conductive phases.

A key prerequisite for efficient electronic transport in cementitious composites is the formation of a continuous conductive network, which is governed by the percolation threshold. Below this threshold, charge transfer occurs primarily through electron tunneling between isolated conductive particles, resulting in limited conductivity. Once the percolation threshold is reached, a continuous three-dimensional network is established, enabling long-range charge transport and a sharp increase in electrical conductivity [17,25]. The relatively low percolation threshold of nanoscale carbon-based fillers (e.g., CNTs, CNFs, and graphene) allows the formation of such networks at low filler contents, minimizing adverse effects on the mechanical integrity of the matrix [17,26,27]. In addition, metal-oxide additions such as ZnO, TiO_2, or SiC can modify the electronic structure of the composite through interfacial energy-filtering effects that enhance the Seebeck coefficient [17,28,29].

Beyond network formation, interface engineering plays a decisive role in optimizing thermoelectric performance by simultaneously regulating charge carrier and phonon transport[17]. Interfaces between conductive fillers and the cementitious matrix can introduce energy barriers that selectively scatter low-energy carriers, thereby enhancing the Seebeck coefficient while maintaining sufficient electrical conductivity. At the same time, these interfaces act as phonon scattering centers, reducing thermal conductivity and improving overall thermoelectric efficiency [17,30].

Park et al. [26] provide experimental evidence that matrix chemistry controls the effectiveness of electronic conduction pathways, primarily through its impact on interface quality and conductive network formation. They investigated the thermoelectric behavior of carbon nanotube-reinforced composites based on both Portland cement and alkali-activated slag binders. Their results demonstrated that replacing the Portland cement matrix with alkali-activated slag significantly increased electrical conductivity and stabilized the Seebeck response. The improved ionic environment and enhanced interfacial bonding between the nanotubes and the AAS matrix promoted more efficient charge transport through the conductive network.

1.4.1.3 Mixed Ionic–Electronic Conduction

Many cementitious systems operate under the mixed ionic–electronic regime introduced in Section 1.3, with ions migrating through the pore solution and electronic carriers transported through conductive filler networks.

Competing ionic and electronic fluxes can produce nonlinear voltage–temperature behavior and polarity inversion; this has been observed experimentally in alkali-activated fly ash–slag blends [8]. Recent studies on reduced graphene oxide (rGO)–reinforced cement systems further demonstrate that a cooperative interaction between ionic and electronic carriers can be deliberately engineered. In these systems, electronic carriers (holes) are provided by rGO, while mobile ions (e.g., Ca^{2+}, Na^{+}, K^{+}) originate from the pore solution. Through controlled conditioning—particularly leaching treatments that reduce OH^{-} concentration—the thermoelectric polarity of the ionic contribution can be aligned with that of the electronic carriers, enabling synergistic charge transport [12].

This alignment results in a so-called mixed "ionic–electronic" thermoelectric cementitious composite (M-TECC), in which both carrier types contribute constructively to voltage generation under a temperature gradient. Consistent with the coupling mechanism outlined in Section 1.3, the rGO system exhibits a transient response characterized by an initial voltage peak followed by stabilization as ionic accumulation progressively compensates the electronic contribution (Figure 1.3) [12].

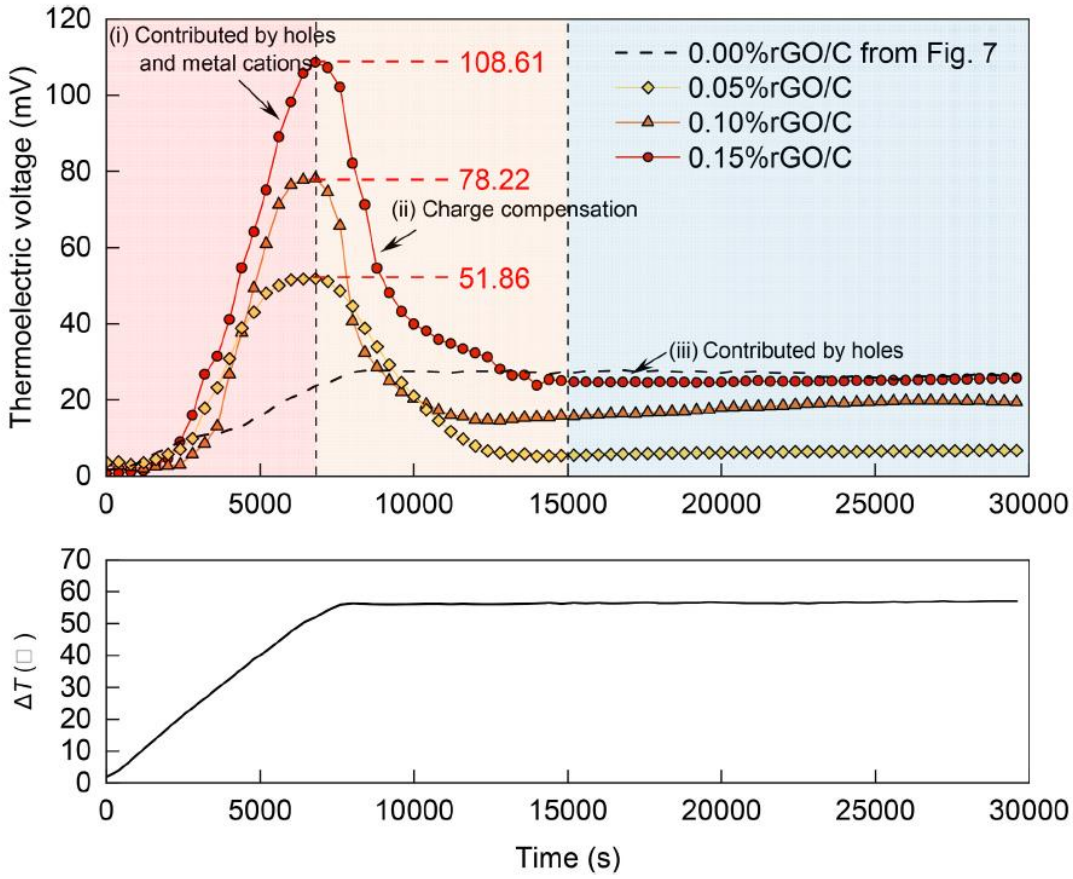


Figure 1.3 (a) Evolution of thermoelectric voltage with temperature after leaching for 0.05–0.15% rGO/C composites; (b) temporal variation of the temperature difference.[12].

This example confirms that the balance between ionic and electronic transport in cementitious systems is highly sensitive to conditioning history and matrix chemistry. Therefore, mixed ionic–electronic behavior distinguishes cementitious thermoelectric materials from conventional solid-state thermoelectrics and provides a versatile platform for performance optimization. By tailoring binder chemistry, pore structure, moisture content, and filler distribution, it is possible to control the relative contributions of ionic and electronic transport and to engineer synergistic interactions between them.

1.4.2. Thermal Transport and Figure of Merit

In cementitious materials, thermal conductivity is primarily governed by the porosity, moisture content, and connectivity of the binder matrix. Geopolymers generally exhibit lower thermal conductivity than Portland cement due to their amorphous structure and gel-like microstructure [24,31]. However, the incorporation of conductive fillers may increase thermal conductivity, which can reduce the temperature gradient across the material.

Consequently, binder design must simultaneously enhance electrical conductivity and the Seebeck coefficient while minimizing increases in thermal conductivity. The complex interaction between these parameters ultimately determines the achievable figure of merit ZT for cementitious thermoelectric materials.

1.4.3. Optimization of Thermoelectric Performance

A range of strategies has been proposed to improve thermoelectric performance in cement-based materials. These strategies can be broadly categorized according to their influence on binder chemistry, composite design, and microstructure and pore-structure engineering.

Binder chemistry plays a critical role in controlling ionic mobility and charge-carrier concentration. Adjusting the composition of alkali-activated systems can increase the concentration of mobile ions and enhance ionic thermoelectric effects [8,24]. Composite design should therefore be used to tune the mixed ionic–electronic balance primarily through control of conductive-network connectivity and pore-solution continuity [17,28,29].

Finally, microstructural design strategies aimed at controlling porosity and moisture distribution can help maintain electric double-layer activity while preserving the interconnected pathways necessary for charge transport [8]. Collectively, these approaches demonstrate that systematic control of binder chemistry, transport balance, and microstructure can significantly improve the thermoelectric properties of cementitious materials.

1.5. Binder Chemistry and Phase Composition

Binder chemistry plays a fundamental role in determining the thermoelectric (TE) behavior of cementitious materials. The chemical composition of the binder and the nature of its reaction products directly influence the type of charge carriers, their mobility, and the transport pathways available for both ions and electrons. Consequently, the

thermoelectric response of cement-based systems is closely linked to the structure and chemistry of the hydrated or activated binder phase.

Comparative studies across Portland cement (PC), alkali-activated slag (AAS), fly ash–slag blends, and metakaolin-based geopolymers demonstrate that binder chemistry governs not only the magnitude of the Seebeck coefficient and electrical conductivity, but also the stability and polarity (p-type or n-type) of the thermoelectric response. These effects arise from differences in pore-solution chemistry, microstructural connectivity, and the electronic structure of the reaction products formed during hydration or alkali activation.

1.5.1. Portland Cement Systems

Ordinary Portland cement represents the most widely used structural binder, yet its intrinsic thermoelectric properties are generally limited. Hydration of Portland cement produces a multiphase microstructure dominated by calcium–silicate–hydrate (C–S–H) gel together with crystalline phases such as portlandite (CH). Figure 1.4 illustrates the characteristic hydration products present in Portland cement systems, including the C–S–H gel network and associated crystalline phases that govern the electrical and thermal transport properties of the material. These phases exhibit wide band gaps (≈4.4–4.5 eV), consistent with low electronic conductivity and, consequently, modest PF in the absence of additional electronic pathways [2]. Conversely, the disordered, porous nature of hydrated cement pastes tends to suppress lattice thermal conductivity relative to ordered crystals, which is beneficial for maintaining ΔT across a structural element [2,3]. The net result is a characteristic trade-off at the composite level: relatively low (k) (favorable), but also low σ (unfavorable), with S and σ constrained by the underlying electronic structure of the hydration products [2]. As a result, unmodified Portland cement typically displays extremely small Seebeck coefficients, on the order of approximately +2.7 μV K^{-1}. The thermoelectric response of such systems is highly sensitive to moisture conditions and pore-solution chemistry [24]. Although conductive fillers can improve electrical conductivity and increase the power factor, the overall thermoelectric performance of Portland cement composites remains constrained by the insulating nature of the hydrated matrix.

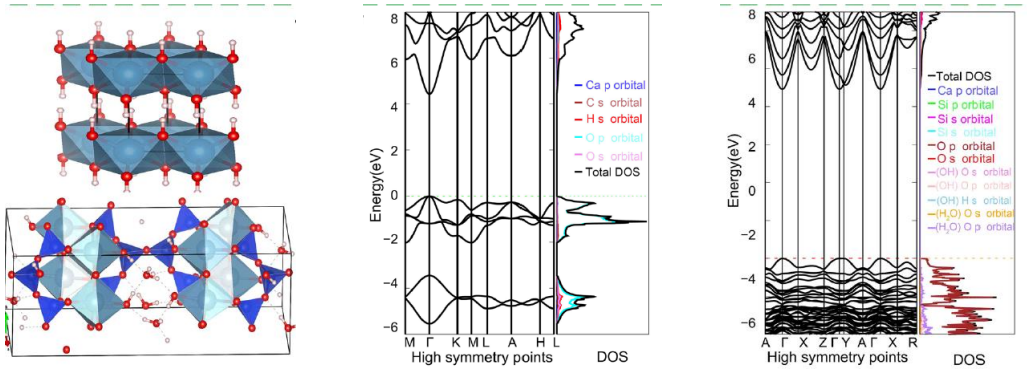


Figure 1.4 Schematic illustration of cement hydration products, showing the C–S–H network and portlandite plate-like phases, along with representative electronic band-gap features.

1.5.2. Alkali-Activated Materials and Geopolymers

Alkali-activated materials (AAMs) and geopolymers provide a fundamentally different binder environment compared with Portland cement. These binders are characterized by highly alkaline pore solutions, tunable Si/Al ratios, and strongly interconnected aluminosilicate networks. As a result, they offer a chemically flexible platform for controlling ionic transport, electrical conductivity, and thermoelectric polarity.

In contrast to Portland cement systems, the pore solution in alkali-activated binders contains high concentrations of mobile ions that can contribute directly to thermoelectric voltage generation. The presence of these mobile species, together with the ability to tailor the chemical composition of the binder, allows the thermoelectric response to be tuned through adjustments in precursor composition, activator chemistry, and curing conditions.

Furthermore, alkali-activated binders typically exhibit lower intrinsic thermal conductivity than Portland cement systems due to their cellular structure and the amount of air entrapped within closed small-cells.[31]. This characteristic supports the maintenance of temperature gradients across structural elements, which is beneficial for thermoelectric energy conversion.

1.5.2.1 Intrinsic Thermoelectric-Enabling Features of Alkali-Activated Cementitious Matrices

Alkali-activated materials (AAMs) and geopolymers exhibit a range of intrinsic physicochemical characteristics that are inherently favorable for thermoelectric (TE) functionality, even in the absence of conductive or semiconductive fillers. Unlike conventional Portland cement systems, where thermoelectric behavior is weak and largely incidental, the TE response of alkali-activated binders arises directly from their chemistry, pore-solution composition, and gel structure. Consequently, the binder phase itself can act as an active functional component in thermoelectric energy conversion.

These characteristics arise from several interconnected structural and chemical features, including the presence of mobile ionic charge carriers, electric double layers (EDL) effects at gel–pore interfaces, the amorphous structure of the aluminosilicate gel, and the existence of a hierarchical pore network. These features enhance the efficiency and magnitude of the previously described transport mechanisms.

- **Structural Characteristics of Alkali-Activated Binders**

The structural architecture of alkali-activated binders differs fundamentally from that of conventional Portland cement hydration products [24]. In Portland cement systems, the primary binding phase is calcium–silicate–hydrate (C–S–H), which typically forms layered structures with significant structural discontinuities as illustrated in Figure 1.5. These discontinuities include microcracks, nanoporosity, and interfaces between different hydration products such as C–S–H, calcium hydroxide, and ettringite. Such heterogeneity can impede charge carrier diffusion and limit the development of sustained electrical potential gradients.

In contrast, alkali-activated binders form continuous three-dimensional aluminosilicate frameworks composed of tetrahedrally coordinated silicon and aluminum atoms (Figure 1.4). Within this network, alkali cations such as Na^+ or K^+ occupy interstitial positions

that balance the negative charge associated with aluminum substitution in the tetrahedral framework. This single-phase, highly interconnected morphology reduces structural discontinuities and promotes more efficient transport of charge carriers.

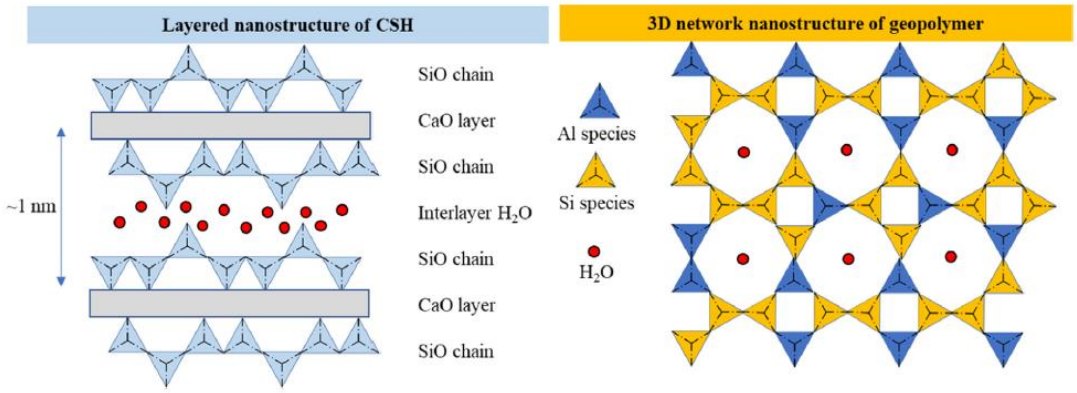


Figure 1.5 Comparative representation of the nanostructures of C–S–H and geopolymer materials[24]

The structural motif of the geopolymer network, often described by the Na–(Al–O–Si–O) framework, bears similarities to certain metal-oxide thermoelectric materials such as Na_xCoO_2. In both systems, the presence of alkali ions within an oxide network contributes to charge transport and influences thermoelectric behavior.

- **Mobile Ionic Charge Carriers in Alkaline Pore Solutions**

Ionic transport dominates thermoelectric response in these systems (see Section 1.4.1.1). Conditioning experiments further illustrate the importance of ionic mobility. Drying-induced suppression of ionic transport leads to a sharp reduction in Seebeck coefficient (see Section 1.4.1.1). Conversely, rehydration restores ionic mobility and re-establishes the thermoelectric response [8]. This behavior highlights a key advantage of cementitious thermoelectric systems: their inherent ability to reversibly regulate performance through environmental moisture. Unlike conventional thermoelectric materials that suffer from irreversible degradation, these systems can recover their functionality via simple rehydration.

- **Electric Double Layer Formation at Gel–Pore Interfaces**

In addition to bulk ionic transport, alkali-activated binders intrinsically form EDL at the interface between negatively charged aluminosilicate gel surfaces and the surrounding electrolyte-filled pores [8]. The negatively charged framework attracts cations from the pore solution, resulting in a layered distribution of ions adjacent to the gel surface.

Under a temperature gradient, ion redistribution within the EDL further enhances thermoelectric voltage. Experimental observations indicate that the EDL can significantly amplify the measured Seebeck response and may even contribute to polarity inversion in certain alkali-activated systems. The existence of this interfacial electrochemical structure therefore, represents an important intrinsic mechanism for thermoelectric voltage generation in porous ionic binders [8,17].

- **Amorphous Aluminosilicate Gel Structure**

The reaction products of alkali activation, commonly described as N–A–S–H and C–A–S–H gels, are predominantly amorphous. This amorphicity introduces structural disorder

and a high density of coordination environments for ionic species. Such disorder facilitates flexible ion migration pathways and enhances the mobility of charge carriers within the binder matrix.

Metakaolin-based geopolymers possess largely amorphous structures, which correlate with the high Seebeck coefficients observed in these systems [24]. Similarly, alkali-activated binders derived from fly ash often exhibit higher amorphous fractions than slag-rich systems, which contributes to their stronger intrinsic thermoelectric responses [8].

- **Hierarchical Pore Networks**

Alkali-activated binders contain a hierarchical pore structure consisting of gel pores typically smaller than 10 nm and capillary pores in the range of approximately 10–100 nm. Their primary role is to facilitate ionic transport, enabling charge migration across multiple length scales.

Microstructural investigations using mercury intrusion porosimetry and electron microscopy demonstrate that pore size distribution and connectivity strongly influence thermoelectric performance. Larger pores enhance transport kinetics and electrical conductivity, while nanoscale pores promote interfacial effects such as EDL formation [8].

- **Low Intrinsic Thermal Conductivity**

In addition to favorable ionic transport properties, alkali-activated binders generally exhibit relatively low thermal conductivity due to their amorphous structure and porous microarchitecture. Comparative studies between Portland cement and alkali-activated systems consistently show that geopolymer matrices possess lower thermal conductivity values [8,24,26]. This characteristic enhances the ability of the material to maintain thermal gradients while simultaneously supporting ionic transport within the pore solution.

- **Chemically Tunable Thermoelectric Polarity**

A distinctive feature of alkali-activated binders is the ability to tune thermoelectric polarity through adjustments in binder chemistry alone, without the need for external doping. Differences in precursor composition and pore-solution chemistry determine which ionic species dominate charge transport.

Fly ash-rich alkali-activated systems frequently exhibit p-type behavior due to the migration of hydroxide, while slag-rich binders may display n-type or bipolar responses depending on sodium cation concentration and ionic mobility. Hybrid fly ash–slag binders can exhibit intermediate behavior as multiple ionic species contribute to thermodiffusion [8,26].

This intrinsic tunability provides an unusual advantage compared with conventional thermoelectric materials, where carrier type is typically controlled through chemical doping.

The intrinsic thermoelectric response of alkali-activated binders arises from the combined effects of their chemistry, microstructure, and pore-solution composition. Mobile ionic charge carriers, electric double layer formation, amorphous gel structures, and

hierarchical pore networks collectively enable significant thermoelectric voltage generation without the need for conductive additions.

These properties position alkali-activated materials as promising platforms for developing multifunctional cementitious systems capable of harvesting low-grade thermal energy from the built environment.

1.5.2.2 Metakaolin-Based Geopolymers

Among alkali-activated binders, metakaolin-based geopolymers have demonstrated particularly strong thermoelectric responses. Seebeck coefficients approaching approximately 2000 μV K^{-1} have been reported, with corresponding figure-of-merit values on the order of $ZT \approx 10^{-4}$ [24]. These values are several orders of magnitude higher than those typically observed in conventional cement pastes, highlighting the unique potential of metakaolin-derived systems.

The origin of the large Seebeck response in metakaolin geopolymers has been the subject of evolving interpretation. Early studies [24,29,32,33] suggested that the thermoelectric behavior is not primarily governed by ionic concentration in the pore solution. In particular, it was observed that variations in ion concentration across different mix designs produced only minor changes in the thermoelectric response, indicating that simple ionic thermodiffusion could not fully explain the measured voltages. Instead, these works attributed the enhanced Seebeck effect to the intrinsic structural characteristics of the geopolymer network. X-ray diffraction analysis of metakaolin precursors reveals a highly amorphous structure dominated by silica and alumina phases (Figure 1.6.a). Upon alkali activation, these phases dissolve and reorganize into a continuous three-dimensional Na–(Al–O–Si–O) aluminosilicate framework. Specifically, this structure was proposed to enable increased charge-carrier density and mobility. Within this interpretation, the thermoelectric response was largely associated with an electronic conduction mechanism, further supported by the suggestion that the disordered structure broadens electronic band edges and facilitates hole transport, consistent with the frequently observed p-type behavior [24].

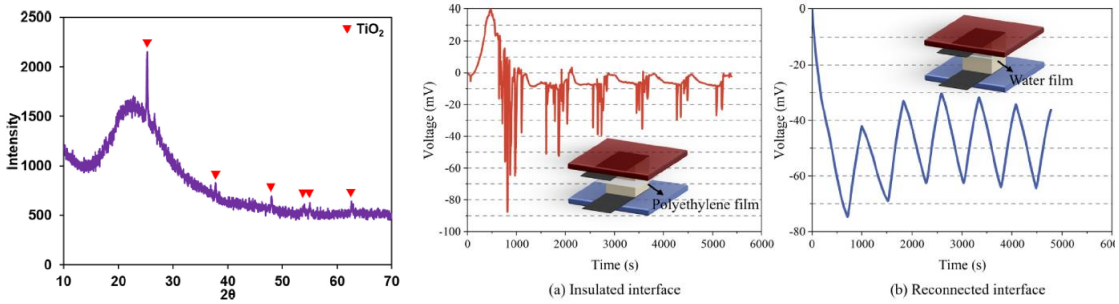


Figure 1.6 (a) XRD pattern of metakaolin [24]. (b) thermoelectric response of geopolymer with an insulated and reconnected interface [18].

However, more recent studies [8,18,19] have revisited this interpretation and provided strong evidence that the thermoelectric response in metakaolin-based geopolymers is predominantly governed by an ionic thermoelectric (i-TE) mechanism**.** Wang et al. [18], in particular, demonstrated that the generated thermovoltage depends on long-range ion migration through the pore solution rather than purely electronic transport. Beyond

conventional observations such as moisture sensitivity and ion-dependent polarity evolution, they performed a transport-blocking experiment in which ion migration was physically interrupted by inserting an insulating barrier within the geopolymer matrix (Figure 1.6.b). Under these conditions, the thermoelectric signal became unstable, noisy, and nearly vanished. Upon restoring ionic pathways and moisture continuity, a stable thermovoltage was immediately recovered.

These findings provide direct evidence that:

(i) The thermoelectric response requires continuous, long-range ionic transport through the bulk pore network, and

(ii) The contribution of electronic conduction or purely interfacial effects is secondary in comparison.

This shift in understanding highlights that the high thermoelectric performance of metakaolin geopolymers arises from a coupled interplay between their highly interconnected amorphous structure and efficient ionic transport pathways, rather than from electronic effects alone.

1.5.2.3 Fly Ash and Slag-Based Alkali-Activated Binders

The thermoelectric behavior of alkali-activated materials is strongly influenced by the composition of the precursor materials, particularly the presence of calcium-bearing phases. Fly ash–based systems typically contain lower calcium contents and form relatively porous aluminosilicate networks, while slag-rich systems generate denser calcium–aluminosilicate–hydrate (C–A–S–H) gels.

An experimental study by Ma et al. [8] demonstrates that these compositional differences significantly affect thermoelectric polarity. Under different temperature gradients between 20 °C and 80 °C, low-calcium alkali-activated fly ash binders often exhibit p-type thermoelectric behavior due to the predominance of sodium cations within the pore solution. In contrast, high-calcium alkali-activated slag systems tend to show n-type responses because hydrolysis of CaO produces an excess of hydroxide ions, which migrate toward the colder region of the material (Figure 1.7.a).

Blended fly ash–slag systems may display intermediate behavior, with thermoelectric polarity evolving during drying as changes in ionic concentration alter the dominant charge carriers. Microstructural analyses (Figure 1.7.b and c) reveal that increased slag content leads to the formation of dense C-(A)-S-H gel, which alters the pore architecture and ion transport pathways compared to the loose, cavity-filled structure of AAF matrices.

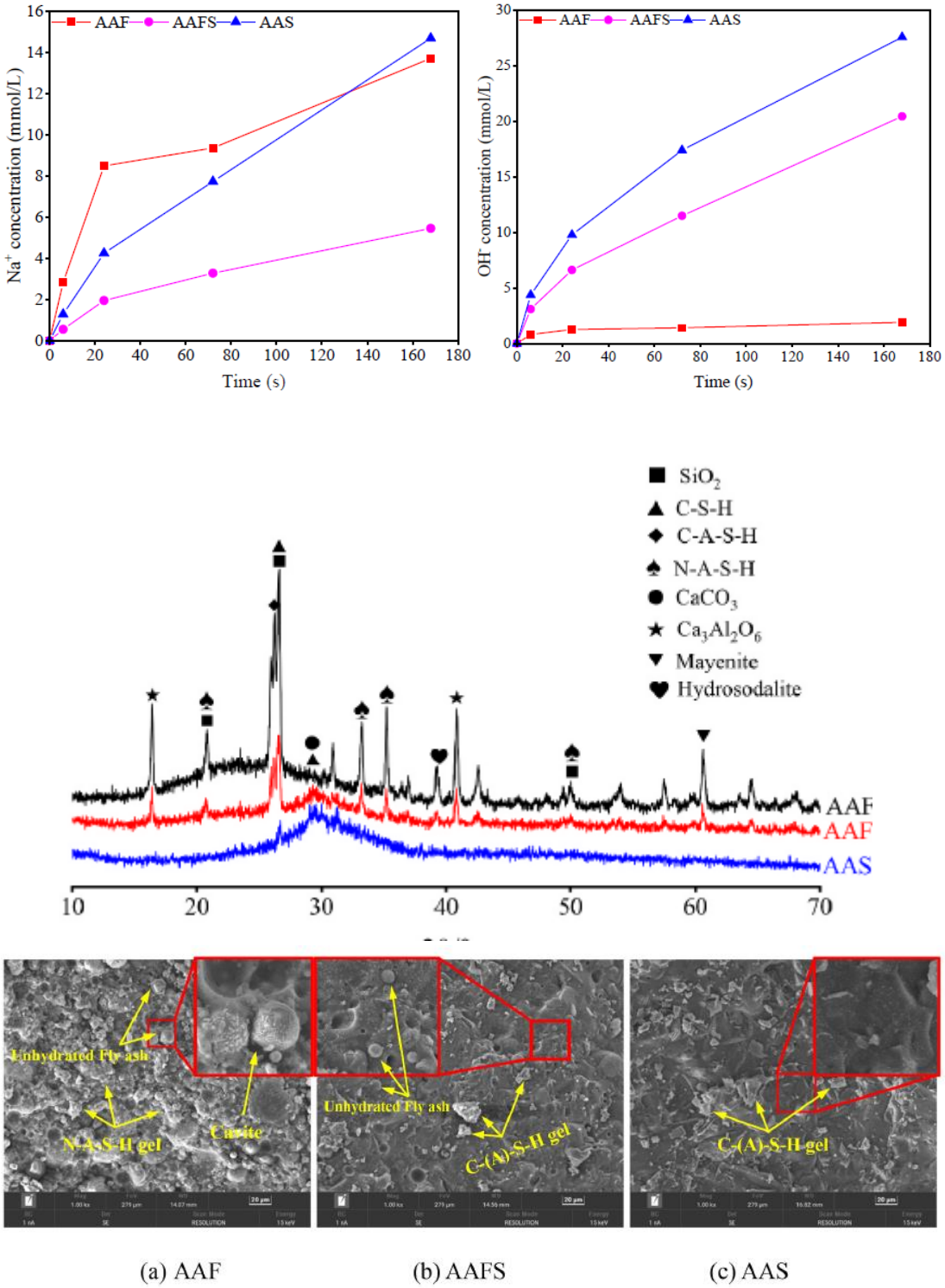


Figure 1.7 Variation in Na^+ and OH^- leaching concentrations; (b) XRD patterns; and (c) SEM images of AAF, AAFS, and AAS [8].

Microstructure governs thermoelectric performance by controlling the confinement, distribution, and mobility of ionic species within the pore network. Dense C-(A)-S-H structures in AAS promote OH^--dominated transport with high thermodiffusive asymmetry, whereas the more open N-A-S-H structure in AAF favors Na^+-dominated transport with reduced Seebeck magnitude because of lower mobility of Na^+. These

observations highlight the critical role of binder composition in controlling both the magnitude and polarity of thermoelectric signals in cementitious systems.

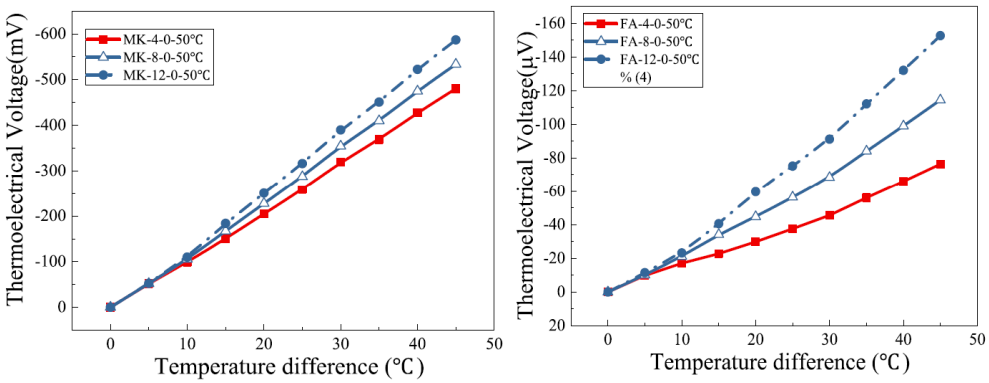
1.5.2.4 Influence of Activator Chemistry and Curing Conditions

In alkali-activated binders, the type and concentration of the activating solution strongly influence reaction kinetics, microstructural development, and thermoelectric properties. The ratio of sodium hydroxide to sodium silicate, for example, directly affects the Si/Al ratio of the resulting geopolymer network and therefore modifies both ionic mobility and structural connectivity.

Experimental investigations have shown that metakaolin-based geopolymers activated exclusively with sodium hydroxide can exhibit higher Seebeck coefficients than mixtures containing sodium silicate [24]. Optimal thermoelectric performance has been observed at Si/Al ratios close to 1 and Na/Al ratios of approximately 1.1, suggesting that the precise balance of aluminum, silicon, and alkali ions within the geopolymer framework plays an important role in controlling thermoelectric behavior.

Comparative studies of metakaolin (MK) and fly ash (FA) based alkali-activated systems have demonstrated that MK-based systems consistently deliver higher Seebeck coefficients and improved stability [33]. This difference is primarily attributed to the higher intrinsic reactivity of MK, which enables more uniform gel formation and facilitates stable ionic transport. As shown in Figure 1.8, increasing the alkali activator concentration leads to a systematic enhancement of the Seebeck coefficient in both MK and FA systems, reflecting the increased availability of mobile ionic species within the pore solution.

Curing temperature further modulates thermoelectric performance (Figure 1.8), with a markedly stronger influence observed in FA-based systems. Due to their higher activation energy, FA geopolymers typically require elevated curing temperatures to achieve sufficient reaction extent and develop effective ionic conduction pathways. In contrast, MK-based systems exhibit relatively stable Seebeck responses across a broader range of curing conditions, indicating a lower sensitivity to thermal activation [29,33]. Additionally, the incorporation of slag has been shown to reduce the Seebeck coefficient, particularly in FA-based mixes. This effect is associated with the formation of denser microstructures, which limit pore connectivity and restrict ionic mobility, ultimately suppressing thermodiffusive charge transport [33].



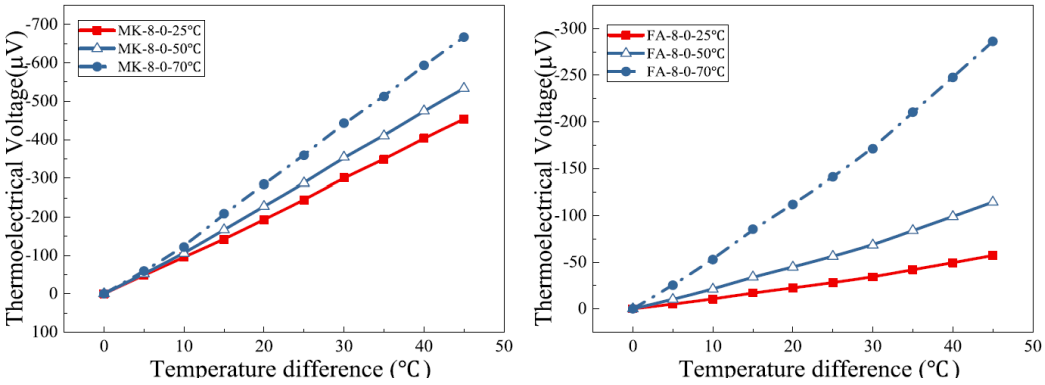


Figure 1.8 Seebeck voltage as a function of temperature difference for geopolymers prepared with (a) different alkali concentrations and (b) different curing temperatures.

1.6. Functional Additions for Thermoelectric Cementitious Composites

The intrinsic thermoelectric response of cementitious matrices is generally limited by the low electrical conductivity of hydration products and the restricted mobility of electronic charge carriers. Consequently, a widely adopted strategy for enhancing thermoelectric performance involves incorporating functional additions that introduce additional charge carriers and create low-resistance transport pathways within the composite.

Over the past two decades, numerous studies have investigated the use of conductive fillers in cement-based systems. These additions span a broad range of materials, including carbon fibers, graphite and graphene derivatives, carbon nanotubes, metals, and metal oxides. Each class of filler modifies electrical and thermal transport through distinct mechanisms, including the formation of percolating conductive networks [2,3], interfacial energy filtering [2], and microstructural modifications that influence pore connectivity and hydration processes [2].

In general, the incorporation of functional fillers improves thermoelectric performance through several complementary effects. First, conductive additions can establish electronic transport pathways that significantly increase electrical conductivity and the resulting power factor. Second, certain fillers can influence the magnitude and polarity of the Seebeck coefficient by modifying carrier type or by enabling p–n thermocouple configurations (carbon vs. steel fibers; p/n pairing) [1,3]. Third, nanostructured additions can introduce interfaces that scatter phonons or selectively filter charge carriers, thereby enhancing the Seebeck coefficient while limiting increases in thermal conductivity. Finally, filler–matrix interactions may influence the hydration process and microstructural evolution of the cement paste, indirectly affecting thermoelectric transport.

These mechanisms collectively explain why the incorporation of functional additions has become the primary strategy for improving the thermoelectric properties of cementitious composites [2,3].

1.6.1. Carbon-Based Fillers

Carbon-based materials represent the most widely investigated class of conductive additions in thermoelectric cementitious composites. Their high electrical conductivity, chemical stability, and compatibility with cementitious matrices make them particularly attractive for establishing electronic transport networks within otherwise insulating binders.

1.6.1.1 Carbon Fibers

Carbon fibers were among the earliest conductive fillers shown to impart measurable thermoelectric functionality to cementitious materials. The pioneering work by Sun et al. [34] demonstrated that carbon fiber–reinforced Portland cement composites exhibit a detectable Seebeck effect, establishing carbon-based reinforcements as viable pathways for introducing electronic conduction into cement matrices.

Subsequent studies showed that thermoelectric performance depends strongly on fiber content, dispersion, and interfacial bonding. An optimal content of ~1 wt.% is frequently reported, corresponding to the formation of a percolating conductive network that maximizes electrical conductivity while preserving microstructural connectivity [35–37].

Surface modification further enhances performance. Bromine-intercalated fibers increase the Seebeck coefficient [36], while pyrolytic-carbon–coated fibers improve both the power factor and figure of merit. Although ZT values remain modest ($ZT \approx 3.11 \times 10^{-3}$ near 55 °C), these results highlight the role of interface engineering in enhancing thermoelectric performance without compromising structural integrity [38].

1.6.1.2 Carbon Nanotubes

CNTs provide one-dimensional, high-aspect-ratio pathways that increase electrical conductivity and tune the Seebeck response in cementitious matrices, while enabling carrier-type control and device-level demonstrations. A landmark study by Tzounis et al. [21] incorporated p- and n-doped MWCNTs into OPC to form p/n legs and assemble a structural TEG, achieving an open-circuit voltage of −0.871 mV at $\Delta T \approx 10$ K, thereby establishing a viable route for cement-based thermoelectric device design.

Vareli et al. [39] developed a structured OPC/SWCNT generator (0.5 wt.%, 28 days), achieving $PF = 2.89 \times 10^{3}$ μW m^{-1} K^{-2} and P_max = 5.02 μW at $\Delta T = 50$ K (see Figure 1.9a), representing a key step toward practical applications. In alkali-activated systems, the same group reported SWCNT composites with $PF = 0.414$ μW m^{-1} K^{-2} and module P_max = 0.695 μW at $\Delta T = 60$ K (Figure 1.9b) [40], highlighting binder chemistry as a factor in performance optimization.

At the device scale, hybrid architectures combining SWCNTs with nanocarbon black (nCB) to enhance carrier filtering and reduce internal resistance have achieved state-of-the-art performance, with $S = +4644.2$ μV K^{-1}, $PF = 1.51 \times 10^{4}$ μW m^{-1} K^{-2}, and P_max = 2401.9 mW (power density = 1.2 W m^{-2}) at $\Delta T = 25$ K [41]. Collectively, these results establish CNTs as versatile additions enabling (i) electronic percolation to enhance $S^2\sigma$, (ii) formation of p/n-type cement legs for thermocouple modules, and (iii) device-level optimization via hybridization and series–parallel configurations.

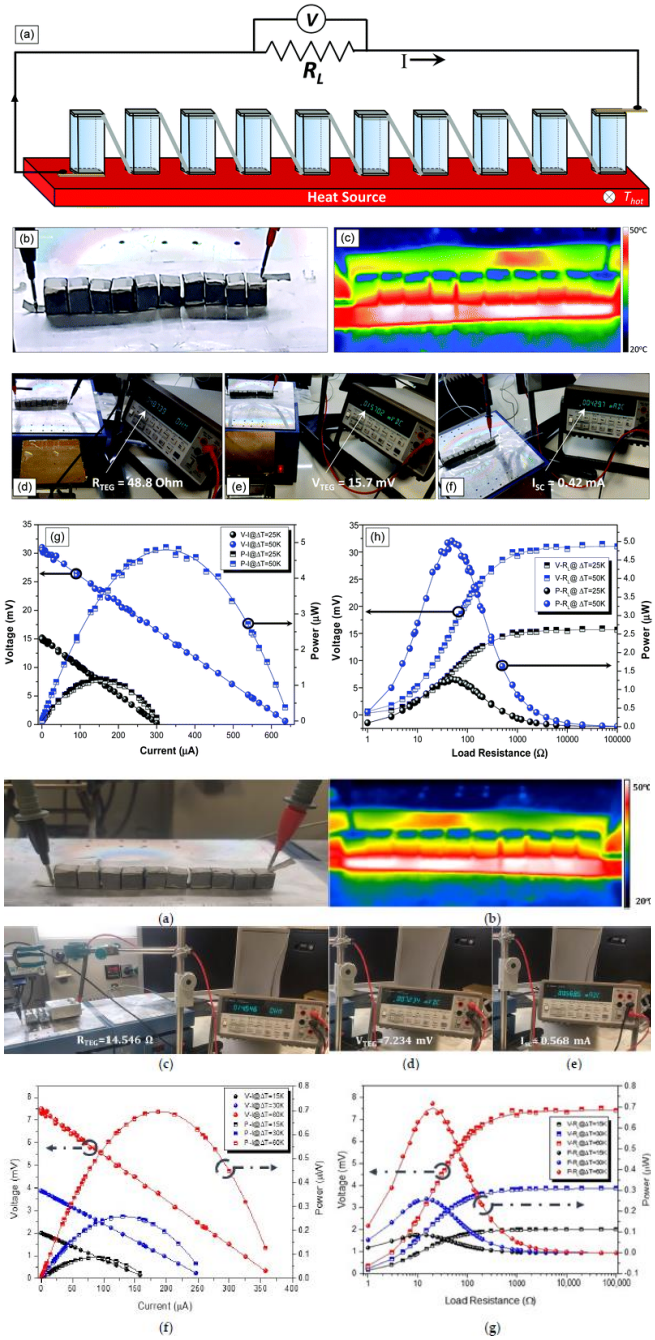


Figure 1.9 Schematic illustration and photographs of cement-based thermoelectric generator (TEG) modules, showing the thermal distribution (IR image), electrical characterization, and output performance of (a) OPC/SWCNT [39] and (b) Alkali-Activated/SWCNT [40].

Building on CNT-enabled 1D transport, the next section examines graphene/graphite additions, where 2D/3D carbon networks further modulate σ, S, and k through percolation and interfacial scattering, offering additional opportunities for energy filtering and contact engineering [1].

1.6.1.3 Graphene and Graphite

Graphite powders and graphene nanoplatelets (GNPs) introduce extended π-electron networks into cement matrices, forming efficient electronic pathways while interacting with pore structure and interfaces. Expanded graphite (EG), with its lamellar high–surface-area sheets, markedly increases electrical conductivity and, within specific

temperature ranges, enhances the Seebeck response, with performance governed by percolation, porosity, and microcrack control. EG–cement composites exhibit semiconducting behavior with temperature-dependent Seebeck coefficients and conductivity increasing from ~0.2 to ~24.8 S cm^{-1} with EG content, alongside ZT on the order of 10^{-4}–10^{-3} at ~70–100 °C; these trends reflect enhanced carrier mobility and anisotropic transport in graphitic layers [42].

Hybrid EG systems further demonstrate the impact of interfacial design. Combining EG with defect-engineered ZnO (oxygen-deficient, reduced atmosphere) increases conductivity and yields significant power factors with elevated |S| and ZT (e.g., PF ~10^2 μW m^{-1} K^{-2} and ZT ~10^{-2} at ~70 °C) [43]. Similar enhancements are reported for EG combined with indium tin oxide (ITO) or MnO_2, improving both conductivity and Seebeck magnitude relative to graphite-only systems [44,45]. Moisture content also plays a critical role: in EG/carbon-fiber composites, |S| peaks at intermediate moisture levels, while conductivity and power factor maximize at slightly lower moisture, highlighting the coupling between ionic/phononic transport and the electronic graphitic network [20].

For graphene-based additions, GNPs enhance thermoelectric response by enabling carrier transport through percolated 2D networks while scattering phonons at graphene–cement interfaces, helping sustain temperature gradients. GNP–cement composites exhibit positive S with conductivity increasing with GNP content. Hybridization with ZnO nanoinclusions further improves conductivity and |S|, yielding order-of-magnitude increases in ZT (from ~10^{-4} to ~10^{-2} depending on composition and temperature) [43]. Incorporating transition-metal oxides (Fe_2O_3, ZnO, MnO_2) alongside GNPs similarly increases |S| above 100 μV K^{-1} while maintaining useful conductivity [46].

1.6.1.4 Carbon Black

Carbon black (CB) is a low-cost, quasi-spherical carbon filler that readily forms conductive networks in cement pastes at moderate dosages, increasing electrical conductivity while largely preserving the matrix's low thermal conductivity. CB-based composites typically exhibit Seebeck coefficients of 7–25 μV K^{-1} and conductivity of ~350–480 S m^{-1}, yielding power factors of 10^{-5}–10^{-4} W m^{-1} K^{-2} and ZT on the order of 10^{-5}–10^{-4} under building-relevant temperatures, positioning CB as a scalable enabler of electronic percolation in cement composites [22].

Beyond electronic transport, CB can interact with ionic thermopower. In mayenite cement ($Ca_{12}Al_{14}O_{33}$) composites, nano-CB promotes positive ionic conduction, indicating coupled ionic–electronic contributions under practical moisture conditions, which is advantageous for room-temperature operation where pore-solution dynamics are significant [22].

At the device scale, CB shows its strongest impact in hybrid architectures with single-walled carbon nanotubes (SWCNTs). Incorporation of nano-carbon black (nCB) increases interfacial area and induces energy filtering via selective scattering of low-energy carriers, enhancing the Seebeck coefficient while reducing internal resistance through a percolated carbon network. A structured hybrid cement-based TEG demonstrated Seebeck coefficients exceeding the millivolt-per-kelvin range and power

factors on the order of 10^{-2} W m^{-1} K^{-2}, enabling high device-level output and ~W m^{-2} power density at modest ΔT [41].

1.6.2. Metallic Fillers

Metallic additions represent another class of conductive fillers capable of enhancing electrical transport in cementitious composites. Among these materials, steel fibers are particularly attractive because they can simultaneously improve mechanical performance and electrical conductivity.

1.6.2.1 Steel Fibers

Although steel fibers (SFs) are primarily introduced for mechanical reinforcement and crack bridging, they also provide electronic pathways in cementitious matrices. Early work by Wen & Chung [47] showed that SF–cement composites can form rectifying junctions, where dissimilar pastes and/or fiber–matrix interfaces exhibit diode-like I–V characteristics consistent with pn-like or nn^+ junction behavior. Combined with the low contact resistance of steel, this explains the marked increase in electrical conductivity as the fiber network approaches percolation. In terms of thermopower, SF systems generally exhibit smaller Seebeck coefficients than CF/CNT analogues (often electron-dominant), with both sign and magnitude governed by interface chemistry, moisture state, and pairing of dissimilar pastes [48].

From an application perspective, SFs enable multifunctional designs where structural integrity and charge transport coexist: they enhance σ while preserving load-bearing capacity, can act as embedded current collectors or electrodes, and—when combined with carbonaceous phases or dissimilar cement matrices—contribute to pn-like configurations for thermocouple modules. However, design must balance conductivity gains against potential increases in thermal conductivity (reducing ΔT) and address durability concerns (e.g., corrosion/passivation, interface stability), as evolution of the steel–cement interface can alter both σ and the Seebeck response over time [3,49,50].

1.6.3. Metal-Oxide Thermoelectric

Transition-metal oxides have emerged as versatile, low-cost additions that can tune both carrier type and carrier energy in cementitious matrices. Two complementary mechanisms are typically implicated: (i) semiconducting contributions from the oxide phase itself (often p- or n-type), and (ii) interfacial energy filtering at oxide–cement (or oxide–carbon) boundaries that scatters low-energy carriers and increases the Seebeck coefficient without proportionally penalizing conductivity. Reviews consistently report large Seebeck gains with oxides such as MnO_2, ZnO, Fe_2O_3, and doped ITO, together with binder/porosity effects that modulate ionic transport and thermal conductivity.

1.6.3.1 Manganese Oxide

Nanostructured MnO_2 exhibits intrinsically high thermopower, which translates into substantial Seebeck enhancement when blended into cement. Ji et al. showed that MnO_2 nanorods increase |S| by 30–200× versus plain or carbon-fiber-reinforced cement, albeit with lower σ; the net result is a higher ZT at building-relevant temperatures [51].

Extending this approach, an MnO_2/carbon-fiber nano-composite optimized at 0.8 wt.% of cement achieved S ≈ 2.88 mV K^{-1} and ZT ≈ 2.12 × 10^{-3}, orders-of-magnitude above CF-only baselines [52].

Surface-modified/coat-treated CFs with MnO_2 further improved both TE and mechanical performance of the sulfate aluminate cement composite, reinforcing the value of oxide–carbon interfaces in these hybrids [53].

1.6.3.2 Zinc Oxide

Multiple studies indicate that nano-ZnO increases S while raising σ (~+37%) and lowering k (~−9%) by altering hydration kinetics (e.g., transient $Zn(OH)_2$ formation) and pore solution chemistry—an unusually favorable three-way shift for PF and ZT [3,30,43,54]. In graphene-oxide hybrids, GNP+ZnO composites tripled S and pushed ZT to ~10^{-2} under moderate ΔT, demonstrating strong oxide–carbon synergy [43].

In alkali-activated materials, a similar ZnO-driven enhancement of thermoelectric performance has been reported. In high-ductility geopolymer composites incorporating red mud, nano-ZnO (0.5–2.0 wt.%) increased the Seebeck coefficient (up to ~29 μV K^{-1}), strongly boosted electrical conductivity (over one order of magnitude), and slightly reduced thermal conductivity, resulting in a ZT increase by more than an order of magnitude. Unlike Portland-cement systems, ZnO did not alter the geopolymer gel structure but improved carrier transport through modified aluminosilicate networks and improved nanoparticle dispersion, particularly in fiber-reinforced matrices [28].

1.6.3.3 Iron Oxide

Nano-Fe_2O_3 has been combined with carbon fibers to create dense, well-dispersed microstructures; with appropriate surfactants, mixes have reached S ≈ 1.12 mV K^{-1} and ZT ≈ 8.5 × 10^{-5} at ~85 °C while improving mechanical properties [55].

Side-by-side comparisons with ZnO show similar Seebeck trends at equal loadings, with ZnO typically delivering higher σ at a given content [56].

1.6.3.4 Copper Oxide

As a p-type semiconductor, Cu_2O can inject hole carriers and shift the net thermopower positive; cement mixes incorporating Cu_2O reported enhanced TE efficiency relative to controls, positioning Cu_2O as a practical, earth-abundant p-type additions for structural TE elements [57].

1.6.3.5 Broader oxide landscape (ITO, $Ca_3Co_4O_9$, etc.)

Beyond the classics, defect-engineered ITO and layered cobaltites have been explored to raise S via band-structure and defect-chemistry control, again leveraging interfaces for energy filtering in carbon-rich matrices [44,58].

Metal-oxide additions provide several levers at once: they can increase S through intrinsic semiconducting behavior and interfacial scattering, shift carrier type (e.g., Cu_2O → p-type), and co-tune σ and k via hydration/pore-structure effects (notably with ZnO/AZO).

1.6.4. Hybrid Carbon–Oxide Systems

Recent studies demonstrate that combining carbon-based fillers with metal oxides can produce synergistic thermoelectric effects. In these hybrid systems, the conductive carbon network provides efficient carrier transport pathways, while oxide nanoparticles modify the electronic structure and introduce interfacial energy-filtering effects.

Examples include graphene–ZnO [43] nanocomposites and graphene combined with transition-metal oxides such as MnO_2 or Fe_2O_3 [46]. These hybrid materials exhibit improved Seebeck coefficients and enhanced power factors due to the combined influence of electronic percolation and interfacial carrier filtering.

1.6.5. Inorganic and Dielectric Functional Fillers

In addition to conductive additions, certain inorganic fillers with limited electrical conductivity can enhance thermoelectric performance via interfacial effects, charge-carrier modulation, and microstructural regulation.

Nano-sized silicon carbide (SiC) has been identified as an effective modifier in geopolymer systems despite its wide bandgap and lack of percolated conductive pathways. Cai and Li [29] showed that incorporating nano-SiC (20–40 nm) significantly increases the Seebeck coefficient in both fly ash- and metakaolin-based geopolymers, with a monotonic dependence on SiC content. The author attributed this enhancement to quantum confinement effects, where reduced dimensionality modifies the density of states near the Fermi level, amplifying the Seebeck coefficient without a proportional rise in electrical conductivity. The effect is more pronounced in metakaolin-based systems due to their finer aluminosilicate gel structure and higher fraction of low-dimensional features, which strengthen interfacial coupling between SiC and the matrix. Consistently, curing temperature exerts limited influence on the Seebeck response, indicating the dominance of filler-induced electronic effects over thermal processing parameters.

In contrast, fully insulating glass beads act as microstructural regulators rather than electronic modifiers. Liang et al. [16] reported that glass bead incorporation significantly enhances the Seebeck coefficient in metakaolin-based geopolymers, reaching 1.24 mV K^{-1} at 50 wt.%—nearly double that of the unmodified matrix. Pore structure analysis revealed a substantial increase in nanopores (10–50 nm), which facilitate ion thermodiffusion and strengthen electric double-layer effects under a temperature gradient. Concurrently, the ultralow thermal conductivity of glass beads (≈0.018 $W \cdot m^{-1} \cdot K^{-1}$) reduces the composite thermal conductivity, sustaining larger internal temperature gradients and further amplifying the thermoelectric voltage.

In both systems, performance gains are achieved without continuous electronic conduction pathways, demonstrating that high Seebeck coefficients in geopolymer thermoelectrics can arise from interfacial polarization, density-of-states modulation, and regulation of ionic transport.

1.6.6. Section Summary

Each class of filler offers distinct mechanisms for tuning electrical conductivity, thermal transport, and Seebeck response. The cumulative research has shown that while carbon-

based reinforcements primarily boost electrical pathways, oxide additions introduce semiconducting behavior, and hybrid systems exploit interfacial synergy to maximize power factor and figure of merit, while inorganic and dielectric additions regulate ionic TE response. These trends are summarized in Figure 1.10, which compares the effect of different fillers on the key thermoelectric parameters, electrical conductivity, thermal conductivity, Seebeck coefficient, and ZT, highlighting both the progress achieved and the diverse strategies pursued to tailor multifunctional cementitious composites.

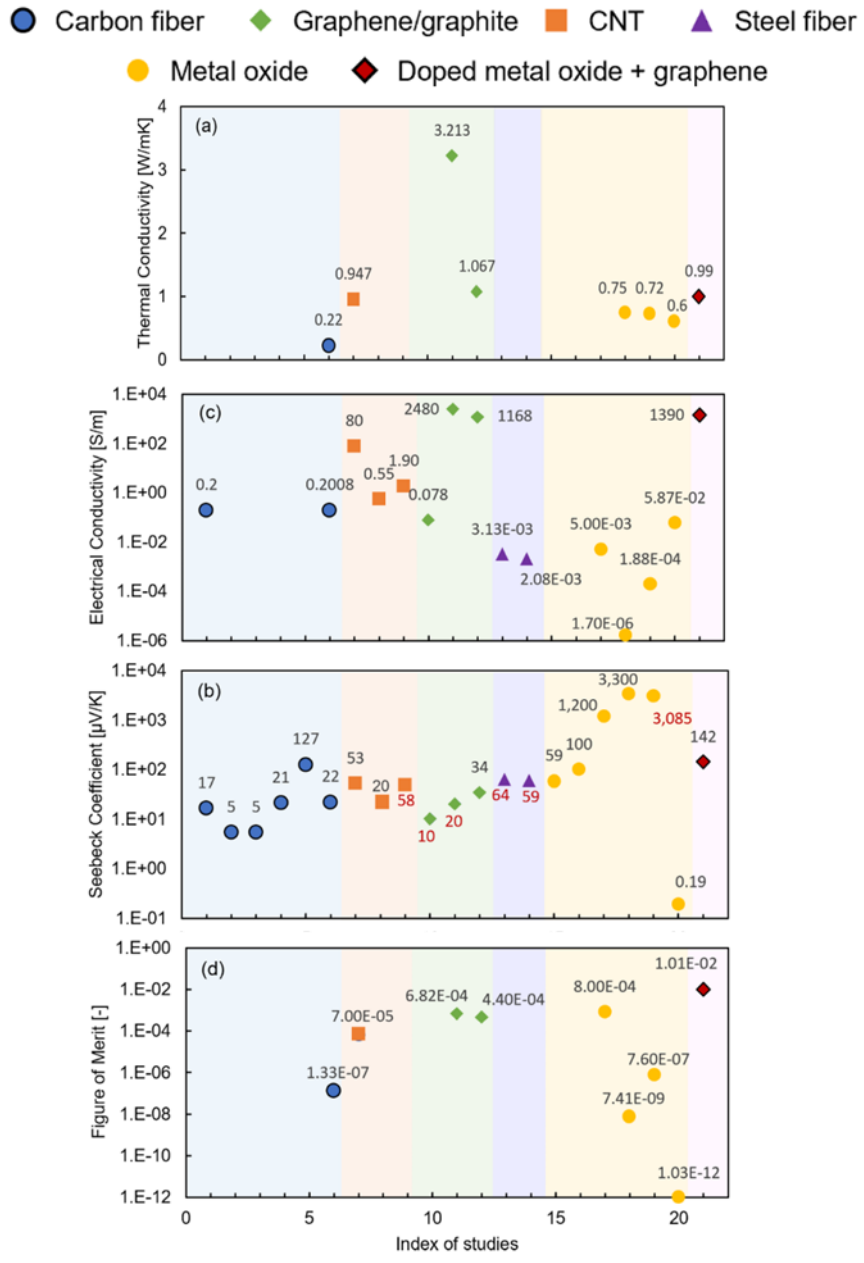


Figure 1.10 Reported effects of functional additives on the thermoelectric performance of cement-based materials.

Although functional fillers can substantially improve electrical conductivity and, in some cases, power factor, this strategy often introduces challenges related to dispersion, cost, percolation control, mechanical compromise, and increased thermal conductivity. For this

reason, the present thesis focuses primarily on ionic and moisture-mediated thermoelectricity in cementitious matrices, where high Seebeck coefficients can be obtained without relying on high filler loadings. Functional additions are therefore treated here as an important comparative route, while the experimental chapters emphasize binder chemistry, pore-solution transport, intrinsic voltage control, and device architecture.

1.7. Microstructure and Pore-Structure Engineering

Although the thermoelectric response of cementitious materials originates from the chemistry of the binder and the presence of mobile charge carriers, the effectiveness of thermoelectric transport is ultimately governed by the microstructural pathways available for carrier migration. In cementitious systems, microstructure—including porosity, pore connectivity, moisture distribution, and interfacial architecture—plays a central role in determining electrical conductivity, ionic mobility, and the magnitude of the Seebeck response.

Across the body of literature on thermoelectric cement-based materials, microstructure engineering emerges as the key link between chemical composition and macroscopic thermoelectric performance [16,17,24,27–29,31,33,59]. Variations in pore size distribution, saturation state, and interfacial structure directly influence both the mobility of ionic species and the formation of EDL within the pore network.

Within this framework, microstructure engineering governs the effectiveness of thermoelectric transport. Filler-based composites rely on percolating electronic networks, while ionic systems exploit electrolyte-filled pore channels.

1.7.1. Porosity, Water Distribution, and Ionic Transport

In alkali-activated materials (AAMs) and geopolymer systems, thermoelectric behavior is strongly governed by the pore network because ionic transport depends on the continuity, size distribution, and saturation of electrolyte-filled pathways. Water is therefore not merely a passive component of the microstructure; its spatial distribution directly determines whether ions can migrate efficiently through the matrix and generate a measurable thermoelectric response [8].

Insights from ^{1}H low-field nuclear magnetic resonance (HLF-NMR) show that water in these systems can be classified into gel interlayer water, adsorbed water, and capillary (free) water, each contributing differently to ionic mobility and transport continuity [8]. This distinction is important because not all pore water contributes equally to thermoelectric transport: mobile ions are most effectively conducted through continuous aqueous pathways, whereas more strongly bound water mainly influences local interfacial environments.

The influence of pore structure is particularly evident when comparing alkali-activated fly ash (AAF), alkali-activated slag (AAS), and blended fly ash-slag (AAFS) systems as discussed in section 1.5.2.3. Because ions are the primary charge carriers in these systems, thermoelectric performance shows a non-linear dependence on moisture state. Under saturated conditions, the abundance of interconnected liquid pathways favors ionic

transport and maximizes electrical conductivity and power factor. During partial drying, evaporation increases the ionic concentration of the remaining pore solution, which can temporarily enhance the Seebeck coefficient. However, further moisture loss progressively breaks pore continuity, sharply reducing electrical conductivity and power factor. In the fully dried state, after prolonged drying of approximately 168 h, the near absence of continuous pore solution suppresses ionic migration almost completely, producing only negligible thermoelectric voltages (approximately −1.8 to 2 mV). Thus, thermoelectric behavior is controlled not simply by the amount of water present, but by the coupled effects of pore connectivity, water distribution, and the concentration and mobility of ionic species such as Na^+ and OH^- within the pore solution [8].

1.7.2. Nanopores and Electric Double-Layer Effects

Beyond this bulk transport effect, pore size also influences thermoelectric response at the nanoscale. In metakaolin-based geopolymers, nanopores in the range of approximately 10–50 nm have been shown to contribute disproportionately to the Seebeck coefficient [16]. Their role is twofold. First, they act as confined ionic transport channels that support thermally driven migration of hydrated cations. Second, because geopolymer pore walls are negatively charged, these confined pores promote electric double-layer (EDL) formation through cation accumulation near the surface. Under a temperature gradient, ion redistribution within these nanopores can therefore generate an additional voltage contribution beyond classical bulk thermodiffusion. Nanoscale pore structure thus affects thermoelectric performance not only by modifying ionic mobility, but also by amplifying interfacial electrochemical effects.

1.7.3. Interfacial Water Layers and Electrode Coupling

A further contribution arises at the electrode–material interface, where microvoids at the electrode–binder boundary accommodate a thin microlayer of water that connects the solid electrode to the electrolyte-filled pore network [8]. Rather than acting as a passive bridge, this interfacial water layer functions as an active gateway that regulates ion entry and exit under a temperature gradient, thereby enabling coupling between bulk ionic transport and external electrical measurement. The presence of these microvoids has been directly evidenced by SEM analysis in recent studies, which revealed discontinuities along the interface where moisture accumulates to form a localized hydrated interphase[18].

Within this interfacial microlayer, electrostatic adsorption and hydrogen-bonding interactions establish a structured environment that regulates ion mobility and charge transfer. Under a temperature gradient, this hydrated interphase acts as a gateway for ions entering and leaving the electrode, thereby enabling the conversion of bulk ionic thermodiffusion into a measurable electrical signal. In this sense, while long-range ion migration through the pore network governs the generation of internal ionic gradients, the electrode interface defines the boundary conditions by controlling ion injection and extraction kinetics [18].

Importantly, the effectiveness of this interfacial coupling depends strongly on the nature of the electrode. Electrodes with high electrochemical activity and favorable interaction

with the electrolyte facilitate rapid and balanced ion exchange across the interface, stabilizing the separation of ionic species (e.g., Na^+ and OH^-) and enhancing the resulting thermoelectric response. In contrast, electrochemically inert or poorly matched electrodes hinder interfacial charge transfer, leading to increased polarization resistance, reduced thermopower, and, in some cases, even reversal of the Seebeck polarity due to altered dominant charge carriers.

This behavior can be understood more fundamentally in terms of interfacial electric fields established within the microlayer of water. As illustrated schematically in Figure 1.11, differences in work function between the electrode and the cementitious matrix generate an initial electric field across the hydrated interface, which governs the preferential adsorption and spatial distribution of ions. Depending on the direction and magnitude of this field, ion accumulation at the interface can either reinforce or oppose the thermally driven ionic flux, thereby enhancing or suppressing the overall Seebeck response [18]. Consequently, the electrode–material interface emerges as a dynamic electrochemical interphase in which the microlayer of water mediates ion transport across phases, and where electrode properties ultimately determine how efficiently bulk ionic transport is translated into usable electrical energy.

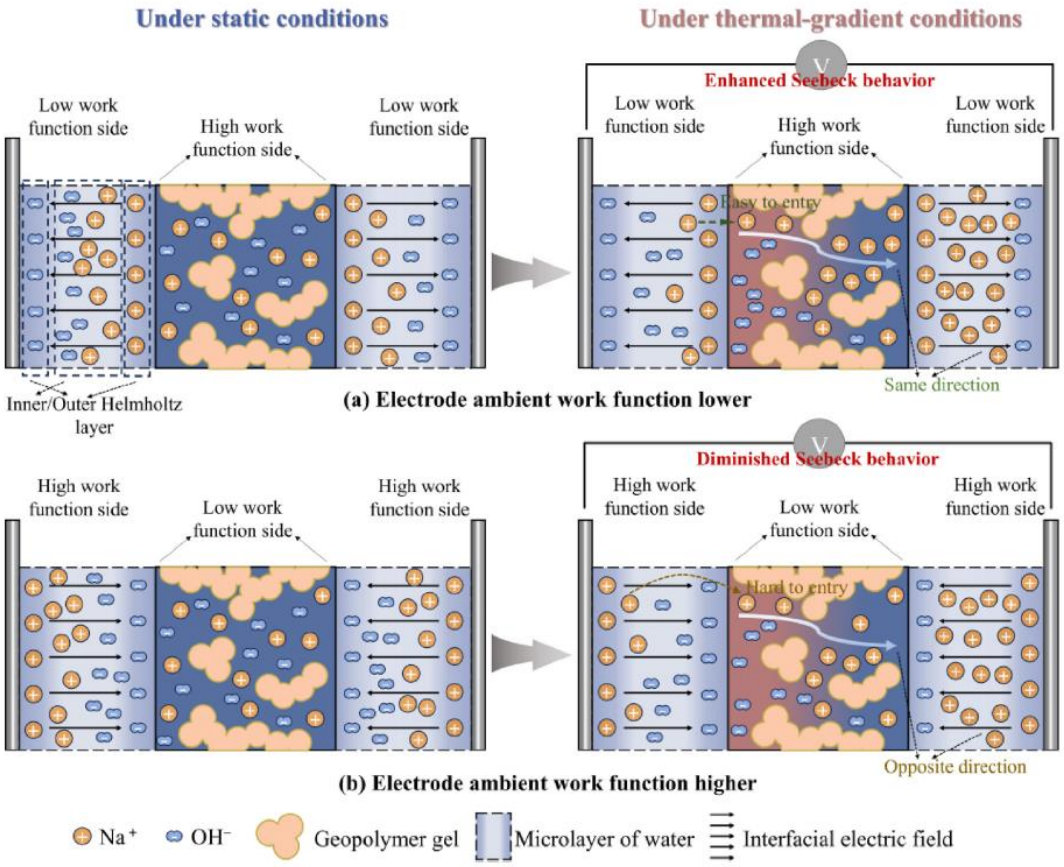


Figure 1.11 Interfacial mechanisms in geopolymer-based ionic thermoelectric materials, highlighting the role of interfacial electric fields [18].

1.7.4. Section Summary

Microstructure and pore-structure engineering play a fundamental role in determining the thermoelectric behavior of cementitious materials. The hierarchical pore network of these materials enables ionic transport across multiple length scales, while nanoscale electric double-layer effects and interfacial water layers amplify thermoelectric voltage generation.

Consequently, the thermoelectric performance of cementitious systems is governed not only by chemical composition but also by the structural organization of the binder matrix. Understanding and controlling pore structure, water distribution, and interfacial coupling therefore represents a key strategy for optimizing thermoelectric materials for energy harvesting applications in the built environment.

1.8. Photothermoelectric Cement-Based Materials

The development of photothermoelectric (PTE) cement-based materials is particularly relevant in the context of urban infrastructure, where solar irradiation represents the dominant and most persistent source of thermal energy [60]. Unlike conventional thermoelectric systems that rely on externally imposed temperature gradients, built environments are inherently exposed to continuous solar radiation, leading to significant surface heating of pavements, roofs, and façades. Surface temperatures in urban areas can reach values on the order of ~60 °C under solar irradiation, particularly during summer conditions, thereby creating natural temperature gradients across structural elements [61]. Given the vast surface area of cement-based infrastructure, this ubiquitous solar-induced heating constitutes a largely untapped energy source. Therefore, integrating energy-harvesting functionality directly into cementitious materials through photothermoelectric effects offers a unique opportunity to convert passive urban surfaces into active energy-generating systems.

Photothermoelectric energy conversion is fundamentally based on the coupling between photothermal and thermoelectric effects. In such systems, incident solar radiation is first absorbed and converted into heat by photothermal components, leading to a localized temperature rise [62]. This thermally induced gradient is subsequently converted into electrical energy through the Seebeck effect, which generates a potential difference between the hot and cold regions of the material. In this sense, PTE systems do not introduce a new transport mechanism but rather extend conventional thermoelectric behavior by integrating light-to-heat conversion within the same material or device. The overall efficiency of this process, therefore depends not only on intrinsic thermoelectric properties—such as Seebeck coefficient, electrical conductivity, and thermal conductivity—but also on optical absorption, thermal management, and the ability to sustain temperature gradients under continuous irradiation. Consequently, PTE cement-based materials require simultaneous optimization of optical, thermal, and electrical properties, distinguishing them from conventional thermoelectric composites.

The first explicit demonstration of photothermoelectric (PTE) behavior in cementitious materials was reported by Wei et al. [61], who investigated carbon-fiber-reinforced cement composites (CFRCs) under simulated solar irradiation. In this work, carbon fibers

served a dual role, enhancing both the electronic conductivity of the matrix and its solar absorptivity. When exposed to sunlight, the surface temperature of the CFRC increased up to 68 °C, generating a through-thickness thermal gradient. As shown in Figure 1.12, this gradient produced a harvestable energy of 8.4×10^{-6} J over 420 minutes of irradiation. The findings revealed that the photothermal efficiency of carbon fibers stemming from their high optical absorption and thermal conductivity significantly amplifies the Seebeck response. Importantly, this study established that cement-based composites can directly convert solar energy into electricity using their intrinsic material properties, distinguishing them from systems that rely on embedded thermoelectric devices and paving the way for self-powered, solar-responsive structural elements.

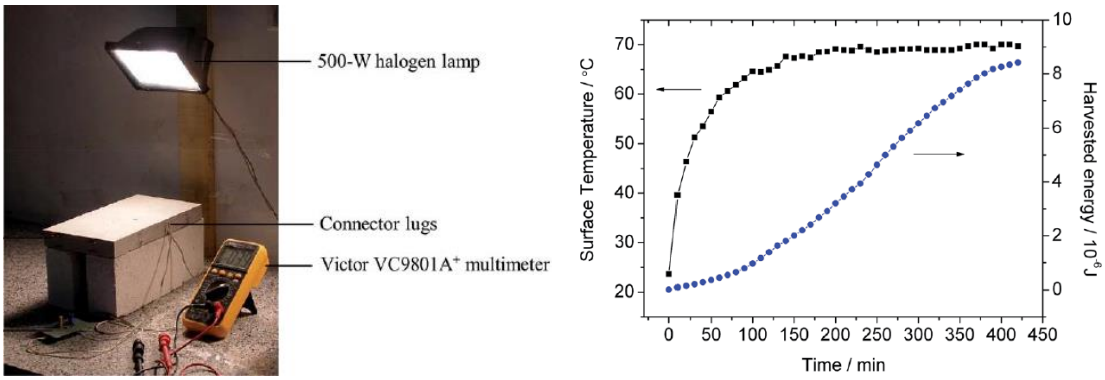


Figure 1.12 (a) Experimental setup used for photothermoelectric energy harvesting from the cement composite; (b) calculated harvested energy as a function of time [61].

Overall, despite the strong conceptual relevance and clear application potential, photothermoelectric cement-based materials remain largely unexplored. Existing studies are scarce and primarily limited to proof-of-concept demonstrations under simulated irradiation conditions. Systematic investigations into material design, optical–thermal coupling, long-term outdoor performance, and scalability are still lacking. In particular, there is a significant research gap in developing cementitious systems specifically engineered for photothermoelectric operation, where optical absorption, thermal gradient generation, and thermoelectric conversion are co-optimized within a unified material framework. Addressing these challenges is essential for advancing cement-based photothermoelectric materials from laboratory-scale demonstrations toward practical implementation in energy-harvesting urban infrastructure.

1.9. Stability and Environmental Response

For thermoelectric cementitious materials to be viable for practical applications in the built environment, their performance must remain stable under fluctuating environmental conditions. Unlike conventional thermoelectric materials used in controlled electronic devices, cement-based systems operate within infrastructure exposed to variations in temperature, humidity, and moisture transport. These environmental factors can significantly influence ionic mobility, pore solution chemistry, and the microstructural state of the binder, all of which affect thermoelectric output.

Consequently, understanding the stability of thermoelectric behavior under environmental cycling is essential for evaluating the long-term performance of cementitious thermoelectric materials.

1.9.1. Influence of Humidity and Moisture Cycling

Moisture content plays a central role in governing the thermoelectric (TE) response of cement-based materials, particularly in systems where ionic conduction dominates. Early work by D. D. L. Chung and co-workers demonstrated that drying significantly increases electrical resistivity while having a comparatively limited effect on the intrinsic Seebeck coefficient, suggesting that liquid-phase connectivity primarily controls charge transport rather than thermopower itself [63]. However, this interpretation reflects predominantly electronically influenced systems and does not fully capture the behavior of modern ionic thermoelectric (i-TE) cementitious materials.

More recent studies have shown that moisture availability directly governs thermoelectric performance in ionically active systems. For example, saturation treatments have been reported to enhance thermoelectric conversion efficiency, while drying leads to a marked reduction in output due to the disruption of continuous ionic pathways [64]. Similarly, investigations into ionic thermoelectric cement systems highlight that water-filled pore networks act as the primary transport medium, enabling long-range ion migration through capillaries, microcracks, and nanoscale channels [65]. In such systems, dehydration suppresses ionic mobility, leading to a sharp decline in thermoelectric response, whereas rehydration restores performance. Moreover, Ma et al. showed that partial drying first increases the Seebeck coefficient in alkali-activated materials due to higher concentration of ions and then results in the thermopower reduction because of interrupted pathways[8].

Despite these advances, systematic studies on humidity cycling remain scarce. Most available work considers only static conditions (fully saturated vs. dried states), with limited attention to cyclic environmental exposure, such as daily humidity fluctuations or long-term moisture aging. Furthermore, quantitative relationships between relative humidity (RH), degree of saturation, and Seebeck evolution are not yet fully established. This represents a critical gap, particularly for real-world applications where cementitious materials are continuously exposed to fluctuating environmental conditions.

1.9.2. Thermal Cycling Stability

Compared to moisture effects, the influence of thermal cycling on thermoelectric cementitious materials has received very limited direct investigation. Most studies evaluate thermoelectric performance under steady-state or short-duration thermal gradients, without addressing the impact of repeated heating–cooling cycles.

Only limited evidence on thermal cycling is currently available. Pure cement paste has been shown to maintain a reproducible thermoelectric sensing response during limited temperature cycles [15], and geopolymer–electrode composites show short-term signal stabilization after a few measurement cycles [18]; however, neither study evaluates long-term thermal fatigue, performance retention, or degradation under extended heating–cooling cycling, leaving thermal cycling stability as a major unresolved gap.

From a fundamental perspective, thermal cycling can affect thermoelectric response through several coupled mechanisms, including thermal expansion mismatch, microcrack evolution, pore structure redistribution, and changes in ionic mobility. In ionic thermoelectric systems, temperature variations also influence the relative contribution of different charge carriers (e.g., cations vs. anions), potentially leading to time-dependent or reversible polarity shifts under varying thermal conditions.

Consequently, thermal cycling stability remains an open research question.

1.9.3. Section Summary

The stability and environmental response of thermoelectric cement-based materials are governed primarily by moisture availability, thermal conditions, and binder microstructure, all of which directly influence charge transport pathways. Overall, while fundamental insights into moisture effects and ionic transport have been established, systematic studies on long-term environmental stability—including humidity cycling, thermal fatigue, and coupled degradation mechanisms—are still lacking**,** representing a key research gap for the practical deployment of cement-based thermoelectric systems.

1.10. Challenges and Research Outlook

1.10.1. Remaining Scientific Challenges

Despite significant progress, cement-based thermoelectric materials and devices still face fundamental limitations that hinder their practical implementation. The most critical issue is their inherently low thermoelectric efficiency, with reported ZT values typically below 10^{-2} and conversion efficiencies far inferior to conventional thermoelectric materials [1,17]. This limitation originates from the intrinsically insulating nature of cement and the difficulty in simultaneously achieving high electrical conductivity, large Seebeck coefficient, and low thermal conductivity within a single system [2].

Beyond intrinsic limitations, the heterogeneous and multiphase structure of cement introduces additional complexity. Charge transport arises from a combination of ionic, electronic, and interfacial mechanisms, all of which are highly sensitive to pore structure, hydration products, and moisture content. This complexity not only complicates mechanistic understanding but also hinders the formation of stable and efficient conductive pathways, particularly given the difficulty of constructing well-dispersed, percolating networks of conductive fillers within the matrix.

Environmental sensitivity represents another major challenge. Thermoelectric performance, particularly in ionic systems, is strongly dependent on moisture and temperature, leading to unstable or diminished response under dry conditions and degradation under extreme environments [17]. At the same time, most studies prioritize thermoelectric enhancement without fully addressing the requirement for structural integrity, despite the fact that cement-based materials must simultaneously satisfy mechanical, durability, and load-bearing constraints. This creates a critical trade-off, as conductive fillers and microstructural modifications may adversely affect mechanical performance.

At the device and application level, additional challenges arise in scaling and integration. Efficient thermal management, minimization of contact resistance, and optimization of device architecture remain unresolved, limiting power output and practical efficiency [1]. Although large-scale deployment is often proposed as a pathway to enhance energy output, clear design strategies for scalable systems are still underdeveloped [17]. Furthermore, there is a lack of systematic studies on long-term performance and real-world operation, particularly under fluctuating environmental conditions, which remains a key barrier to practical implementation [3].

Overall, the field is constrained by coupled material, structural, and environmental challenges, and future progress will require integrated approaches that simultaneously address transport optimization, microstructural control, durability, and scalable device design.

1.10.2. Motivation for the Present Thesis

The present thesis is motivated by the need to advance cement-based thermoelectric materials from laboratory-scale demonstrations toward practical, scalable energy-harvesting systems for the built environment. Despite their inherent advantages, abundance, low cost, structural functionality, and compatibility with large urban surfaces, cementitious materials have traditionally exhibited limited thermoelectric performance and an incomplete mechanistic understanding. Key challenges include intrinsically low output in conventional systems, dependence on costly additions, insufficient insight into ionic transport mechanisms, and a lack of systematic evaluation under realistic environmental conditions. Addressing these limitations requires an integrated approach combining material design, mechanism clarification, architectural innovation, and environmental validation.

A primary motivation of this work was to identify sustainable cementitious matrices capable of delivering enhanced thermoelectric performance without compromising scalability. Initial investigations on geopolymer-based hybrid cement and copper-slag-modified concrete demonstrated that geopolymer systems can achieve significantly higher Seebeck coefficients than conventional cementitious materials. At the same time, these studies revealed two critical aspects: the presence of intrinsic voltage, which can distort thermoelectric measurements if not properly accounted for, and the dominant role of ionic transport in governing the thermoelectric response. These findings redirected the focus from conventional electronic-conduction-based strategies toward the engineering of pore-solution chemistry and ion mobility as primary design parameters.

Building on this foundation, a further motivation was to elucidate the role of precursor chemistry in controlling ionic thermoelectric behavior. The investigation of kaolin-clay-based geopolymers demonstrated that thermoelectric performance is strongly governed by temperature-dependent ionic mobility within the aluminosilicate network. The observation of a transition between n-type and p-type behavior highlighted the dynamic nature of charge transport in these systems, emphasizing that thermoelectric response is not an intrinsic constant but a function of ion type, concentration, and operating

conditions. This established precursor selection as a critical parameter not only for sustainability but also for controlling transport mechanisms and functional performance.

Complementary to this, the study of GGBF slag-based geopolymers provided insight into the relationship between activator chemistry, microstructure, and thermoelectric performance. By varying the alkaline solution content, it was shown that thermoelectric properties are governed by a balance between ionic concentration, pore connectivity, and structural integrity. While increased activator content enhances ionic mobility and conductivity, excessive amounts disrupt the microstructure and reduce transport efficiency.

Beyond material optimization, an additional motivation arose from the intrinsic limitation of small temperature gradients in conventional cement-based thermoelectric systems. This constraint prompted the transition toward device-level design through the development of a photothermoelectric cement concept. The chessboard-like architecture addressed this limitation by exploiting the contrasting optical properties of cementitious materials to generate horizontal temperature gradients under solar irradiation. By combining a solar-absorbing geopolymer/copper-slag segment with a reflective white-cement segment, this approach enabled enhanced thermoelectric output while maintaining material scalability and compatibility with construction practices.

Finally, the practical deployment of cement-based thermoelectric systems necessitates an understanding of their behavior under real environmental conditions. The observed dependence of ionic transport on moisture and temperature highlighted that environmental factors are not secondary effects but fundamental components of system performance. The environmental study was therefore motivated by the need to quantify the influence of relative humidity, temperature, and dynamic climatic cycles on thermoelectric response. The results demonstrated that humidity stabilizes ionic pathways and enhances voltage output, while temperature governs thermodiffusive mobility, leading to strongly climate-dependent performance. These findings establish cement-based thermoelectric materials as inherently environment-responsive systems.

Overall, the motivation of this thesis is structured around a progressive objective: to transform cement-based thermoelectricity from a material-level phenomenon into a scalable, environmentally adaptive, and practically viable energy-harvesting technology. This is achieved through three interconnected stages: (i) material exploration using hybrid cement, slag-based, and kaolin-based geopolymers to establish fundamental mechanisms; (ii) development of a photothermoelectric cement architecture to overcome intrinsic limitations in temperature gradient generation; and (iii) systematic investigation of environmental effects to bridge the gap between laboratory performance and real-world application.

Chapter II

Experimental Methods

The experimental framework adopted in this thesis is designed to systematically investigate the thermoelectric and photothermoelectric behavior of cement-based materials across multiple length scales, ranging from fundamental material characterization to device-level performance evaluation. The studies presented in subsequent chapters are based on a series of complementary experimental campaigns, each targeting specific material systems, including geopolymer-based hybrid cement, kaolin-derived geopolymers, GGBFS-based systems, and photothermoelectric cement composites.

Given that the preparation protocols for each material system are described in detail within the corresponding results chapters, the present chapter focuses exclusively on the characterization techniques and measurement methodologies employed to evaluate structural, thermal, electrical, and thermoelectric properties. This approach avoids redundancy while providing a unified description of the experimental tools used throughout the thesis.

A combination of physicochemical characterization, transport measurements, and device-level testing was employed to establish direct correlations between composition, microstructure, and functional performance. These methods were selected to capture the key mechanisms governing ionic transport, intrinsic voltage behavior, and thermoelectric response in cementitious systems.

2.1. Materials Characterization

2.1.1. Structural and Chemical Characterization

The chemical composition and mineralogical structure of the raw materials and cementitious systems were characterized using X-ray fluorescence (XRF) and X-ray diffraction (XRD). These analyses were performed to identify the oxide composition of the precursors, aggregates, and binders, as well as the crystalline and amorphous phases formed after curing or thermal treatment.

Mineralogical analysis was carried out by XRD using a PANalytical X'Pert diffractometer equipped with a Cu tube. The measurements were performed at 40 kV and 40 mA using Cu Kα radiation, with a mean wavelength of $\lambda = 1.5418$ Å. For the geopolymer-based hybrid cement and copper slag systems, diffractograms were recorded over a 2θ range of 5–80°. The obtained patterns were processed using PANalytical X'Pert HighScore software, and the crystalline phases were identified by comparison with the PDF-2 database of the International Centre for Diffraction Data (ICDD). This procedure was used to determine the phase assemblage of copper slag aggregates, geopolymer-based hybrid cement, and the corresponding cured composites.

For the kaolin clay-based system, XRD measurements were conducted using a Bruker D8 Advance diffractometer. The raw and calcined clays were analyzed over a 2θ range of

10–90°, with a scan step of 0.05° and an average measuring time of 50 s per point. Cu Kα radiation (λ = 1.5418 Å) was generated at 40 kV and 40 mA, and the resulting patterns were analyzed using Diffrac.EVA software. This analysis enabled identification of the transformation of kaolinite into metakaolinite after calcination, as evidenced by the disappearance of kaolinite reflections and the formation of a broad amorphous halo.

XRF analysis was used to determine the bulk oxide composition of the raw materials. For the geopolymer-based hybrid cement, copper slag, white cement, and GGBFS systems, powder samples were fused with Spectromelt A12 flux at an approximate flux-to-sample ratio of 20:1 to produce borated glass beads. The chemical analysis was then performed under vacuum using a PANalytical AXIOS sequential wavelength-dispersive X-ray fluorescence spectrometer equipped with an Rh tube. Loss on ignition (LOI) was also determined by heating an aliquot of each sample at 1050 °C for 1 h in a muffle furnace.

This combined XRD–XRF approach provided the basis for linking raw material chemistry and phase composition to the thermoelectric behavior of the investigated systems. In particular, it allowed identification of Fe-rich fayalite and spinel phases in copper slag, kaolinite-to-metakaolinite transformation in the kaolin-derived geopolymer, and the Ca-rich composition of GGBFS, which is relevant to the formation of C–A–S–H-type gel phases and the resulting ionic transport pathways.

2.1.2. Thermal and Microstructural Analysis

Thermal and microstructural analyses were performed to evaluate the role of water content, pore structure, and reaction development in the ionic transport behavior of the investigated cementitious systems. Since ionic thermoelectricity in cement-based materials is strongly governed by pore solution chemistry and moisture state, these analyses were essential for linking the physical structure of the matrix to its electrical and thermoelectric response.

Thermogravimetric analysis (TGA) and derivative thermogravimetric analysis (DTG) were used to assess thermal stability and water-related transformations. The TGA/DTG was carried out using a TA Instruments TGA Q500 under nitrogen atmosphere. For the geopolymer-based hybrid cement and copper-slag-containing systems, TGA was performed after curing up to 900 °C to investigate water loss and its influence on thermoelectric behavior. In the kaolin clay-based system, TGA/DTG was carried out, from 30 to 900 °C at a heating rate of 10 °C min^{-1}, using approximately 100 mg of sample in a platinum crucible. This analysis was used to determine the dehydroxylation temperature of kaolinite and to select the calcination temperature required for metakaolinite formation. For the GGBFS-based geopolymer system, TGA/DTG was conducted over the range of 25–800 °C to identify thermal events associated with free and physically bound water, interlayer or structurally retained water, hydrated phase dehydration, and carbonate decomposition.

Mercury intrusion porosimetry (MIP) was employed to investigate pore structure and pore size distribution in the geopolymer-based hybrid cement systems. The measurements were performed using an AutoPore IV 9500 mercury porosimeter (Micromeritics, USA). To ensure representative and comparable measurements, specimens were taken from the

central region of the samples and dried at approximately 50 °C for 24 h before testing to minimize the influence of ongoing hydration. Total porosity and total pore area were obtained directly from the intrusion data using the AutoPore IV 9500 V1.09 software.

For the GGBFS-based geopolymer system, the geopolymerization process and microstructural development were additionally monitored by isothermal conduction calorimetry and ultrasonic pulse velocity (UPV). Isothermal conduction calorimetry was performed using a TAM AIR calorimeter (Thermometric AB, Sweden) to record heat evolution during geopolymerization and evaluate the influence of alkaline solution-to-slag ratio on reaction kinetics. UPV measurements were carried out using an Ultrasonic Tester BP-700 (UltraTest GmbH, Germany) over a 24 h period to follow the development of the solid matrix and changes in internal connectivity during early reaction stages.

Mechanical performance was evaluated through non-destructive dynamic elastic modulus measurements. The ultrasonic pulse transit time was recorded using the Ultrasonic Tester BP-700, and bulk density was determined from the mass and geometrical dimensions of each specimen. The dynamic Young's modulus was then calculated assuming a constant Poisson's ratio of 0.22.

Together, TGA/DTG, MIP, calorimetry, UPV, and dynamic elastic modulus measurements provided complementary information on water state, pore structure, reaction progress, and matrix stiffness. These parameters are directly relevant to ionic thermoelectric behavior, since the concentration and mobility of charge carriers depend on the amount and distribution of pore water, the connectivity of the pore network, and the evolution of the geopolymeric or cementitious matrix.

2.1.3. Spectroscopic and Optical Characterization

Spectroscopic and optical characterization was performed to investigate chemical bonding evolution, phase transformation at the molecular scale, and light–material interactions in the investigated cementitious systems. These analyses are essential for linking geopolymerization processes and optical properties to the thermoelectric and photothermoelectric performance.

Attenuated total reflectance Fourier-transform infrared spectroscopy (ATR-FTIR) was employed for the kaolin clay-based system to monitor structural changes during calcination and geopolymerization. Measurements were carried out using an FTIR-6300/ATR-6000 spectrometer equipped with a diamond crystal plate. Spectra were recorded over the range of 4000–500 cm^{-1} with a resolution of 4 cm^{-1} and 200 scans.

The FTIR analysis enabled identification of key transformations in the aluminosilicate framework. In the raw kaolin clay, bands at approximately 3698 and 3620 cm^{-1} correspond to O–H stretching vibrations of structural hydroxyl groups, while bands near 1112 and 1005 cm^{-1} are attributed to Si–O–T (T = Si or Al) vibrations. Following calcination, the disappearance of hydroxyl-related bands confirms dehydroxylation and the formation of metakaolinite. In the geopolymer samples, the main Si–O band shifts to lower wavenumbers (≈986 cm^{-1}), indicating the formation of Si–O–Al linkages and the development of the geopolymeric network. Additionally, broad bands near 3400 and 1647 cm^{-1} are associated with physically adsorbed and bound water within the pore structure.

For the photothermoelectric cement system, optical characterization was conducted to quantify the contrast in solar absorption and thermal radiation properties between the different cementitious components. Infrared emissivity measurements were performed using a gold-coated integrating sphere (121 configuration) coupled to a Jasco 6300 spectrometer equipped with a mercury–cadmium–telluride (MCT) detector. Measurements were carried out at room temperature, with background spectra recorded immediately before each measurement to minimize instrumental and environmental noise. The reported emissivity values correspond to the average of multiple measurements for each sample.

Reflectance measurements were used to evaluate the optical response of the materials in the visible and near-infrared regions. These measurements are particularly relevant for the design of photothermoelectric systems, where controlled light absorption is required to generate temperature gradients. The cementitious components exhibited distinct optical behavior: the high-absorbance (black) segment showed significantly lower reflectance, enabling efficient solar energy absorption, while the high-reflectance (white) segment exhibited reflectance values in the range of approximately 0.65–0.87, limiting heat uptake. This contrast in optical properties is a key factor in generating the lateral temperature gradient within the photothermoelectric cement cell.

Overall, the combination of FTIR and optical measurements provides complementary insight into both the chemical structure and light–matter interaction of the investigated systems, enabling a direct link between material chemistry, optical contrast, and thermoelectric performance.

2.2. Thermoelectric Measurements

2.2.1. Thermal Conductivity Measurements

Thermal conductivity was measured to evaluate heat transport in the investigated cementitious and geopolymer systems, since the ability to maintain a temperature gradient is a key requirement for thermoelectric performance. The measurements were carried out using a modulated differential scanning calorimeter, MDSC Q2000, from TA Instruments.

The method was based on the analysis of two disc-shaped specimens prepared from the same material but with different thicknesses. A very thin specimen, with a thickness below 0.5 mm, was used to determine the specific heat capacity, C_p. Owing to its small thickness, this specimen reached thermal equilibrium rapidly, as its thickness was below the thermal penetration length. A second, thicker specimen, with a thickness of approximately 1.5 mm, was used to determine the apparent heat capacity, C, where the temperature distribution across the sample thickness is non-uniform.

The thermal conductivity, λ, was then calculated according to:

$$\lambda = \frac{8LC^2}{C_P M d^2 P} \quad \textit{Equation 2.1}$$

where λ is the thermal conductivity in W m^{-1} K^{-1}, C is the apparent heat capacity of the thick specimen, C_p is the specific heat capacity of the thin specimen, L is the thickness of the thick specimen, M is its mass, d is its diameter, and P is the modulation period.

This approach was applied to the geopolymer-based hybrid cement and copper-slag-containing composites, as well as to the kaolin and GGBFS-based geopolymer system. The measurements enabled comparison of heat transport as a function of composition and temperature, providing information on the ability of each material to sustain thermal gradients under thermoelectric operating conditions.

Overall, thermal conductivity measurements provided an essential parameter for evaluating thermoelectric performance, since lower thermal conductivity favors the retention of temperature gradients, while excessive heat transport can reduce the effective temperature difference available for voltage generation.

2.2.2. Electrical Transport Measurements

Electrical transport properties were investigated using two-probe AC impedance spectroscopy to evaluate the ionic conduction behavior of the cementitious and geopolymer-based systems. These measurements were essential for determining the DC conductivity and for understanding the influence of temperature, water content, and pore connectivity on charge transport.

Impedance spectroscopy measurements were performed using a Novocontrol Alpha-A broadband dielectric spectrometer. For the geopolymer-based hybrid cement and GGBFS-based geopolymer systems, spectra were recorded over a frequency range of 10 Hz to 10 MHz using an AC voltage amplitude of 1 V. The specimens were prepared as disc-shaped samples from the same batches used for thermoelectric measurements, and gold-coated disc electrodes with a diameter of 10 mm were placed on both sides of the samples to ensure reproducible electrical contact. Temperature-dependent measurements were carried out from 30 °C to 160 °C at a heating rate of 1 °C min^{-1}.

For the kaolin clay-based geopolymer system, the electrical response was also analyzed using two-probe AC impedance spectroscopy with the same broadband dielectric spectrometer. In this case, spectra were collected over a broader low-frequency range, from 10 mHz to 10 MHz, using a voltage amplitude of 1 V, allowing a more detailed analysis of slow ionic relaxation and electrode polarization effects.

The real part of the complex conductivity, σ′(f), was analyzed as a function of frequency and temperature. At high frequencies, the conductivity response reflects localized or subdiffusive motion of mobile ions, whereas at intermediate frequencies a frequency-independent plateau corresponds to long-range diffusive transport. The decrease in conductivity observed at low frequencies was attributed to electrode polarization, which is commonly observed in ionic conductors and cementitious materials with mobile pore-solution ions.

To quantitatively describe the conductivity spectra, the data were fitted using Jonscher's power law:

$$\sigma(f) = \sigma DC[1 + (\frac{f}{f_0})n] + Af \quad \textit{Equation 2.2}$$

where σ_{DC} is the direct current conductivity, f_0 represents the characteristic frequency associated with the onset of diffusive motion, n is related to the dimensionality of charge transport, and A accounts for the nearly constant loss contribution at high frequency. This

analysis enabled separation of the bulk ionic conductivity from frequency-dependent polarization and relaxation processes.

The temperature-dependent conductivity measurements were used to identify changes in the dominant charge transport mechanism. In the investigated geopolymer systems, conductivity initially increased with temperature due to enhanced ion mobility, followed by a decrease at higher temperatures as bulk water evaporated from the pore network. This behavior confirmed that ionic species within the pore solution are the dominant charge carriers and that the electrical response is strongly governed by moisture state and pore connectivity. In the kaolin-based geopolymer, the fitted parameter n further indicated a transition from predominantly one-dimensional ion diffusion at lower temperatures to more restricted three-dimensional hopping-type transport after water loss.

2.2.3. Seebeck Measurements

Thermoelectric characterization was performed by monitoring the time-dependent open-circuit voltage under controlled temperature gradients. This measurement was central to evaluating the Seebeck response of the cementitious and geopolymer-based systems, while also distinguishing the true thermoelectric voltage from the intrinsic voltage commonly observed in cement-based materials.

For conventional thermoelectric measurements, a custom-built Seebeck setup was used, as shown schematically in Figure 2.1. The two sides of the specimens were polished with sandpaper up to 400 mesh to improve electrode contact. Both sides of the samples were covered with copper adhesive, while silver paste and thin copper adhesive were applied approximately 4 mm from the hot and cold sides to record the thermoelectric voltage. A ceramic heating plate was placed on the top surface of the specimen to impose the temperature gradient, while the lower side acted as the colder region. The temperatures at both electrode positions were monitored using p-type thermocouples connected to a PicoLog data logger. The voltage difference between the two copper connections was recorded using a Keithley 2100 6½-digit multimeter connected to LabVIEW software for real-time data acquisition.

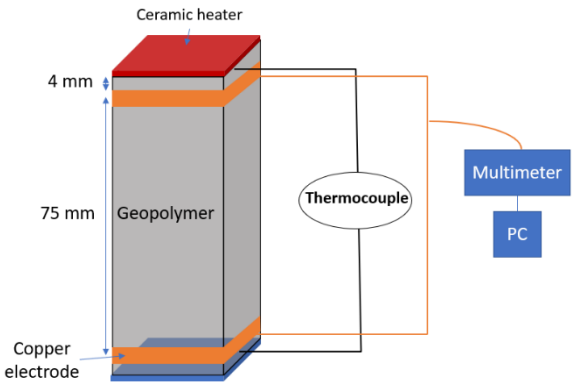


Figure 2.1 The schematic experimental setup of the Seebeck measurement.

Before applying any thermal gradient, the open-circuit voltage was first monitored under isothermal conditions to evaluate the intrinsic voltage of each sample. This step is

essential because cementitious materials can exhibit a significant initial voltage difference between their two electrodes even in the absence of external heating. The magnitude, sign, and time evolution of this intrinsic voltage can vary between samples, including specimens prepared from the same batch. Therefore, the temperature gradient was applied only after the intrinsic voltage reached a stable and constant value, typically for at least 1 h. This protocol was adopted to avoid overestimation or underestimation of the Seebeck coefficient caused by the intrinsic voltage offset.

After applying different temperatures on the top surface of the samples the corresponding temperature difference, ΔT, was measured between the two electrode positions for each applied temperature. The Seebeck coefficient was then calculated from the stabilized thermoelectric voltage response using $S=\Delta V/\Delta TS$. The voltage evolution was monitored and interpreted to understand the mechanism behind the TE voltage generation of different samples.

2.3. Device-Level and Photothermoelectric Measurements

To evaluate the interaction of cement-based photothermoelectric (PTE) materials with environmental conditions and to assess their performance under realistic operating scenarios, a combination of surface characterization, controlled laboratory measurements, and outdoor testing was conducted. Particular emphasis was placed on the role of moisture, solar irradiation, and environmental dynamics in governing ionic transport and thermoelectric response.

2.3.1. Surface Wettability and Moisture Interaction

The interaction of the cementitious materials with atmospheric moisture was evaluated through water contact angle measurements. These measurements provide insight into surface wettability and the ability of the material to absorb and retain moisture, which directly influences ionic transport pathways.

Contact angle measurements were performed using an optical tensiometer (UI-122XLE-M, IDS, Germany). A droplet of distilled water (2 μL) was deposited on the sample surface and allowed to stabilize before image acquisition. The contact angle was determined using the ellipse-fitting method, and measurements were repeated at multiple locations on each sample to account for surface heterogeneity.

This analysis was used to assess the hydrophilic nature of the cementitious matrices and to correlate surface wettability with the observed self-rechargeability behavior under ambient humidity conditions.

2.3.2. Indoor Photothermoelectric Measurements under Controlled Irradiation

Indoor PTE measurements were conducted to systematically evaluate the thermoelectric response under controlled irradiation conditions and the resulting temperature differences. A solar simulator based on a halogen lamp was used to reproduce solar radiation with adjustable intensity, as shown in Figure 2.2.

The light source consisted of a high-power lamp (500 W) providing irradiation levels up to 1200 W m^{-2} at the sample surface. The irradiation intensity was measured using a

calibrated thermopile pyranometer (MicroCache 2381), enabling accurate control and monitoring of the incident solar irradiance during experiments.

Samples were exposed to different irradiation levels to investigate the relationship between solar irradiance input and thermoelectric output. The temperature difference between the hot and cold regions of the samples was monitored using thermocouples, while the generated voltage was recorded continuously. These measurements allowed evaluation of the PTE response under steady and controlled laboratory conditions, isolating the effect of irradiation intensity from environmental fluctuations.

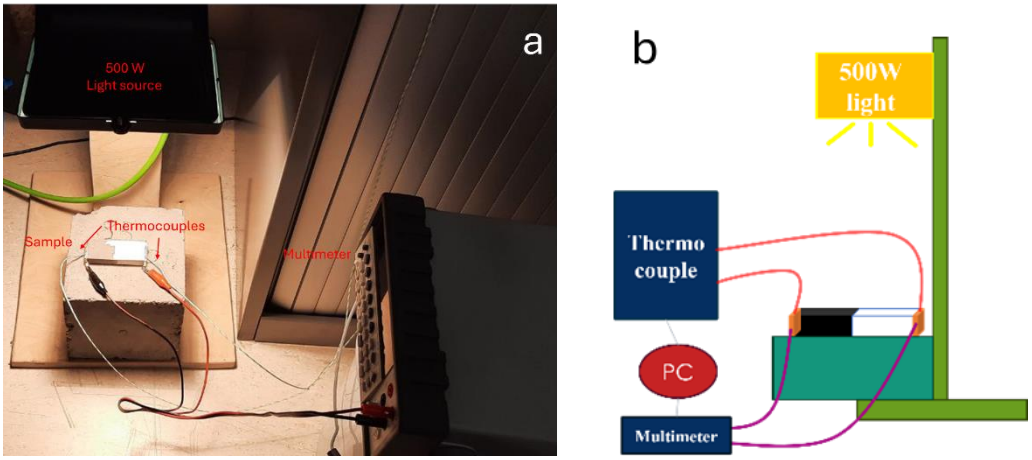


Figure 2.2 (a) Setup for the indoor PTE test. (b) Schematic of the Seebeck measurement setup

2.3.3. Outdoor Photothermoelectric Measurements

To assess real-world performance, outdoor measurements were conducted under natural solar irradiation on the rooftop of the Centro de Física de Materiales (CFM), San Sebastián, Spain. In these experiments, PTE cells were exposed to continuously varying environmental conditions, including solar radiation, ambient temperature, relative humidity, and wind.

The experimental setup (Figure 2.3) consisted of PTE cells connected in series, with voltage output monitored continuously throughout the day. Environmental parameters were simultaneously recorded using dedicated sensors:

- Solar irradiance was measured using a thermopile pyranometer (MicroCache 2381),
- Ambient temperature and relative humidity were monitored using an ATMOS 14 sensor,
- Wind speed was measured using an ATMOS 22 ultrasonic anemometer.

These measurements enabled direct correlation between environmental fluctuations and the electrical response of the PTE system.

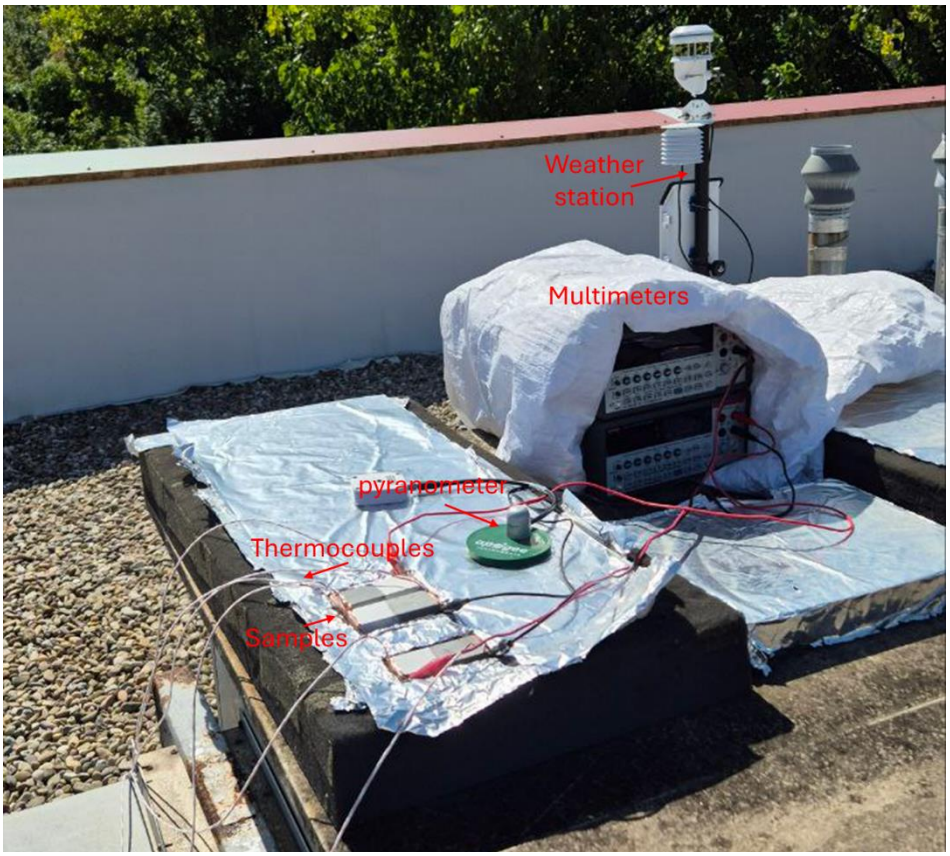


Figure 2.3 The PTE setup for the outdoor measurements.

2.3.4. Controlled Environmental Chamber Measurements

To systematically investigate the influence of environmental parameters, experiments were conducted in a climatic chamber equipped with a solar simulator. The chamber (ATT DM340SR) allows precise control of temperature, relative humidity, and irradiation intensity within a confined test volume. The setup is illustrated in Figure 2.4, and the connection and the data logging system were similar to PTE measurements.

The chamber operates over a wide range of conditions, with temperature control typically within ±1 °C and relative humidity adjustable between approximately 10% and 98%. The integrated halogen solar lamp provides irradiation levels up to ~1200 W, enabling simulation of realistic solar exposure scenarios.

This setup enables controlled replication of both static and dynamic environmental conditions, bridging the gap between laboratory and outdoor testing.

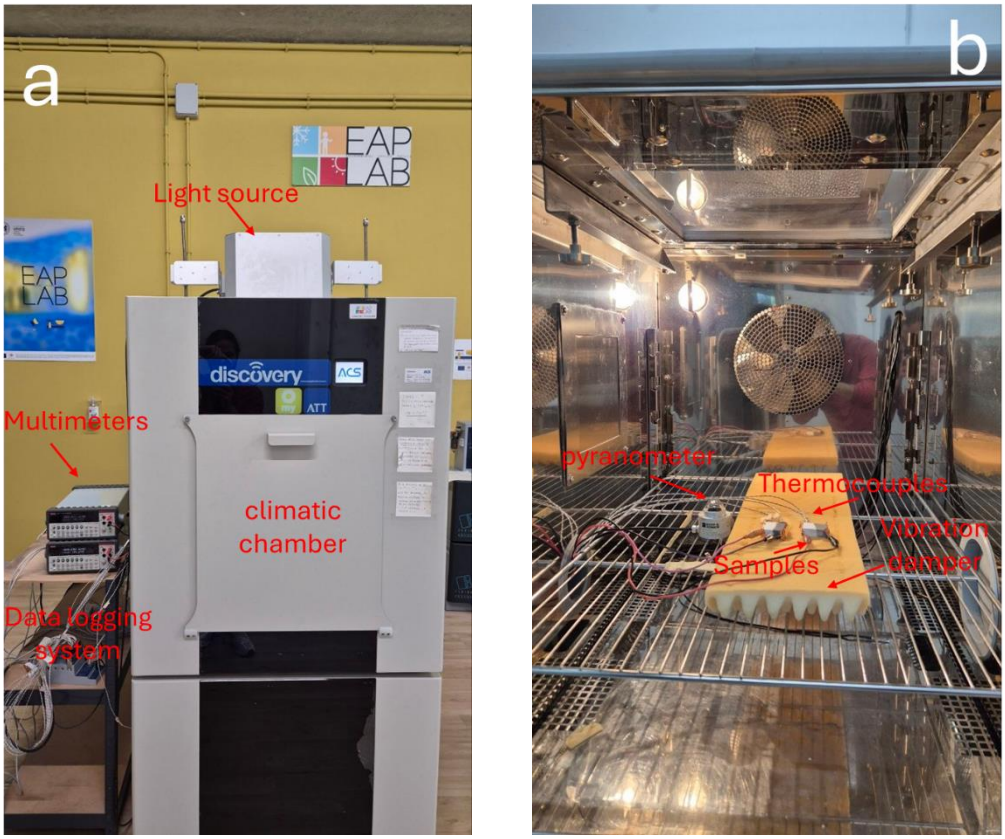


Figure 2.4 (a) the climatic chamber and the data logging system for temperature and voltage, (b) the samples configuration inside the climatic chamber

2.3.4.1 Static Environmental Testing

Under static conditions, the PTE response was evaluated at fixed temperatures and relative humidity levels to decouple their individual effects on ionic transport and thermoelectric behavior.

Measurements were performed at multiple temperatures (e.g., 10 °C, 25 °C, and 40 °C) and relative humidity levels (e.g., 30%, 60%, and 90%) under constant irradiation (~900 W m^{-2}). These conditions allowed systematic investigation of:

- the effect of temperature on ionic mobility and thermodiffusion,
- the effect of relative humidity on pore-solution connectivity and ionic conductivity.

Additionally, the influence of environmental history was evaluated by preconditioning samples under different night-time humidity levels prior to testing. This approach enabled assessment of the rehydration capability of the materials and their ability to recover thermoelectric performance after drying.

2.3.4.2 Dynamic Environmental Testing

To replicate real-world operating conditions, dynamic experiments were performed by simulating 24-hour climatic cycles corresponding to different geographical locations and seasons.

The climatic chamber was programmed to reproduce temperature, relative humidity, and irradiation profiles representative of selected cities with distinct climatic conditions, such

as dry (Cairo), moderate (Madrid), and humid (Singapore) environments. These simulations included both summer and winter scenarios, incorporating diurnal variations in environmental parameters.

The environmental boundary conditions used for these simulations were derived from meteorological datasets obtained from the Open-Meteo platform, which provides high-resolution historical and forecast weather data, including solar irradiance, ambient temperature, and relative humidity. These data were used to construct realistic temporal profiles of environmental conditions, ensuring that the imposed laboratory cycles closely mimic real climatic behavior.

Under these dynamic conditions, the PTE response was continuously monitored, allowing evaluation of the time-dependent coupling between thermal gradients, moisture transport, and ionic conduction. Unlike static tests, these measurements capture transient effects and reveal the sensitivity of the system to evolving environmental conditions.

Overall, the combined use of surface characterization, controlled indoor testing, climatic chamber experiments, and outdoor measurements provides a comprehensive framework for evaluating cement-based PTE materials. This multi-scale approach enables direct correlation between surface properties, environmental conditions, and thermoelectric performance, demonstrating that these systems behave as environment-responsive energy materials whose performance is governed by both instantaneous conditions and environmental history.

Chapter III

Sustainable Geopolymer Concrete for Thermoelectric Energy Harvesting

The preceding chapter established that cementitious materials, particularly alkali-activated systems, offer a promising platform for harvesting low-grade thermal energy due to their intrinsic ionic transport, tunable chemistry, and scalability within urban infrastructure. Building on this framework, the present chapter focuses on the experimental development and characterization of geopolymer-based thermoelectric cement composites, with particular emphasis on understanding the role of binder composition, microstructure, and addition incorporation in governing thermoelectric performance. In line with the challenges identified in the literature, namely incomplete understanding of their underlying transport mechanisms, particularly the role of intrinsic voltage and ionic contributions, this work investigates an industrially relevant hybrid geopolymer system and evaluates its thermoelectric behavior under controlled conditions. Special attention is given to the incorporation of copper slag as a low-cost, sustainable additive, aiming to enhance the Seebeck response while maintaining structural and environmental viability. Through this approach, the chapter seeks to establish a direct link between material design strategies and thermoelectric functionality, thereby advancing the development of scalable cement-based energy harvesting systems while aligning with the broader objectives outlined in the thesis introduction

3.1. Experimental

3.1.1. Materials and Sample Preparation

An industrial geopolymer-based hybrid cement (GHC), supplied by Považská cementáreň a.s., was employed in this study for the preparation of both cement paste and cement concrete specimens. In contrast to many of the previous studies focused on laboratory-scale formulations, the use of an industrially produced geopolymer system enables direct assessment of thermoelectric performance in materials that are inherently compatible with large-scale production and practical construction applications. The hybrid binder consisted of 90% geopolymer and 10% ordinary Portland cement (OPC), with a particle size distribution ranging from 0.8 μm to 100 μm, and the majority of particles falling within the 0.8–10 μm range. The geopolymer phase was derived from fly ash, granulated blast furnace slag (GBFS), and highly alkaline wastewater originating from red mud deposits. The detailed chemical composition of the hybrid cement and its constituent raw materials has been reported in a separate study [66].

To further enhance the thermoelectric response while preserving scalability and material sustainability, copper slag (CS) was incorporated as a recycled aggregate. The selection of CS is motivated by the limitations associated with conventional functional additions, which often increase material cost and may adversely affect mechanical performance,

thereby restricting large-scale applicability. In contrast, copper slag, an abundant byproduct of copper smelting and refining, with an estimated generation of 2.3–3 tons per ton of produced copper, consists primarily of metal oxides that can contribute to improved Seebeck response without compromising structural integrity. Despite ongoing recycling efforts, significant quantities of CS remain stockpiled, highlighting its potential as a sustainable construction material. Its incorporation as an aggregate, potentially replacing a substantial fraction of natural aggregates, offers both environmental and functional advantages by reducing the demand for natural aggregates and lowering the energy footprint associated with cement production [67,68]. In addition, the presence of metal-oxide phases provides an opportunity to investigate the mechanisms governing enhanced thermoelectric voltage generation in such composite systems. Prior to mixing, the copper slag was processed using a sieve shaker with a maximum sieve size of 120 µm to ensure controlled particle size distribution. The chemical compositions of both the GHC and CS aggregates are summarized in Table 3.1.

Table 3-1 Chemical composition of the Geopolymer-based hybrid cement GHC and CS aggregates.

	SiO_2	Al_2O_3	Fe_2O_3	MnO	MgO	CaO	Na_2O	K_2O	TiO_2	P_2O_5	SO_3	Loss of Ignition (%)
GHC	35.86	13.51	4.63	0.06	1.79	23.93	3.36	1.97	0.61	0.21	5.02	5.51
CS	22.01	8.86	50.87	0.80	1.48	7.90	0.43	0.24	0.18	0.54	0.25	2.63

Two compositions were prepared: a reference geopolymer-based hybrid cement paste (GHC) and a composite incorporating 75 wt.% copper slag (GHC-75CS). For clarity, these formulations are hereafter referred to as GHC and GHC-75CS, respectively. The preparation procedure involved an initial dry mixing step, in which the cement and aggregates were blended using a mechanical mixer at 300 rpm until a homogeneous mixture was obtained. Subsequently, distilled water was added, and the mixture was further processed at 700 rpm for 1.5 minutes. After a resting period of 1 minute, the mixing step was repeated to promote uniform dispersion and ensure consistency of the slurry (Figure 3.1a and b).

The resulting mixtures were then cast into sealed cubic silicone molds and maintained under static conditions for 24 h before demolding. Following demolding, all specimens were cured in water for seven days, as illustrated in Figure 3.1c. A constant water-to-cement ratio (w/c) of 0.6 was maintained for all formulations to ensure comparability across samples.

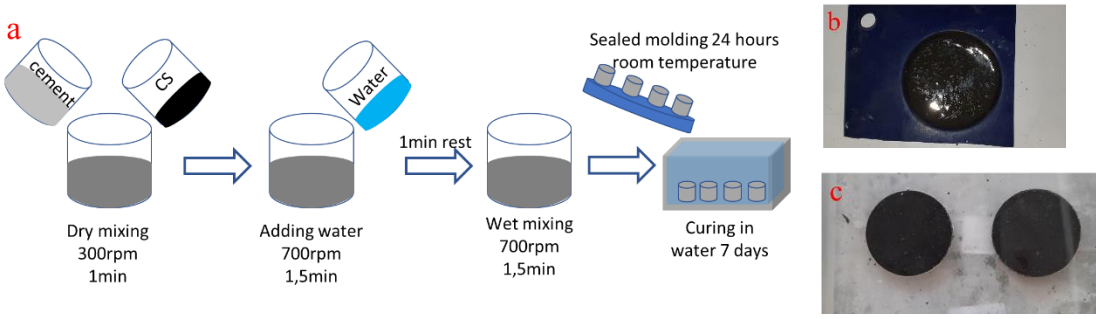


Figure 3.1 (a) Experimental setup for sample preparation, (b). cement paste, (c). curing samples in water.

3.1.2. Material Characterization

A combination of complementary characterization and measurement techniques was employed to systematically evaluate the developed cementitious systems. Structural and chemical analyses were carried out using X-ray diffraction (XRD) and X-ray fluorescence (XRF), while thermogravimetric analysis (TGA) and mercury intrusion porosimetry (MIP) were used to assess thermal behavior and pore structure. Mechanical performance was evaluated through dynamic elastic modulus measurements. In addition, thermal conductivity, electrical conductivity (via impedance spectroscopy), intrinsic voltage, and thermoelectric response were investigated to elucidate the transport mechanisms governing material performance. The selection of these techniques enables a comprehensive correlation between composition, microstructure, and functional properties. Detailed descriptions of the experimental setups, instrumentation, and measurement protocols are provided in Chapter II; therefore, only the relevant results and their discussion are presented in this chapter.

3.2. Results and Discussion

3.2.1. Material Characterization

3.2.1.1 Structural Analysis

The aggregates used in this study were characterized by X-ray diffraction (XRD) and X-ray fluorescence (XRF) to determine their chemical composition and crystalline phase assemblage. The XRD analysis revealed that the copper slag (CS) aggregates are primarily composed of fayalite and spinel phases. The characteristic peaks of fayalite (orthorhombic Fe_2SiO_4) are identified in Figure 3.2a and denoted by "F," while the mixed oxides of the spinel group are indicated by "sp." These spinel-type cubic mixed oxides (e.g., $MgAl_2O_4$, referred to as spinel ss) can accommodate a wide range of cations within their structure, including divalent species (Mg^{2+}, Ni^{2+}, Mn^{2+}, Co^{2+}) and trivalent species (Al^{3+}, Cr^{3+}, Mn^{3+}, Co^{3+}, V^{3+}), forming solid solutions without significantly altering their crystallographic structure or diffraction patterns. The observed magnetic behavior of the sample further suggests that these phases are compositionally close to magnetite ($Fe^{2+}Fe^{3+}{}_2O_4$).

The bulk chemical composition of the CS aggregate, determined by XRF and summarized in Table 3.1, confirms the presence of minor metallic elements such as Zn, Cu, Ni, Cr, and Sn, which may be incorporated into the oxide structure. In addition to fayalite and spinel phases, the XRD pattern indicates the presence of silicate phases of the pyroxene type, denoted by "si." The loss on ignition (LOI) analysis of CS shows an apparent mass gain rather than mass loss, which is primarily attributed to the oxidation of ferrous oxide (FeO) to ferric oxide (Fe_2O_3) during heating.

Following seven days of curing, the phase composition of the GHC and GHC-75CS pastes was further examined by XRD, as shown in Figure 3.2b. The elevated background intensity, particularly in the 20–35° 2θ range, indicates the presence of a substantial amorphous (non-crystalline) fraction. Superimposed on this background, distinct diffraction peaks corresponding to multiple crystalline phases are observed, including

hexagonal ettringite ($Ca_6Al_2(SO_4)_3(OH)_{12}\cdot 26H_2O$, labeled "Et"), quartz (SiO_2, "Q"), and mullite ($Al_6Si_2O_{13}$, "M"). In addition, a broad diffraction feature centered at approximately 29.5° 2θ, labeled "T," is attributed to tobermorite, a crystalline analogue of the C–S–H gel. Importantly, the incorporation of CS aggregates does not lead to significant changes in the overall phase assemblage of the cementitious matrix, as evidenced by the similarity of the XRD patterns.

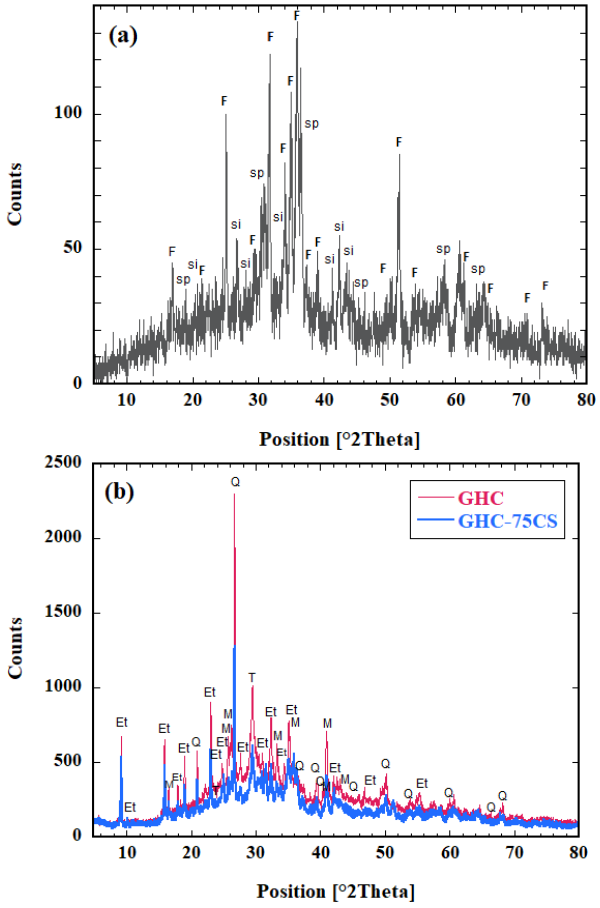


Figure 3.2 XRD pattern of (a) industrially prepared CS aggregate. And (b) X-ray diffraction of GHC and GHC-75CS after curing.

3.2.1.2 Thermogravimetric Analysis

The thermogravimetric analysis (TGA) results for GHC and GHC-75CS, obtained at a heating rate of 10 K/min, are presented in Figure 3.3. The mass loss observed below 200 °C is primarily attributed to the evaporation of bulk water within the pore structure. The incorporation of copper slag (CS) in the GHC-75CS composite leads to a significant reduction in bulk water content, decreasing from 23.2% in the reference GHC sample to 6.5%. While a reduction in water content is expected due to the replacement of cementitious material with aggregates, the observed decrease of approximately 72% exceeds the anticipated proportional reduction based on aggregate volume alone. This deviation suggests that the incorporation of CS modifies the pore structure and water retention capacity of the matrix, which may, in turn, influence transport properties and overall thermoelectric performance.

Further insights are obtained from the derivative thermogravimetric (DTG) curves, which exhibit two additional mass-loss peaks in the temperature ranges of 400–500 °C and above 700 °C. The peak centered around 450 °C is associated with the dehydroxylation of portlandite ($Ca(OH)_2$), consistent with the presence of 10% ordinary Portland cement (OPC) in the hybrid binder [69]. The high-temperature peak is attributed to the decomposition of calcite and dihydroxylation processes occurring within the cementitious matrix [70].

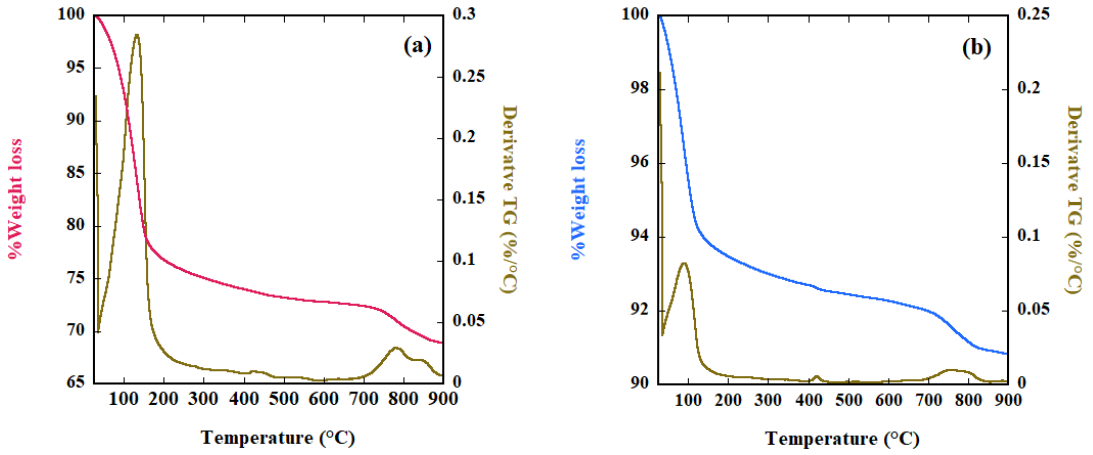


Figure 3.3 Thermogravimetric analysis (TG and DTA) (a) GHC and (b) GHC-75CS.

3.2.1.3 Mercury Intrusion Porosimetry

Figure 3.4 presents the Mercury Intrusion Porosimetry (MIP) results for both GHC and GHC-75CS samples. Overall, a comparable pore size distribution is observed between the two systems; however, distinct differences in porosity characteristics can be identified. The GHC sample exhibits a slightly lower total porosity of 38%, whereas the GHC-75CS composite shows an increased porosity of 42%.

A more detailed examination of the MIP curves indicates that GHC contains a population of pores with diameters below 10 nm, a feature that is not observed in the GHC-75CS sample. The higher porosity in GHC-75CS is therefore primarily attributed to the presence of larger pores, which contribute disproportionately to the total pore volume. This trend is further supported by the analysis of the total pore area, which is measured to be 43.18 m^2/g for GHC and 29.82 m^2/g for GHC-75CS.

Given that the total pore area reflects the internal surface area of the pore network, the combination of lower porosity and higher pore surface area in GHC suggests a finer pore structure, characterized by smaller pore sizes and a higher density of internal interfaces. In contrast, the reduction in total pore area alongside increased porosity in GHC-75CS indicates a shift toward a coarser pore architecture dominated by larger pore domains.

These observations collectively indicate that the incorporation of CS aggregate modifies the pore structure of the cementitious matrix, leading to a redistribution of pore sizes and a reduction in interfacial surface area. Such microstructural changes are expected to influence mass transport, moisture retention, and ion distribution within the pore network, thereby altering the internal physicochemical environment of the material.

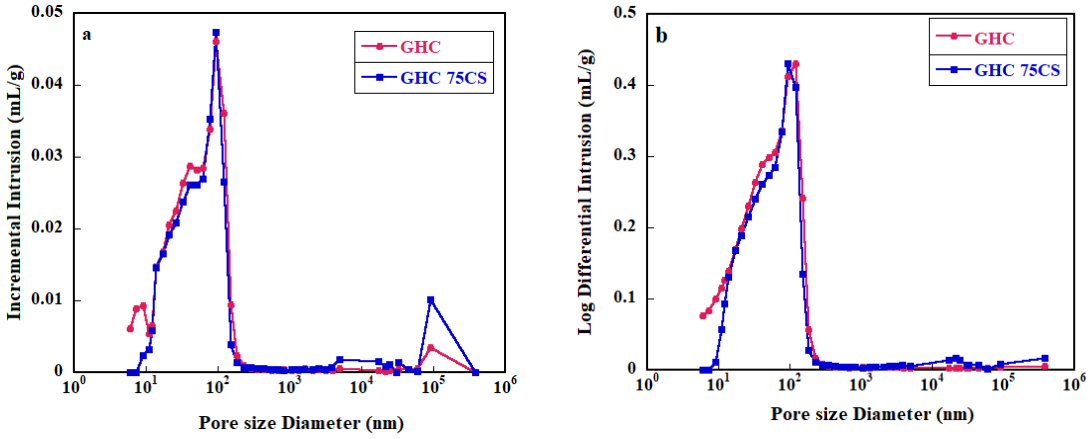


Figure 3.4 (a) Incremental intrusion vs. pore size diameter. (b) log differential intrusion vs. pore size diameter

3.2.1.4 Mechanical Properties

The results of the dynamic elastic modulus measurements are presented in Figure 3.5. The bulk densities of the samples were first determined, yielding values of 1648 kg/m³ for GHC and 2100 kg/m³ for GHC-75CS, corresponding to an increase of approximately 27% upon incorporation of copper slag. The addition of 75 wt.% CS aggregate results in an increase of the elastic modulus by approximately 16% before thermal exposure (Figure 3.5). This enhancement is consistent with previous studies investigating the effect of copper slag on the mechanical performance of cementitious materials. The observed improvement can be attributed to several factors, including the contribution of copper slag to the geopolymerization process [71], the development of a denser microstructure [72], and improved interfacial bonding between the CS aggregates and the surrounding matrix [73].

Upon thermal loading, the elastic modulus of both GHC and GHC-75CS decreases with increasing temperature. In the case of GHC, the most pronounced reduction occurs during the initial heating stage at 90 °C, beyond which further temperature increases result in only minor additional changes. In contrast, the reduction in elastic modulus for GHC-75CS follows a more gradual and continuous trend with increasing temperature. This degradation in mechanical stiffness is primarily associated with moisture loss at elevated temperatures [74]. Notably, the extent of water evaporation in GHC-75CS is lower than that in GHC, which correlates with a reduced overall loss in mechanical properties. Specifically, GHC-75CS exhibits a total decrease in elastic modulus of 22.6%, accompanied by a weight loss of 4.5%, whereas GHC shows a significantly larger reduction of 42%, corresponding to a weight loss of 7.8%.

These results indicate that the incorporation of copper slag not only enhances the initial mechanical properties of the geopolymer matrix but also improves its resistance to thermal degradation. Even after thermal exposure, the elastic modulus of GHC-75CS remains comparable to that of the as-prepared GHC sample, highlighting the beneficial role of CS aggregates in maintaining structural integrity under elevated temperature conditions.

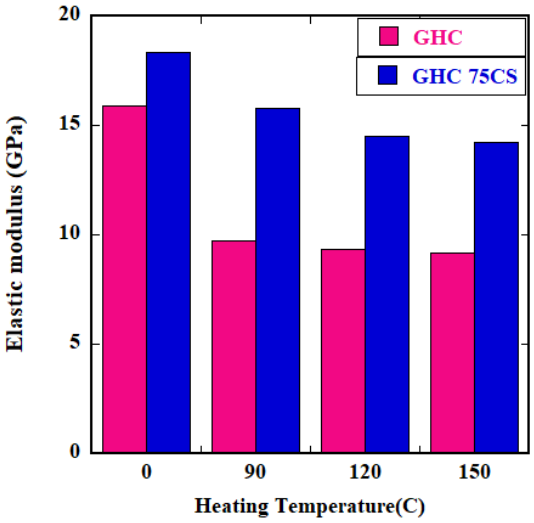


Figure 3.5 The elastic modulus of the GHC and GHC 75CS as a function of increasing temperature

3.2.1.5 Intrinsic Voltage

Figure 3.6 presents the temporal evolution of the open-circuit voltage (V_{OC}) for both samples prior to the application of any temperature gradient. In both cases, a pronounced initial voltage difference is observed between the electrodes at the onset of measurement, indicating the presence of an intrinsic voltage within the material. This phenomenon was first reported by Panchapakesan et al. [75] in conventionally prepared cement pastes without admixtures. Notably, the sign, magnitude, and temporal evolution of this inherent voltage can vary even among samples produced from the same mixture.

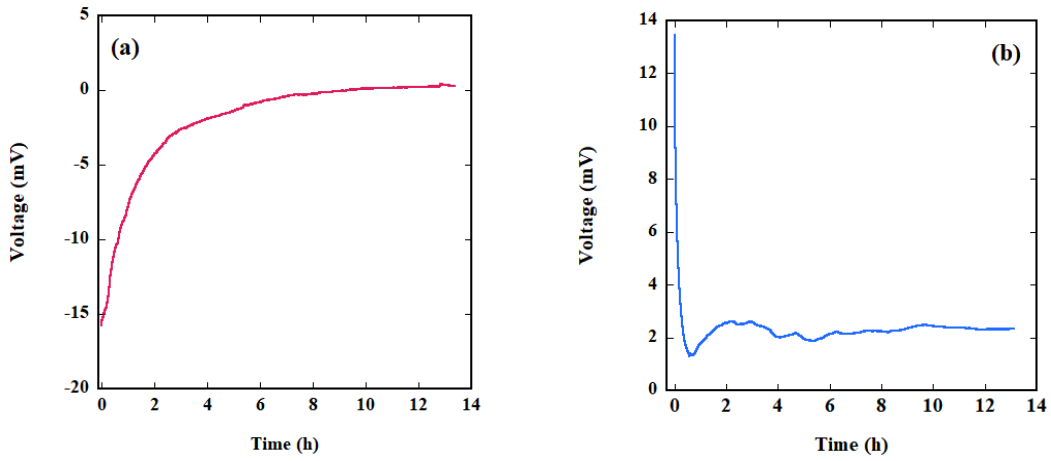


Figure 3.6 Intrinsic voltage between two electrodes before applying temperature differences (a) cement paste and (b) cement paste with 75% CS aggregates.

This variability is further illustrated in Figure 3.7a, which shows the distinct V_{OC} behavior of two samples obtained from the same batch. The observed divergence highlights the non-deterministic nature of the intrinsic voltage in as-prepared cementitious systems, consistent with previous reports in the literature [23]. However, it can be seen that after stabilization the voltage remains nearly constant over long period of time (Figure 3.7b).

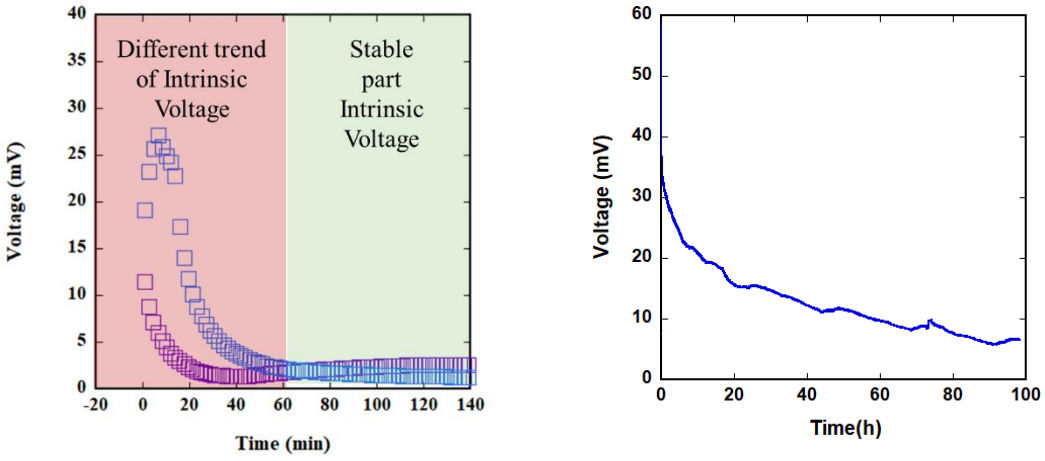


Figure 3.7 (a) Evolution of the intrinsic voltage over time for two GHC75CS from the same batch (b) open circuit voltage measurement over 100h

Despite its evident presence, the influence of intrinsic voltage on the thermoelectric behavior of cement-based materials has not been systematically addressed in the available literature. Li et al. [24] reported the occurrence of an inherent voltage during thermoelectric measurements of both OPC and geopolymer systems, including a metakaolin-based geopolymer exhibiting a Seebeck coefficient of 2000 µV/°C alongside an intrinsic voltage of approximately −10 mV. However, the potential impact of this intrinsic voltage—and its temporal evolution—on the measured thermoelectric response was not considered.

3.2.2. Thermoelectric Properties

3.2.2.1 Thermal Conductivity

The thermal conductivity of the cement pastes, with and without copper slag (CS) incorporation, was measured as a function of temperature, and the results are presented in Figure 3.8. The data indicate that the addition of CS aggregate contributes to a more stable thermal conductivity response across the investigated temperature range. This behavior is consistent with previous findings by Caggiano et al. [76], who reported that the thermal conductivity of geopolymer systems exhibits limited sensitivity to temperature variations.

The average thermal conductivity values were determined to be 0.49 W/m·K for GHC and 0.58 W/m·K for GHC-75CS, which fall within the typical range reported for cement-based composites containing metal oxide phases [45]. The relatively low thermal conductivity of these materials is advantageous for thermoelectric applications, as it facilitates the maintenance of temperature gradients within the material.

A more detailed analysis reveals that at 50 °C, the thermal conductivity of GHC-75CS is approximately 16% lower than that of the reference GHC paste. However, with increasing temperature, this trend reverses: at 150 °C and 250 °C, the thermal conductivity of the CS-containing composite becomes approximately 19% to 32% higher than that of GHC. This temperature-dependent behavior suggests that the incorporation of CS aggregates

modifies heat transport mechanisms within the matrix, potentially through changes in phase composition, pore structure, and solid–solid contact pathways.

These results indicate that CS incorporation can influence thermal transport differently across temperature regimes, with potential implications for thermoelectric performance. In particular, the reduced thermal conductivity at low to intermediate temperatures may enhance temperature gradient retention within the operational range typical for cement-based energy harvesting systems, while the increased conductivity at higher temperatures reflects the evolving contribution of the solid phase to heat transfer.

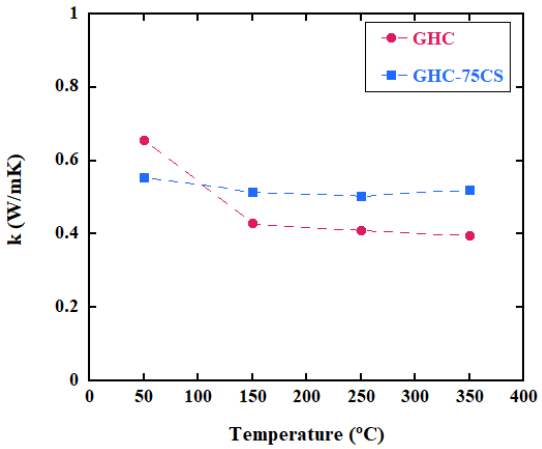


Figure 3.8 Thermal conductivity of pure cement paste and cement concretes at different temperatures.

3.2.2.2 Electrical Conductivity

To evaluate the effect of temperature on electrical transport, two-probe impedance spectroscopy measurements were conducted at a heating rate of 1 °C/min up to 160 °C. The resulting DC conductivity as a function of temperature is presented in Figure 3.9. At 30 °C, the electrical conductivities of GHC and GHC-75CS were measured as 2.3×10^{-3} S m^{-1} and 3.0×10^{-4} S m^{-1}, respectively.

The temperature-dependent conductivity behavior exhibits two distinct regimes. In the initial stage, a slight increase in electrical conductivity is observed at lower temperatures. This is followed by a second stage, in which conductivity decreases with further temperature increase. The pronounced drop in conductivity around 100 °C is correlated with the evaporation of bulk water, indicating that ionic charge carriers dominate the conduction mechanism in these systems. As water is progressively removed during heating, the mobility of ions within the pore solution is significantly reduced, leading to a marked decrease in conductivity.

This interpretation is consistent with the thermogravimetric analysis, which showed a substantial reduction in bulk water content in the CS-containing sample. Consequently, the lower electrical conductivity of GHC-75CS at room temperature can be attributed to the reduced availability of mobile ionic species. More broadly, the electrical conductivity of cementitious materials is strongly influenced by microstructural features, particularly pore size distribution and connectivity (tortuosity). As discussed in Section 3.1.3 the MIP results indicate that GHC contains a higher fraction of pores with diameters below 10 nm.

However, such fine pores do not significantly contribute to ionic transport, as noted by Mindess and Young [77].

In contrast, the GHC-75CS sample exhibits a higher proportion of larger pores. Considering both the reduced bulk water content (as indicated by TGA) and the presence of these larger pore domains, it can be inferred that ionic transport pathways are less effective in this system. In addition, the inclusion of aggregates is known to modify pore geometry and increase tortuosity, which can further hinder charge transport and increase electrical resistivity, as reported by Sengul [78]. These observations are consistent with the porosimetry results and confirm that the incorporation of CS significantly alters the pore structure of the cementitious matrix.

It is also observed that the addition of CS stabilizes the initial conductivity regime and increases the slope of the conductivity–temperature curve, effectively extending the operational temperature range of the material from approximately 70 °C to 90 °C. Following drying, the CS-containing sample exhibits higher conductivity compared to the reference paste, which can be attributed to an increased contribution from electronic conduction within the matrix. However, despite the high aggregate content, the intrinsic electrical conductivity of CS (approximately 1.0×10^{-7} S m^{-1}) is relatively low. As a result, the enhancement in electronic conductivity is limited and does not fully compensate for the reduction in ionic conductivity associated with decreased water content.

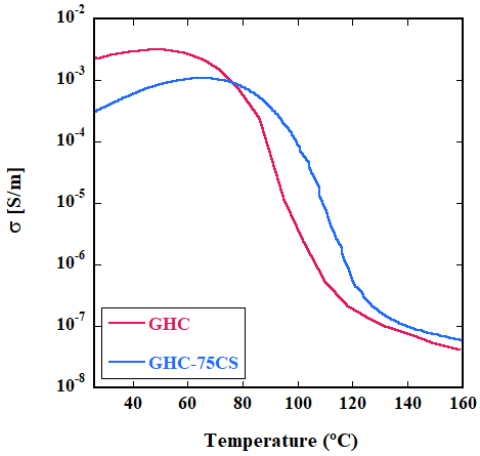


Figure 3.9 The heating ramp's effect on the electrical conductivity of the samples.

3.2.2.3 Seebeck Behavior

To evaluate the influence of intrinsic voltage on thermoelectric measurements, the approach reported by Li et al. [24] was initially applied to the GHC-75CS composite. Figure 3.10 illustrates the variation of thermoelectric voltage as a function of the applied temperature difference (ΔT). Notably, the presence of intrinsic voltage results in a clear deviation of the voltage–ΔT relationship from the origin. Using the conventional definition of the Seebeck coefficient, calculated from the slope of the ΔV–ΔT curve ($S = \Delta V/\Delta T$), an apparent value of 4392 μV K^{-1} was obtained.

However, further analysis revealed that this value is significantly influenced by the intrinsic voltage contribution and does not accurately represent the true thermoelectric

response of the material. To address this limitation, a modified measurement protocol was adopted, in which temperature gradients were applied only after the intrinsic voltage had stabilized to a constant value for a minimum duration of 1 h.

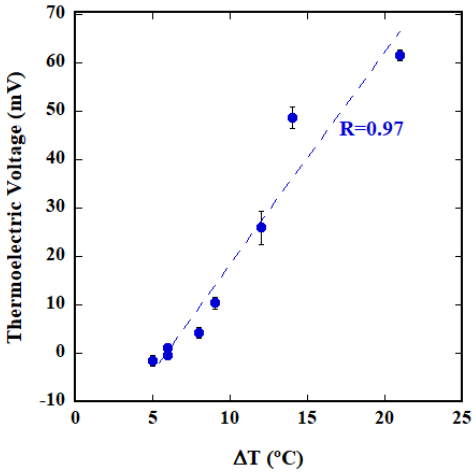


Figure 3.10 Thermoelectric voltage of GHC-75CS as a function of different temperature differences (ΔT) with the linear fit of y = 4.392x-25.725

Therefore, the Seebeck coefficient was determined from the thermoelectric voltage by measuring the time-dependent open-circuit voltage (V_{OC}). To evaluate the Seebeck behavior, three temperature levels, 90 °C, 120 °C, and 150 °C, were applied to the top surface of the samples. For each applied temperature, the corresponding temperature difference (ΔT) between the two electrodes was recorded. The resulting ΔT values were 27, 42, and 55 K for GHC, and 30, 49, and 58 K for GHC-75CS, respectively. The observed differences in ΔT at identical applied temperatures are attributed to variations in thermal conductivity between the two systems.

These temperature conditions were selected to systematically assess the thermoelectric response of the materials and to examine the influence of ionic transport under increasing thermal gradients. In particular, the temperature of 90 °C corresponds to the operational range discussed in this study, while higher temperatures enable partial drying of the samples from the heated surface, thereby allowing investigation of the effect of thermal gradients on ion migration across the material.

Figure 3.11 presents the temporal evolution of the open-circuit voltage during heating at the first applied temperature for both GHC and GHC-75CS samples. The voltage profiles exhibit three distinct stages. For the GHC-75CS sample, an enlarged view of the first and second stages is also provided for clarity. In Stage I, corresponding to the initial activation of the ceramic heater, the temperature difference increases rapidly. During this stage, the absolute voltage shifts toward more negative values with increasing temperature.

This is followed by Stage II, in which the voltage reverses direction and progresses toward more positive values after reaching a minimum V_{OC} of −3.3 mV for GHC and −11.8 mV for GHC-75CS. Finally, in Stage III, the open-circuit voltage stabilizes and reaches a steady-state value. It is important to note that both Stage II and Stage III occur under conditions of relatively stable ΔT, indicating that the observed voltage evolution is

governed by internal transport processes rather than further changes in the applied temperature gradient.

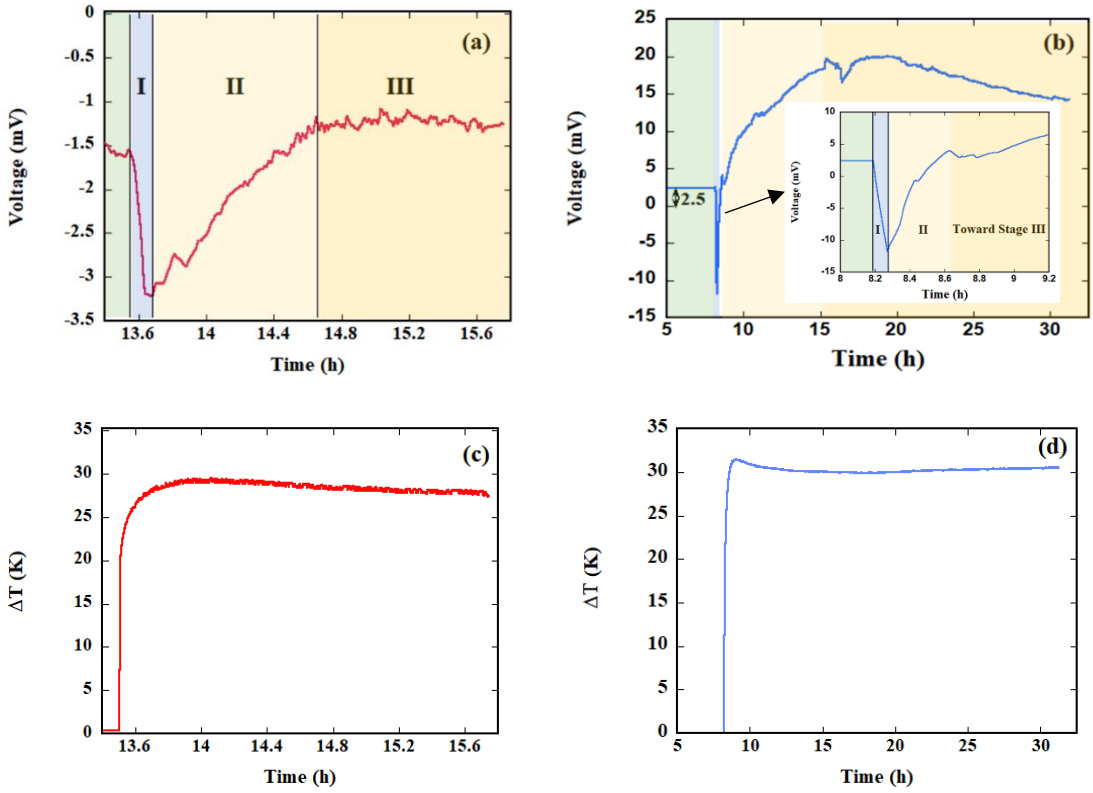


Figure 3.11 (a) Voltage profile of GHC and (b) GHC-75CS at the applied temperature of 90 °C, (c) the temperature difference between two electrodes of GHC, and (d) GHC-75CS.

Figure 3.12 presents the voltage profiles of GHC and GHC-75CS at three different temperature differences. It is important to note that, in this study, the temperature was applied sequentially and continuously, without any intermediate cooling between successive temperature steps.

For the GHC sample, the voltage profiles obtained at 90 °C and 120 °C are nearly identical, indicating a comparable thermoelectric response within this temperature range. However, upon further increasing the temperature to 150 °C (Figure 3.12c), a noticeable behavior change is observed. Specifically, the magnitude of the negative voltage peak is significantly reduced, and the duration of both Stage I and Stage II is extended. This is reflected in the longer time scale of the voltage evolution in Figure 3.12c compared to Figures 3.12a and b.

In contrast, the response of the GHC-75CS sample exhibits a more pronounced temperature dependence. With increasing temperature, the magnitude of the negative peak decreases progressively and eventually disappears at 150 °C, indicating the complete suppression of Stage I under these conditions. In addition, during Stage III, the voltage profile shows a gradual decrease in V_{OC}, and the rate of this decline becomes steeper with increasing temperature.

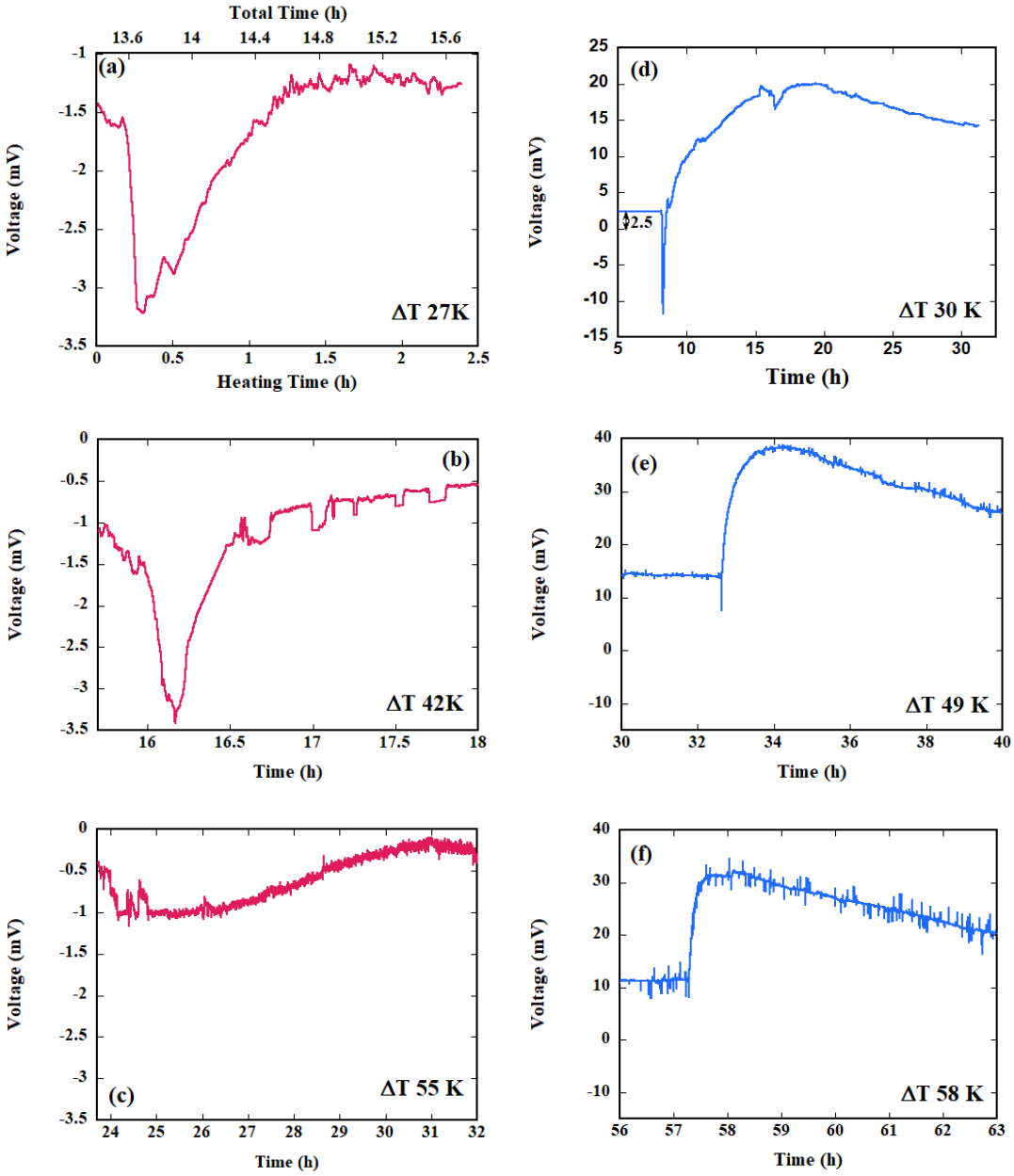


Figure 3.12 (a), (b), and (c) evolution of thermoelectric voltage with three applied temperatures for GHC, and (d), (e), and (f) for GHC-75CS.

A clear distinction between the two systems is observed during Stage III of the voltage evolution. For the reference GHC paste, the stabilized voltage remains close to the initial intrinsic value measured before the application of the temperature gradient. In contrast, the GHC-75CS sample exhibits a reversal in voltage polarity, with the stabilized value not only changing sign but also reaching a higher absolute magnitude than the initial negative peak. Considering that the sign convention in this study is defined with respect to the cold side, this behavior indicates a transition in the dominant thermoelectric response of GHC-75CS from n-type to p-type during the course of the measurement.

To further investigate the origin of the charge carriers, controlled drying experiments were performed. It is well established that drying reduces the concentration of mobile ions in

the pore solution; accordingly, Cui et al. [12,15] proposed that moderate drying (e.g., at 60 °C) can be used to distinguish between ionic and electronic contributions to thermoelectric behavior. Figure 3.13 presents the voltage profiles of GHC-75CS after drying at 60 °C and 105 °C overnight. The 60 °C was selected based on the literature, while 105 °C was selected to ensure the removal of the bulk water based on TGA results.

Following drying at 60 °C, the sample exhibits a pronounced intrinsic voltage of approximately 18 mV at the beginning of the measurement. In contrast, drying at 105 °C leads to the disappearance of the intrinsic voltage, supporting the hypothesis that the electret-like behavior in cementitious systems is of ionic origin. After stabilization of the intrinsic voltage, a temperature of 70 °C was applied to the top surface of the sample. The results show that drying at 60 °C suppresses the initial negative peak (Stage I) and reduces the magnitude of the stabilized voltage in Stage III.

For the sample dried at 105 °C, the V_{OC} response is characterized by oscillations around zero, indicating the absence of a stable thermoelectric signal. A similar behavior is observed for the pure GHC paste, where the thermoelectric voltage fluctuates around zero after drying at both 60 °C and 105 °C. This instability is attributed to the significant reduction in electrical conductivity following drying, which limits charge transport and leads to increased voltage fluctuations [12].

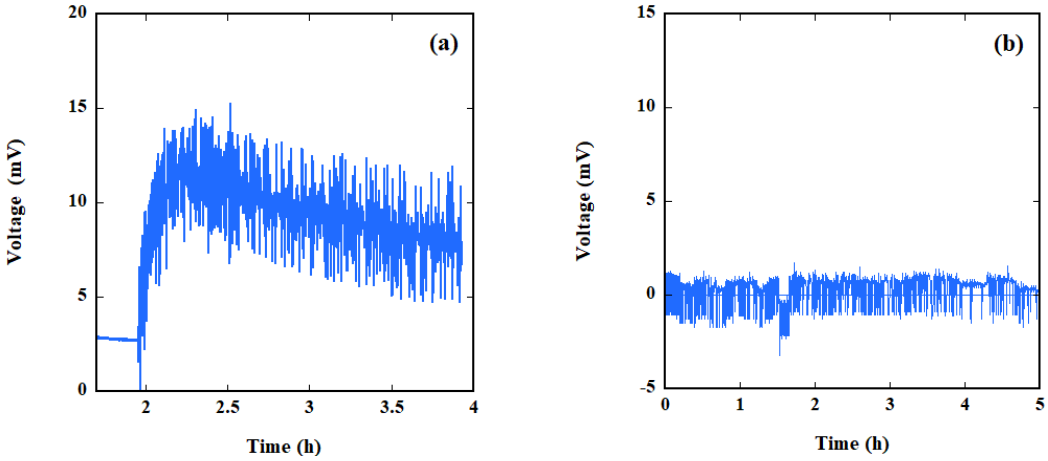


Figure 3.13 The variation of the open circuit voltage of dried GHC-75CS at applied 70 °C (a) dried at 60 °C overnight, and (b) dried at 105 °C overnight.

Based on these observations, the thermoelectric voltage generated in both cement paste and concrete can be attributed to the thermal diffusion of ions driven by the Soret effect. In this mechanism, the bulk pore solution does not exhibit macroscopic charge separation; instead, differences in ionic mobility under an applied temperature gradient lead to the preferential accumulation of specific ionic species at the electrode interfaces.

In contrast to electronic charge carriers, ions are not able to traverse the external circuit. Rather, they migrate through the pore solution and accumulate at the electrode surfaces, where they form localized charge regions. This accumulation gives rise to the formation of an electrical double layer (EDL) at the electrode–electrolyte interface. The establishment of the EDL induces a corresponding redistribution of electronic charge

carriers in the external circuit, with charges of opposite sign accumulating at the electrode surface to maintain electrochemical equilibrium.

Figure 3.14 schematically illustrates the thermally driven diffusion of cations and anions and their respective contributions during the different stages of voltage evolution under an applied temperature gradient.

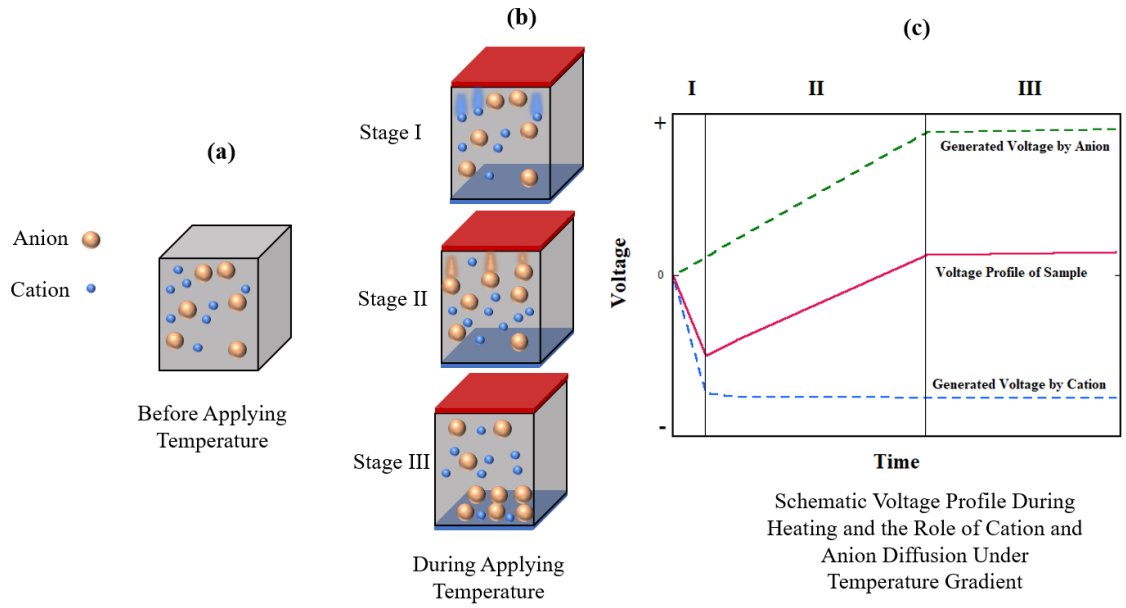


Figure 3.14 Schematic view of (a) ions in the initial stage before applying ΔT, (b) diffusion of ions during different stages of the voltage profile, (c) the role of different ions diffusion on voltage profile

The open-circuit voltage evolution reveals that the initial negative peak appears within the first few seconds after activation of the heater and reaches its maximum (negative) value after approximately 396 s for GHC and 288 s for GHC-75CS. Honorio et al. [79] reported that metal cations such as Na^+ and K^+ exhibit higher diffusion rates than OH^- ions in the pore solution. Accordingly, the negative voltage observed during Stage I can be attributed to the preferential migration of these cations away from the electrical double layer at the hot electrode.

This interpretation is further supported by the temperature-dependent measurements. As the applied temperature increases and partial drying occurs near the heated surface, the initial negative peak progressively diminishes and eventually disappears. The measured voltage corresponds to the potential difference between the cold and hot electrodes ($\Delta V = V_C - V_H$). Since ions cannot pass through the external circuit, the depletion of cations from the double layer at the hot electrode increases the local potential (V_H), thereby resulting in a more negative ΔV.

Previous studies have shown that OH^- ions exhibit a stronger tendency to accumulate at the cold side under a temperature gradient compared to alkali cations [80]. Consequently, Stage II can be interpreted as an OH^--dominated regime, in which the removal of OH^- from the hot electrode reduces the potential difference between the electrodes. In Stage

III, the accumulation of OH^- within the double layer at the cold electrode leads to the stabilization of both V_C and ΔV, resulting in a steady and positive voltage.

Transitions between n-type and p-type thermoelectric behavior have been previously reported in cementitious systems exhibiting ionic thermoelectricity. Cui et al. [12] demonstrated that ion leaching significantly reduces the concentration of OH^- ions, enabling metal cations such as Ca^{2+}, Na^+, and K^+ to dominate the thermoelectric response and induce a transition from n-type to p-type behavior. Similarly, in another study [10], cement samples subjected to immersion in a saturated NaOH solution exhibited a temperature-dependent shift in voltage polarity, further highlighting the role of ionic composition and temperature sensitivity in governing thermoelectric response.

In the present study, a transition from n-type to p-type behavior is observed during Stage II for the GHC-75CS sample, despite the nominally constant temperature difference and initial ion concentration. This behavior can be attributed to the differing diffusion rates and transport dynamics of ionic species, which evolve during heating. In addition, the progressive drying of the material reduces the contribution of mobile cations, thereby modifying the relative dominance of ionic species. These observations indicate that the thermoelectric response of cementitious systems is governed by spatially and temporally evolving ionic transport processes within the pore network under a temperature gradient.

Figure 3.15 compares the Seebeck coefficients of GHC and GHC-75CS at different temperatures. The Seebeck coefficient was determined from the stabilized voltage values corresponding to Stage III at each temperature. For both materials, the Seebeck coefficient decreases with increasing temperature, which can be attributed to water loss at elevated temperatures. The selected temperature range was intentionally chosen to simulate semi-drying conditions and to monitor the migration of ions from the hot to the cold side. As a result, repeated heating leads to a hysteresis effect associated with moisture loss, causing a progressive reduction in the Seebeck voltage after each thermal cycle. To minimize this effect, sealing strategies may be employed during measurements to preserve the internal moisture content.

Independent measurements of the copper slag aggregate confirmed the absence of intrinsic thermoelectric behavior in this material. Nevertheless, the incorporation of CS into the cement matrix leads to a significant increase in both negative and positive voltage magnitudes. This behavior is likely associated with modifications to the pore structure and ionic environment of the composite. In particular, the substantial reduction in bulk water content suggests an increase in effective ion concentration within the pore network. Furthermore, the distinct temperature-dependent responses observed across TGA, electrical conductivity, and Seebeck measurements collectively indicate that the addition of CS alters the pore architecture and, consequently, the ionic thermoelectric behavior of the geopolymer system.

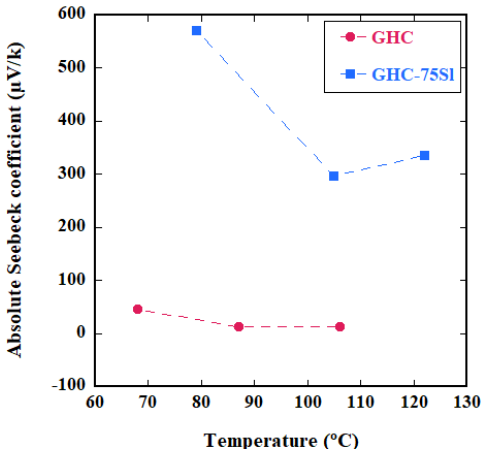


Figure 3.15 Seebeck coefficient of cement paste and concrete at the measured temperature.

3.2.2.4 TE Performance and Figure of Merit

Figure 3.16 presents a comparison of the thermoelectric figure of merit (ZT) for GHC and GHC-75CS. Although ZT is reported to enable comparison with conventional thermoelectric metrics, its interpretation in cement-based ionic systems must be treated with caution. Unlike steady-state electronic thermoelectrics, the voltage response here is time-dependent and influenced by ion accumulation, electrode polarization, intrinsic voltage, and moisture redistribution. Therefore, ZT should be considered a comparative material indicator rather than a direct predictor of device conversion efficiency. The results indicate that GHC-75CS achieves a maximum ZT value of 1.7×10^{-7}, whereas the reference GHC sample exhibits a significantly lower value of 2.4×10^{-9}. Although these values remain relatively low in absolute terms, they are consistent with the range typically reported for cement-based composites incorporating metal oxide phases [45].

The substantial enhancement in ZT observed for GHC-75CS is primarily attributed to the increase in the Seebeck coefficient following the incorporation of CS aggregate. As demonstrated in the previous sections, this elevated Seebeck response arises predominantly from ionic charge carriers within the pore solution. In comparison, Ghosh et al. [43] reported a cement composite containing 10% graphene and 10% ZnO_2 with a significantly higher ZT value of 1.0×10^{-2}, which was associated with a high electrical conductivity of 1390 S m^{-1} and a Seebeck coefficient of 142 μV K^{-1}. Despite the lower electrical conductivity of the present system, the relatively high Seebeck coefficient of 570 μV K^{-1} observed for GHC-75CS highlights the potential for further improving thermoelectric performance through strategies that enhance electrical conductivity.

These findings suggest promising pathways for the development of more efficient thermoelectric cementitious materials. In particular, the introduction of conductive fillers offers a viable approach to simultaneously improve electrical conductivity while maintaining or further enhancing the Seebeck coefficient, thereby increasing the overall figure of merit. In addition, the results of this study demonstrate that the properties of the pore solution, specifically ion concentration, mobility, and distribution, play a critical role in governing thermoelectric performance. This highlights the importance of ionic

thermoelectric mechanisms as a complementary strategy for optimizing ZT in cement-based systems.

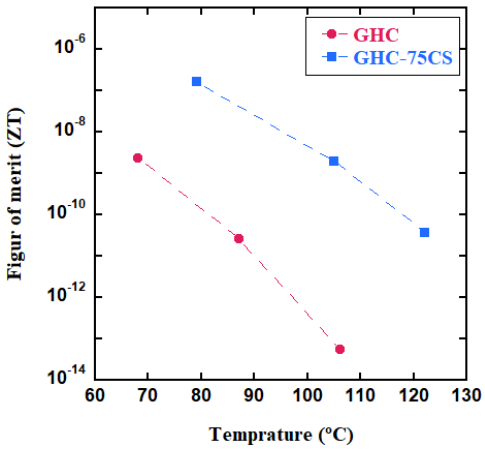


Figure 3.16 The calculated figure of merit (ZT) of GHC and GHC-75CS.

3.3. Conclusion

This study investigated the potential of geopolymer-based hybrid cement incorporating commercially recycled copper slag aggregates as a cost-effective and sustainable material for thermoelectric energy harvesting. A primary focus was placed on the influence of intrinsic voltage on thermoelectric measurements. An intrinsic voltage of approximately 15 mV was consistently observed in both cement paste and cement concrete, and this contribution was found to significantly affect the measured Seebeck response. To address this limitation, a modified measurement protocol was developed to isolate and eliminate the influence of intrinsic voltage. Using this approach, a Seebeck coefficient of 570 μV K^{-1} was obtained, representing one of the highest values reported for cementitious systems of this type.

In parallel, the mechanical performance of the material was evaluated. The incorporation of CS aggregate resulted in an increase of approximately 16% in the elastic modulus prior to thermal exposure, and further improvements in mechanical stability were observed at elevated temperatures. These results confirm that the addition of CS not only enhances functional performance but also maintains, and in some cases improves, the structural integrity of the composite.

Furthermore, the experimental results demonstrate that both the reference cement paste and the CS-containing composite exhibit ionic thermoelectric behavior, governed by the thermal diffusion of ions within the pore solution network under an applied temperature gradient. This finding highlights the dominant role of ionic charge carriers in the thermoelectric response of these systems.

Overall, this chapter provides a new perspective for improving thermoelectric performance in cementitious materials by emphasizing the role of pore solution chemistry and ionic transport mechanisms, rather than relying exclusively on conventional conductive additives. These insights underscore the importance of incorporating ionic thermoelectric contributions into the design and optimization of cement-based materials for energy harvesting applications.

Chapter IV

Kaolin Clay-Based Geopolymer for Ionic Thermoelectric Energy Harvesting

Building on insights from geopolymer-based hybrid cement systems, in which ionic thermoelectric behavior and the critical role of pore-solution chemistry were established, the present chapter extends the investigation to a model geopolymer system derived from kaolin clay. While the previous chapter focused on industrially scalable materials and composite design strategies, this section aims to isolate and fundamentally examine the mechanisms governing ionic thermoelectric (i-TE) response in a simplified, well-defined binder system. In this context, kaolin clay-based geopolymers provide a controlled platform for studying ion transport phenomena due to their well-characterized aluminosilicate framework, tunable ionic content, and high intrinsic ionic conductivity.

Recent studies have highlighted that ionic charge carriers play a dominant role in the thermoelectric behavior of such systems, with temperature-dependent ion mobility and water content critically influencing both electrical conductivity and Seebeck response. In particular, kaolin-derived geopolymers exhibit distinct transitions in charge transport mechanisms, including dimensional changes in ionic motion and polarity shifts from n-type to p-type behavior under thermal gradients. Motivated by these observations, the present chapter systematically investigates the thermoelectric performance of kaolin-based geopolymer materials, with emphasis on elucidating the relationship between temperature, moisture state, and ionic transport mechanisms. Through this approach, the chapter aims to provide a more fundamental understanding of i-TE behavior in cementitious systems, thereby complementing the material design strategies explored in the previous chapter and advancing the development of chemically tunable thermoelectric cement-based materials.

4.1. Experimental

4.1.1. Materials and Sample Preparation

The kaolin-containing clay, designated as Ikere white (IKW), was sourced from a natural deposit located in Ekiti State, Nigeria. Representative samples of both the raw and calcined clay are presented in Figure 4.1. To prepare the alkaline activating solution,



Figure 4.1 Pictures of raw (IKWRC) and calcined (IKWCC) IKW clay

NaOH pellets (molecular weight: 40 g/mol, Sigma-Aldrich, Germany) and a sodium silicate solution (density: 1.39 g/mL; 12.0–13.0 wt.% Si-based; 13.4–14.0 wt.% NaOH basis, Sigma-Aldrich, USA) were utilized. An 8 M NaOH/Na_2SiO_3 solution with a 1:1 ratio was employed as the activator. This solution was prepared by dissolving the appropriate amount of NaOH pellets in deionized water, allowing the solution to cool to room temperature, followed by mixing with the sodium silicate solution and aging for 24 h before use.

The geopolymer was synthesized by mixing the calcined clay (IKWCC) with the prepared alkaline solution to produce the IKW-based geopolymer (IKWG). The activator concentration was selected based on previous studies on Nigerian clay geopolymers [81], and the activator-to-solid ratio was fixed at 0.63. The mixing process was carried out using a Hobart electric mixer (Heidolph Hei-TORQUE 400, speed range 200–2000 rpm), involving an initial mixing step of 90 s, followed by a resting period of 60 s, and a subsequent mixing step of 90 s at 1200 rpm to ensure homogeneity.

The resulting geopolymer paste was cast into prismatic molds (75*25*25 mm^3) and compacted by vibration using an end-to-end shaker (Ovan) at 125 rpm for approximately 5 minutes. To prevent moisture loss during early-stage curing, the molds were sealed with a vinyl sheet. The samples were demolded after 2 days, subsequently stored in sealed plastic containers, and cured at room temperature for 28 days before characterization.

4.1.2. Material Characterization

A combination of complementary characterization and measurement techniques was employed to systematically investigate the structure–property relationships governing ionic thermoelectric behavior in the kaolin-based geopolymer system. Structural and chemical evolution during calcination and geopolymerization was analyzed using X-ray diffraction (XRD), X-ray fluorescence (XRF), and Fourier-transform infrared spectroscopy (FTIR), while thermogravimetric analysis (TGA) and calorimetry were used to assess thermal stability, water content, and reaction kinetics. The development of the pore structure and its implications for ionic transport were further evaluated through thermal and microstructural analyses. Electrical transport properties were probed using impedance spectroscopy, enabling detailed investigation of frequency- and temperature-dependent conduction mechanisms. In addition, time-dependent voltage measurements and controlled thermal protocols were employed to evaluate intrinsic voltage and thermoelectric response, with particular emphasis on ion migration dynamics and polarity transitions. The integration of these techniques enables a mechanistic understanding of the interplay between microstructure, moisture state, and ionic transport. Detailed descriptions of the experimental setups and measurement protocols are provided in Chapter II; therefore, only the relevant results and their discussion are presented in this chapter.

4.2. Results and Discussion

4.2.1. Material Characterization

The thermogravimetric (TGA) and derivative thermogravimetric (DTG) curves of the IKW clay are presented in Figure 4.2a. The mass loss remains relatively constant up to approximately 400 °C, which is primarily attributed to the removal of physically adsorbed water from the external surfaces of the raw clay through dehydration processes. A more significant mass loss is observed within the temperature range of 400–700 °C, corresponding to the dehydroxylation of kaolinite and its transformation into metakaolinite, also referred to as calcined clay. This process can be described by the reaction $2Al_2Si_2O_5(OH)_4 \rightarrow 2Al_2Si_2O_7 + 4H_2O$. The total mass loss in this temperature interval is approximately 12.1%, indicating the kaolinite content present in the raw material. Based on these results, a calcination temperature of 700 °C was selected to ensure complete dehydroxylation.

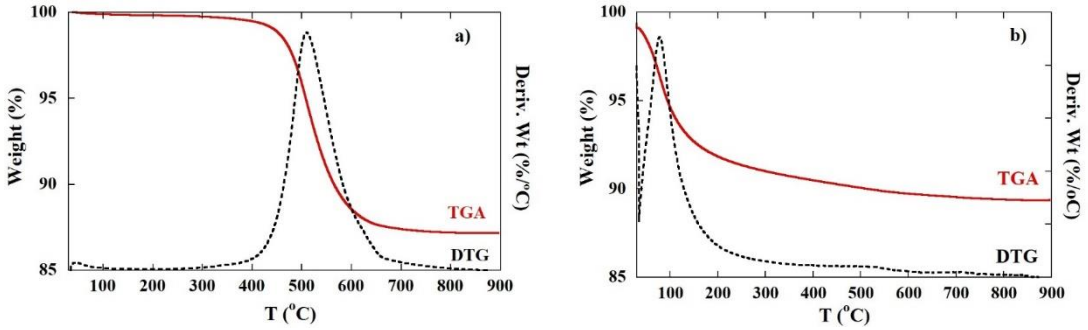


Figure 4.2 TGA/DTG curves of the three IKW raw clay (a) and IKW geopolymer (b)

The oxide composition of the calcined clay, determined by XRF and summarized in Table 4.1, shows that SiO_2 and Al_2O_3 are the predominant components, while TiO_2 (anatase) and Fe_2O_3 are present in notable quantities. The SiO_2/Al_2O_3 ratio of IKW is approximately 1:3. Considering that the typical ratio for high-kaolinite clays is close to 1:1 [82], this composition, together with the TGA results, confirms the high kaolinite content of the IKW clay. Such characteristics indicate that the material is well-suited as a precursor for geopolymer synthesis. In addition, the presence of K_2O suggests the occurrence of illite as a secondary phase within the clay.

Table 4-1 Oxide composition of IKW clay (wt. %)

Clay	SiO_2	Al_2O_3	Fe_2O_3	MnO	MgO	CaO	K_2O	TiO_2	P_2O_5	SO_3
IKW	53.9	40.2	0.59	0.02	0.12	0.03	0.05	2.08	0.05	0.03

The X-ray diffraction (XRD) patterns of the raw IKW clay (IKWRC) and the calcined clay (IKWCC) are presented in Figures 4.3a and b, respectively. In the raw clay, kaolinite is identified as the dominant crystalline phase. In addition, secondary contributions from quartz and anatase are observed, as indicated by distinct diffraction peaks. The presence of anatase is consistent with the XRF results, which revealed a significant TiO_2 content in the material.

Upon calcination, the most significant structural transformation is the conversion of kaolinite into metakaolinite [81]. This transformation is evidenced by the disappearance of the sharp diffraction peaks associated with crystalline kaolinite and the emergence of a broad amorphous halo centered at approximately $2\theta \approx 25°$, as shown in Figure 4.3b. To further analyze the crystalline phase contributions, the amorphous background was subtracted from the experimental diffractogram, allowing the identification of residual crystalline phases within the limits of experimental uncertainty.

The remaining sharp diffraction peaks are predominantly attributed to anatase, indicating that this phase remains largely unaffected by the calcination process. Additional minor peaks are also observed, which may correspond to quartz and other unidentified crystalline phases present in the system.

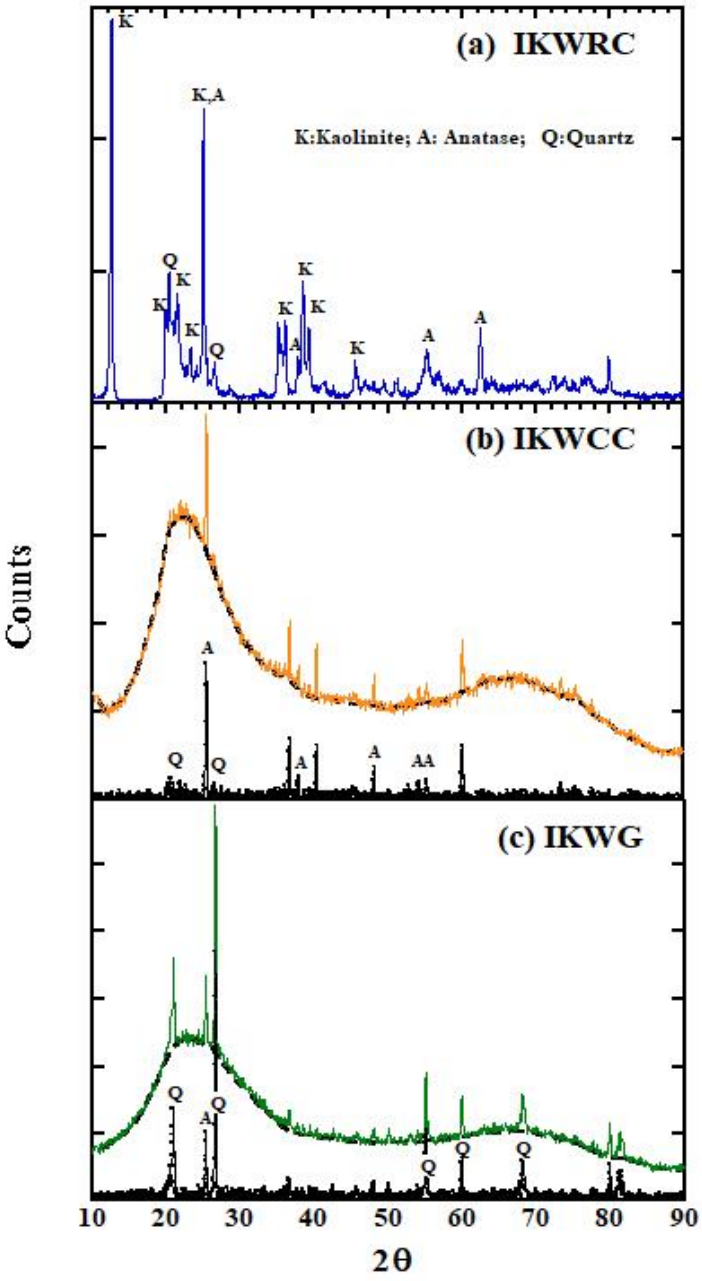


Figure 4.3 XRD patterns of (a) IKW raw clay (IKWRC), (b) calcined clay (IKWCC), and (c) geopolymer (IKWG). In (b) and (c), the estimated amorphous contribution (dashed lines) has been subtracted, yielding the crystalline contribution (black lines). From comparison

The Fourier-transform infrared (FTIR) spectra of the raw and calcined clay, illustrating the main functional groups, are presented in Figures 4.4a and b, respectively. In the raw clay, absorption bands at 3698 and 3620 cm^{-1} are attributed to the stretching vibrations of hydroxyl (OH) groups bonded to the octahedral aluminum sheets [81]. The bands observed at approximately 1112 and 1005 cm^{-1} correspond to the stretching vibrations of Si–O–T bonds (T = Si or Al). In addition, the band at 908 cm^{-1} is associated with Al–OH bending vibrations arising from inner hydroxyl groups. A characteristic doublet at 801 and 753 cm^{-1} is assigned to Si–O stretching vibrations of quartz, while the band at 538 cm^{-1} corresponds to Si–O bending vibrations, further confirming the presence of quartz. These observations are consistent with the XRD results (Figure 4.3), which also indicate quartz as a secondary phase in the IKW clay.

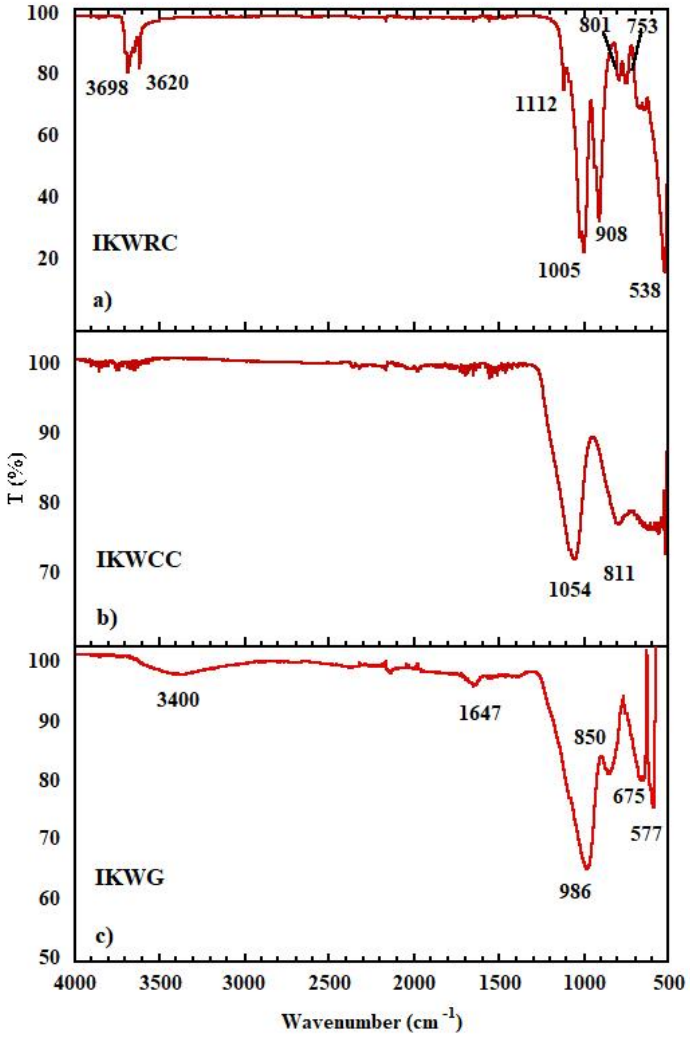


Figure 4.4 ATR-FTIR spectra of (a) IKW raw clay (IKWRC), (b) calcined clay (IKWCC), and (c) geopolymer (IKWG).

Significant modifications are observed in the FTIR spectrum after calcination. The disappearance of the OH^-related bands confirms the dehydroxylation of kaolinite. In particular, the Al–OH bending vibration at 908 cm^{-1}, associated with octahedrally coordinated aluminum (Al(VI)), vanishes, while new bands appear around 811 cm^{-1}, indicating the formation of tetrahedrally coordinated aluminum (Al(IV)). This structural transformation reflects the formation of a reactive metakaolinite phase, which is highly susceptible to alkaline activation and subsequent geopolymerization.

The reactivity of the calcined clay was further assessed using isothermal conduction calorimetry, and the normalized heat flow and cumulative heat release are presented in Figure 4.5. The geopolymerization process proceeds through two main stages: an initial dissolution and hydrolysis of the reactive (amorphous) components (Peak 1, P1), followed by the formation of the geopolymer network (Peak 2, P2), in agreement with previous studies [81]. Between these stages, a dormant period is observed, during which the concentration of dissolved species increases until reaching the threshold required for condensation reactions. The initial stage is characterized by a strongly exothermic peak, analogous to the pre-induction period in cement hydration. This is followed by the dormant stage, after which a broad exothermic peak emerges, reaching its maximum intensity after approximately 3 h. It should be noted that, since the mixing of IKWCC and the activator was performed outside the calorimeter, the full extent of the first peak (P1) could not be captured. The second peak (P2) is associated with the formation of aluminosilicate species and their subsequent polymerization into a sodium aluminosilicate hydrate (N–A–S–H) gel [83]. After 48 h, the reactions are nearly complete, with a cumulative heat release of approximately 108 J/g, confirming the successful geopolymerization of the IKW system.

The structural evolution of the geopolymer was further analyzed using TGA/DTG, as shown in Figure 4.2b. The majority of the mass loss (9.6 wt.%) occurs below 180 °C, corresponding to the evaporation of physically bound and pore water. Over the full temperature range of 30–900 °C, a total mass loss of 12.3 wt.% is observed. The mass loss between 180 and 350 °C (1.4 wt.%) is attributed to the release of structurally bound water within the sodium aluminosilicate framework [84], while the remaining loss (1.15 wt.%) is associated with the dehydroxylation of silanol and aluminol groups [85].

The XRD pattern of the IKW-based geopolymer is shown in Figure 4.3c. A pronounced diffuse halo is observed, confirming the predominantly amorphous nature of the material, which is characteristic of the formation of N–A–S–H gel. Superimposed on this amorphous background, sharp diffraction peaks corresponding to quartz and anatase are still present, indicating that these phases remain largely unreacted during geopolymerization, consistent with the observations for the calcined clay (Figure 4.3b).

The FTIR spectrum of the geopolymer (Figure 4.4c) further confirms the formation of the aluminosilicate network. The broad bands at approximately 3400 and 1647 cm^{-1} are associated with the presence of both adsorbed and structurally bound water [81]. A prominent absorption band at around 986 cm^{-1}, shifted from the band at approximately 1054 cm^{-1} in the calcined clay, is attributed to Si–O stretching vibrations within the geopolymer network. This shift reflects the substitution of Si–O–Si bonds by Si–O–Al

bonds, indicating the formation of the N–A–S–H gel structure. Additional bands at approximately 850 cm^{-1} correspond to non-condensed Si–OH groups [86], while the bands observed at 577 and 675 cm^{-1} are assigned to Si–O–Al bending vibrations [87].

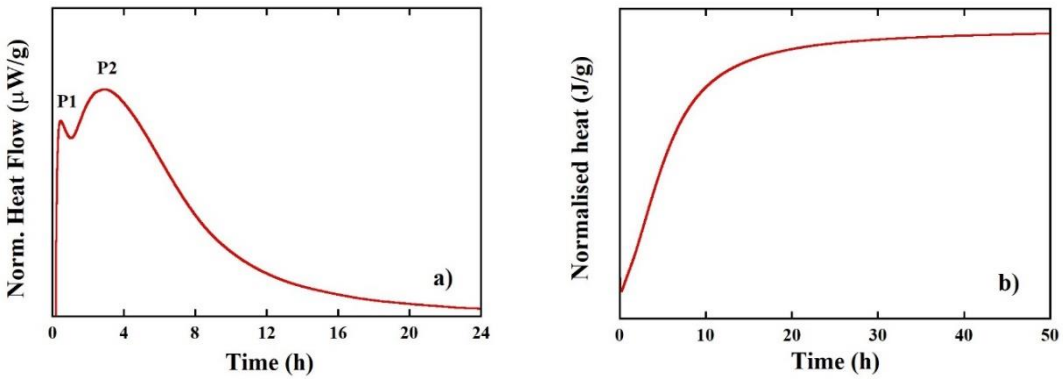


Figure 4.5 Curves of heat flow (a) and total quantity of heat released (b) of IKW calcined clay.

Taken together, the results from TGA, XRD, FTIR, and calorimetric analyses provide a comprehensive understanding of the structural and chemical evolution of the IKW system and its direct implications for ionic transport. The dehydroxylation of kaolinite and the formation of metakaolinite, as evidenced by TGA and XRD, lead to a highly disordered aluminosilicate structure that is subsequently transformed into an amorphous N–A–S–H gel upon alkaline activation. This structural transformation, confirmed by FTIR through the shift from Si–O–Si to Si–O–Al bonding environments and the transition from octahedral to tetrahedral aluminum coordination, results in a negatively charged framework composed of AlO_4^- units.

The presence of these structural charges necessitates the incorporation of alkali cations (e.g., Na^+ and K^+) to maintain electrostatic neutrality. A fraction of these cations remains weakly bound within the pore network and contributes to ionic mobility. In addition, the calorimetric results indicate the formation of a continuous geopolymeric network following the dissolution and reorganization of reactive species, which defines the connectivity of the pore structure and the distribution of the pore solution. The TGA results of the geopolymer further confirm the presence of both physically bound and structurally retained water, which plays a critical role in enabling ion transport within the material.

Consequently, the combined structural, compositional, and microstructural characteristics identified in this section govern the concentration, mobility, and distribution of ionic species within the pore solution. These factors are central to the ionic thermoelectric behavior of the material, as thermally driven ion diffusion under a temperature gradient depends strongly on the availability of mobile charge carriers, the connectivity of transport pathways, and the interaction between ions and the aluminosilicate framework. Therefore, the characterization results presented here establish the fundamental basis for understanding the temperature-dependent ionic transport and thermoelectric response discussed in the following sections.

4.2.2. Thermoelectric Properties

4.2.2.1 Thermal Conductivity

The thermal characterization of the IKW-based geopolymer is presented in Figure 4.6. Within the investigated temperature range (50–350 °C), the heat capacity (C_P) exhibits a relatively stable behavior, with an average value of approximately 0.975 J/(g·K).

In contrast, the thermal conductivity shows a slight decrease with increasing temperature. The maximum value is observed at 50 °C (k = 0.69 W/m·K), while the minimum value is recorded at 350 °C (k = 0.576 W/m·K). These values are consistent with those reported for other cementitious materials exhibiting thermoelectric behavior. In particular, the thermal transport properties measured in this study are comparable to those of cement-based systems incorporating metal oxide nanoparticles [54].

From a thermoelectric perspective, the relatively low thermal conductivity of the material is advantageous, as it promotes the retention of temperature gradients across the sample. This facilitates the development of thermally driven ionic transport under a temperature difference, which is essential for enhancing the thermoelectric voltage in ionic thermoelectric systems.

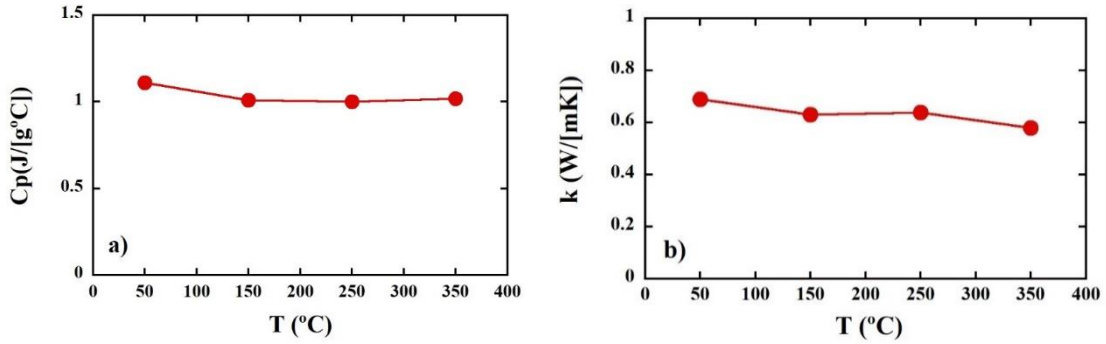


Figure 4.6 (a) Specific heat capacity, and (b) thermal conductivity as a function of temperature of IKW-geopolymer.

4.2.2.2 Electrical Conductivity

A comprehensive understanding of the electrical conductivity mechanisms in cementitious systems is essential for identifying the optimal temperature range for thermoelectric performance and for guiding mix design strategies aimed at improving the figure of merit. In this context, a detailed investigation of the electrical transport properties of the IKW-based geopolymer was conducted. Figure 4.7 presents the real part of the complex conductivity, σ′(f), obtained from impedance spectroscopy measurements at 300 K.

According to linear response theory, the AC conductivity spectra reflect the temperature-dependent dynamics of mobile charge carriers [88]. At high frequencies, the mean square displacement $\langle r^2(t) \rangle$ is characterized by subdiffusive motion, and σ′(f) exhibits a frequency-dependent response due to interactions between ions and their local environment. Below a characteristic threshold frequency, f_0, the transport mechanism transitions from subdiffusive to diffusive behavior, resulting in a frequency-independent

conductivity plateau. The decrease in σ′(f) observed in the low-frequency region is attributed to electrode polarization effects [89].

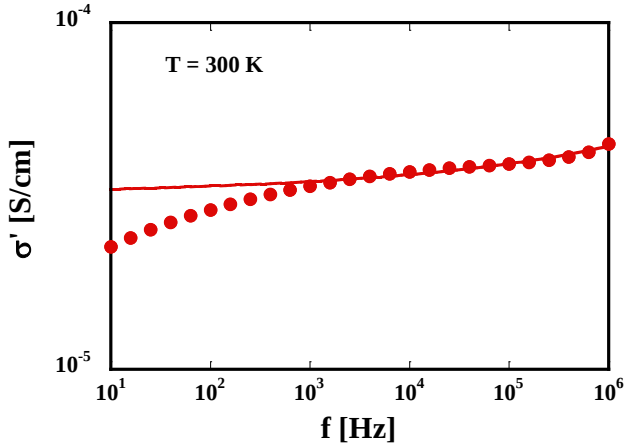


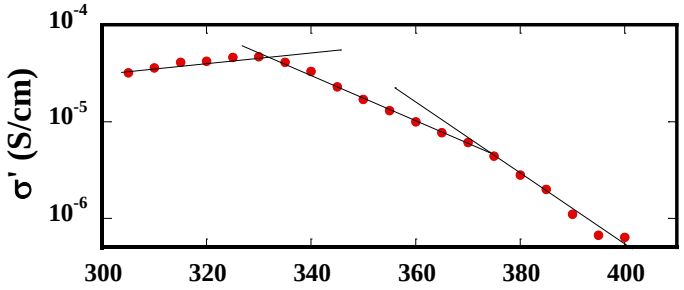
Figure 4.7 Real part of complex conductive function measured by Impedance Spectroscopy as a function on frequency at 300K

To quantitatively describe the experimental data, the impedance spectra were analyzed using Jonscher's power law:

$$\sigma(f) = \sigma DC[1 + (\frac{f}{f_0})n] + Af \quad \textit{Equation 4.1}$$

where σ_{DC} represents the direct current conductivity, f_0 corresponds to the onset frequency of diffusive motion, n is a parameter related to the dimensionality of charge transport, and A accounts for the nearly constant loss contribution arising from higher-frequency processes beyond the experimental window.

The results of the fitting analysis are presented in Figure 4.8. The electrical conductivity initially increases with temperature, reaching a maximum value of 5.1×10^{-5} S/cm at T = 330 K. Beyond this temperature, a decrease in conductivity is observed, which can be divided into two distinct regimes: a gradual decline between 330 and 370 K, followed by a more pronounced drop at temperatures above 370 K. The critical temperature at which this transition occurs is associated with the evaporation of bulk water from the larger pores of the geopolymer network, indicating that ionic transport is the dominant conduction mechanism.



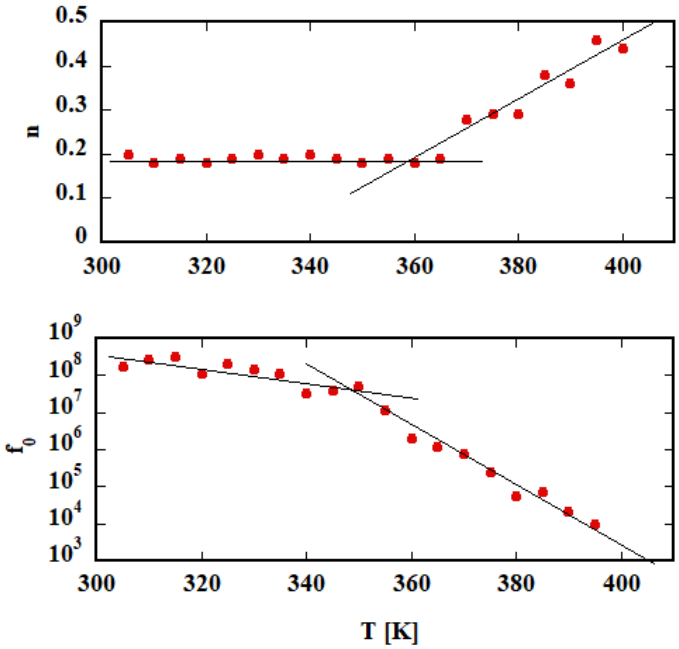


Figure 4.8 Fitting results of electrical conductivity

Further insight into the transport behavior is obtained by analyzing the temperature dependence of the parameters n and f_0. At lower temperatures, n values are approximately 0.2, indicative of one-dimensional charge transport. However, above approximately 360 K, a sharp increase in n is observed, approaching values around 0.7, which correspond to three-dimensional transport mechanisms [90]. This transition suggests a change in the dominant conduction pathway, from one-dimensional diffusion along continuous water-filled channels to a three-dimensional hopping mechanism within a more confined environment. A similar temperature-dependent trend is observed for f_0, supporting the occurrence of a transition in the primary conduction process.

Notably, the identified critical temperature range is slightly higher than the peak observed in the derivative TGA curve associated with bulk water loss, further confirming the strong correlation between moisture content and electrical transport. Based on these observations, the following mechanism is proposed for the electrical conductivity of the IKW-based geopolymer. At low temperatures, electrical conduction is primarily governed by the movement of ions within bulk water present in larger pore channels. As the temperature increases beyond approximately 330 K, partial evaporation of bulk water leads to a reduction in conductivity, although ionic transport remains active within smaller pores. At higher temperatures (360–370 K), the complete removal of bulk water induces a transition in the transport mechanism, with charge carriers shifting from one-dimensional diffusion to three-dimensional hopping. In this regime, electrical conductivity is predominantly governed by ions associated with structurally bound water and surface sites within the porous geopolymer network, resulting in a more pronounced decrease in conductivity.

The temperature-dependent evolution of electrical conductivity provides direct insight into the mechanisms governing the thermoelectric response of the IKW-based geopolymer. As demonstrated, the transition from bulk water–dominated ionic transport

to surface- and structurally bound water–mediated conduction with increasing temperature reflects a progressive change in ion mobility and transport pathways. Since the Seebeck effect in ionic systems arises from the differential thermodiffusion of ionic species, these changes in conduction mechanism are expected to significantly influence both the magnitude and polarity of the thermoelectric voltage. In particular, the reduction of bulk water and the associated transition in transport dimensionality are likely to modify the relative contributions of cations and anions under a temperature gradient. Consequently, the conductivity results establish the fundamental basis for interpreting the temperature-dependent Seebeck behavior and the observed transitions in thermoelectric response discussed in the following section.

4.2.2.3 Seebeck Coefficient Measurements

Figure 4.9 presents the temporal evolution of the Seebeck voltage. Prior to the application of any temperature gradient, a significant intrinsic voltage of −106 mV was observed, consistent with previous reports in the literature [23,24] and the trend for hybrid cement (see Chapter III). To isolate the true thermoelectric response of the material, it is necessary to allow this intrinsic voltage to stabilize as described in Chapter III. After approximately 40 h, a stable value of V = −19.6 mV was reached, at which point a temperature of T_1 = 60 °C was applied to the sample using a ceramic heater.

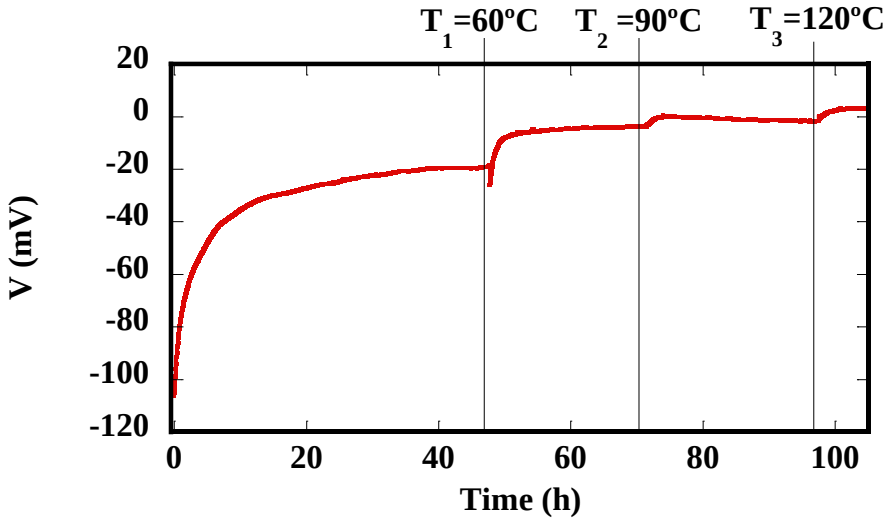


Figure 4.9 Seebeck voltage profile as a function of time

The response of the IKW-based geopolymer to the applied temperature gradient is shown in Figure 4.10a. Initially, a rapid increase in absolute voltage toward negative values is observed, reaching −26.1 mV within the first 5 minutes, followed by a pronounced decrease. This decrease gradually slows after approximately 1 h, and a new steady-state voltage of V = −3.9 mV is achieved and lasts for about 25 h. The observed behavior suggests that mobile cations (e.g., Na^+ from the activator) initially migrate toward the cold side, leading to the rapid voltage increase, followed by the subsequent response of anions (e.g., OH^-) under the applied thermal gradient. The extended stabilization time reflects the complexity of the underlying processes, including the evolution of the temperature gradient, redistribution of ions within the pore network, and the formation of interfacial charge regions.

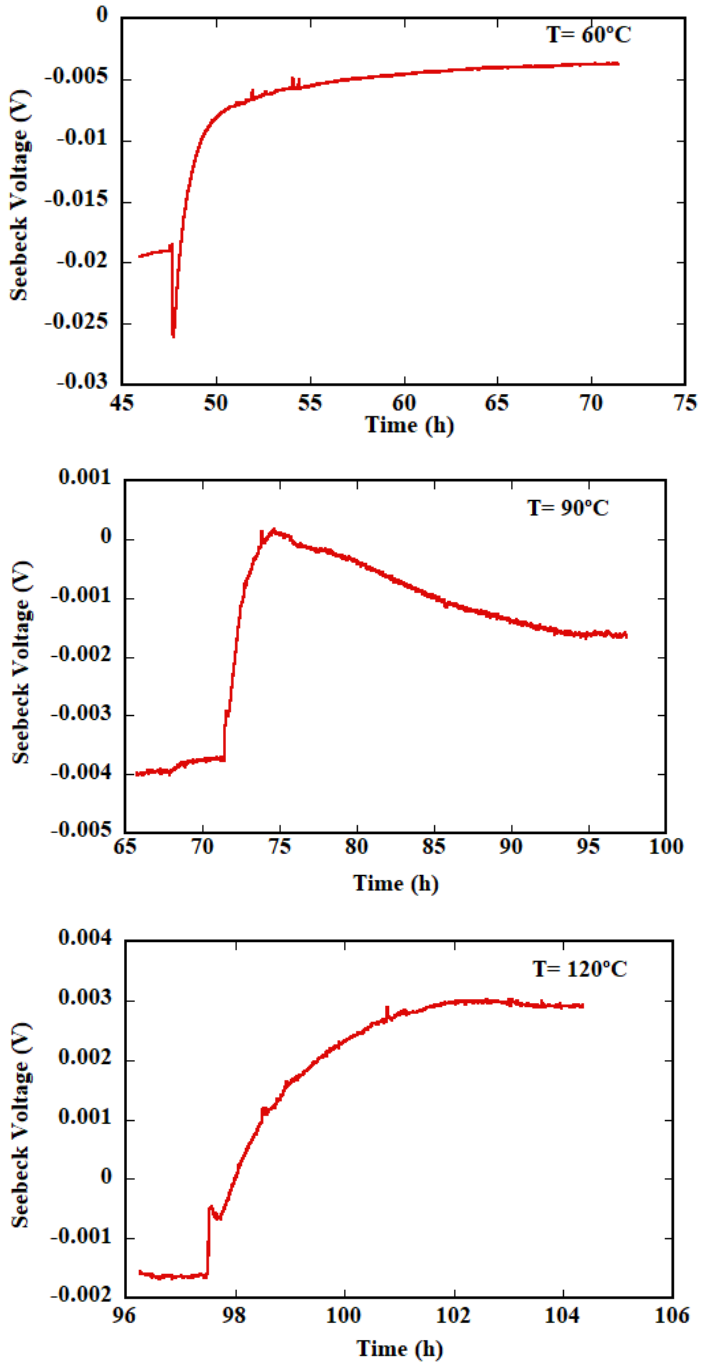


Figure 4.10 Seebeck Voltage measured for different applied temperatures

When a higher temperature of T_2 = 90 °C is applied (Figure 4.10b), the voltage initially moves toward positive values, reaching a maximum value of approximately 0.15 mV after 3 h. This behavior indicates a dominant contribution from anions migrating toward the cold side. Subsequently, the voltage evolves toward negative values again, stabilizing at V = −1.6 mV after approximately 25 h, suggesting either a renewed contribution from cations or a reduction in the concentration of mobile anions. This behavior can be explained by the progressive loss of water at elevated temperatures, as supported by TGA and electrical conductivity results. In particular, the evaporation of water from larger pores at the hot side leads to the depletion of mobile OH^- ions, thereby altering the balance of charge carriers contributing to the thermoelectric response.

At an even higher temperature of T_3 = 120 °C (Figure 4.10c), the Seebeck voltage increases further, and a faster stabilization is observed, with a steady-state value of V = 2.9 mV reached after approximately 7 h. The Seebeck coefficient ($S = \Delta V/\Delta T$), calculated from the stabilized voltage values, is presented in Figure 4.11. The obtained values are comparable to those reported in the current state of the art for cementitious materials and geopolymers, typically ranging from −182 μV K^{-1} to 42 μV K^{-1}.

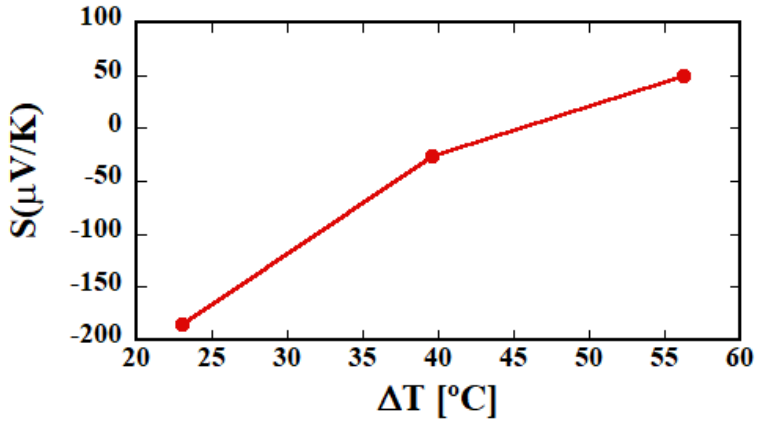


Figure 4.11 Seebeck Coefficient of IKW-geopolymer

Furthermore, a transition from negative (p-type) to positive (n-type) thermoelectric behavior is observed with increasing temperature difference. This dual nature of the IKW-based geopolymer, governed by the relative contributions of different ionic species, highlights its potential for application in solid-state thermoelectric generators (TEGs), where polarity control is a desirable feature.

4.2.2.4 TE Performance and Figure of Merit

The ZT results indicate that the IKW-based geopolymer performs most effectively in the low-temperature range, with the highest figure of merit obtained at 60 °C (Figure 4.12). The sharp decrease in ZT at 90 °C is mainly due to moisture loss and the associated reduction in ionic conductivity, despite the material's relatively low thermal conductivity. At higher temperatures, the progressive depletion of mobile water and the transition from bulk-water-assisted ion diffusion to more restricted hopping transport limit charge mobility, resulting in significantly lower ZT values. The slight recovery at 120 °C may arise from the increased Seebeck response associated with polarity changes and altered cation/anion contributions. Still, this improvement is insufficient to compensate for the reduced ionic conductivity. Therefore, the ZT behavior confirms that this geopolymer is more suitable for low-temperature ionic thermoelectric energy harvesting rather than operation at elevated temperatures.

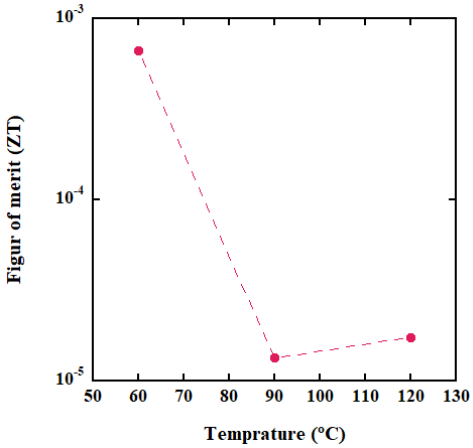


Figure 4.12 The calculated figure of merit (ZT) of IKW-geopolymer.

When compared with cement-based thermoelectric systems incorporating conductive additives (Chapter I, Section 6.6), the present results fall within the intermediate range of reported ZT values (~10^{-5}–10^{-4}). Systems based on graphene/graphite and doped metal oxides typically exhibit higher ZT values (up to ~10^{-3}–10^{-2}) due to significantly enhanced electrical conductivity, while maintaining moderate Seebeck coefficients. In contrast, metal oxide-based systems often show large Seebeck coefficients (up to several thousand μV K^{-1}) but suffer from extremely low electrical conductivity, leading to very low ZT values (~10^{-7}–10^{-12}). The IKW-based geopolymer differs fundamentally from these systems, as its performance is governed by ionic transport rather than electronic conduction. Consequently, although its electrical conductivity is lower than that of electronically enhanced composites, it achieves competitive ZT values within the broader landscape of cementitious thermoelectrics without the need for costly conductive fillers. This highlights a distinct advantage of ionic thermoelectric systems, particularly for low-temperature applications where moisture-assisted ion transport can be effectively maintained.

4.3. Conclusions

This Chapter provides comprehensive insights into the thermoelectric behavior of a kaolinite-derived geopolymer, enabling a deeper understanding of the mechanisms governing its performance and its potential for energy conversion applications.

From a thermal perspective, the material exhibits a slight decrease in thermal conductivity with increasing temperature, ranging from 0.69 W/m·K at 50 °C to 0.576 W/m·K at 350 °C. These values are comparable to those reported for state-of-the-art thermoelectric cementitious materials and are favorable for maintaining temperature gradients within the system.

The electrical conductivity analysis reveals that, at low temperatures, charge transport is primarily governed by ions present in bulk water within the larger pore channels of the geopolymer network. As the temperature increases beyond a critical threshold, the progressive evaporation of bulk water induces a transition in the transport mechanism, with charge carriers shifting from one-dimensional diffusion to three-dimensional hopping. This transition results in a decrease in electrical conductivity.

The Seebeck measurements further confirm that ionic species are the dominant contributors to thermoelectric behavior in this system. Initially, positive ions migrate toward the cold side of the sample, followed by the response of negative ions under the applied temperature gradient. The measured Seebeck coefficients range from −182 to 42 $\mu V\ K^{-1}$, which are consistent with values reported in current state-of-the-art studies. The observed relationship between temperature, electrical conductivity, and Seebeck response indicates that the IKW-based geopolymer is particularly suitable for low-temperature applications, such as the recovery of low-grade waste heat.

A notable finding of this study is the observation of a temperature-dependent transition from n-type to p-type thermoelectric behavior. This polarity switching, governed by the relative contributions of different ionic species, introduces new possibilities for the design of thermoelectric capacitors and multifunctional energy devices.

Overall, the results demonstrate that the IKW-based geopolymer exhibits significant potential for thermoelectric energy conversion and storage. Its combination of ionic transport-driven thermoelectric behavior, tunable polarity, and compatibility with sustainable material systems positions it as a promising candidate for the development of structural, solid-state thermoelectric generators.

Chapter V

GGBF slag-based geopolymer for ionic thermoelectric energy harvesting

Building upon the previous investigations of geopolymer-based hybrid cement systems and kaolin-derived model geopolymers, which respectively established the role of scalable material design and fundamental ionic transport mechanisms, the present chapter extends the study to ground granulated blast furnace slag (GGBFS)-based geopolymers. In contrast to the preceding systems, GGBFS-based geopolymers introduce a calcium-rich chemistry, leading to the formation of hybrid gel phases (C–A–S–H and N–A–S–H) and a distinct pore-solution environment that can significantly influence ionic transport behavior. As highlighted in recent studies, the concentration of alkaline activator plays a critical role in controlling dissolution kinetics, gel formation, pore connectivity, and ion concentration within the geopolymer matrix, all of which directly affect thermoelectric performance.

Motivated by these considerations, this chapter systematically investigates the ionic thermoelectric (i-TE) response of GGBFS-based geopolymers by varying the alkaline solution-to-slag ratio (AS/S), to elucidate the interplay between composition, microstructure, and ion transport. Particular emphasis is placed on understanding how variations in activator content modify the pore-solution chemistry and transport pathways, thereby governing electrical conductivity and Seebeck behavior under thermal gradients. Through this approach, the chapter seeks to bridge the gap between fundamental ionic transport mechanisms and practical material optimization, advancing the development of high-performance, sustainable geopolymer systems for thermoelectric energy harvesting applications.

5.1. Experimental

5.1.1. Materials and Sample Preparation

In this study, ground granulated blast furnace slag (GGBFS), sourced from Nippon Steel (China), was employed as the primary precursor material. The alkaline activating system consisted of a sodium silicate solution (density: 1.39 g/mL; Si content: 12.0–13%; Na content: 13.4–14%) and sodium hydroxide pellets (molecular weight: 40 g/mol), both supplied by Sigma-Aldrich, Germany.

The chemical composition and phase characteristics of the GGBFS were determined using X-ray fluorescence (XRF) and X-ray diffraction (XRD), as summarized in Table 5.1 and Figure 5.1. The results indicate that the slag is predominantly composed of SiO_2 (34%), CaO (41.8%), Al_2O_3 (13%), and Fe_2O_3 (0.34%). The relatively high CaO content is particularly significant, as it promotes the formation of calcium-rich gel phases (e.g., C–A–S–H), which can modify the pore solution chemistry and influence ionic mobility and transport pathways within the geopolymer matrix.

Table 5-1 Chemical composition of GGBF slag

Sample	SiO2	Al2O3	Fe2O3t	MnO	MgO	CaO	K2O	TiO2	P2O5	SO3	GOI
slag	34.05	13.05	0.34	0.23	5.41	41.88	0.38	0.57	0.01	1.65	0.28

Geopolymer samples were prepared by first formulating the alkaline solution through the mixing of sodium silicate and sodium hydroxide. This activating solution was subsequently combined with the slag precursor to initiate geopolymerization. To improve the workability of the mixture, additional water was incorporated. The fresh mixtures were then cast into cylindrical molds with approximate dimensions of 46 × 50 mm for Seebeck coefficient measurements. Following casting, the samples were sealed in plastic bags and cured for 28 days to ensure proper geopolymerization. The detailed compositions of the prepared samples are provided in Table 5.2.

To enhance measurement repeatability and reduce variability associated with microstructural heterogeneities, a consistent pretreatment procedure was implemented prior to Seebeck measurements. Following the 28-day curing period, the samples were first dried overnight at 50 °C and then conditioned at 75% relative humidity (RH) for 24 hours.

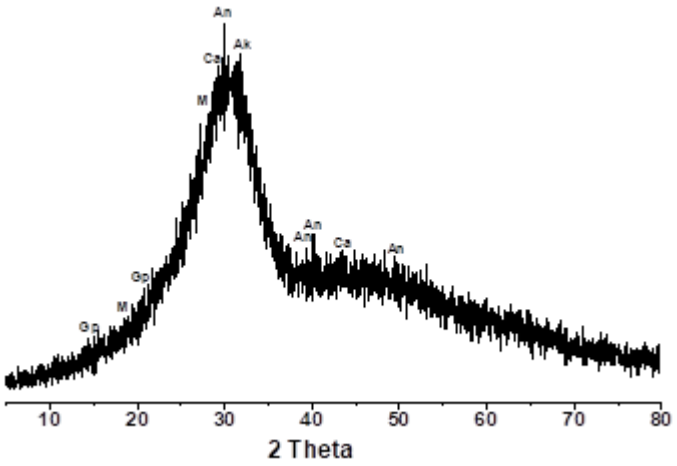


Figure 5.1 XRD pattern of GGBF slag

Table 5-2 Chemical composition of the prepared samples per weight

Sample ID	Slag	AS/S	AS	Na_2SiO_3/ NaOH	Na_2SiO_3	NaOH	Water	extra water
S 0.3/12	180	0.3	54	2.5	38.6	15.4	32.1	10
S 0.4/12	180	0.4	72	2.5	51.4	20.6	42.9	8
S 0.45/12	180	0.45	81	2.5	57.9	23.1	48.2	5

5.1.2. Material Characterization

A combination of complementary characterization and measurement techniques was employed to systematically investigate the relationship between composition,

microstructure, and thermoelectric performance in GGBFS-based geopolymer systems. Chemical and phase characterization was carried out using X-ray fluorescence (XRF) and X-ray diffraction (XRD), while thermogravimetric analysis (TGA) was used to assess thermal stability and water-related transformations. The geopolymerization process and microstructural evolution were further monitored through isothermal conduction calorimetry and ultrasonic pulse velocity (UPV) measurements, providing insight into reaction kinetics and matrix development. Mechanical performance was evaluated via dynamic elastic modulus measurements. Thermal conductivity was determined using differential scanning calorimetry-based methods, while electrical transport properties were analyzed using impedance spectroscopy to capture temperature-dependent ionic conduction. In addition, thermoelectric behavior was assessed through time-dependent open-circuit voltage measurements under controlled thermal gradients, with particular attention to the role of intrinsic voltage and ionic transport. The integration of these techniques enables a comprehensive understanding of how activator content governs pore structure, ionic mobility, and overall thermoelectric response. Detailed experimental procedures are provided in the methodology section; therefore, only the relevant results and their interpretation are discussed here.

5.2. Results and Discussion

5.2.1. Material Characterization

5.2.1.1 Isothermal Conduction Calorimetry

Figure 5.2 presents the normalized heat flow and cumulative heat release recorded during the geopolymerization of slag, as determined by isothermal conduction calorimetry. The reaction between the slag precursor and the alkaline solution proceeds rapidly, and since the initial mixing was performed outside the calorimeter, the early stages of the dissolution process were not captured [91,92]. Nevertheless, the calorimetric response provides valuable insight into the key stages of the reaction.

The initial sharp exothermic peak is attributed to the rapid dissolution of slag particles in the highly alkaline environment. During this stage, Ca^{2+}, Al^{3+}, and SiO_4^{4-} species are released into the pore solution, resulting in a high concentration of mobile ionic species. The availability and concentration of these ions are strongly dependent on the solid-to-liquid ratio, where lower liquid contents lead to more concentrated ionic environments, while higher liquid contents dilute the system and may reduce the intensity of the reaction.

Following the dissolution stage, the system enters an induction period characterized by a relatively low heat flow. This stage corresponds to the stabilization of the supersaturated solution, during which ionic species diffuse and begin to reorganize [93]. The subsequent main exothermic peak is associated with polycondensation reactions, in which silicate and aluminate species recombine with calcium to form C–A–S–H and N–A–S–H gel phases and interconnected geopolymeric networks [94,95]. This stage is critical for the development of the material's microstructure and mechanical performance.

The higher heat flow observed for sample S0.3 can be attributed to its increased binder content [96]. This enhanced heat release indicates more intensive polycondensation

activity, leading to a more developed geopolymer matrix [97]. These calorimetric findings are consistent with the results obtained from elastic modulus measurements and ultrasonic pulse velocity tests (Figure 5.4). In particular, sample S0.3 exhibits the highest elastic modulus and ultrasonic velocity values, indicating a greater degree of geopolymer gel formation compared to samples S0.4 and S0.45. This correlation confirms that the higher binder content in S0.3 contributes to the formation of a more compact and mechanically robust geopolymer network.

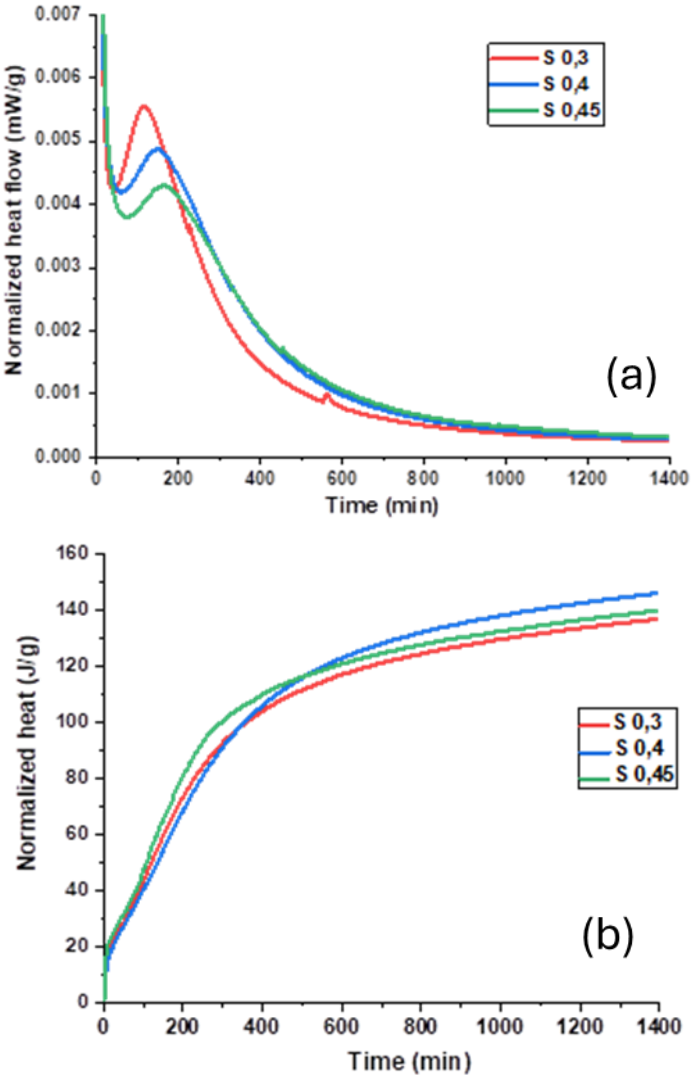


Figure 5.2(a) The normalized heat flow and (b) the total heat of the prepared sample as a function of time

5.2.1.2 X-ray Diffraction

X-ray diffraction (XRD) analysis was conducted to investigate the evolution of reaction products with varying alkaline solution-to-slag (AS/S) ratios, and the results are presented in Figure 5.3. A noticeable shift of the broad amorphous halo toward lower 2θ values is observed following slag activation, which serves as a clear indication of the geopolymerization process. This shift reflects the reorganization of the aluminosilicate framework into a more polymerized gel structure, characteristic of geopolymer formation. In addition, an increase in the intensity of diffraction peaks corresponding to gypsum (labeled “Gp”) and akermanite (“Ak”) is observed, along with the emergence of new

peaks associated with anorthite ("An"). These changes highlight the dual nature of the reaction, involving both amorphous and crystalline phases. While the amorphous phase plays a dominant role in gel formation, the crystalline phases undergo partial transformation, contributing to the overall structural stability of the material.

The mechanical performance of the samples shows a strong correlation with the observed XRD results. In particular, the sample with a lower AS/S ratio exhibits a higher degree of gel formation, as evidenced by the more pronounced changes in the diffraction patterns [98]. This increased gel content leads to the formation of a denser and more cohesive matrix, which is directly reflected in the enhanced mechanical properties. The higher compressive strength and elastic modulus observed for this sample (Figure 5.5) further confirm the beneficial effect of increased gel formation on the structural performance of the geopolymer.

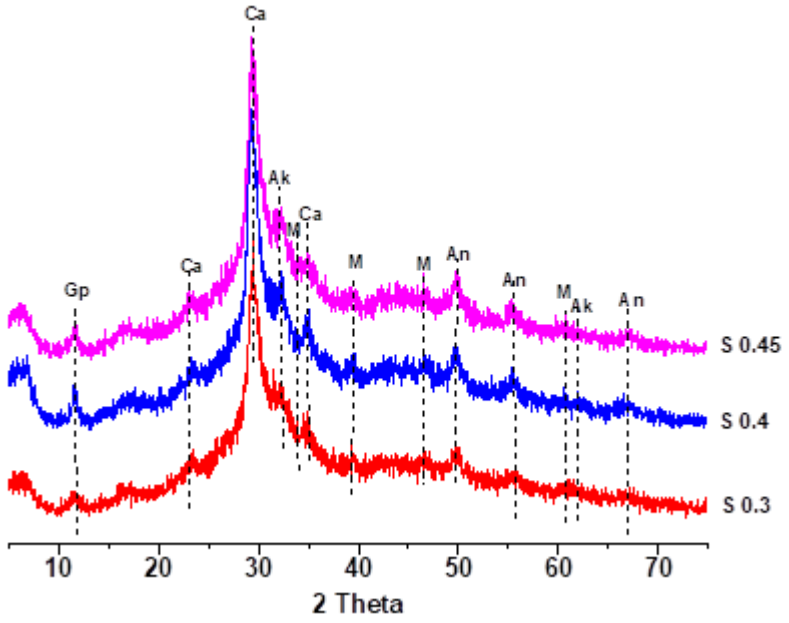


Figure 5.3 XRD patterns of S0.3, S0.4, and S0.45 (Ca: calcite, Ak: akermanite, Gp: gypsum, An: anorthite, M: mullite)

5.2.1.3 Ultrasonic Pulse Velocity

Figure 5.4 illustrates the evolution of ultrasonic pulse velocity (UPV) over time for the geopolymer samples S0.3, S0.4, and S0.45. The UPV curves can be divided into three distinct stages. The initial stage corresponds to a rapid condensation process, characteristic of the interaction between slag and the alkaline activator. In contrast to previous studies where an induction or inactive period was observed [96], no such stage is evident in the present results. This observation is consistent with the isothermal calorimetry data, confirming the highly reactive nature of the slag-based system.

The maximum UPV value of 3317 m/s was recorded for sample S0.3 at an activator concentration of 12 M, which also exhibited the highest elastic modulus [99]. The elevated UPV values in this stage indicate the formation of a dense and hardened geopolymer matrix, reflecting the progression of polycondensation reactions. A higher degree of condensation results in a more rigid and well-developed polymer network [96].

The subsequent decrease in UPV is attributed to the evaporation of water from the system [100]. Although the samples were sealed in plastic bags to minimize moisture loss, partial evaporation still occurred, influencing the measured UPV values. The presence of residual water within the geopolymer matrix remains essential, as it supports continued polycondensation reactions and contributes to the development of improved mechanical properties.

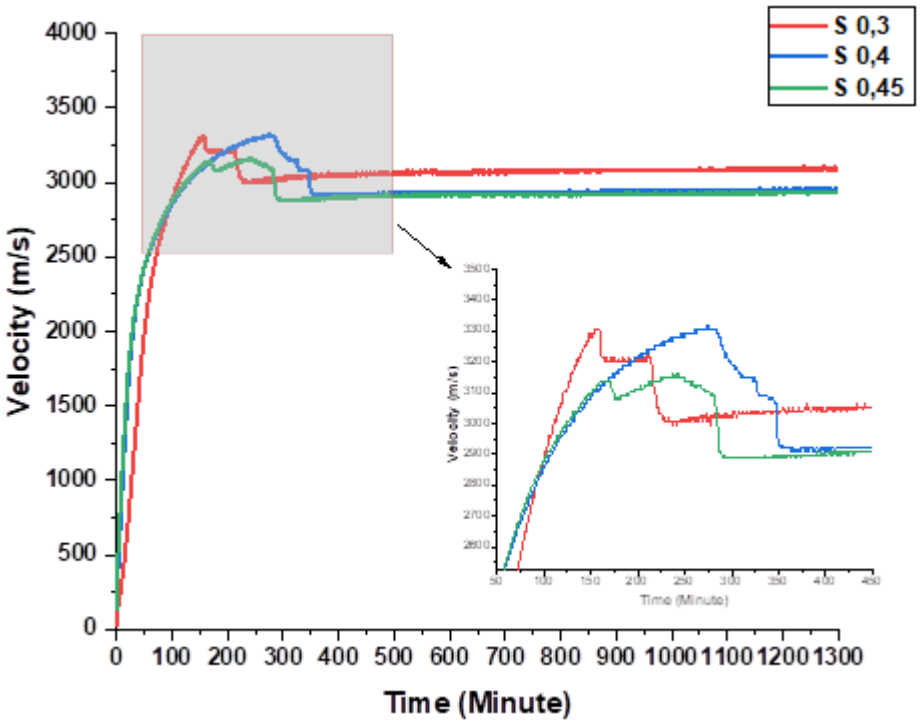


Figure 5.4 Development of the ultrasonic pulse velocity over time of the samples S0.3, S0.4, and S0.45

5.2.1.4 Mechanical Properties

Figure 5.5 presents the evolution of the elastic modulus of the geopolymer samples measured at 1, 7, and 28 days for different alkaline solution-to-slag (AS/S) ratios. The measurements were conducted in accordance with EN 12390-13 ("UNE-EN 12390-13:2014"). An increase in elastic modulus is observed for all samples over time, reflecting the continuation of the geopolymerization process [101]. This time-dependent enhancement is attributed to the progressive formation and densification of the geopolymer gel, which leads to improved structural integrity and stiffness of the material.

A clear decreasing trend in elastic modulus is observed with increasing AS/S ratio. This behavior is consistent with the findings of Lopes et al. [102], who reported that higher alkaline solution contents can adversely affect the geopolymerization process. The excess liquid phase dilutes the reactive environment, thereby reducing the concentration of aluminosilicate species available for gel formation. As a result, the extent of reaction is diminished, leading to a lower degree of geopolymer gel formation.

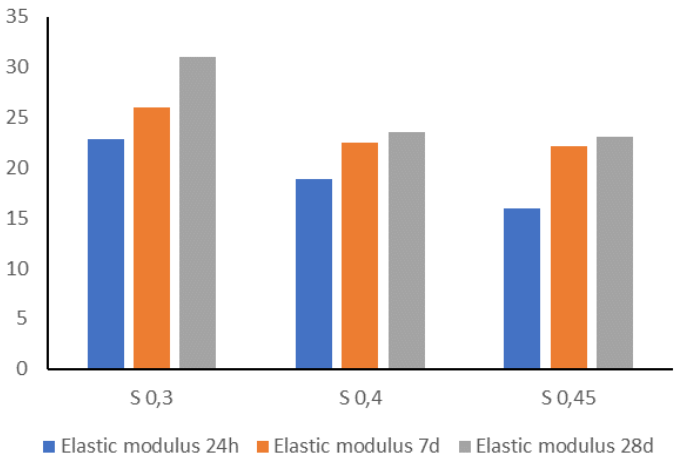


Figure 5.5 The elastic modulus of the samples S0.3, S0.4 and S0.45 after 1day, 7days and 28days

This effect is further supported by the work of Chen et al. [91], which demonstrated that increasing the AS/S ratio weakens the bonding network within the geopolymer matrix. The reduced gel formation, combined with incomplete cross-linking of the reaction products, results in a less rigid microstructure and, consequently, a lower elastic modulus. In addition, the higher liquid content may introduce increased porosity and microstructural defects, further compromising the mechanical performance of the material.

5.2.1.5 Thermogravimetric Analysis

Thermogravimetric analysis (TGA) of the geopolymer samples was performed over a temperature range of 25–800 °C to evaluate thermal events associated with water loss, phase transformations, and decomposition reactions. The evolution of mass as a function of temperature is presented in Figure 5.6.

The first major mass loss is observed between 50 and 200 °C and is attributed to the evaporation of free and physically bound water, as well as the dehydroxylation of hydrated phases such as ettringite [103]. This dehydration process is characteristic of alkali-activated slag systems, where water associated with the gel structure is progressively released upon heating [104].

A second mass loss peak appears in the temperature range of 300–450 °C, corresponding to the removal of interlayer or structurally bound water, along with the dehydration of C–S–H phases [104]. At higher temperatures, between 650 and 800 °C, a third mass loss is observed, which is attributed to the decomposition of calcite ($CaCO_3$), resulting in the release of CO_2. The relatively low intensity of this event suggests a limited degree of carbonation in the geopolymer formulations investigated in this study.

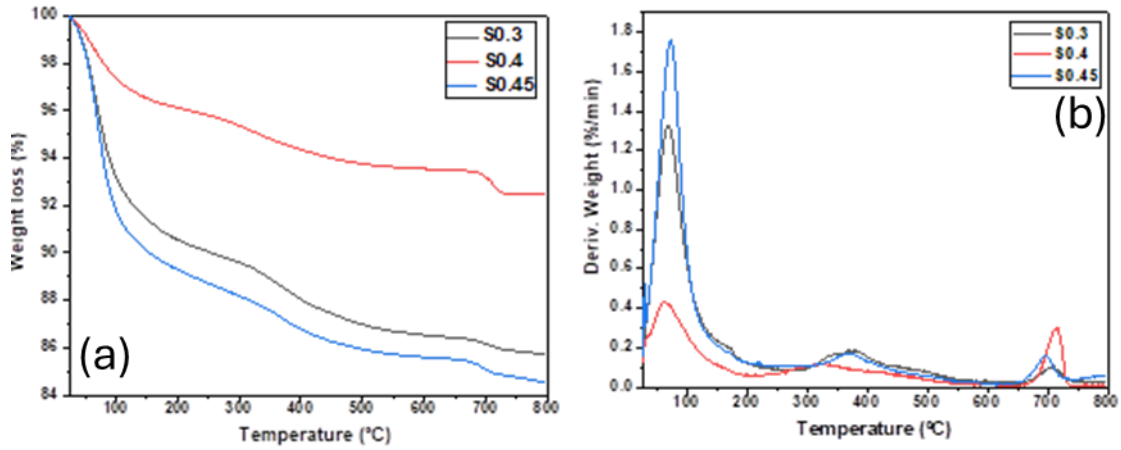


Figure 5.6 Thermogravimetric analysis of the samples S0.3, S0.4 and S0.45 (a) TGA, (b) DTGA

Taken together, the results from calorimetry, XRD, UPV, elastic modulus, and TGA provide a coherent picture of how variations in the alkaline solution-to-slag (AS/S) ratio govern the evolution of the geopolymer microstructure and, consequently, the ionic transport properties of the system. The calorimetric analysis demonstrates that lower AS/S ratios promote more intense dissolution and polycondensation reactions, leading to a higher degree of gel formation. This is consistent with the XRD results, which indicate a greater transformation of the amorphous phase and the development of a more polymerized aluminosilicate network in samples with lower liquid content.

The mechanical characterization, including UPV and elastic modulus measurements, further confirms that reduced AS/S ratios result in a denser and more cohesive microstructure, with improved connectivity of the geopolymer gel phases. In contrast, higher AS/S ratios introduce excess liquid, which dilutes the reactive species, reduces the extent of gel formation, and promotes the formation of a more porous and less interconnected network. The TGA results complement these findings by highlighting the role of water in different states, including free, interlayer, and structurally bound water, which are progressively released with increasing temperature and are directly linked to the availability of mobile ionic species.

From the perspective of ionic transport, these structural and compositional variations have critical implications. Lower AS/S ratios are expected to result in higher concentrations of ionic species within a more confined pore network, where transport is governed by a combination of bulk and interfacial mechanisms. Conversely, higher AS/S ratios, while initially providing greater amounts of free water, lead to dilution of ionic species and reduced effective charge carrier concentration, which can limit ionic conductivity. Moreover, the evolution of water content and pore structure, as evidenced by TGA and UPV, suggests a transition from bulk water–dominated transport toward more restricted ion motion within gel-associated or adsorbed water layers as the system densifies or dries.

Therefore, the characterization results collectively establish that the AS/S ratio is a key parameter controlling not only the geopolymerization kinetics and resulting microstructure but also the concentration, mobility, and transport pathways of ionic species. These factors are expected to directly influence the electrical conductivity and

thermoelectric response of the material, providing the foundation for the analysis presented in the subsequent sections.

5.2.2. Thermoelectric Properties

5.2.2.1 Thermal Conductivity

The thermal conductivity of the geopolymer samples, presented in Figure 5.7, exhibits a clear dependence on the alkaline solution-to-slag (AS/S) ratio, which directly controls the amount of activator in the system. The sample with the lowest ratio (S0.3) shows the highest thermal conductivity within the investigated temperature range of 50–70 °C, reflecting the formation of a denser and more continuous matrix that facilitates heat transfer through solid conduction pathways. In contrast, the S0.45 sample, prepared with the highest activator content, exhibits the lowest thermal conductivity. This behavior can be attributed to the development of a more porous microstructure, resulting from excess liquid phase that disrupts gel formation and promotes heterogeneous pore distribution. The intermediate composition (S0.4) displays moderate thermal conductivity values, with a slight increase observed as a function of temperature, suggesting a balance between matrix densification and pore formation.

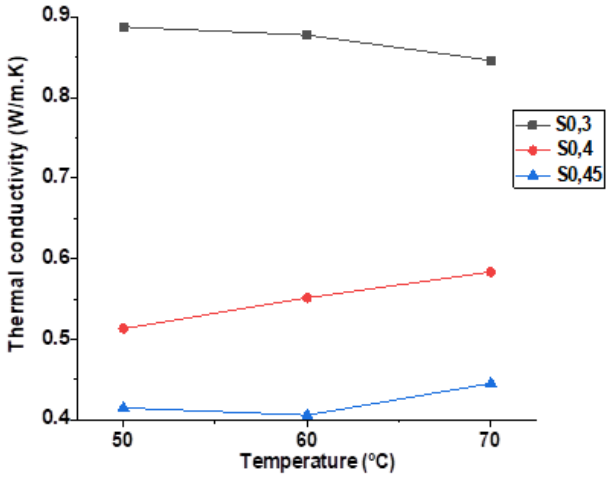


Figure 5.7 The thermal conductivity of the samples prepared with different AS/S ratios

These observations are consistent with previous studies [105–107], which reported that increasing NaOH concentration enhances precursor dissolution while simultaneously promoting pore coarsening, whereas higher sodium silicate content tends to favor polycondensation and matrix densification. The combined influence of activator composition and dosage therefore governs the trade-off between porosity and structural connectivity in the hardened geopolymer. As a result, the AS/S ratio plays a critical role in determining the thermal transport properties of the material through its impact on microstructural development.

5.2.2.2 Electrical Conductivity

Electrical conductivity represents a critical parameter governing the performance of thermoelectric materials, as it directly influences charge transport and energy conversion efficiency. At lower temperatures (20–70 °C), the conductivity of all samples increases with temperature, following an Arrhenius-type behavior characteristic of thermally

activated ionic conduction (Figure 5.8). This regime reflects the enhancement of ionic mobility as thermal energy enables charge carriers to overcome energy barriers associated with ion transport, indicating that this temperature range is particularly relevant for energy harvesting applications.

Among the investigated compositions, the sample with the highest alkaline solution-to-slag ratio (S0.40, black curve) exhibits slightly higher conductivity compared to the others. The higher electrical conductivity of the samples S0.40 and S0.45 is consistent with the presence of a higher concentration of mobile alkali ions (e.g., Na^+) in the pore solution. However, the relatively modest increase in conductivity suggests that increasing the activator content only marginally enhances the effective ionic conductivity, indicating that the overall ion concentration within the pore network is not significantly altered.

At temperatures in the range of approximately 70–80 °C, all samples reach a maximum in conductivity, followed by a sharp decline. This behavior is consistent across all compositions and correlates with the TGA results, which indicate the removal of free and loosely bound water. The presence of this water phase is essential for facilitating ionic transport, either through hydrated ion motion or proton hopping mechanisms. As the temperature exceeds the dehydration threshold, the progressive loss of water leads to a more rigid and dry matrix, significantly limiting ionic mobility and resulting in a pronounced decrease in electrical conductivity.

At higher temperatures (above ~100 °C), the conductivity stabilizes at very low values (on the order of 10^{-9}–10^{-10} S/cm), indicating minimal residual ionic transport in the absence of free water. Notably, the S0.3 sample (black curve) retains comparatively higher conductivity after dehydration, suggesting the presence of more stable ionic pathways or a greater contribution from structurally bound water. This behavior indicates that, even under reduced moisture conditions, the material is capable of sustaining limited ionic transport through confined or surface-associated mechanisms. Such retained ionic mobility under partially dehydrated conditions is indicative of a more stable and interconnected transport network within the geopolymer matrix.

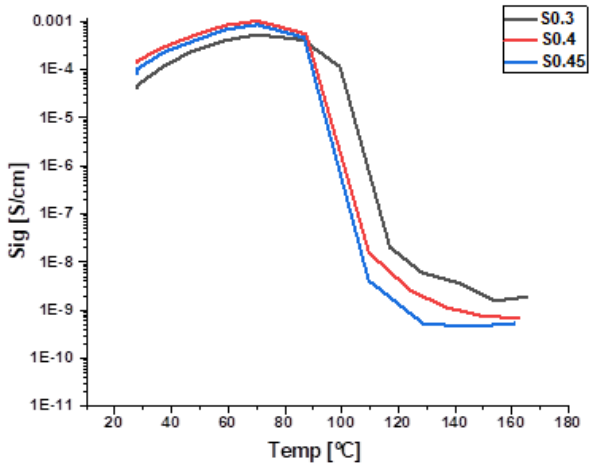


Figure 5.8 The electrical conductivity of the samples with different alkali activator concentrations as a function of temperature

5.2.2.3 Seebeck Behavior

To evaluate the thermoelectric performance of the samples, the open-circuit voltage (V_{OC}) was monitored as a function of time under three different temperature gradients.

All samples exhibit thermoelectric responses characteristic of cement-based ionic thermoelectric materials as described in previous chapters (Figure 5.9). Upon application of a temperature gradient, the voltage initially shifts toward positive values, regardless of the intrinsic voltage or alkali activator content. After reaching a maximum, the voltage progressively decreases toward negative values before stabilizing. For most samples, a steady-state value is reached within approximately 70 to 100 min. An exception is observed for the sample with an AS/S ratio of 0.4 at 50 °C, which displays a non-monotonic behavior. After reaching a minimum during the second stage, the voltage increases again before stabilizing after approximately 190 min.

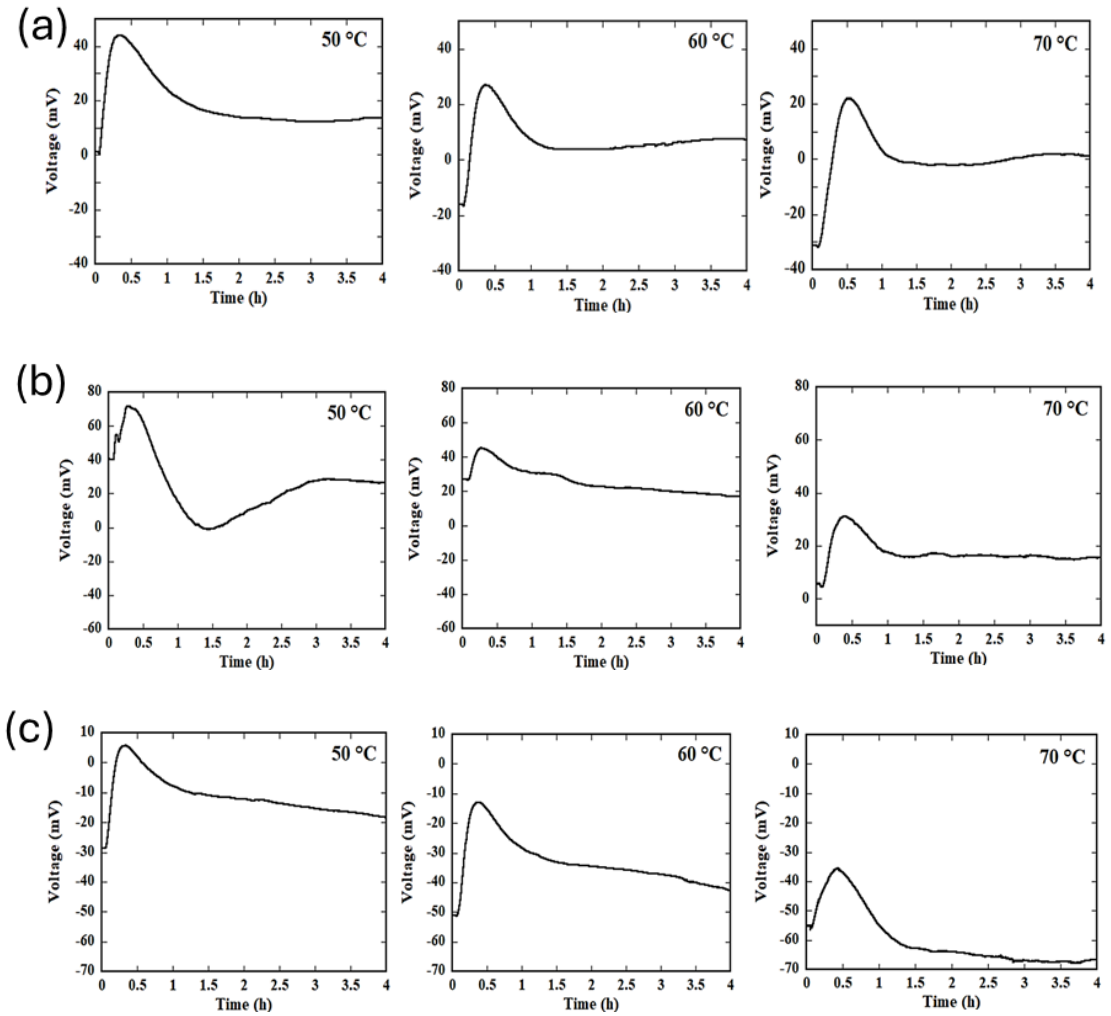


Figure 5.9 The thermovoltage generated under different applied temperatures for samples prepared using different AS/S ratios, (a) 0.3, (b) 0.4, (c) 0.45

In chapter III, it has been shown that the intrinsic voltage of cement-based thermoelectric materials can significantly influence the measured thermoelectric response. As described in the experimental methodology, a preconditioning protocol was applied before measurement to minimize this effect. At the lowest applied temperature, the sample with

the lowest activator content (S0.3) exhibits an intrinsic voltage close to zero, consistent with earlier observations indicating that drying procedures can suppress this contribution. However, with increasing activator content, the intrinsic voltage becomes more pronounced and cannot be fully eliminated.

This behavior can be attributed to the higher concentration of alkali species and the presence of locally trapped ions within the geopolymer gel matrix. Upon rehydration, these ions generate localized electric fields, which induce charge accumulation at the sample surface. Consequently, although increasing the activator content is intended to enhance the concentration of mobile ions in the pore solution, it also promotes the formation of persistent heterogeneous charge distributions within the matrix, thereby affecting the measured thermoelectric voltage. Since ionic charge carriers cannot traverse the external circuit, the generated voltage in ionic thermoelectric systems is inherently transient. Nevertheless, the measurable response is defined by the difference between the intrinsic voltage and the peak voltage, and the absolute voltage at a given time is sufficient to drive current when connected to an external load. For this reason, the Seebeck coefficient was calculated using the absolute peak voltage values, which persist for a sufficiently long duration to enable effective energy harvesting.

All samples prepared with different alkaline solution contents exhibit Seebeck coefficients among the highest values reported for cementitious thermoelectric materials (Figure 5.10). Table 5.3 summarizes the intrinsic voltage, peak voltage, and the corresponding voltage differences for all samples at the three applied temperatures. The results demonstrate that the intrinsic voltage introduces a significant offset, which directly influences the apparent thermoelectric response. At low activator content (AS/S = 0.30), the intrinsic voltage is negligible, and the measured voltage change primarily reflects the intrinsic thermoelectric behavior. At an intermediate ratio (0.40), the intrinsic voltage becomes positive, partially compensating the thermoelectric contribution and reducing the effective ΔV with increasing temperature. At the highest ratio (0.45), the intrinsic voltage shifts strongly negative and, in some cases, exceeds the thermoelectric contribution, leading to reduced or even inverted apparent responses.

Table 5-3 TE Voltage characteristics of the samples at three applied temperatures.

Alkaline solution/Slag		**0.3**	**0.4**	**0.45**
50 °C	V_{int}	0	40.60	-28.60
	V_{peak}	44.00	71.60	5.800
	ΔV	44.00	32.00	34.00
60 °C	V_{int}	-16.07	27.00	-51.00
	V_{peak}	27.00	45.40	-13.00
	ΔV	42.00	18.30	39.00
70 °C	V_{int}	-31.20	5.50	-55.00
	V_{peak}	22.300	31.10	-35.00
	ΔV	54.50	25.30	21.00

Overall, the intrinsic voltage acts as a composition- and time-dependent baseline that can enhance, suppress, or reverse the observed thermoelectric signal. It should be noted that, according to the literature, intrinsic voltage fluctuations are generally difficult to control [23].

Despite these complexities, clear trends in the Seebeck coefficient as a function of composition and temperature are observed. Increasing the AS/S ratio from 0.30 to 0.40 results in only a marginal increase in the Seebeck coefficient, which becomes negligible at higher temperatures. A further increase to an AS/S ratio of 0.45 leads to a reduction in the Seebeck coefficient and, in some cases, a reversal in sign, primarily driven by the influence of intrinsic voltage.

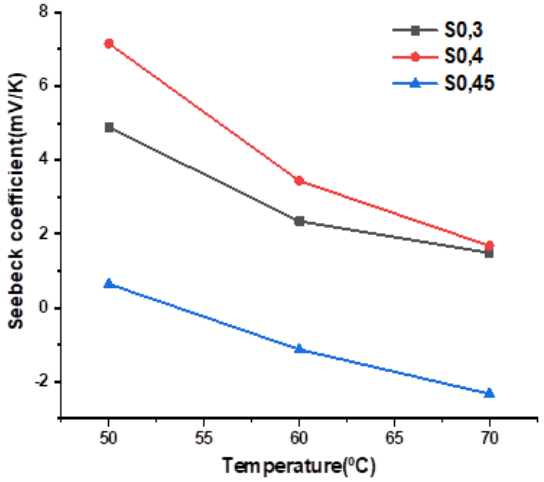


Figure 5.10 The Seebeck coefficient of the samples prepared with three alkali concentrations under different applied temperatures

The observed decrease in Seebeck coefficient with increasing alkaline solution content can be rationalized in terms of ionic transport behavior. In ionic thermoelectric systems, the Seebeck coefficient is governed by both the concentration and mobility of charge carriers. Although higher activator contents are expected to increase the concentration of mobile ions (e.g., Na^+, K^+), an excessive ionic concentration can promote local polarization effects and charge screening within the pore solution. In addition, the formation of heterogeneous charge distributions within the gel matrix can hinder effective ion diffusion under a thermal gradient. As a result, the increased ionic concentration does not necessarily translate into enhanced thermoelectric performance, but instead may lead to reduced ion diffusivity and altered thermoelectric response.

5.2.2.4 TE Performance and Figure of Merit

Figure 5.11 presents the variation of the dimensionless figure of merit (ZT) as a function of temperature for geopolymer samples prepared with different alkaline solution-to-slag (AS/S) ratios. The results indicate that thermoelectric efficiency is strongly influenced by both activator content and temperature. At the lowest activator content (S0.3), the ZT values remain low and nearly constant across the investigated temperature range. This behavior reflects relatively stable but limited ionic transport, as the reduced concentration of mobile ions constrains improvements in both electrical conductivity and thermoelectric voltage (see Figure 5.11).

In contrast, the sample with intermediate activator content (S0.4) exhibits the highest ZT at 50 °C, reaching values approximately one order of magnitude greater than those of the other compositions. This enhanced performance can be attributed to a favorable balance between ionic mobility and thermoelectric voltage generation at lower temperatures. However, with increasing temperature, a significant decline in ZT is observed. This reduction is associated with the combined effects of intrinsic voltage contributions, which partially offset the thermoelectric signal, and the progressive loss of water from the matrix, which limits ionic mobility.

The sample with the highest activator concentration (S0.45) displays a distinct behavior, with very low ZT values at 50 °C followed by a gradual increase as the temperature rises. This delayed improvement is attributed to the strong influence of intrinsic voltage at lower temperatures, which masks the effective thermoelectric response. As the temperature increases, the relative contribution of intrinsic voltage decreases, while enhanced ionic mobility partially restores the thermoelectric response, leading to a progressive increase in ZT.

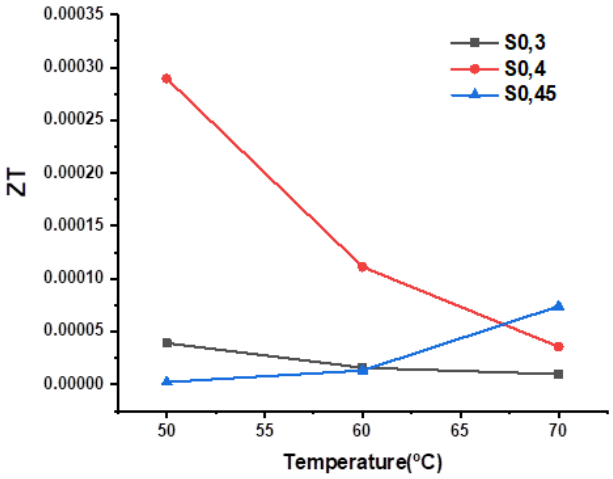


Figure 5.11 The thermoelectric figure of merit for samples with different AS/S ratios

Overall, these results highlight a trade-off between activator content and thermoelectric performance. A moderate AS/S ratio (0.4) provides optimal performance at lower temperatures, whereas excessive activator content introduces parasitic voltage effects that suppress performance under these conditions but become less significant at higher temperatures. Conversely, insufficient activator content (0.3) results in consistently low ZT values due to limited ionic transport.

It is important to note that the Seebeck coefficients obtained for all compositions are among the highest reported for cement-based thermoelectric materials, and the corresponding ZT values are comparable to those of cementitious composites incorporating functional additives. Considering that such additives often increase material cost and may adversely affect mechanical properties, alkali-activated geopolymers represent a promising, cost-effective, and structurally robust alternative for thermoelectric applications. Their ability to achieve competitive performance without the use of expensive or performance-compromising additives highlights their potential for sustainable energy harvesting systems.

5.3. Conclusion

This study systematically evaluated the thermoelectric performance of ground granulated blast furnace slag (GGBFS)-based geopolymers synthesized with varying alkaline solution-to-slag (AS/S) ratios. The combined characterization results demonstrate that the AS/S ratio plays a central role in governing geopolymerization kinetics, microstructural development, and the resulting transport properties. Microstructural analyses revealed that increasing the AS/S ratio reduces the extent of gel formation, resulting in a more porous, less interconnected matrix, which is directly reflected in the observed decrease in mechanical strength.

Despite these variations, all compositions exhibited pronounced ionic thermoelectric behavior, with Seebeck coefficients among the highest reported for cementitious systems. A key finding of this work is the significant influence of intrinsic voltage on the measured thermoelectric response. Depending on the activator content and temperature, intrinsic voltage can either enhance or suppress the apparent thermoelectric signal, thereby strongly affecting the calculated figure of merit. These results highlight that controlling intrinsic voltage is critical for achieving reliable and reproducible thermoelectric performance, as its contribution may outweigh the expected benefits associated with increased ionic concentration.

The analysis of electrical conductivity indicates similar trends across all compositions, with only moderate variations as a function of AS/S ratio. In contrast, thermal conductivity exhibits a more pronounced dependence on composition and plays a decisive role in determining the overall thermoelectric efficiency. The calculated ZT values identify the intermediate composition (S0.4) as the most effective system, owing to an optimal balance between electrical conductivity, thermal transport, and thermoelectric voltage generation.

Importantly, the ZT values obtained in this study are comparable to those reported for cementitious systems modified with functional additives. However, the present approach achieves this performance without the use of costly or potentially detrimental additives, preserving both the sustainability and mechanical integrity of the material. These findings demonstrate that GGBFS-based geopolymers represent a promising class of environmentally friendly and structurally robust materials for thermoelectric applications, particularly in the context of low-grade waste heat recovery and distributed energy harvesting.

Chapter VI

A Chessboard-Like Photothermoelectric Cement Cell: A New Design for Scalable and High-Efficiency Solar Energy Conversion

The results presented in the previous chapters established a consistent mechanistic framework for ionic thermoelectric (i-TE) behavior in cementitious materials, demonstrating that thermoelectric voltage originates from the thermodiffusion of ions within the pore solution under an applied temperature gradient. Across geopolymer-based hybrid cement, kaolin-derived geopolymers, and GGBFS-based systems, the thermoelectric response was shown to be governed by a complex interplay between pore structure, water state, ionic concentration, and interfacial charge accumulation. These studies collectively highlighted that optimizing thermoelectric performance requires not only increasing ionic content but also carefully controlling microstructure and transport pathways to balance ion mobility and diffusion.

However, despite achieving high Seebeck coefficients and identifying the governing mechanisms, a fundamental limitation remains in conventional cement-based thermoelectric systems: the inefficient generation and maintenance of temperature gradients. In most previously studied configurations, the thermal gradient is applied vertically, inherently restricting the achievable ΔT due to the relatively high thermal mass and low thermal conductivity contrast within cementitious materials. This limitation directly constrains the practical energy harvesting capability of ionic thermoelectric cement systems.

To overcome this challenge, the focus of this chapter shifts from material-level optimization to system-level design, where the insights gained from ionic transport mechanisms are translated into a functional and scalable device architecture. In particular, the understanding that ionic thermoelectric response is highly sensitive to temperature distribution, ion mobility, and environmental conditions provides a foundation for engineering spatially controlled thermal gradients within cement-based structures.

In this context, a novel photothermoelectric (PTE) cement system is introduced, in which the thermal gradient is generated laterally rather than vertically by exploiting differences in optical properties between cementitious components. This approach utilizes a chessboard-like arrangement of high-absorbance and high-reflectance cement composites to induce a stable horizontal temperature gradient under solar irradiation. This design directly addresses the intrinsic limitation of conventional systems by decoupling thermal gradient generation from bulk heating and instead relying on controlled solar absorption.

Moreover, this transition from material design to device engineering enables the integration of multiple key factors identified in earlier chapters, including ionic transport pathways, intrinsic voltage effects, and moisture-dependent conductivity, into a unified system capable of operating under real-world environmental conditions. The resulting PTE cement cell not only demonstrates enhanced thermoelectric performance but also

introduces additional functionalities such as scalability, self-rechargeability through ambient humidity, and compatibility with large-scale construction materials.

Therefore, this chapter bridges the gap between fundamental ionic thermoelectric behavior and practical energy harvesting applications, presenting a design strategy that transforms cementitious materials from passive structural components into active energy-generating systems.

6.1. Experimental

6.1.1. Materials and Sample Preparation

For the present study, an industrial geopolymer-based hybrid cement (GHC), supplied by Považská cementáreň a.s., was employed as the binder for fabricating the distinct sections of the thermoelectric (TE) cells, differentiated by their light-absorption characteristics. The segment designed to exhibit higher light absorbance is hereafter referred to as the "black part". To enhance the ionic thermoelectric (iTE) response of this section, 75 wt.% copper slag (CS) aggregate was incorporated. In contrast, the high-reflectance counterpart ("white part") was prepared using white cement (BL I 52.5 R) supplied by Cementos Cruz (Spain).

The chemical compositions of GHC, white cement (BLWC), and CS are presented in Table 6.1. Detailed information regarding the chemical composition analysis (XRF) and the characterization techniques is described in Chapter II.

Table 6-1 Chemical compositions of the different parts of the PTE cell

	SiO_2	Al_2O_3	Fe_2O_3	MnO	MgO	CaO	Na_2O	K_2O	TiO_2	P_2O_5	SO_3	Loss on Ignition (%)
GHC	35.86	13.51	4.63	0.06	1.79	23.93	3.36	1.97	0.61	0.21	5.02	5.51
BLWC	20.74	3.76	0.16	LD	0.52	62.94	LD	0.64	0.23	0.05	3.26	4.06
CS	22.01	8.86	50.87	0.80	1.48	7.90	0.43	0.24	0.18	0.54	0.25	2.63

A uniform preparation protocol was adopted for both sections. Initially, dry mixing of the cement and aggregates was performed using a Hei-TORQUE 200 overhead stirrer at 300 rpm to ensure homogeneous distribution. Distilled water was then added, and the mixture was stirred at 700 rpm for 1.5 min. After a resting period of 1 min, the mixing step was repeated to ensure adequate homogeneity.

The mixtures were subsequently cast into sealed cubic silicon molds incorporating a centrally positioned plastic barrier to separate the two sections. Each sample had dimensions of 8 × 2 × 0.7 cm, with each individual section measuring 4 × 2 × 0.7 cm. The barrier ensured separation during casting while preventing premature mixing. After 5 min, the barrier was removed, allowing the formation of a continuous pore solution network between both sections. The samples were demolded after 24 h and cured for 28 days in distilled water. A constant water-to-cement ratio (w/c) of 0.6 was maintained for all compositions.

To improve the repeatability of the measurements and minimize variability arising from microstructural inhomogeneities, a standardized pretreatment protocol was applied prior

to Seebeck testing. After the 28-day curing period, the samples were dried overnight at 50 °C and subsequently conditioned at 75% relative humidity (RH) for 24 h.

To further enhance the energy output of the cement-based PTE cells, several modifications were introduced in terms of sample geometry, electrode configuration, and ionic conductivity. The baseline preparation protocol remained unchanged; however, mold dimensions were reduced to decrease the electrode spacing. Specifically, the modified samples had dimensions of 2 × 0.7 × 4 cm, corresponding to a 50% reduction in electrode distance.

In addition, to reduce contact resistance, conventional copper electrodes were replaced with soldered wires connected to silver paint electrodes, thereby improving electrical contact at the interface. Finally, the ionic conductivity of the samples was enhanced through exposure to a 3.5 wt.% NaCl solution (equivalent to seawater concentration). After drying at 50 °C overnight following curing, the samples were immersed in the saline solution for 1 h, then removed and allowed to rest for 24 h before measurement.

6.1.2. Material Characterization

A combination of material characterization, device-level measurements, and environmental testing was employed to investigate the performance of the chessboard-like PTE cement system. The chemical composition of the constituent materials was analyzed using X-ray fluorescence (XRF), while their optical properties, which are critical for inducing temperature gradients, were evaluated through infrared emissivity and reflectance measurements. A controlled fabrication protocol was adopted to produce composite samples with distinct light-absorbing (black) and light-reflecting (white) regions, enabling the generation of horizontal thermal gradients within a single cell. The thermoelectric response was assessed through time-dependent open-circuit voltage measurements under both laboratory-controlled irradiation and real outdoor conditions. Indoor experiments allowed systematic variation of irradiation intensity and cell configuration, whereas outdoor measurements captured the influence of environmental factors such as solar irradiance, relative humidity, and wind on device performance. Additional investigations, including contact angle measurements and cyclic drying–rehydration tests, were conducted to evaluate moisture interaction and self-rechargeability. The electrical output under load was further analysed to quantify power and energy harvesting capabilities. This multi-scale experimental approach enables a comprehensive understanding of the coupling between optical design, ionic transport, environmental conditions, and energy generation in cement-based PTE systems. Detailed procedures are provided in the methodology section (Chapter II); therefore, only the key results and their interpretation are discussed in the following.

6.2. Results and Discussion

6.2.1. Thermoelectric Properties of the PTE Components

To overcome the inherent limitations associated with vertically imposed thermal gradients in conventional cement-based thermoelectric (TE) systems, a photothermoelectric (PTE) composite was developed to generate a controlled horizontal temperature gradient. This

design was achieved by integrating materials with complementary optical and thermoelectric properties, enabling differential solar absorption and localized heating within the system.

In addition to the magnitude of the temperature gradient, the intrinsic thermoelectric performance of the individual components plays a critical role in determining the overall efficiency of the PTE cell. Figure 6.1a and 6.1b present the voltage profile and corresponding temperature gradient of the black component. The experimental sample consisted of a rectangular prism with dimensions of 20 × 20 × 80 mm^3. A temperature gradient was established by heating the top surface of the sample to 70 °C using a 20 × 20 mm^2 ceramic heater.

It is observed that the voltage profile does not originate from a zero baseline but instead exhibits an initial offset due to the intrinsic voltage of the samples. As demonstrated in previous chapters, this intrinsic voltage can significantly influence thermoelectric measurements in cement-based materials. Therefore, to minimize this effect and to ensure reproducible starting conditions, a pretreatment protocol was implemented. This procedure involved drying the samples at 50 °C overnight, followed by conditioning in a controlled humidity environment for 8 h before testing. This approach not only standardizes the initial state of the samples but also takes advantage of the inherent moisture reabsorption capacity of cementitious materials, which contributes to stabilizing the photothermoelectric (PTE) response under realistic conditions.

Upon activation of the heater, the voltage profile of the black component shifts toward negative values. After accounting for the intrinsic voltage contribution, a peak voltage difference of 7 mV is observed. Considering the corresponding temperature difference of 31.9 K between the electrodes, the Seebeck coefficient at the peak is calculated to be 219 $\mu V\ K^{-1}$. With continued heating, the voltage profile evolves and eventually stabilizes at a positive value of +15.5 mV. This transition reflects the temperature-dependent dynamics of ionic migration under an applied thermal gradient, consistent with previous observations in Chapter III.

For the white cement sample, a lower target temperature of 50 °C was selected to better represent outdoor operating conditions. Figures 6.1c and 6.1d show that the sample initially exhibits an intrinsic voltage of approximately −3.5 mV. After allowing this value to stabilize for 1 h, the heater was activated, resulting in a rapid but relatively small negative voltage peak, followed by a low and stable voltage response. This behavior is consistent with the relatively mild temperature gradient applied in this configuration.

The Seebeck coefficient calculated at the voltage peak for the white cement sample is 132 $\mu V\ K^{-1}$. These results indicate that, despite its lower thermal response, white cement provides a suitable matrix for ionic transport and contributes effectively to the overall thermoelectric behavior of the composite system.

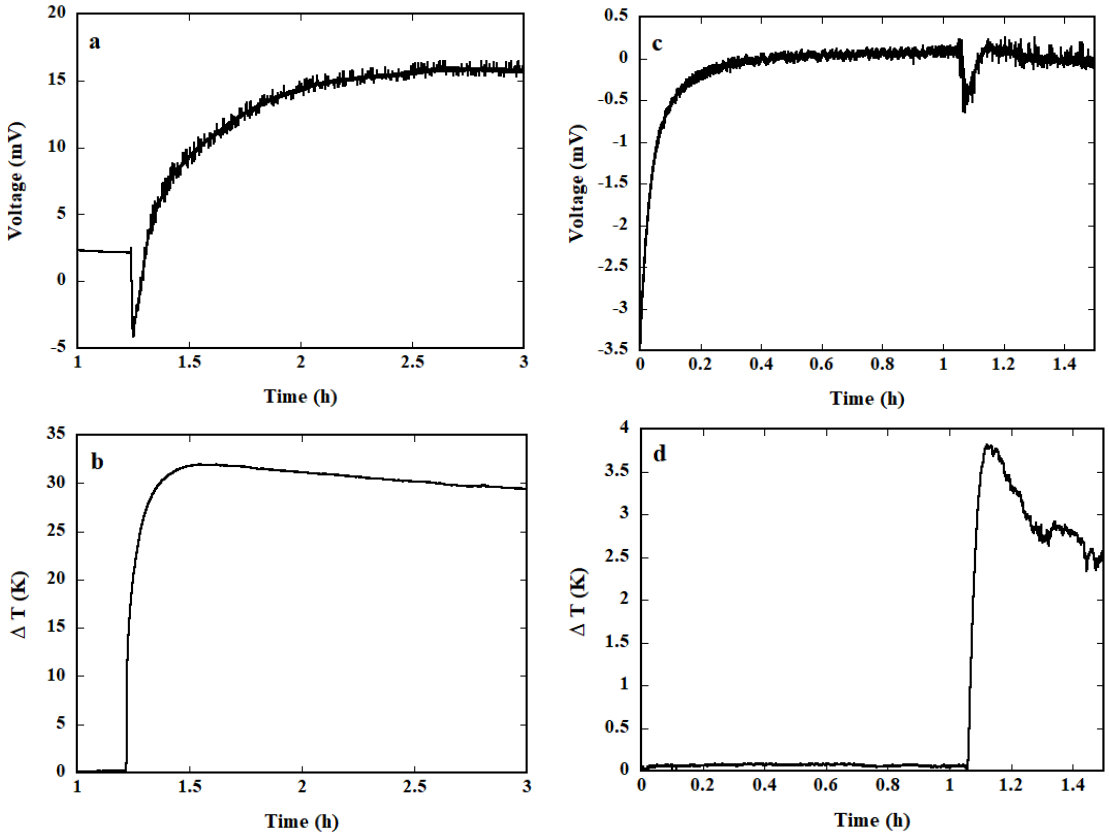


Figure 6.1 The voltage profile and temperature gradient of (a,b.) geopolymer hybrid cement with 75 wt.% copper slag aggregate (black) (c,d). white cement (white).

6.2.2. Proof of Concept of the PTE Cell Design and Performance

The prepared PTE cell is shown in Figure 6.2a. The reflectance spectra reveal distinct optical responses, particularly in the visible and near-infrared (NIR) regions, highlighting the strong dependence of optical behavior on cement composition (Figure 6.2b). The black segment, characterized by lower reflectance, exhibits enhanced solar absorption and thus functions as the "hot electrode". In contrast, the white segment, with a reflectance ranging from 0.65 to 0.87, reflects a significant portion of the incident radiation, thereby minimizing heat absorption and acting as the "cold electrode". This pronounced optical contrast is essential for establishing and maintaining a stable temperature gradient across the cell (Figure 6.2c).

To assess the PTE performance, the sample was exposed to a light source with an intensity of 850 W m^{-2}, generated by a 500 W lamp. Under these conditions, the temperature difference across the cell stabilized after approximately 30 min (Figure 6.2d), confirming the capability of the system to sustain a thermal gradient suitable for PTE energy conversion.

The black segment was specifically engineered to exhibit high thermoelectric performance, whereas the white segment was selected for its effective thermal reflectance, enabling passive cooling. The resulting temperature gradient drives the migration of ionic charge carriers—primarily metal cations (Na^+, K^+) and anions (OH^-)—from the hot region toward the cold region. This ion migration generates an electrical

potential, which is evaluated by monitoring the open-circuit voltage of the sample during operation.

The resulting voltage profile follows a characteristic trend governed by the competing migration of cations and anions within the pore solution (Figure 6.2e). In the initial stage, cation migration dominates due to their inherently higher mobility in cementitious pore environments. Molecular dynamics simulations reported by Honorio et al. [79] indicate that K^+ and Na^+ possess significantly higher diffusion coefficients, in the range of 1.4–4.1 × 10^{-9} m^2/s and 1.3–3.8 × 10^{-9} m^2/s, respectively, compared to 0.8–1.8 × 10^{-9} m^2/s for OH^-. This disparity implies a lower effective activation energy for cation transport, supporting the initial dominance of cation-driven thermodiffusion and the observed negative PTE voltage. The corresponding Seebeck coefficient reaches 0.539 mV K^{-1}, indicating peak thermoelectric response under these conditions.

As the system temperature increases and the hot side exceeds approximately 80 °C, OH^- ions acquire sufficient thermal energy to overcome their activation barrier, leading to a transition toward anion-dominated transport. In the second stage, the increasing contribution of anions counterbalances the cationic flux, resulting in a gradual reversal of the voltage polarity. In the final stage, a dynamic equilibrium between cationic and anionic transport is established, leading to stabilization of the voltage signal. The observed polarity reversal at approximately 80 °C, across different temperature gradients and irradiation conditions, is therefore attributed to a thermally activated shift in the dominant migrating ionic species.

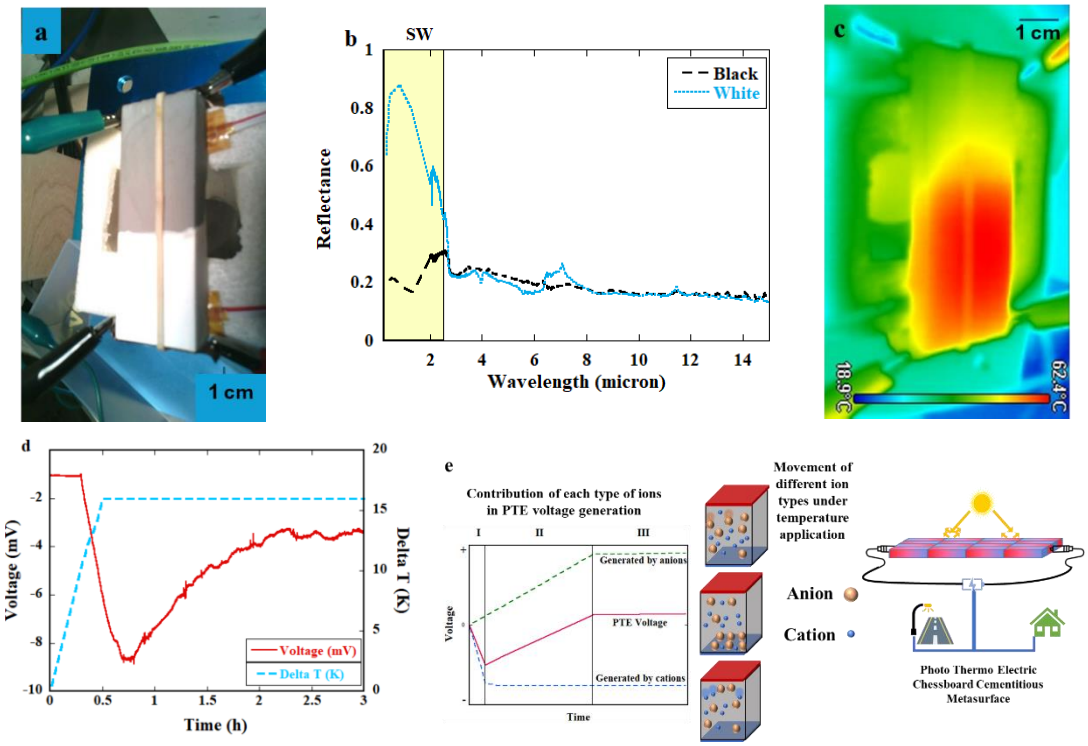


Figure 6.2 Digital photograph of the PTE cell prepared using two types of cement composites, (b) Light reflectance of the two parts of the PTE cell (black and white) and their difference in solar window (SW) obtained via FTIR spectroscopy, (c) Temperature distribution throughout the PTE cell under exposure to light at 850 W m^{-2} obtained by thermal camera after 30 minutes of illumination, (d) Temperature gradient

induced in the PTE cell under 850 W m⁻² irradiation monitored by thermocouples and the induced PTE voltage, (e) Schematic of the mechanism of the PTE cell.

6.2.3. Temperature and Light Power Dependence of the PTE Cell Performance

In addition to the imposed temperature gradient, both the absolute temperature and irradiation power play a critical role in governing the thermoelectric response of the PTE cell through their influence on ionic transport. Since irradiation power directly controls heat absorption, it determines not only the magnitude of the temperature gradient but also the absolute temperature reached within the system. Consequently, understanding the response of the PTE cell under varying irradiation conditions is essential for evaluating its performance under realistic solar exposure.

The effect of irradiation intensity on the temperature gradient and voltage response is presented in Figure 6.3, together with the corresponding quantitative values summarized in Table 6.2. When the PTE cell was exposed to a low irradiation intensity of 450 W m⁻², a temperature gradient of approximately 9 K was established. However, this thermal difference proved insufficient to induce significant ionic migration, resulting in voltage fluctuations around the zero baseline throughout the measurement period.

Upon increasing the irradiation intensity to 700 W m⁻² and 950 W m⁻², a characteristic voltage profile emerged, consistent with the behavior previously observed under 850 W m⁻² irradiation. In both cases, the voltage evolution can be divided into three distinct stages. The initial stage is characterized by a negative voltage peak, reaching values of −2.47 mV and −11.86 mV for irradiation intensities of 700 W m⁻² and 950 W m⁻², respectively. This is followed by a gradual decrease in the absolute voltage, ultimately leading to stable values of −0.98 mV and −4.95 mV after approximately one hour.

A notable observation is the non-linear relationship between irradiation power, temperature gradient, and voltage response. As expected, increasing irradiation intensity leads to higher temperature gradients; for instance, the temperature difference increases from 12 K at 700 W m⁻² to 16 K at 850 W m⁻². However, this relatively modest increase in ΔT results in a disproportionate enhancement in the voltage response, with the peak voltage increasing by a factor of approximately 3.5, corresponding to a significant increase in the effective Seebeck coefficient. Furthermore, even when the temperature gradient remains constant (16 K for both 850 W m⁻² and 950 W m⁻²), an additional increase in irradiation power leads to a further 37% increase in peak voltage.

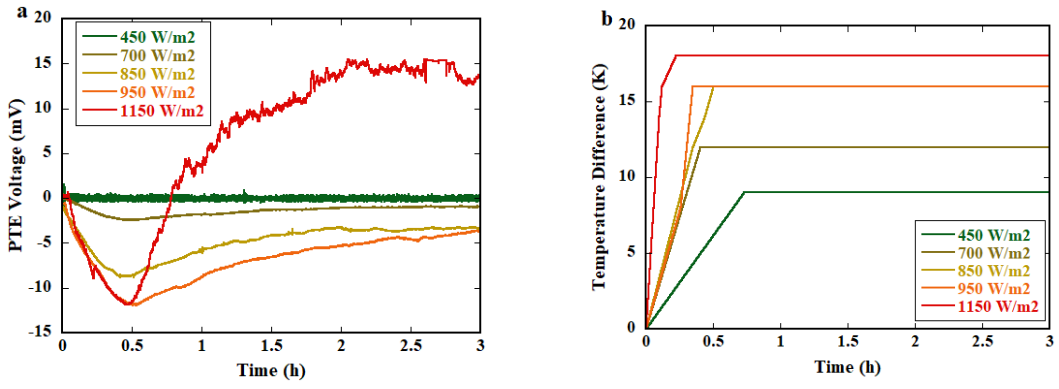


Figure 6.3 PTE measurement of a single cell at different irradiation powers, (b) temperature differences created under different irradiation.

This behavior highlights the strong dependence of ionic thermoelectric response on absolute temperature, rather than solely on the temperature gradient. As irradiation intensity increases, both the hot and cold regions of the cell experience elevated temperatures, which enhances ionic mobility and alters the relative contributions of different charge carriers. This complex behavior can be attributed to the pronounced temperature dependence of ion migration processes. For instance, Xiong et al. [108] demonstrated that, in ionic thermoelectric $MAPbI_3$ perovskites, the mobility of ionic species is strongly temperature-dependent, with I^- ions exhibiting higher mobility at lower temperatures, whereas MA^+ ions require higher thermal activation to participate significantly in charge transport.

Table 6-2 Summarized result of PTE measurement for different irradiation powers

Light Power ($W\ m^{-2}$)	$T_{White\ electrode}$ (°C)	$T_{Black\ electrode}$ (°C)	ΔT (K)	V_{Valley} (mV)	V_{stable} (mV)	S_{Valley} ($mV\ K^{-1}$)	S_{Stable} ($mV\ K^{-1}$)
450	36	45	9	0	0	0	0
700	44	56	12	-2.47	-0.98	0.205	0.081
850	44	60	16	-8.62	-3.22	0.538	0.201
950	50	66	16	-11.86	-4.95	0.988	0.309
1150	63	81	18	-11.65	14.60	0.647	0.811

At the highest irradiation intensity of 1150 W m^{-2}, a distinct transition in the voltage profile is observed, characterized by a reversal in voltage polarity during the second stage (Figure 6.3a). This behavior is consistent with the response observed in the black segment (Figure 6.1) and the results presented in Chapter III. The polarity reversal reflects a shift in the dominant charge carrier, associated with the activation of anionic species at elevated temperatures.

Importantly, this transition occurs despite differences in the applied temperature gradients. For example, while the GHC 75CS sample exhibited a temperature gradient of approximately 30 K and the PTE cell a gradient of 18 K under 1150 W m^{-2} irradiation, both systems reached a similar absolute temperature of approximately 80 °C at the hot side. This observation indicates that the transition in thermoelectric behavior is governed primarily by absolute temperature rather than ΔT.

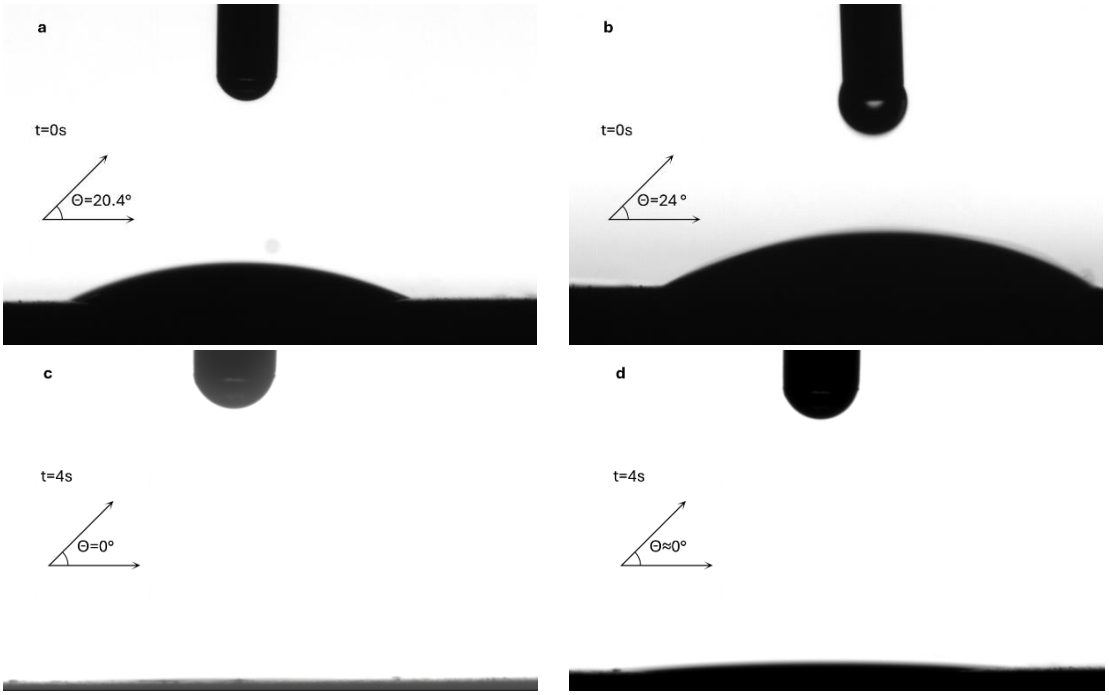
The temperature of approximately 80 °C, therefore, represents a critical threshold for these ionic thermoelectric systems, at which anions such as OH^- acquire sufficient thermal energy to overcome their activation barrier and contribute significantly to charge transport. Beyond this point, the enhanced mobility of anions can surpass that of cations, leading to a reversal in the net thermoelectric voltage. This thermally activated transition in dominant charge carriers provides a consistent explanation for the observed voltage polarity change across different material systems and irradiation conditions.

6.2.4. Rechargeability of PTE Cells (effect of relative humidity)

In addition to thermal and optical factors, environmental conditions play a critical role in determining the performance and durability of ionic thermoelectric (iTE) systems. A major challenge associated with iTE materials is the loss of the ionic transport medium

through evaporation or leakage, as charge transport is primarily facilitated by water or liquid phases within the pore network [108,109]. This inherent sensitivity makes the thermoelectric response strongly dependent on external parameters such as temperature and relative humidity (RH). In cement-based systems, prolonged exposure to temperatures above approximately 50 °C can lead to gradual dehydration, thereby reducing ionic mobility and, consequently, thermoelectric performance [15].

To address this limitation, the intrinsic moisture reabsorption capability of different parts of the PTE cell was investigated as a potential self-recharging mechanism. Contact angle measurements were conducted to evaluate the hydrophilicity of both segments of the PTE cell. As shown in Figure 6.4a–d, the initial contact angles were 20.4° for the black component and 24° for the white component, indicating strong wettability. Notably, both samples completely absorbed the deposited water droplets within approximately 4 s, confirming their highly hydrophilic nature and their ability to efficiently uptake moisture from the surrounding environment.



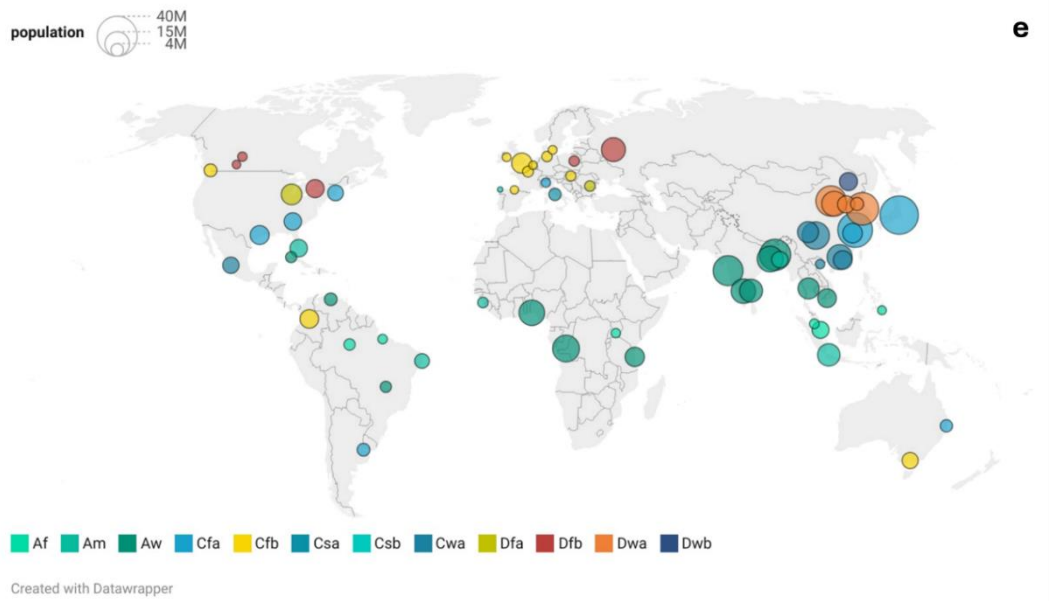


Figure 6.4 Contact angle measurement of two segments of PTE cell at time 0s and 4s, (a) and (c) black component, (b) and (d) white component, (e) map of the major cities of the representative climate zone

Building on this property, the rechargeability of the PTE system was evaluated through repeated drying–rehydration cycles. Before each test cycle, the samples were dried in an oven and subsequently conditioned in a controlled humidity environment, as described in the experimental section. Under illumination, each drying step effectively reset the PTE voltage to zero, reflecting the depletion of mobile ionic species due to water loss. However, upon rehydration, the samples consistently recovered their ability to generate thermoelectric voltage, reproducing similar voltage profiles across multiple cycles (Figure 6.5). These results demonstrate that the system exhibits a reversible and stable thermoelectric response, enabled by the reintroduction of moisture into the pore network.

Chi et al. [15] proposed the use of epoxy sealing to mitigate evaporation in ionic thermoelectric cement systems during thermoelectric operation. However, this method may compromise optical properties and is therefore not suitable for photothermoelectric applications, where light absorption and reflection are critical design parameters. In contrast, the present approach leverages the natural hygroscopic behavior of cement to maintain functionality without requiring external encapsulation.

To further evaluate the practical applicability of this recharge mechanism, the environmental conditions required for operation were assessed in the context of global climate zones. The recharge process is activated when the ambient relative humidity exceeds approximately 50%. As illustrated in Figure 6.4e, most major urban areas worldwide are located in climate zones such as humid subtropical (Cfa), monsoon-influenced (Am), tropical rainforest (Af), and certain oceanic climates (Cfb), where nighttime RH during warm seasons typically exceeds this threshold. In contrast, arid and desert climates (e.g., BWh), characterized by persistently low humidity, are less favorable for this mechanism.

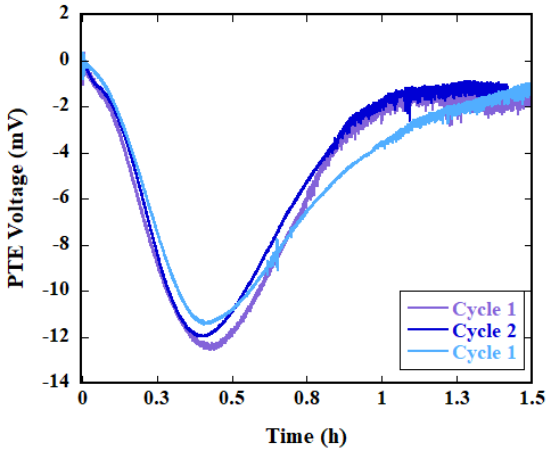


Figure 6.5 The PTE voltage of the sample, under 950 W m^{-2} light illumination. Before each cycle the sample was dried and stored in humidity chamber at RH 50%

These observations indicate that the proposed PTE system is inherently compatible with the environmental conditions of the majority of densely populated regions worldwide. The ability to passively recharge through ambient humidity, combined with stable thermoelectric performance under cyclic operation, highlights the potential of this approach for real-world deployment in building-integrated energy harvesting applications.

6.2.5. Connection of PTE Cells (chessboard concept)

To further evaluate the scalability of the proposed system, the performance of multiple PTE cells connected in series was investigated. The voltage response of a two-cell configuration under an irradiation intensity of 850 W m^{-2} is presented in Figure 6.6a. During the initial stage, characterized by a pronounced negative voltage peak, the series-connected system generated approximately 81% of the cumulative peak voltage obtained from individual cells (Figure 6.2d). Specifically, while a single cell exhibited a peak voltage of −8.6 mV, the two-cell configuration reached −13.9 mV, which is 3.3 mV lower than the expected additive value.

This reduction is accompanied by a decrease of approximately 10% in the temperature gradient across the system (Figure 6.6b), arising from the interaction between adjacent cells and the overall sample configuration. As a result, the Seebeck coefficient per cell in the series arrangement was calculated to be 0.480 mV K^{-1}, corresponding to only an 11% reduction compared to the single-cell configuration. Notably, during the second stage of the voltage profile, the decay rate of the thermoelectric signal was slower than that observed for a single cell. This behavior can be attributed to the reduced temperature gradient and the associated moderation of anion migration dynamics in the coupled system.

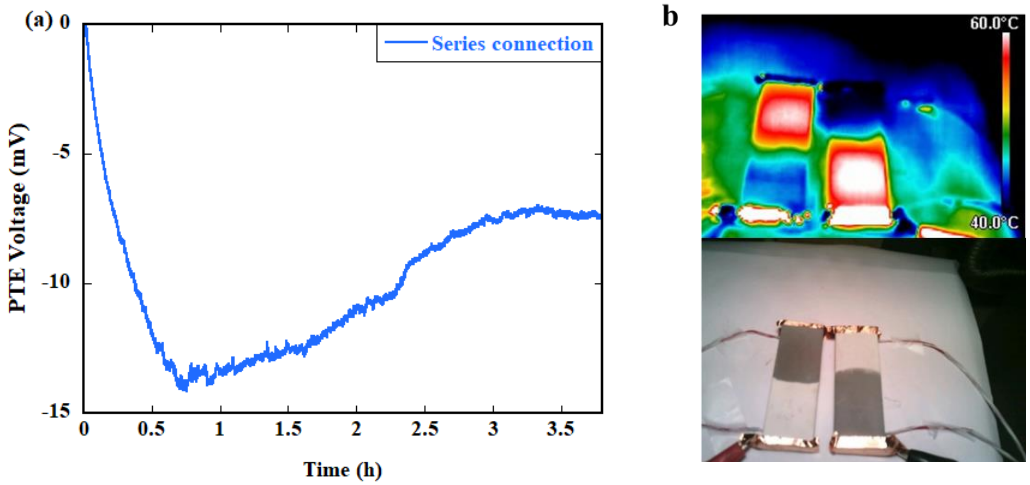


Figure 6.6 Voltage profile of two PTE cells connected in series under 850 W m^{-2}. (b) The temperature gradient induced in the connected system, and the digital photograph of the connected cells

The observed decrease in thermoelectric voltage upon series connection is consistent with previous studies on cement-based thermoelectric materials. For instance, Vareli et al. [39] reported a reduction of up to 95% when ten cement-based TE cells were connected in series. In comparison, the present system exhibits a more moderate reduction, indicating improved scalability of the PTE configuration. However, as the number of connected cells increases, the cumulative voltage deviates further from the ideal additive behavior. This trend is illustrated in Figure 6.6, where configurations of four and six cells retain approximately 83% and 61% of the sum of the individual voltages, respectively.

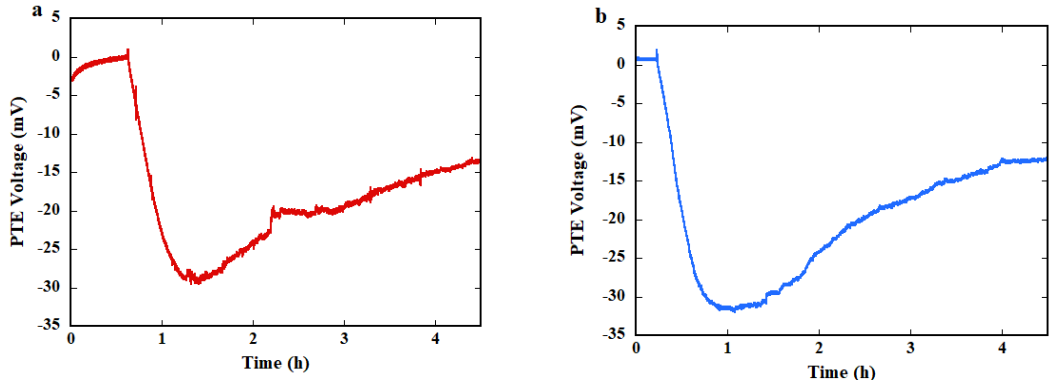


Figure 6.7 The open circuit voltage of (a) four PTE cells connected in series (b) six PTE cells connected in series.

This progressive reduction in voltage output is primarily attributed to engineering factors, including electrical contact losses, thermal coupling between adjacent cells, and slight reductions in the effective temperature gradient due to the chessboard configuration. These effects become more pronounced as the number of cells increases, leading to increased thermal and electrical crosstalk within the system.

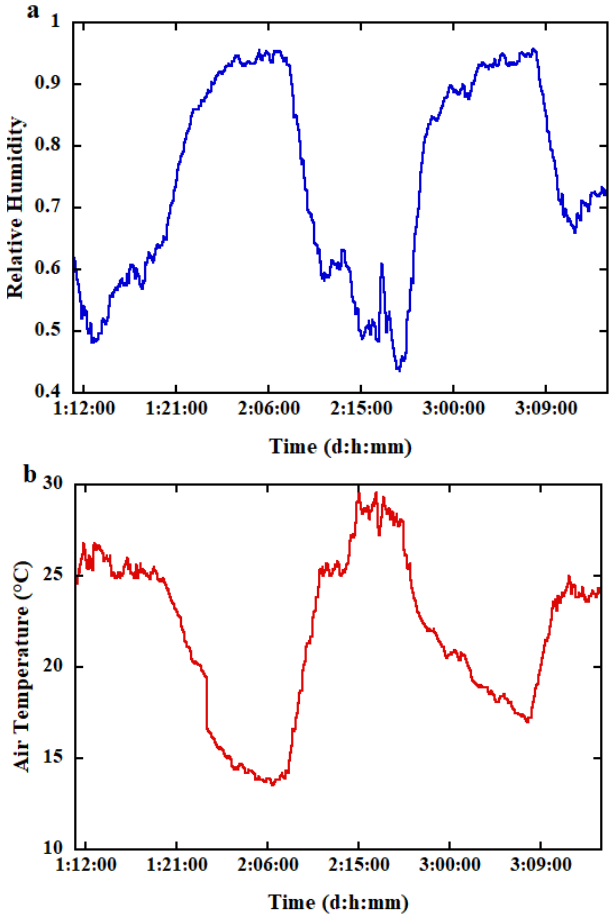
From a design perspective, these limitations can be mitigated through optimized system architecture. One practical approach involves the use of smaller sub-arrays of PTE cells connected to a centralized energy harvesting unit, thereby reducing cumulative losses while preserving modularity and scalability. Based on the present results, the two-cell configuration provides the most favorable balance between voltage output, thermal

gradient preservation, and system simplicity. Consequently, this configuration was selected for subsequent outdoor performance evaluation.

Overall, these findings demonstrate that PTE cement-based systems exhibit strong potential for scalable energy harvesting applications, provided that appropriate design strategies are implemented to manage inter-cell interactions and maintain effective thermal gradients.

6.2.6. Outdoor Measurements (connected samples)

The performance of the developed PTE cell under real-world conditions was evaluated through outdoor field testing. During the measurements, key environmental parameters, including relative humidity (RH), solar irradiance, ambient temperature, and wind conditions, were continuously monitored to assess their influence on thermoelectric performance (Figure 6.8). The experiments were conducted over three predominantly sunny days, with short periods of partial cloud coverage. A gentle breeze was present throughout the measurements, with a maximum wind speed of approximately 3 m/s and gusts reaching up to 5.5 m/s.



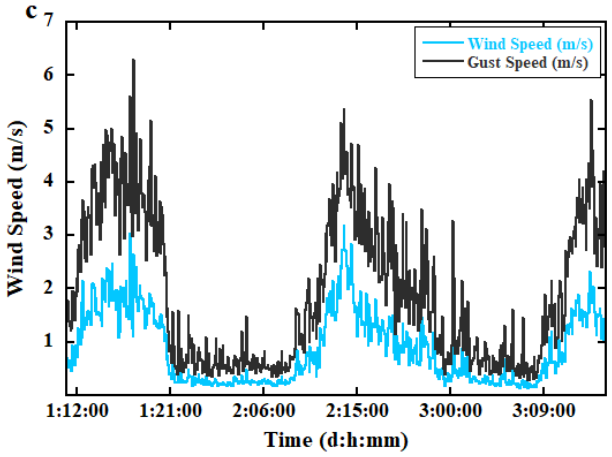


Figure 6.8 (a) relative humidity, (b) air temperature, and (c) wind and gust speed during outdoor measurement.

On the first day of testing, the ambient temperature during solar exposure was approximately 25 °C, while RH varied between 50% and 60%. The measurement began at 11:00 AM, with an initial solar irradiance of 590 W m^{-2}, which increased to approximately 830 W m^{-2} by 14:00. Despite this relatively high irradiation level and a measured temperature gradient of approximately 7 K, the thermoelectric voltage remained low and unstable, fluctuating between −1 mV and −2 mV (Figure 6.9). This limited response is attributed to the prior drying of the samples, which reduced the available water content within the pore network and suppressed ionic transport without having time for reabsorbing humidity before the test.

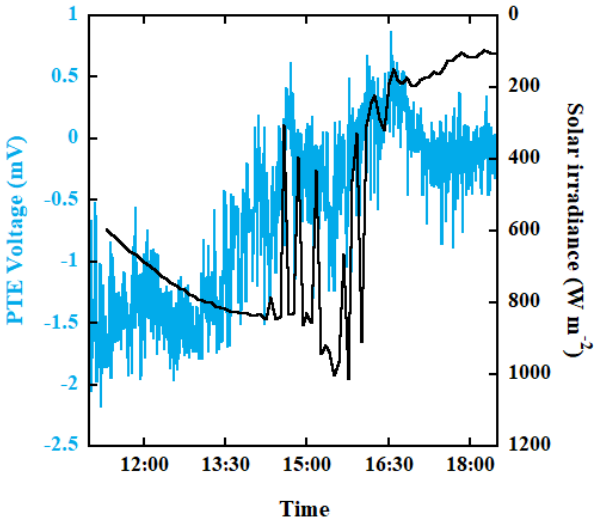


Figure 6.9 The PTE voltage generated under solar radiation on the first day of outdoor measurement

Following this initial test, RH increased significantly overnight, reaching values above 90–95%, which enabled moisture reabsorption by the samples. On the second day, the thermoelectric response was markedly enhanced. The PTE activity began at a solar irradiance of approximately 325–380 W m^{-2}, with an ambient temperature of 25 °C. As the solar irradiance increased, the temperature rose to approximately 29 °C during the measurement period, while RH remained between 50% and 60% during the day and again increased in the afternoon.

The voltage profile began to shift toward negative values at approximately 9:50 AM, corresponding to a solar irradiance of ~380 W m^{-2} and the establishment of a small temperature gradient (~1 K) (Figure 6.10 a and b). As the irradiation increased, the thermoelectric response intensified, reaching a peak voltage of −52 mV at approximately 700 W m^{-2} with a temperature gradient of 5.5 K around midday. The voltage remained relatively stable for an extended period of approximately seven hours under sustained solar exposure, with minor oscillations associated with transient cloud coverage.

On the third day (Figure 6.10c), a similar correlation between solar irradiance and thermoelectric voltage was observed, confirming the repeatability and cyclability of the PTE response. However, the lower peak solar irradiance on this day resulted in a reduced voltage output, further demonstrating the sensitivity of the system to environmental conditions.

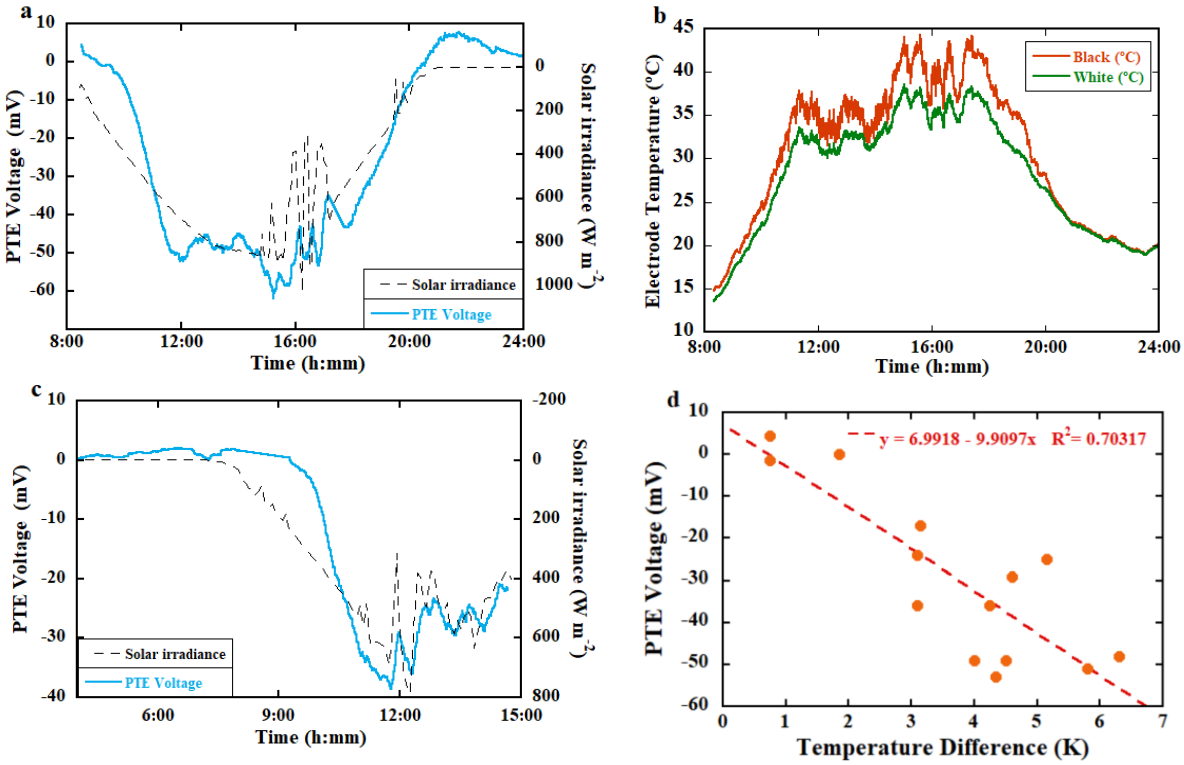


Figure 6.10 (a) PTE voltage and solar irradiance during the second day of measurement. (b) Temperature induced in each electrode. (c) PTE voltage and solar irradiance during the third day of measurement. (d) PTE voltage vs. temperature difference and fit to the data for extraction of the Seebeck coefficient

It is important to emphasize the critical role of relative humidity in governing the thermoelectric performance. Monitoring RH is essential for two main reasons. First, elevated RH facilitates moisture absorption within the cementitious matrix, particularly after drying or prolonged operation, thereby restoring ionic transport pathways. Second, it has been reported that the energy conversion efficiency of ionic thermoelectric materials is strongly influenced by ambient humidity levels [110]. In the present study, the increase in RH during nighttime was essential for reactivating the thermoelectric response of the system.

A comparison between indoor and outdoor measurements reveals significant differences in system behavior. Under controlled laboratory conditions, where RH, irradiation, and

airflow are fixed, the thermoelectric response exhibits a rapid voltage peak within approximately 30 min, followed by a gradual decay (Figure 6.3a). In contrast, under outdoor conditions, the voltage develops more gradually but reaches substantially higher values and remains stable for extended durations. Notably, the peak voltage measured outdoors was approximately 3.7 times higher than that obtained under equivalent artificial irradiation.

To explain this difference, a detailed temperature analysis was conducted. Under laboratory conditions, the sample temperature reached approximately 63 °C under similar irradiation power, which is about 30 °C higher than that observed during outdoor testing. Since thermoelectric behavior in these systems is governed by the relative contributions of ionic species, this difference in absolute temperature is critical. At higher temperatures, anion migration becomes more dominant, partially counteracting the cation-driven voltage as described in Section 2.3 of this Chapter. In contrast, the lower temperatures encountered outdoors suppress anion activation, thereby prolonging cation-dominated transport and enhancing the magnitude and stability of the negative voltage peak.

Figure 6.4d presents the voltage response of two PTE cells connected in series over two days of outdoor operation. The slope of the linear fit corresponds to a Seebeck coefficient of 9.910 mV K^{-1}, with an average value of 4.955 mV K^{-1} per cell, representing one of the highest values reported for cement-based thermoelectric materials. It should be noted that, unlike electronic thermoelectric systems, ionic thermoelectric materials exhibit a time delay between the establishment of a temperature gradient and the development of thermoelectric voltage [110]. Furthermore, fluctuations in environmental conditions, including solar irradiance, wind, and cloud coverage, introduce deviations from ideal linear behavior, resulting in an approximate determination of the Seebeck coefficient.

Overall, these results demonstrate that the proposed PTE system can operate effectively under real environmental conditions. The combination of moisture-driven rechargeability, stable voltage output under solar irradiation, and sensitivity to naturally occurring climatic variations highlights the strong potential of cement-based PTE materials for applications such as self-powered sensing and energy harvesting in smart infrastructure.

6.2.7. PTE Cells for Solar Energy Harvesting

6.2.7.1 Energy Conversion Principles and Performance Metrics

The evaluation of open-circuit voltage and Seebeck coefficient provides important insight into the thermoelectric potential of ionic thermoelectric (iTE) materials. However, these parameters alone are insufficient to fully describe their practical performance. Under an applied temperature gradient, ionic species accumulate at the electrode interfaces, generating an internal electric field. As a result, these systems operate analogously to ionic thermoelectric capacitors (iTECs), as illustrated in Figure 6.11.

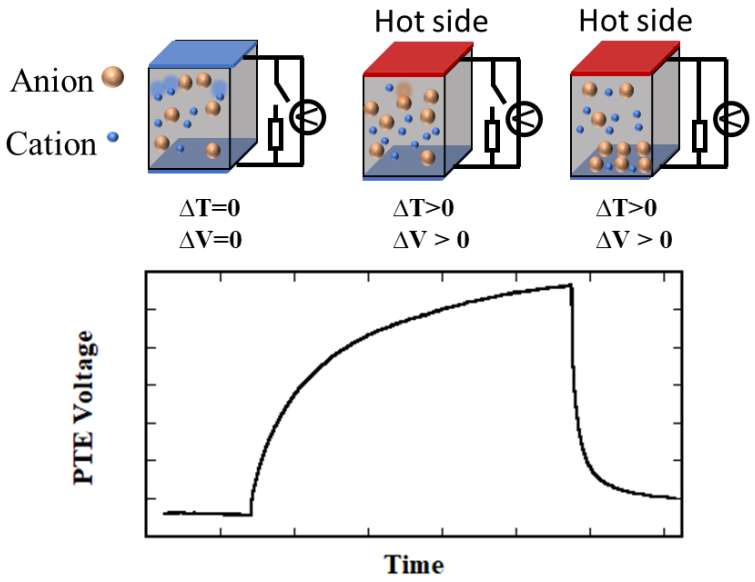


Figure 6.11 Working principle of an iTEC in the charging stage

When an external load is connected, electronic charge carriers flow through the circuit to compensate for the accumulated ionic charges. Since ions cannot traverse the external circuit, this leads to a reduction in the measured voltage under load conditions. Consequently, evaluating the power output becomes essential for assessing the energy conversion efficiency of the system.

The instantaneous power, P(t), dissipated across a resistive load is defined as:

$$P(t) = \frac{V(t)^2}{R} \quad \textit{Equation 6.1}$$

$$E = \int_0^T \frac{V(t)^2}{R} dt \quad \textit{Equation 6.2}$$

where V(t) is the time-dependent voltage, and R is the external resistance. The total harvested energy, E, is obtained by integrating the power over time (Equation 6.2)

These parameters provide a more comprehensive measure of performance, particularly for applications such as self-powered sensing and distributed energy harvesting systems.

6.2.7.2 Power Output and Internal Resistance Limitations

The voltage output of the PTE cell was measured under an irradiation intensity of 850 W m^{-2} while connected to external loads ranging from 72 kΩ to 2.7 MΩ (Figure 6.12). As expected, the maximum power output occurs when the external load matches the internal resistance of the system. In the present case, the highest power output was obtained at a load of 2.7 MΩ, corresponding to the total internal resistance, including both material and contact contributions.

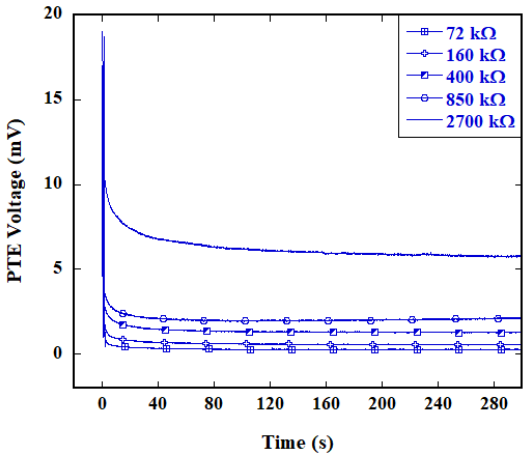


Figure 6.12 The voltage output of the as-produced sample connected to different external loads

Despite this optimal matching condition, the high internal resistance significantly limits the energy harvesting capability, resulting in a total energy output of only 2.81 μJ m^{-2} over a period of five minutes under constant irradiation.

The resistance of the PTE cell can be described by:

$$R = \frac{L}{\sigma A} \quad \textit{Equation 6.3}$$

where L is the distance between electrodes, A is the cross-sectional area, and σ is the electrical conductivity. It is important to note that the total internal resistance is the sum of the intrinsic material resistance and the contact resistance at the electrode interfaces, making electrode quality a critical factor.

Impedance spectroscopy analysis (Figure 6.13) reveals two distinct semicircles in the Nyquist plot: a depressed high-frequency arc associated with bulk material response, and a low-frequency arc attributed to electrode effects [111–114]. The intersection point between these arcs provides an estimate of the resistance of the material and contacts, highlighting the significant contribution of interfacial resistance to the overall system performance [112].

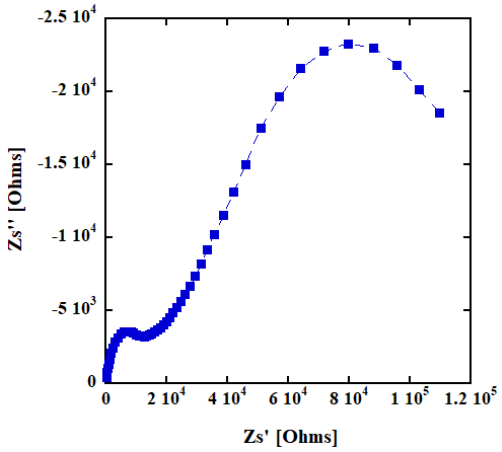


Figure 6.13 The Nyquist plot of the Geopolymer hybrid cement with 75% copper slag aggregates

6.2.7.3 Strategies for Resistance Reduction and Performance Enhancement

To overcome the limitations imposed by high internal resistance, three primary strategies were implemented to enhance energy output:

- **Sample Size Optimization:** The sample dimensions were reduced to 2 × 0.7 × 4 cm, effectively decreasing the electrode spacing and reducing resistance.
- **Contact Resistance Reduction:** Copper electrodes were replaced by soldered wires connected to silver paint electrodes, significantly improving interfacial conductivity.
- **Conductivity Enhancement:** Samples were doped with a 3.5 wt.% NaCl solution (equivalent to seawater) to increase ionic concentration within the pore network.

The combined effect of these modifications on resistance and conductivity is summarized in Table 6.3. It should be emphasized that the reported values correspond to the overall PTE cell performance, including contacts, rather than intrinsic material properties.

The as-received sample exhibited a high resistance of approximately 2.7 MΩ. Reducing the sample size resulted in a substantial decrease in resistance, exceeding expectations based on geometric scaling alone. This behavior can be attributed to improved pore connectivity and the formation of more efficient ionic transport pathways in smaller samples.

Table 6-3 The total resistance and the electrical conductivity of different PTE cells for solar energy harvesting

Sample Name	Sample Size (cm)	Electrode	Pretreatment after drying	Resistance (kΩ)	Conductivity (S m^{-1})
BWB1	2×0.7×8	Copper tape	RH 75%	2760.32	$2.07*10^{-4}$
BWB2	2×0.7×8	Soldered wire	3.5 %wt. NaCl solution	7.51	$7.61*10^{-2}$
BWS1	2×0.7×4	Copper tape	RH 75%	387.20	$7.38*10^{-4}$
BWS2	2×0.7×4	Soldered wire	RH 75%	38.40	$7.14*10^{-3}$
BWS3	2×0.7×4	Soldered wire	3.5 %wt. NaCl solution	2.67	$1.07*10^{-1}$

Electrode configuration also plays a critical role. Previous studies by Cheng et al. [109] demonstrated that replacing Ag electrodes with single-walled carbon nanotubes (SWNTs) can increase harvested energy by up to a factor of 4. In the present work, replacing copper tape with silver paint reduced resistivity by approximately one order of magnitude.

Furthermore, doping with standard seawater (an aqueous 3.5 wt.% NaCl solution with a conductivity of 5 S m^{-1} at room temperature) significantly increased ionic conductivity by enhancing the availability of mobile ions within the pore structure, thereby improving the overall iTE response.

6.2.7.4 Effect of Modifications on Voltage and Energy Output

The impact of these modifications on voltage output was evaluated by connecting the PTE cells to different external loads under 850 W m^{-2} irradiation (Figure 6.14), while the corresponding energy output over the first five minutes is summarized in Table 6.4. An external resistance of 72 kΩ was selected as a reference for comparative analysis, as the tested samples exhibited internal resistances spanning from 2.6 kΩ to 2.7 MΩ. This load, therefore, provided a consistent and representative basis for comparing the voltage outputs across different configurations. Under an irradiation intensity of 850 W m^{-2}, the

voltage output of the samples increased with increasing electrical conductivity (Figure 6.14).

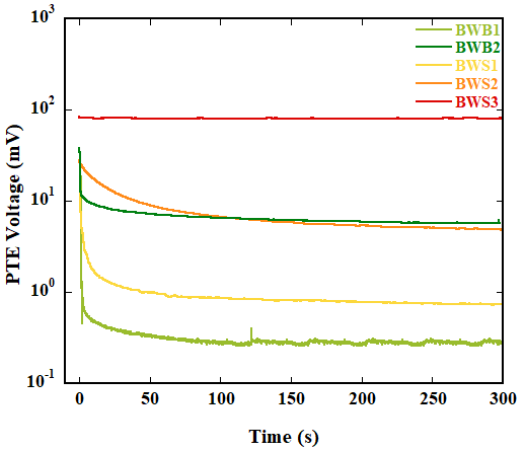


Figure 6.14 Voltage output of samples prepared based on different strategies (Table 6.3) connected to a 72 kΩ external load.

Doping the as-received sample with seawater resulted in a 4.5-fold increase in Seebeck voltage (Figure 6.15a), which is attributed to the increased ion concentration within the pore network [15].

Reducing the sample size further enhanced performance by significantly lowering internal resistance. Notably, the BWS1 sample maintained the temperature gradient despite reduced dimensions, although the absolute temperature decreased slightly, resulting in an overall increase in voltage output (Figure 6.15b).

Modification of the electrode configuration (BWS2) increased the time constant of the PTE cell, thereby improving its energy harvesting capability (Figure 6.15c). This behavior is consistent with previous observations [109], where electrode materials with higher effective surface area enhanced charge transfer dynamics.

The fully optimized sample (BWS3), incorporating reduced dimensions, improved electrode configuration, and seawater doping, exhibited a substantial increase in both Seebeck voltage and energy output (see Figure 6.15d and Table 6.4). Although intrinsic voltage was present due to the high ionic concentration, it remained stable over extended periods (exceeding 12 h), with a steady value of approximately 22 mV. During the first five minutes, the voltage remained stable at approximately 80 mV when connected to an external load, indicating that the improved conductivity effectively mitigates voltage drop under load conditions. Similar behavior has been reported in perylene bisimide-based iTE systems [115].

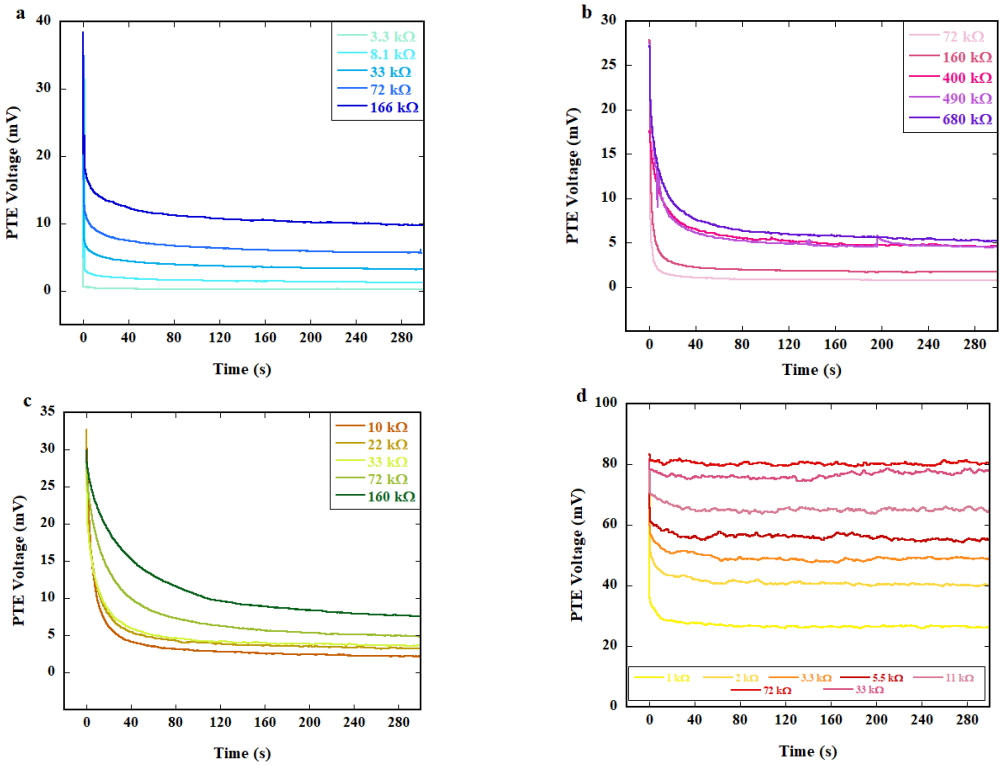


Figure 6.15 The voltage output of the samples connected to different external loads under 850 W m^{-2} lamp irradiation, after different modifications of (a) BWB2 as-received sample, doped with seawater, (b) BWS1 as-received sample, reduced size, (c) BWS2 sample with reduced size and Ag electrodes, (d) BWS3 sample after decreasing the size utilizing Ag electrodes and doping with standard seawater

Table 6-4 Areal dissipated/harvested energy over different external loads for different sample modifications

BWB1		BWB2		BWS1		BWS2		BWS3	
R (kΩ)	Energy (μJ m^{-2})	R (kΩ)	Energy (μJ m^{-2})	R (kΩ)	Energy (μJ m^{-2})	R (kΩ)	Energy (μJ m^{-2})	R (kΩ)	Energy (μJ m^{-2})
72	0.65	3.3	250.03	72	14.78	10	689.94	1	270478.10
160	0.49	8.1	137.65	160	15.28	22	474.56	2	316985.70
400	0.99	33	96.91	400	32.08	33	355.09	3.3	273841.30
850	0.99	72	122.30	490	21.58	72	343.68	33	66730.97
2700	2.81	160	146.91	680	26.99	160	304.23	72	33575.91

6.2.7.5 Scalability and Practical Implications

Figure 6.16a and b present the maximum power and the corresponding area-normalized harvested energy for each sample during a five-minute connection to the optimal external load, where the load resistance was selected to match the internal resistance of each PTE cell.

Reducing the electrode distance resulted in an 86% decrease in internal resistance, leading to a 23.4-fold increase in energy generation per unit area (Figure 6.16b). A comparison between BWS1 and BWS2 indicates that the use of silver paint electrodes enhanced the harvested energy by up to 56-fold. Furthermore, immersing the samples in a NaCl solution increased both electrical conductivity and voltage output, resulting in a higher Seebeck coefficient.

The fully optimized BWS3 sample exhibited outstanding performance, generating 33,575 μJ m^{-2}, which corresponds to an enhancement of 5.1 × 10^4 compared to the unoptimized

configuration (Figure 6.16b). To evaluate performance stability, BWS3 was connected to a 3.3 kΩ load for a duration of one hour. As shown in Figure 6.16c, the voltage output exhibited a controlled decay over time but remained substantial, reaching 25.3 mV after one hour, corresponding to a total harvested energy of 1.81×10^6 μJ m^{-2}.

The implemented optimizations substantially enhanced the energy harvesting capability of the PTE cells, establishing them as strong candidates for ionic thermoelectric capacitors (iTECs) in practical heat-to-electricity conversion applications. Compared to some of the best iTE materials in the state-of-the-art (Figure 6.16d), the cement-based PTE system achieves comparable performance while maintaining key advantages such as low cost, wide availability, and ease of processing.

In contrast, many existing iTE systems rely on ionogels, ionic liquids, graphene oxide, or specialized polymers (e.g., PVDF-HFP, PBI), which involve high material costs, complex processing conditions, and limited scalability. These materials often require expensive precursors, organic solvents, and noble metal electrodes, leading to costs on the order of hundreds of dollars per square meter. In comparison, the cement-based system developed in this study can be produced at a material cost well below $1 per m^2, showing its potential for ultra-low-cost, large-area applications.

Overall, this combination of competitive performance, low cost, and scalability positions cement-based PTE systems as promising candidates for large-area, low-grade heat energy harvesting applications, where affordability and deployability are critical.

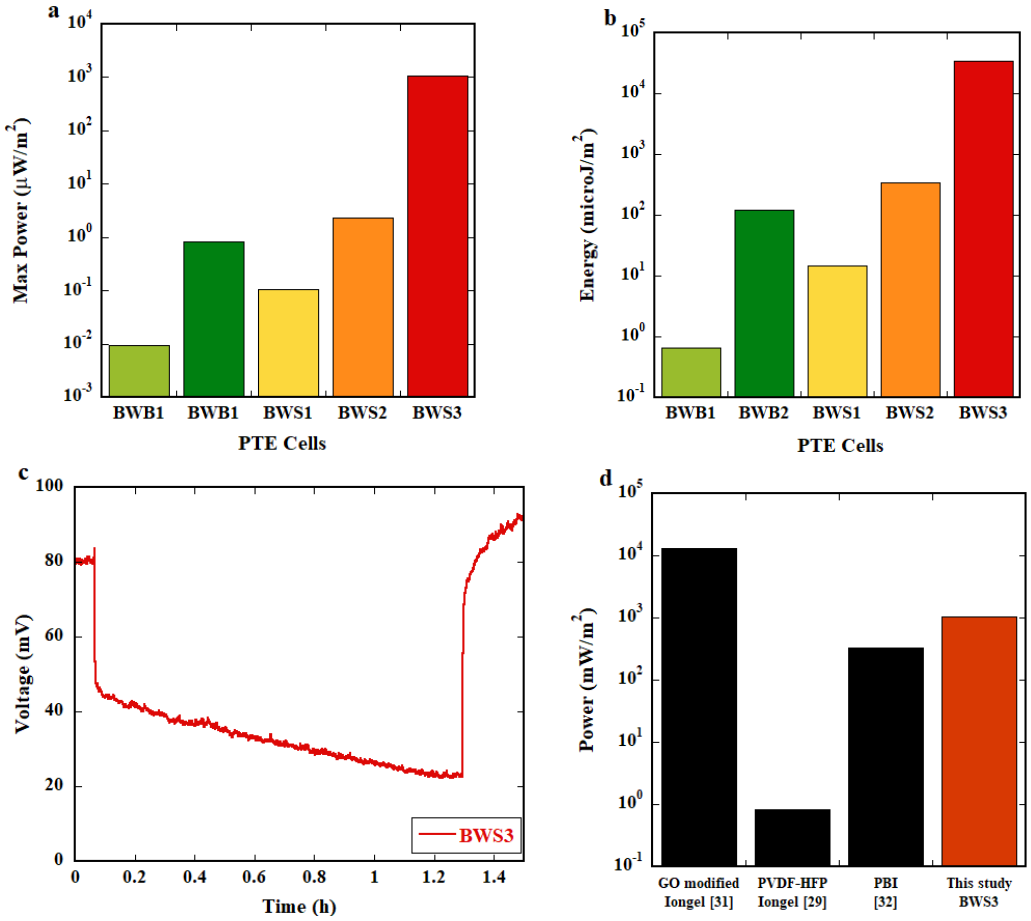


Figure 6.16 (a) Maximum power obtained for the different samples. (b) Energy harvested over a period of 5 minutes for each sample connected to a 72 kΩ external load. (c) Voltage profile of the BWS3 sample connected

to a 3.3 kΩ load for more than 1 h. (d) The comparison of the max power of the cement-based PTE cell with the state-of-the-art PTE materials [109,115,116].

6.3. Conclusion

This chapter demonstrates the potential of photothermoelectric (PTE) cementitious systems as a viable approach for sustainable energy conversion, building upon the mechanistic understanding of ionic thermoelectric behavior established in the previous chapters. By leveraging the distinct optical properties of different cement-based materials, a novel design strategy was developed in which alternating high-absorbance and high-reflectance segments are arranged in a chessboard configuration to generate controlled lateral temperature gradients. This approach effectively overcomes the limitations associated with conventional vertical-gradient systems and significantly enhances energy conversion performance.

The measured Seebeck coefficient of 9.9 mV K^{-1} for two series-connected PTE cells in a real-world setting confirms the effectiveness of this design and highlights the suitability of cement-based materials for low-temperature energy harvesting applications. Furthermore, the demonstrated rechargeability and cyclability under real environmental conditions, enabled by the intrinsic moisture reabsorption capability of cement, underline the robustness and practical relevance of the system.

In addition, several engineering strategies were implemented to optimize the energy output, including the reduction of internal resistance, improvement of electrode contacts, and enhancement of ionic conductivity. These modifications resulted in a substantial increase in performance, achieving energy harvesting values of up to 1.81×10^6 μJ m^{-2} over one hour, which are competitive with state-of-the-art PTE materials.

Importantly, the use of industrial cement as the primary material offers a distinct advantage in terms of cost, availability, and scalability. As one of the most widely used construction materials worldwide, cement provides a unique platform for integrating energy harvesting functionality directly into infrastructure.

Overall, the findings of this chapter establish a clear pathway from fundamental ionic thermoelectric mechanisms to practical device implementation, demonstrating that cement-based PTE systems can serve as efficient, durable, and scalable solutions for ambient energy harvesting in the built environment.

Chapter VII

Interplay of Ionic Transport and Environmental Conditions in Cement-Based Photo-Thermoelectric Materials

Building upon the fundamental understanding of ionic thermoelectric (iTE) mechanisms established in the previous chapters, ranging from pore-scale ion transport in cementitious matrices to device-level optimization of photothermoelectric (PTE) cells, this chapter shifts the focus from material design toward environmental functionality. While earlier results demonstrated that cement-based systems can achieve high Seebeck coefficients and effective energy harvesting through tailored composition and architecture, they also revealed a critical limitation: the strong sensitivity of ionic transport to external conditions, particularly temperature and moisture. This sensitivity, although often considered a drawback, can instead be interpreted as an opportunity to develop climate-responsive energy systems, in which performance is inherently coupled to environmental stimuli.

In cement-based PTE materials, the thermoelectric response originates from the thermally driven migration of ions within a water-mediated pore network. As a result, parameters such as temperature and relative humidity (RH) do not merely influence performance in a secondary manner, but directly govern the availability, mobility, and continuity of ionic charge carriers. Previous chapters have shown that temperature controls the activation of ion transport, while moisture content determines the connectivity of conductive pathways and the stability of the generated voltage. Furthermore, discrepancies observed between controlled laboratory measurements and outdoor experiments highlighted that real-world performance cannot be accurately predicted without explicitly accounting for environmental dynamics.

Motivated by these observations, the present chapter aims to systematically investigate the influence of environmental parameters on the PTE performance of cement-based systems, with a particular focus on temperature and relative humidity under controlled conditions. The approach adopted here is based on isolating and quantifying the individual and coupled effects of these parameters through static experiments, complemented by simulated summer climatic conditions representative of real operating environments. Although a full seasonal analysis is beyond the scope of the current stage, the inclusion of summer profiles enables a first-order assessment of system behavior under realistic and energetically relevant conditions, where solar irradiation and ambient temperatures are at their peak.

In this context, the experimental framework follows the use of a programmable climatic chamber to impose controlled temperature and humidity conditions while monitoring the time-dependent PTE response. Static measurements are used to decouple the roles of thermal activation and moisture availability, while simulated summer conditions provide insight into the coupled and time-dependent behavior of the system under realistic

environmental variations. Particular attention is given to the role of humidity not only during operation but also during preconditioning stages, reflecting the importance of environmental history and moisture cycling in governing ionic transport.

Through this combined analysis, this chapter aims to bridge the gap between intrinsic material behavior and real-world performance, advancing the understanding of cement-based PTE systems as environmentally adaptive energy materials. The results provide critical insights into the conditions required for optimal operation and establish design guidelines for the deployment of these systems in different climatic scenarios.

7.1. Experimental

7.1.1. Materials and Sample Preparation

The cement-based photothermoelectric (PTE) samples employed in this study were prepared using the same materials and processing protocol described in Chapter VI, ensuring consistency with the previously developed system. Briefly, the base matrix consisted of an industrial geopolymer hybrid cement (GHC) comprising 90 wt.% geopolymer and 10 wt.% ordinary Portland cement. The high-absorbance ("black") segment was produced by incorporating 75 wt.% copper slag aggregate into the GHC, while the low-absorbance ("white") segment was fabricated using commercial white cement.

To maintain reproducibility, the same standardized mixing procedure was adopted, involving initial dry homogenization of the constituents followed by the addition of distilled water at a constant water-to-cement ratio of 0.6. In contrast to the configuration used in Chapter VI, the samples in this study were cast into silicone molds with dimensions of 4 × 2 × 0.7 cm, with each segment occupying half of the specimen (2 × 2 × 0.7 cm). A temporary barrier was inserted during casting to separate the two sections and removed after a short period to ensure continuity of the pore solution across the interface. The samples were demoulded after 24 h and subsequently cured in distilled water for 28 days.

Before testing, all samples underwent the same preconditioning protocol described previously, consisting of drying at 50 °C followed by equilibration under controlled relative humidity conditions, in order to minimize variability associated with microstructural inhomogeneities and moisture distribution.

The chemical composition of the raw materials (GHC, copper slag, and white cement) was determined by X-ray fluorescence (XRF), and the corresponding results are reported in Table 6.1 (see Chapter VI).

7.1.2. Material Characterization

A combination of controlled environmental testing and device-level measurements was employed to systematically investigate the coupled influence of temperature, relative humidity, and environmental dynamics on the photothermoelectric (PTE) performance of cement-based systems. Experiments were conducted using a programmable climatic chamber with independent control of temperature, relative humidity, and solar irradiation, enabling precise replication of both steady-state and time-dependent conditions. Detailed

descriptions of the experimental setup and measurement procedures are provided in Chapter II; therefore, the present chapter focuses on the analysis and interpretation of the results.

7.2. Results and Discussion

7.2.1. Effect of Environmental Parameters on the PTE Response (static condition)

To clarify the influence of environmental conditions on the photothermoelectric (PTE) response of cement-based systems, a systematic study was carried out under controlled static conditions. Particular emphasis was placed on the combined effect of temperature and relative humidity, as these parameters directly regulate ionic transport within the pore solution and, consequently, the mechanism of voltage generation.

7.2.1.1 The Effect of Temperature and Relative Humidity During PTE Working Time

To investigate the influence of environmental conditions, the photothermoelectric (PTE) response of the samples was evaluated under constant light irradiation of 900 W m^{-2} at different ambient temperatures (10 °C, 25 °C, and 40 °C) and relative humidity levels (30%, 60%, and 90%) during PTE operation (Figure 7.1).

Under light illumination, all samples exhibited a similar voltage evolution, characterized by a rapid pre-minimum drop followed by a slower post-minimum recovery. This behavior originates from the opposing migration of cations and anions within the pore solution under the applied thermal gradient as described in the previous chapters. At early times, cation transport dominates due to their generally higher mobility in cementitious porous networks. As the system temperature increases, OH^- ions progressively acquire sufficient thermal energy to overcome their activation barrier, leading to the observed shift toward more positive voltage values during the second stage.

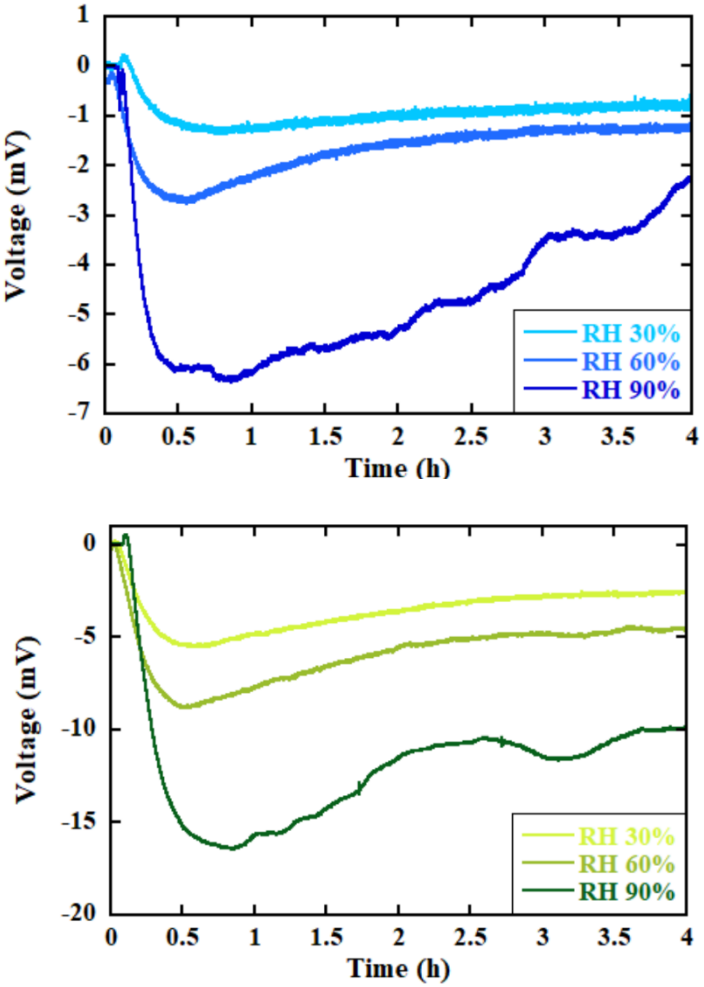
At 10 °C (Figure 7.1.a), the generated voltage reached relatively low negative values, with minimum responses ranging from approximately −1 mV at 30% RH to −6 mV at 90% RH. Increasing relative humidity consistently enhanced the magnitude of the PTE response, indicating that moisture facilitates charge transport by improving ionic conductivity within the cement matrix. Nevertheless, even at high humidity, the overall voltage levels remained limited compared to those obtained at higher temperatures.

At 25 °C (Figure 7.1.b), the absolute voltage values increased compared to 10 °C, with minima ranging from approximately −5 mV (30% RH) to −15 mV (90% RH). As in the lower temperature case, increasing RH amplified the PTE response, although the influence of humidity became more pronounced at this intermediate temperature. The combination of enhanced thermal activation and improved ionic connectivity due to absorbed moisture resulted in more efficient charge carrier separation. This distinction highlights the different roles of the governing parameters: relative humidity primarily determines the availability and continuity of the ionic transport medium, whereas temperature controls the thermally activated mobility of the charge carriers within that medium. The observed behavior therefore reflects a coupled mechanism in which

moisture defines the transport pathways, while temperature governs the rate of ion migration along these pathways.

At 40 °C (Figure 7.1.c), the PTE response reached its highest magnitude, with minimum voltages ranging from approximately −10 mV (30% RH) to −30 mV (90% RH). The same trend of increasing voltage with increasing RH was observed; however, the influence of temperature was dominant, as the higher thermal energy significantly intensified the photo-induced thermoelectric effect.

These results further indicate that relative humidity does not simply slowly enhance ionic conductivity but instead governs the continuity of the pore solution network. Under low RH conditions, partial disconnection of aqueous pathways likely occurs, leading to reduced voltage output and increased internal resistance. In contrast, higher RH ensures continuous ionic pathways and a more stable thermoelectric response.



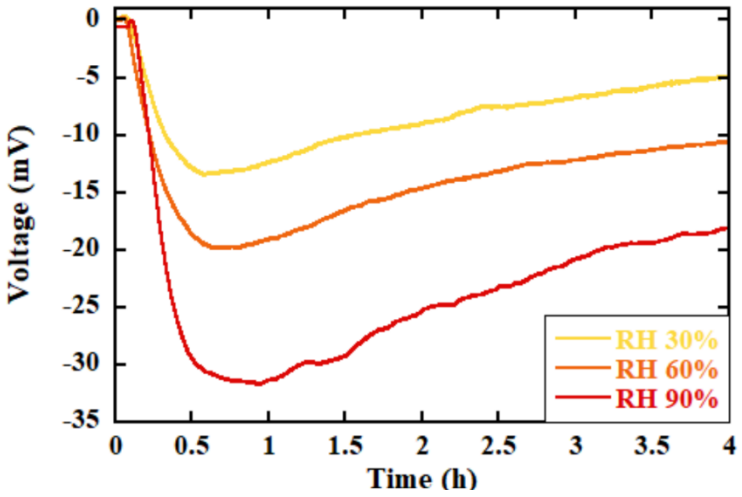


Figure 7.1 The PTE voltage response of the sample under different RH and temperatures, (a) 10 ºC, (b) 25 ºC, (c) 40 ºC

A quantitative comparison of the absolute maximum voltages obtained from these measurements (Figure 7.2) further emphasizes the synergistic interaction between temperature and relative humidity. At all investigated temperatures, $|V|_{max}$ increases monotonically with RH, confirming that moisture availability enhances ionic conduction. However, the rate of this increase becomes significantly more pronounced with temperature: the voltage rise between 60% and 90% RH is relatively small at 10 °C (≈2–3 mV), more evident at 25 °C (≈8 mV), and markedly stronger at 40 °C (≈12 mV). This non-linear amplification demonstrates that the influence of RH is not independent but strongly coupled with thermal activation. While RH governs the continuity of the pore solution network, temperature controls how effectively these pathways are utilized. As a result, high humidity alone does not lead to high performance at low temperatures, and elevated temperatures cannot compensate for insufficient moisture. The maximum response is therefore achieved only when both parameters are simultaneously favorable, indicating that the PTE behavior is governed by a synergistic coupling between ionic pathway availability and thermally activated ion mobility.

The initial voltage rate (dV/dt) in the pre-minimum stage becomes more negative with increasing temperature and RH. This regime is dominated by cationic thermodiffusion, whose mobility and transference increase as temperature activates transport and higher RH enhances ionic conductivity and establishes continuous aqueous pathways. The steepness of the initial voltage drop is therefore governed by the ease of ionic motion under the thermal gradient and scales with both ionic conductivity, which increases with RH and temperature ($\sigma \propto (RH, T)$), and the thermodiffusive mobility of ions, which follows an Arrhenius-type dependence on temperature ($\propto \exp(-E_a,cat/RT)$). This explains the steeper voltage drops observed at higher RH and temperature. In contrast, the time required to reach the voltage minimum (0.4–0.7 h) remains nearly constant across all conditions, indicating that this transition is primarily governed by thermal equilibration and the interfacial RC time constant of the system. This suggests the existence of an intrinsic system-level timescale associated with thermal gradient establishment and electrode double-layer formation, rather than bulk ionic transport alone.

Following the voltage minimum, the recovery slope (dV/dt) increases with RH at a given temperature, reflecting facilitated ionic transport in more hydrated pore networks. However, as temperature increases, the relative influence of RH diminishes. Although higher humidity continues to enhance conductivity, thermally activated mobility of both cations and anions becomes dominant, reducing differences in recovery slopes among RH conditions. This trend indicates that humidity primarily governs recovery kinetics at low to moderate temperatures, whereas temperature becomes the dominant factor at higher conditions. This transition also suggests an evolution in the dominant transport mechanism during operation: the early-stage response is controlled by ion availability and pathway connectivity (RH-dependent), while later stages are governed by thermally activated diffusion processes.

The observed PTE behavior further indicates that anion (OH^-) thermodiffusion is most likely associated with a higher activation energy ($E_a,OH^- > E_a,cat$) as described in earlier chapters. Consequently, although the anionic flux increases with temperature, within the investigated range (10–40 °C) it does not exceed the cationic contribution, and the voltage remains negative over the 4 h measurement period.

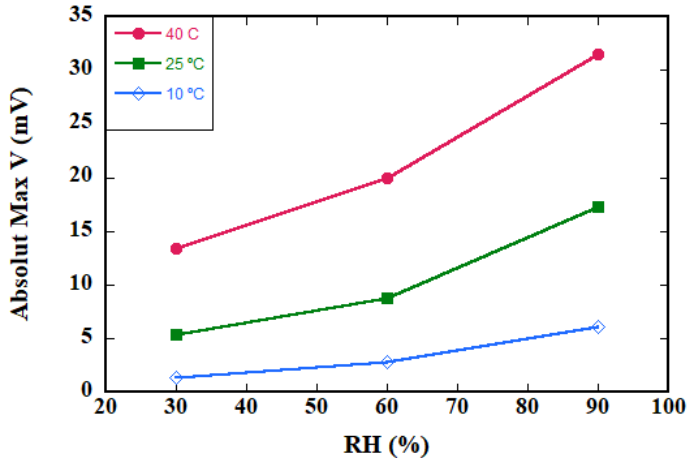


Figure 7.2 Absolute maximum voltage (|V|max) vs. relative humidity at 10, 25, and 40 °C under 900 W m^{-2} irradiation.

Overall, these results demonstrate that temperature and relative humidity are intrinsically coupled through their control over ionic transport. While temperature enhances ion mobility, its effect can only be fully realized when sufficient moisture is present to maintain continuous conductive pathways. This coupling explains why elevated temperature alone cannot compensate for severe drying conditions, a behavior that should be taken into account in real-world applications.

7.2.1.2 Influence of Night-Time Relative Humidity

To further examine the influence of environmental history, the effect of night-time relative humidity on the subsequent PTE response was systematically investigated. The samples were preconditioned overnight at RH levels of 10%, 30%, 60%, and 90% at 25 °C, followed by testing under identical conditions of 25 °C, 60% RH, and 900 W m^{-2} irradiation for 4 h. Before preconditioning, all samples were dried to eliminate residual moisture. This approach builds upon the findings of Chapter VI, in which the same PTE system exhibited a rechargeable response after drying, where storage at 50% RH for 8 h

was sufficient to restore the original voltage output under subsequent illumination. These observations demonstrate that night-time humidity can effectively rehydrate the cementitious matrix and recover the ionic transport pathways responsible for PTE generation. This behavior can be interpreted as a form of environmental memory, where the thermoelectric response is governed not only by the instantaneous operating conditions but also by the prior moisture history of the material. The ability of the system to regain its performance after exposure to moderate humidity highlights the reversible nature of ionic pathway formation within the cementitious network.

The results (Figure 7.3) clearly indicate that night-time humidity strongly influences the PTE performance on the following day. Samples stored under dry conditions (≤ 30% RH) exhibited significantly lower voltage outputs accompanied by pronounced fluctuations, reflecting unstable behavior and elevated internal resistance. These oscillations suggest that insufficient overnight rehydration prevented the full restoration of ionic pathways, resulting in partial disconnection of conduction channels and limited ion mobility. In this regime, the increased signal variability further points to dynamic instability of the ionic network, likely associated with continuous moisture loss during illumination. This leads to time-dependent variations in internal resistance, emphasizing the importance of maintaining sufficient moisture content for stable device operation. Notably, the sample conditioned at 10% RH showed the fastest voltage decay under illumination, which can be attributed to both the lack of initial water content and accelerated evaporation.

In contrast, preconditioning at 60% and 90% RH led to a substantial improvement in both the magnitude and stability of the PTE response. Under these conditions, the material reabsorbs atmospheric moisture overnight, restoring continuous ionic transport networks and recovering its thermoelectric functionality. Consistent with the rechargeable behavior reported previously, exposure to 60% RH during the night was sufficient to fully restore the original PTE performance, while conditioning at 90% RH resulted in an additional enhancement of the voltage output exceeding 100%. This increase further indicates that the system does not necessarily operate at its intrinsic maximum under standard conditions but remains strongly dependent on its hydration state. Consequently, environmental control or targeted moisture management strategies can be considered as effective approaches for optimizing performance in practical applications.

Overall, these findings demonstrate that cement-based PTE systems should be regarded as history-dependent energy materials, whose performance is governed by both instantaneous environmental conditions and prior exposure to humidity. This characteristic distinguishes them from conventional thermoelectric materials and has important implications for real-world deployment, where daily humidity cycles are expected to continuously modulate device behavior.

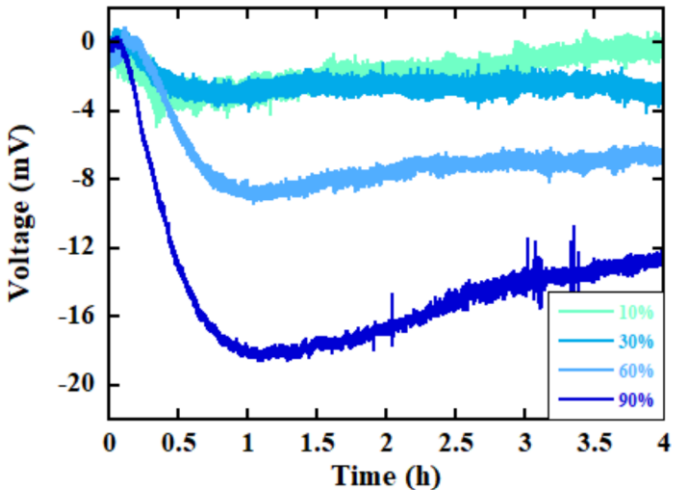


Figure 7.3 Influence of night-time RH (10%, 30%, 60%, 90%) on the subsequent PTE performance measured at 25 °C, 60% RH, and 900 W m⁻².

7.2.2. Performance Under Dynamic Climatic Conditions

To assess the photothermoelectric (PTE) performance of the cement-based ionic cell under realistic environmental conditions, dynamic experiments were carried out in a climatic chamber reproducing daily summer profiles for three representative cities with distinct thermo-hygrometric characteristics: Cairo (dry), Madrid (moderate), and Singapore (humid). These simulations were designed to reflect typical sunny-day conditions, enabling a comparative analysis of how different climatic regimes influence the PTE response.

In contrast to static experiments, these dynamic tests involve continuously changing light irradiation, temperature, and relative humidity, which induce a transient evolution of ionic transport within the material. Accordingly, the PTE behavior cannot be described solely by instantaneous environmental values. Still, it must be interpreted as the outcome of coupled, time-dependent thermal and moisture gradients developing within the cementitious matrix.

7.2.2.1 Cairo (Dry Climate)

Under simulated Cairo summer conditions, the PTE voltage was generated immediately upon light exposure (Figure 7.4). With the illumination initiated at 200 W m⁻², a voltage difference between the two sides of the sample developed rapidly. During the first hour of testing, the irradiation level was nearly constant, resulting in a stable, quasi-steady voltage output, clearly demonstrating the sensitivity of the PTE response to environmental parameters. As both irradiation intensity and temperature increased over the course of the morning, the voltage magnitude rose accordingly, reaching its maximum (negative) value at the point of highest solar irradiation (960 W m⁻²). In contrast to the static experiments, where the voltage minimum occurred after a short period under constant conditions, the dynamic test showed that the minimum coincided with the peak irradiation. This indicates that the system continuously evolves toward a new equilibrium as environmental conditions change (Figure 7.4a). This difference in voltage behavior under controlled conditions and real-world experiment was also observed in the

experiments described in Chapter VI. Such behavior reflects the inability of the system to reach a true steady state under rapidly varying conditions, emphasizing the inherently dynamic nature of ionic transport in cement-based PTE materials. The observed voltage response therefore, represents a transient balance between thermal driving forces and moisture-limited ionic mobility.

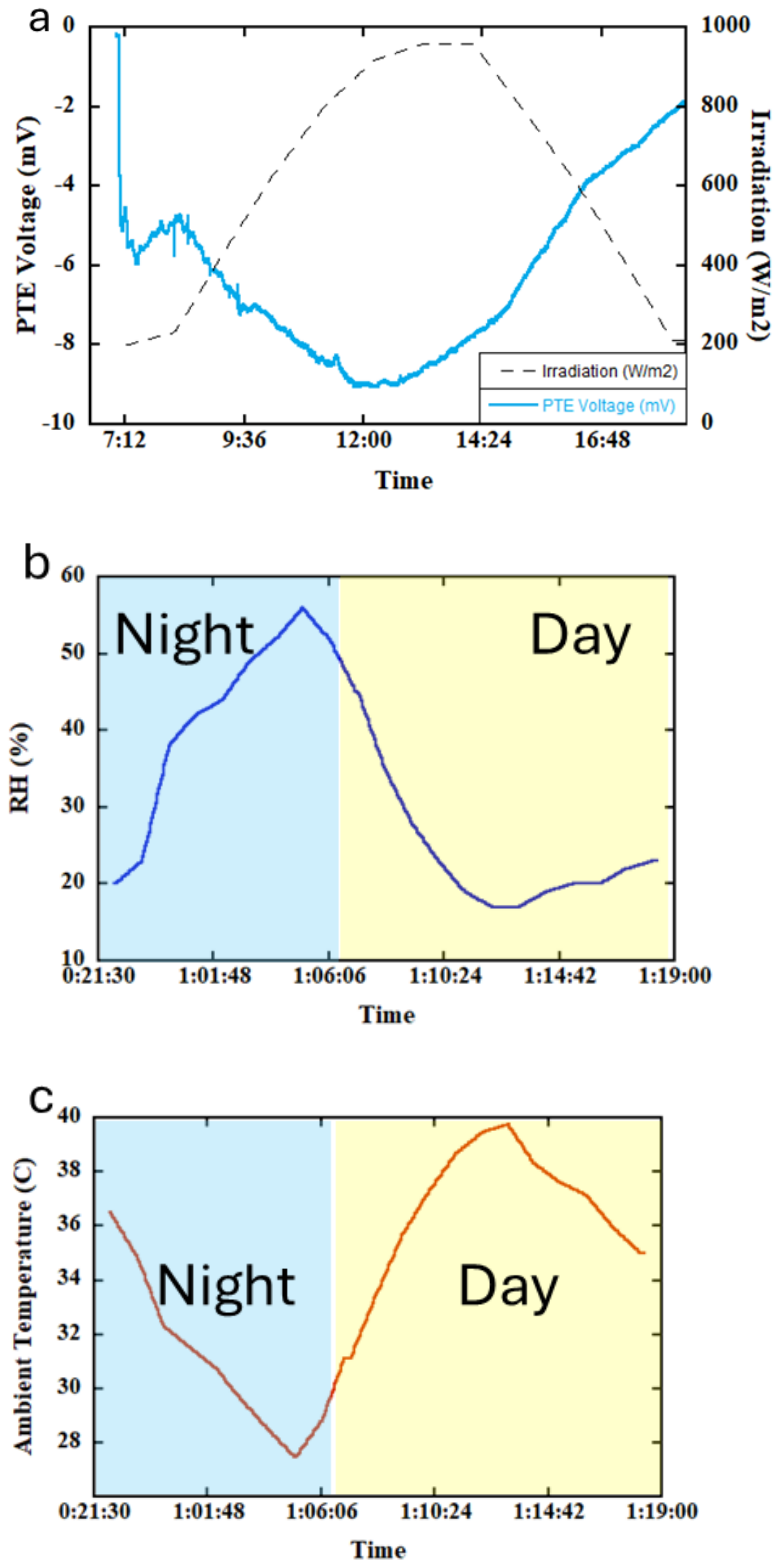
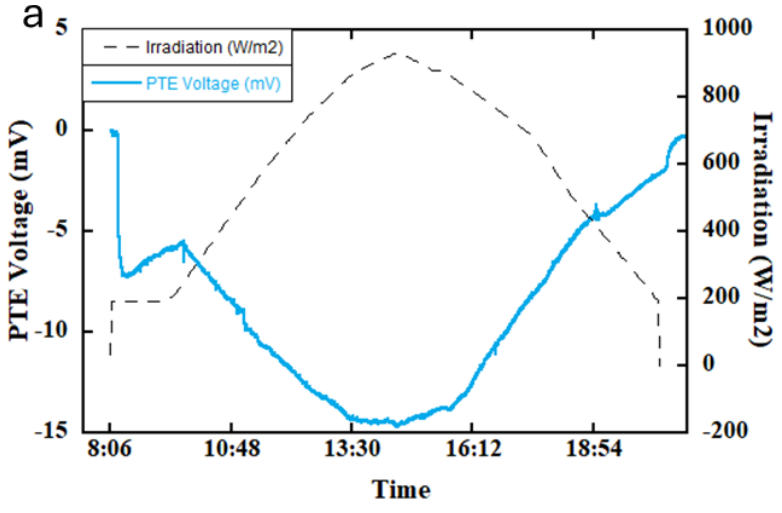


Figure 7.4 The PTE response vs solar irradiance under Cairo summer condition (X axis demonstrates local time), (b) the RH before and during the illumination, (c) the ambient temperature before and during illumination. The time format is D:hh:mm

The average night-time relative humidity was approximately 48%, decreasing to 28% during daytime conditions and reaching a minimum of 18% at peak irradiation, as shown in Figure 7.4 b. These low humidity levels would be expected to reduce PTE performance, as previously discussed under static conditions. However, the elevated daytime temperatures, averaging 35 °C and reaching a maximum of 39 °C (Figure 7.4c), together with the high irradiation intensity, effectively compensated for the reduced moisture availability. As a result, the maximum absolute voltage approached values comparable to those observed for the as-prepared sample under 60% RH and 25 °C. The peak absolute voltage reached approximately 9 mV, followed by a gradual decrease over a period of about five hours as the irradiation intensity declined.

7.2.2.2 Madrid (Moderate Climate)

A comparable trend was observed under the simulated conditions for Madrid (Figure 7.5a). Upon illumination, the cell generated a distinct PTE voltage that increased with irradiation intensity, reaching a maximum value of −14.6 mV at 960 W m^{-2}. The higher voltage compared to the Cairo case highlights the positive impact of increased humidity, despite the lower temperatures (Figure 7.5b). During the experiment, Madrid exhibited an average temperature approximately 13 °C lower than Cairo, a condition that would typically reduce ionic mobility (Figure 7.5c). However, this limitation was offset by the significantly higher relative humidity, with average night-time RH around 70% and daytime RH around 42%, which promoted more efficient ionic conduction and enhanced moisture retention within the material.



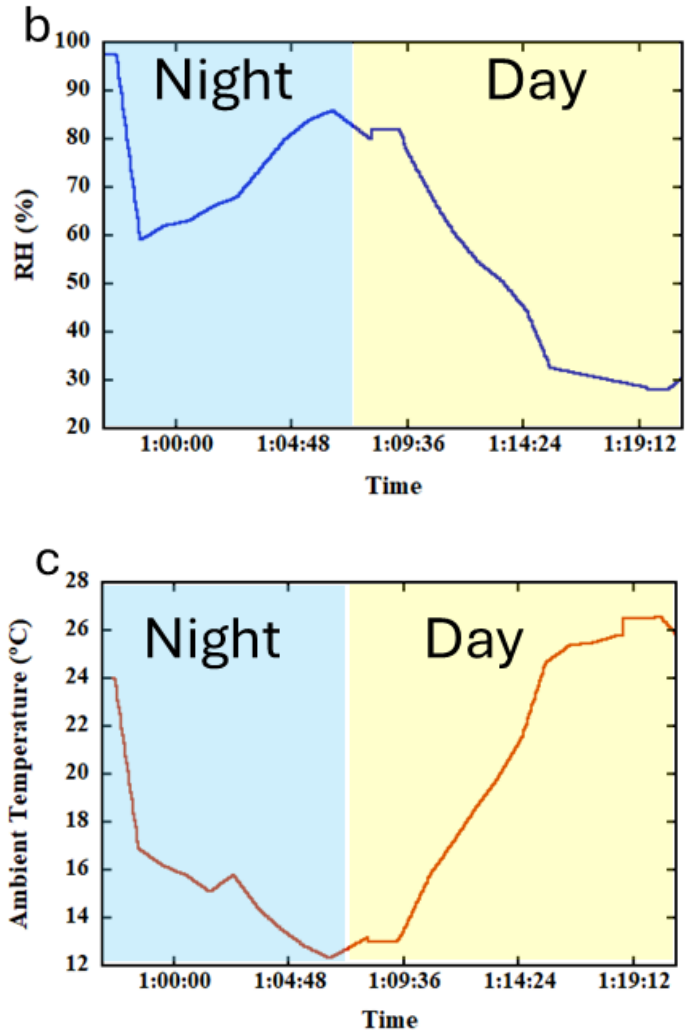


Figure 7.5 The PTE response vs solar irradiance under Madrid summer condition (X axis demonstrates local time), (b) the RH before and during the illumination, (c) the ambient temperature before and during illumination, (e) The time format is D:hh:mm

These results confirm that moderate humidity levels can effectively compensate for reduced thermal activation, in agreement with the trends identified in the static measurements. The findings further demonstrate that maintaining sufficient moisture ensures continuous ionic transport pathways and reduces internal resistance, thereby sustaining the PTE response. Overall, this behavior suggests that moderate climatic conditions may offer more favorable operating environments than high-temperature but low-humidity scenarios.

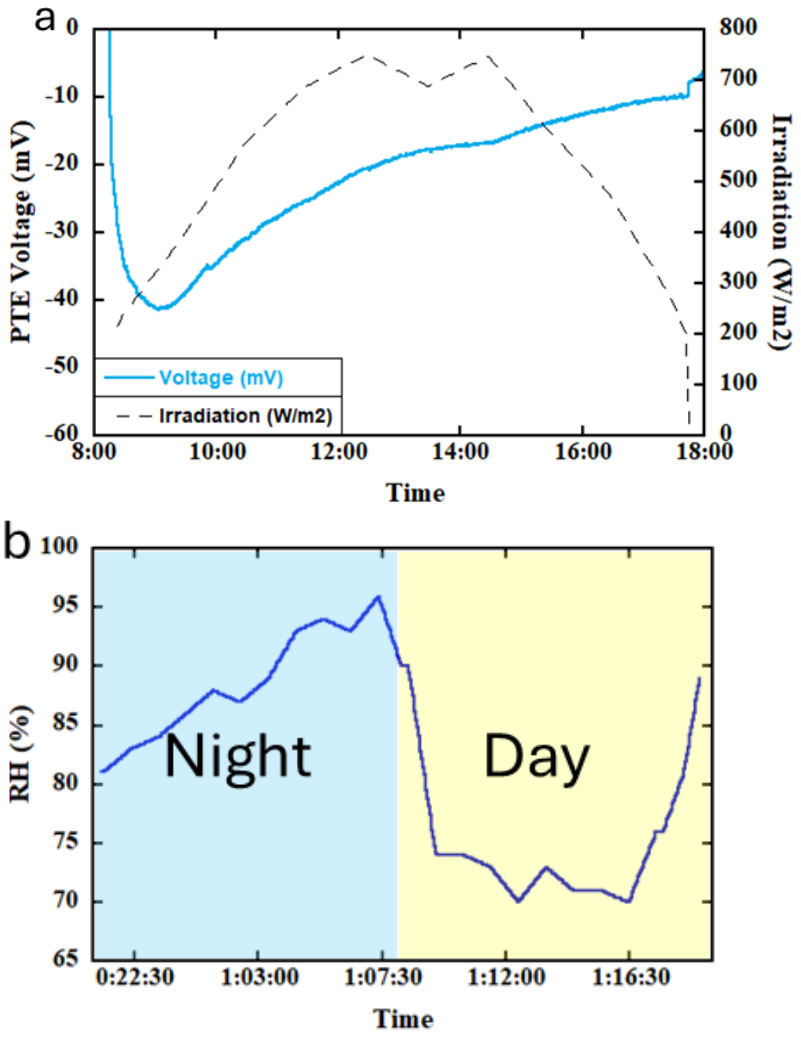
7.2.2.3 Singapore (Humid Climate)

Under simulated Singapore conditions, the voltage response exhibited a distinctly different behavior, as shown in Figure 7.6a. Following light exposure, the voltage increased rapidly, reaching a maximum absolute value of 41 mV after approximately 50 minutes, and then gradually decreased over the remainder of the test. This value represents the highest voltage recorded among all investigated climatic scenarios. The improved performance can be attributed to the combination of very high humidity,

average night-time RH of 95% and daytime RH of 81% (Figure 7.6b), together with moderate temperatures (average 28 °C, peak 30 °C; Figure 7.6c).

While the elevated humidity promotes ionic transport and reduces internal resistance, the moisture present near the surface tends to evaporate as the temperature approaches 30 °C. This partial drying of the surface region likely contributes to the subsequent decrease in voltage, as the continuity of ionic conduction pathways becomes progressively disrupted. It is important to note that, in the case of Singapore, the increase in irradiation and temperature was less pronounced than in Cairo or Madrid, and therefore insufficient to fully offset the gradual loss of surface moisture. Nevertheless, even after this decay, the PTE voltage remained consistently higher than in the other two cases throughout the test duration. These observations indicate that although high humidity is critical for achieving maximum voltage output, long-term stability requires a balance between moisture availability and thermal conditions to prevent progressive drying during operation.

Overall, the dynamic experiments demonstrate that both instantaneous humidity and prior moisture conditioning play a central role in determining PTE performance under realistic environmental variations. While higher irradiation and temperature enhance thermodiffusive processes, sufficient ambient humidity is essential to sustain ionic conductivity and maintain voltage stability, particularly during prolonged illumination.



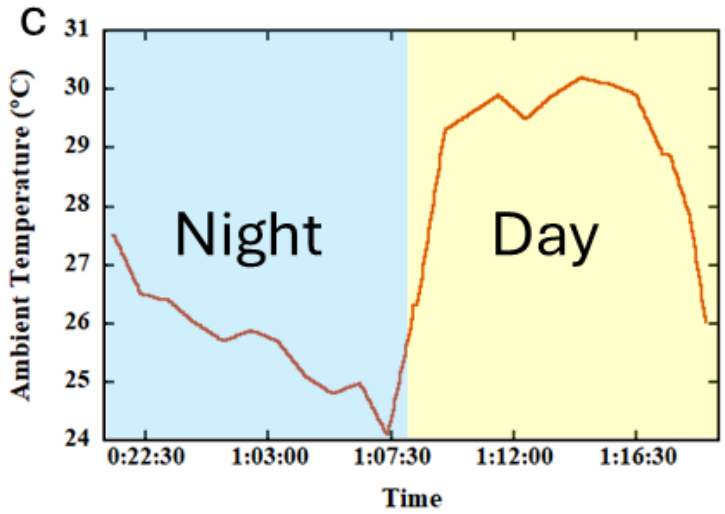


Figure 7.6 (a) The PTE response vs solar irradiance under Singapore summer condition (X axis demonstrates local time), (b) the RH before and during the illumination, (c) the ambient temperature before and during illumination. The time format is D:hh:mm

A comparison of the simulated summer conditions across the three representative climates further highlights the coupled influence of temperature, humidity, and irradiation on PTE behavior. The maximum absolute voltages ($|V_{max}|$) followed the trend Singapore (41 mV) > Madrid (14.6 mV) > Cairo (9 mV). Although Cairo experienced the highest irradiation (960 W m^{-2}) and temperature (T_{avg} = 35 °C, T_{peak} = 39 °C), its relatively low humidity (night RH = 48%, day RH = 28%) limited ionic transport and voltage generation. In contrast, Madrid, despite its lower average temperature (22 °C), achieved higher voltages due to significantly greater ambient humidity (night RH = 70%, day RH = 42%), which preserved continuous ionic pathways. Singapore produced the strongest PTE response owing to its very high humidity (night RH = 95%, day RH = 81%) combined with moderate temperature (average 28 °C), conditions that favor efficient ionic thermodiffusion and minimize internal resistance.

Taken together, these results demonstrate that cement-based PTE materials function as climate-responsive systems, where performance arises from the coupled interaction of temperature, humidity, and irradiation. Unlike conventional thermoelectric materials, their behavior depends not only on instantaneous conditions but also on moisture retention and environmental history. This underscores the importance of considering real climatic cycles in the design and evaluation of such systems, as static laboratory measurements alone may not adequately capture their performance under practical operating conditions.

7.3. Conclusion

The findings presented in this chapter establish a comprehensive understanding of the role of environmental conditions in governing the photothermoelectric (PTE) response of cement-based ionic systems. Rather than acting as secondary external influences, temperature and relative humidity are shown to directly control the fundamental mechanisms of ionic transport by regulating both charge carrier mobility and the continuity of the aqueous conduction network. Their effects are intrinsically coupled,

such that optimal performance is achieved only when sufficient thermal activation coincides with adequate moisture availability.

Under static conditions, the results demonstrate that relative humidity dictates the formation and stability of conductive pathways, while temperature determines the efficiency of ion migration within these pathways. This interplay leads to a non-linear, synergistic response, where neither parameter alone is sufficient to maximize performance. The identification of distinct transport regimes, from cation-dominated initial responses to thermally activated recovery behavior, further clarifies the dynamic evolution of the PTE signal and highlights the existence of intrinsic system-level timescales.

Beyond instantaneous conditions, the study reveals that environmental history plays a decisive role in defining device behavior. Night-time humidity is shown to restore ionic pathways and recover thermoelectric functionality, introducing a form of reversible, history-dependent response that is unique to water-mediated systems. This characteristic emphasizes that cement-based PTE materials cannot be treated as static devices but must instead be considered adaptive systems whose performance evolves with moisture cycling.

The dynamic climatic simulations extend these insights to realistic operating scenarios, demonstrating that PTE performance emerges from the combined and time-dependent interaction of irradiation, temperature, and humidity. The comparison across representative climates confirms that high humidity environments enable superior voltage generation, while low-humidity conditions can significantly limit performance even under elevated temperatures and solar input. At the same time, excessive drying during operation can lead to performance decay, underscoring the need for a balance between thermal input and moisture retention.

Overall, this chapter bridges the gap between intrinsic material behavior and real-world functionality, establishing cement-based PTE systems as climate-responsive energy materials. The results provide a clear framework for understanding how environmental parameters govern performance and offer practical guidance for optimizing these systems under different climatic conditions. Importantly, they highlight that effective deployment requires not only material and device design but also consideration of environmental exposure and moisture management strategies to ensure sustained and reliable operation.

Chapter VIII

Conclusion: Summary, Implications, and Future Work

8.1. Summary of the Thesis

This thesis investigated cement-based thermoelectric and photothermoelectric materials as multifunctional systems for harvesting low-grade heat and solar energy from the built environment. The central motivation was based on the fact that urban infrastructure continuously absorbs, stores, and dissipates large amounts of thermal energy, particularly under solar irradiation, while conventional energy-harvesting technologies are often not compatible with the scale, cost, durability, and structural requirements of construction materials. Cementitious materials, by contrast, are already widely deployed across buildings, pavements, bridges, and urban surfaces. Therefore, introducing thermoelectric functionality into cement-based systems offers a route toward infrastructure that is not only load-bearing but also capable of contributing to distributed energy generation.

The thesis first established the scientific background required to understand thermoelectric energy conversion in cementitious systems. Unlike conventional inorganic thermoelectric materials, where electronic charge carriers dominate, cement-based materials can exhibit ionic, electronic, or mixed ionic–electronic transport depending on binder chemistry, pore-solution composition, moisture state, microstructure, and the presence of functional fillers. This distinction is particularly important because hydrated and alkali-activated cementitious matrices contain mobile ions within their pore solution. Under a temperature gradient, these ions can undergo thermodiffusion, leading to charge separation and measurable thermoelectric voltage. The literature review, therefore, identified ionic thermoelectricity as a key mechanism for cement-based energy harvesting and highlighted the need to understand how pore structure, water distribution, intrinsic voltage, and environmental conditions affect the measured response.

The experimental work began with geopolymer-based hybrid cement modified with recycled copper slag aggregates. This system was selected because it combines industrial scalability, sustainability, and functional potential. The results showed that both the reference geopolymer hybrid cement and the copper-slag-containing composite exhibit significant intrinsic voltage before the application of a temperature gradient. This intrinsic voltage was identified as a critical source of bias in Seebeck measurements, since it can shift the voltage–temperature relationship and lead to an overestimation or misinterpretation of the thermally induced response. By introducing a refined measurement protocol in which the intrinsic open-circuit voltage was allowed to stabilize before applying the thermal gradient, the true thermoelectric contribution could be more reliably separated. This represents one of the main methodological contributions of the thesis.

The same study also demonstrated that the thermoelectric response of the geopolymer-based materials is governed predominantly by ionic transport through the pore solution.

The voltage evolution, drying experiments, electrical conductivity behavior, and temperature-dependent response all supported the interpretation that mobile ions and moisture-mediated pathways control charge separation under thermal gradients. The incorporation of copper slag influenced not only the optical and physical properties of the material, but also its pore structure, water content, electrical conductivity, and mechanical stability. Importantly, the use of recycled industrial aggregate showed that functional thermoelectric performance can be pursued without abandoning the sustainability and scalability requirements of construction materials.

The investigation was then extended to kaolin-clay-based and GGBF-slag-based geopolymers. These systems provided a broader understanding of how precursor chemistry, activator content, reaction products, thermal conductivity, and ionic mobility govern the thermoelectric behavior of alkali-activated binders. The kaolin-based geopolymer served as a model aluminosilicate system, clarifying the role of ionic conduction in a relatively well-defined geopolymer matrix. The GGBF-slag-based system, by contrast, allowed the influence of alkaline solution-to-slag ratio to be examined. Across these systems, the results confirmed that the magnitude, stability, and polarity of the thermoelectric response cannot be explained by ion concentration alone. Instead, they arise from the combined effects of pore connectivity, ion mobility, binder chemistry, moisture availability, thermal transport, and microstructural evolution.

Building on this material-level understanding, the thesis then moved from thermoelectric materials to photothermoelectric device design. A chessboard-like photothermoelectric cement cell was developed by combining two cementitious components with contrasting optical properties: a dark geopolymer/copper-slag segment designed to absorb solar radiation and generate heat, and a reflective white-cement segment designed to remain comparatively cooler. Under illumination, this optical contrast generated a lateral temperature gradient across the cell, enabling the coupling of photothermal heating with ionic thermoelectric voltage generation. This design represents a conceptual shift from conventional thermoelectric systems, where temperature gradients are usually imposed externally, toward cement-based devices that can generate their own temperature gradients under sunlight.

The photothermoelectric cell demonstrated voltage generation under controlled indoor irradiation, under different light intensities, and under outdoor solar exposure. The connection of multiple cells further confirmed the scalability of the concept, although voltage retention decreased with increasing number of connected units, indicating that device geometry, thermal coupling, contact resistance, and cell-to-cell interactions require further optimization. Outdoor measurements showed that the system can operate under real environmental conditions, validating the practical relevance of the design beyond laboratory testing. Further optimization of electrode configuration, ionic doping, geometry, and load matching improved the harvested energy output, demonstrating that device-level engineering is essential for converting high open-circuit voltage into useful electrical energy.

The final experimental part of the thesis examined the environmental response of cement-based photothermoelectric materials. This step was essential because ionic

thermoelectricity in cementitious systems is inherently dependent on water-mediated transport. Controlled environmental chamber tests showed that relative humidity and temperature are not secondary external variables, but fundamental parameters controlling the continuity of ionic pathways and the mobility of charge carriers. Under static conditions, humidity governed moisture availability and ionic pathway stability, while temperature influenced thermally activated ion migration. Their effects were strongly coupled, meaning that high temperature alone was insufficient when moisture was limited, and high humidity alone was insufficient without adequate thermal activation.

Dynamic climatic simulations further demonstrated that photothermoelectric performance depends on the time-dependent interaction of irradiation, temperature, and humidity. The comparison between representative climates showed that humid environments can support stronger voltage generation by maintaining stable ionic pathways, whereas dry conditions can suppress performance even when solar irradiation and temperature are high. The night-time humidity experiments also revealed a moisture-rechargeable behavior: after drying, exposure to sufficiently humid conditions restored ionic pathways and recovered the photothermoelectric response. This finding is particularly important because it shows that cement-based ionic thermoelectric systems are not static devices. Their performance evolves with environmental history, moisture cycling, and climatic exposure.

Overall, the thesis establishes cement-based thermoelectricity as a coupled material–device–environment phenomenon. At the material level, binder chemistry, pore solution, moisture state, and ionic mobility determine the thermoelectric response. At the device level, optical contrast, electrode configuration, geometry, resistance, and load matching control the conversion of this response into usable electrical output. At the environmental level, humidity, temperature, irradiation, and moisture history determine whether the ionic pathways required for operation remain active. The main contribution of this thesis is therefore not only the demonstration of cement-based thermoelectric and photothermoelectric performance, but also the development of a mechanistic framework for understanding how these systems function under realistic conditions.

8.2. Scientific and Practical Implications

The findings of this thesis have several scientific implications for the field of multifunctional cementitious materials. First, they confirm that ionic thermoelectricity must be considered a central mechanism in hydrated and alkali-activated cement-based systems. This challenges interpretations that treat cementitious thermoelectric behavior mainly as an electronic transport medium or attribute performance enhancement only to conductive fillers. In cementitious matrices, mobile ions, pore solution chemistry, water distribution, and electrode interfaces can dominate the measured voltage response. As a result, thermoelectric cement design requires approaches that are different from those used for conventional solid-state thermoelectrics.

Second, the identification of intrinsic voltage as a significant measurement artefact has important methodological consequences. Cement-based materials can exhibit pre-existing electrochemical potentials even before a temperature gradient is applied. If this

intrinsic voltage is not separated from the thermally induced voltage, the Seebeck coefficient may be incorrectly estimated. The refined measurement approach developed in this thesis, therefore, provides a more reliable protocol for evaluating ionic thermoelectric materials and may be useful for future studies on cement-based and other porous ionic systems.

Third, the thesis shows that cementitious thermoelectric performance is governed by a balance between transport mechanisms rather than by a single property. A high Seebeck coefficient alone is not sufficient for efficient energy harvesting if electrical resistance remains high. Similarly, improving electrical conductivity is not beneficial if it increases thermal conductivity excessively or suppresses the ionic contribution. The design of cement-based thermoelectric materials must therefore integrate pore-structure control, moisture management, ionic mobility, electrode coupling, thermal-gradient preservation, and device-level resistance optimization.

From a practical perspective, the results suggest that cement-based thermoelectric and photothermoelectric systems are most promising for low-power, distributed applications rather than large-scale electricity generation. Their potential lies in powering embedded sensors, structural health monitoring systems, environmental monitoring nodes, or autonomous low-power devices integrated into infrastructure. In this context, the key advantage of cement-based systems is not maximum conversion efficiency, but their compatibility with large surface areas, low cost, passive operation, and integration into existing construction materials.

The photothermoelectric cell developed in this thesis also introduces a new design strategy for harvesting solar energy using cementitious materials. Instead of attaching an external thermoelectric module to a structure, the material itself can be designed to generate a temperature gradient through spatially controlled optical properties. This opens a pathway toward multifunctional surfaces that combine solar absorption, thermal management, and electrical energy harvesting. The chessboard-like design is particularly relevant because it demonstrates that device architecture can compensate for the intrinsically modest performance of cementitious materials by improving thermal-gradient formation and scalability.

The environmental results further imply that deployment strategies must be climate-specific. Cement-based ionic photothermoelectric systems are likely to perform better in environments where sufficient humidity is available to maintain or restore ionic conduction pathways. In dry climates, additional moisture-retention strategies, surface treatments, encapsulation concepts, or internal water reservoirs may be required. Therefore, the performance of these materials cannot be assessed only by standard laboratory measurements under fixed temperature and humidity. Realistic climatic cycles, day–night moisture exchange, and seasonal exposure must be included in future evaluation protocols.

8.3. Limitations of the Present Work

Although this thesis advances the understanding and design of cement-based thermoelectric and photothermoelectric materials, several limitations remain. First, the

electrical power output of the developed systems is still low compared with conventional thermoelectric technologies. This is expected for cementitious ionic systems, which can exhibit large Seebeck coefficients but generally suffer from high internal resistance and limited charge mobility. Therefore, further improvements in conductivity, electrode coupling, and device geometry are needed before practical implementation.

Second, the long-term durability of the photothermoelectric response under repeated environmental cycling remains to be fully established. The thesis demonstrated moisture rechargeability and operation under controlled and outdoor conditions, but extended testing over months or years is necessary to assess aging, ion redistribution, leaching, carbonation, cracking, electrode degradation, and changes in pore connectivity.

Third, although the role of humidity was clearly demonstrated, the detailed distribution and dynamics of water inside the cementitious matrix were not directly resolved at the pore scale. Techniques such as nuclear magnetic resonance, neutron imaging, X-ray tomography, or advanced impedance mapping could provide deeper insight into how bound water, capillary water, interfacial water layers, and drying fronts contribute to ionic thermoelectric behavior.

Fourth, the present device designs were evaluated mainly at laboratory and small prototype scales. Scaling to larger panels, pavement elements, façade components, or modular arrays will introduce additional challenges related to thermal cross-talk, nonuniform irradiation, contact resistance, mechanical constraints, and connection losses. These aspects require dedicated engineering studies.

Finally, the thesis focused primarily on voltage generation and harvested energy under selected load conditions. A complete device-level assessment should also include power-management electronics, energy storage, intermittency, integration with sensors, and comparison with the energy demands of realistic infrastructure monitoring systems.

8.4. Future Work

Future research should first focus on reducing the internal resistance of cement-based ionic thermoelectric systems while preserving their high Seebeck response. This may be achieved through controlled ionic doping, optimized pore-solution chemistry, improved moisture retention, and better electrode–cement interfaces. The use of stable salts, ion-selective additives, hydrogel-like internal reservoirs, or hybrid ionic–electronic pathways could improve charge transport without compromising the structural role of the cementitious matrix.

A second important direction is the development of mixed ionic–electronic cementitious composites. The results of this thesis show that ionic transport provides large thermopower but limited conductivity. Introducing carefully selected conductive fillers, such as carbon-based nanomaterials, conductive oxides, or recycled conductive aggregates, could enhance electrical conductivity while maintaining the ionic contribution. However, this strategy must be optimized carefully, because excessive electronic conduction may reduce the Seebeck coefficient, increase thermal conductivity, or disturb moisture-mediated transport.

Future studies should also investigate electrode design in greater depth. Since ionic thermoelectric systems rely on charge accumulation and exchange at interfaces, electrode material, geometry, surface chemistry, and contact stability are critical. Silver-based electrodes, corrosion-resistant conductive coatings, porous electrodes, and ion-compatible interlayers may improve charge transfer and reduce contact resistance. Long-term stability of these interfaces under moisture cycling and alkaline conditions should be a priority.

At the device level, future work should optimize the photothermoelectric architecture. The chessboard-like design demonstrated in this thesis provides a strong proof of concept, but larger and more efficient configurations are possible. Future designs should explore different black–white geometries, segment dimensions, electrode spacing, thermal insulation strategies, surface coatings, and array connections. Numerical modelling of heat transfer, moisture transport, and ionic charge migration would be valuable for guiding these designs before fabrication.

Environmental durability and climate-specific performance should also be central to future research. Long-term outdoor testing in different climates is necessary to determine how seasonal changes, rain, wind, solar intensity, freeze–thaw cycles, drying, carbonation, and aging affect performance. Since humidity was shown to be a key controlling factor, future systems may need passive moisture-management strategies, such as hygroscopic additives, vapor-permeable encapsulation, or surface treatments that reduce excessive drying while allowing environmental recharge.

Another promising direction is the integration of cement-based photothermoelectric systems with low-power electronics. Rather than evaluating the material only as an isolated generator, future work should connect the harvested energy to practical devices such as temperature sensors, humidity sensors, strain gauges, wireless nodes, or structural health monitoring systems. This would clarify the realistic operating requirements and help define target values for voltage, current, power, storage capacity, and duty cycle.

Finally, future research should include life-cycle, cost, and sustainability analyses. Since one of the main advantages of cement-based energy-harvesting materials is their scalability and compatibility with infrastructure, their environmental benefit must be evaluated not only in terms of energy output but also in terms of raw material use, embodied carbon, durability, recyclability, and compatibility with existing construction practices. The use of industrial by-products such as copper slag and GGBF slag is particularly promising in this context and should be further developed.

8.5. Final Remarks

This thesis demonstrates that cementitious materials can be designed not only as passive structural media, but also as active energy-harvesting systems. By clarifying the role of ionic transport, correcting for intrinsic-voltage effects, linking binder chemistry to thermoelectric behavior, developing a solar-driven photothermoelectric cement cell, and evaluating performance under realistic environmental conditions, the work provides a foundation for a new class of multifunctional cement-based materials.

The broader significance of the thesis lies in showing that the built environment itself can become a platform for distributed energy harvesting. Although cement-based thermoelectric and photothermoelectric systems are still at an early stage of development, their compatibility with large-area infrastructure, low-grade heat sources, solar exposure, and low-power sensing applications makes them scientifically and technologically relevant. Continued progress will require the integration of materials chemistry, ionic transport physics, device engineering, environmental testing, and construction-scale design. Within this framework, cement-based thermoelectricity offers a promising route toward smart, adaptive, and energy-active infrastructure.

References

[1] J. Wei, Y. Liu, D. Liu, E. Lv, X. Lei, Recent advances in cement-based thermoelectric devices, Sustain. Energy Fuels 9 (2025) 4220–4237. https://doi.org/10.1039/d5se00567a.

[2] W. Li, C. Du, L. Liang, G. Chen, Cement-Based Thermoelectric Materials, Devices and Applications, Nanomicro Lett. 18 (2026). https://doi.org/10.1007/s40820-025-01866-2.

[3] V.P. Singh, M. Kumar, R.S. Srivastava, R. Vaish, Thermoelectric energy harvesting using cement-based composites: a review, Mater. Today Energy 21 (2021). https://doi.org/10.1016/j.mtener.2021.100714.

[4] S.I. Basha, S.S. Shah, D.Y. Yoo, Advancements in thermoelectric properties of cement and geopolymer composites reinforced with carbon-based nanomaterials, Journal of Building Engineering 104 (2025). https://doi.org/10.1016/j.jobe.2025.112312.

[5] G.J. Snyder, E.S. Toberer, Complex thermoelectric materials, Nat. Mater. 7 (2008) 105–114. https://doi.org/10.1038/nmat2090.

[6] J. He, T.M. Tritt, Advances in thermoelectric materials research: Looking back and moving forward, Science (1979). 357 (2017). https://doi.org/10.1126/science.aak9997.

[7] C.B. Vining, An inconvenient truth about thermoelectrics, Nat. Mater. 8 (2009). https://doi.org/10.1038/nmat2361.

[8] H. Ma, S. Li, M. Su, J. Feng, Research on thermoelectric seebeck effect and water-ion interaction mechanism of alkali-activated fly ash/slag materials, Journal of Building Engineering 113 (2025). https://doi.org/10.1016/j.jobe.2025.114082.

[9] H. Cheng, Q. Le, Z. Liu, Q. Qian, Y. Zhao, J. Ouyang, Ionic thermoelectrics: Principles, materials and applications, J. Mater. Chem. C Mater. 10 (2022) 433–450. https://doi.org/10.1039/d1tc05242j.

[10] Y. Cui, Y. Wang, Y. Wei, Ionic thermoelectric effect and mechanism of cement-based materials, Fuhe Cailiao Xuebao/Acta Materiae Compositae Sinica 39 (2022) 302–312. https://doi.org/10.13801/j.cnki.fhclxb.20210311.001.

[11] D. Zhao, A. Würger, X. Crispin, Ionic thermoelectric materials and devices, Journal of Energy Chemistry 61 (2021) 88–103. https://doi.org/10.1016/j.jechem.2021.02.022.

[12] Y. Cui, Y. Wei, Mixed “ionic-electronic” thermoelectric effect of reduced graphene oxide reinforced cement-based composites, Cem. Concr. Compos. 128 (2022). https://doi.org/10.1016/j.cemconcomp.2022.104442.

[13] A.K.K. Kyaw, G.D.H. Wong, T.A. Yemata, J. Xu, Effective ionic Seebeck component suppression in mixed ion-electron conductor via chemical

treatment, Org. Electron. 69 (2019) 7–12. https://doi.org/10.1016/j.orgel.2019.02.014.

[14] U. Ail, M.J. Jafari, H. Wang, T. Ederth, M. Berggren, X. Crispin, Thermoelectric Properties of Polymeric Mixed Conductors, Adv. Funct. Mater. 26 (2016) 6288–6296. https://doi.org/10.1002/adfm.201601106.

[15] Y. Wei, Y. Cui, Y. Wang, Ionic thermoelectric effect of pure cement paste and its temperature sensing performance, Constr. Build. Mater. 364 (2023). https://doi.org/10.1016/j.conbuildmat.2022.129898.

[16] T. Liang, S. Wang, D. Yan, Y. Liu, S. Chen, Enhancing thermoelectric performance of geopolymers via glass bead doping to regulate pore structure, Constr. Build. Mater. 496 (2025). https://doi.org/10.1016/j.conbuildmat.2025.143740.

[17] Z. Li, K. Chen, W. Dong, J. Tang, S.P. Shah, W. Li, Emerging thermoelectric cementitious nanocomposites: Mechanisms, design and performance, Advanced Nanocomposites 2 (2025) 227–250. https://doi.org/10.1016/j.adna.2025.09.002.

[18] S. Wang, J. Mao, J. Lin, S. Chen, Y. Liu, D. Yan, Dissecting the role of geopolymer-electrode interfaces in ionic thermoelectrics: electrochemical activity and energy-level matching governing Seebeck behavior, Cem. Concr. Compos. 167 (2026). https://doi.org/10.1016/j.cemconcomp.2025.106444.

[19] S. Jeon, N. Das, E.H. Yang, Unveiling thermoelectricity of metakaolin-based geopolymer for sustainable energy harvesting, Constr. Build. Mater. 501 (2025). https://doi.org/10.1016/j.conbuildmat.2025.144275.

[20] J. Wei, Q. Zhang, L. Zhao, L. Hao, Z. Nie, Effect of moisture on the thermoelectric properties in expanded graphite/carbon fiber cement composites, Ceram. Int. 43 (2017) 10763–10769. https://doi.org/10.1016/j.ceramint.2017.05.088.

[21] L. Tzounis, M. Liebscher, R. Fuge, A. Leonhardt, V. Mechtcherine, P- and n-type thermoelectric cement composites with CVD grown p- and n-doped carbon nanotubes: Demonstration of a structural thermoelectric generator, Energy Build. 191 (2019) 151–163. https://doi.org/10.1016/j.enbuild.2019.03.027.

[22] C. Rudradawong, M. Kitiwan, T. Goto, C. Ruttanapun, Positive ionic conduction of mayenite cement Ca12Al14O33/nano-carbon black composites on dielectric and thermoelectric properties, Mater. Today Commun. 22 (2020). https://doi.org/10.1016/j.mtcomm.2019.100820.

[23] C.Y. Huang, D.D.L. Chung, Controlling and increasing the inherent voltage in cement paste, Advances in Cement Research 21 (2009) 31–37. https://doi.org/10.1680/adcr.2008.00001.

[24] J. Li, B.W.Y. Tay, J. Lei, E.H. Yang, Experimental investigation of Seebeck effect in metakaolin-based geopolymer, Constr. Build. Mater. 272 (2021). https://doi.org/10.1016/j.conbuildmat.2020.121615.

[25] R. Piao, D. Lee, S.Y. Woo, J.W. Jeong, S.Y. Hiew, S.J. Lee, D.Y. Yoo, Carbon material-based thermoelectric ultra-high-performance alkali-activated concrete, Compos. B Eng. 297 (2025). https://doi.org/10.1016/j.compositesb.2025.112279.

[26] H. Min Park, S. Park, I.J. Shon, G.M. Kim, S. Hwang, M. Wook Lee, B. Yang, Influence of Portland cement and alkali-activated slag binder on the thermoelectric properties of the p-type composites with MWCNT, Constr. Build. Mater. 292 (2021). https://doi.org/10.1016/j.conbuildmat.2021.123393.

[27] G. Karalis, M. Liebscher, J. Mersch, J. Zhao, K.H. Ly, P. Machata, T. Köberle, M. Micusik, L. Tzounis, I. Weidinger, C. Cherif, V. Mechtcherine, Carbon nanotube fibers as efficient p- and n-type thermoelements within geopolymers: A route for large-scale thermal energy harvesting from building structures, Cem. Concr. Compos. 153 (2024). https://doi.org/10.1016/j.cemconcomp.2024.105699.

[28] L.P. Guo, B.C. Lyu, J.O. He, J.T. Lu, B. Chen, Mechanical and thermoelectric properties of high ductility geopolymer composites with nano zinc oxide and red mud, Constr. Build. Mater. 455 (2024). https://doi.org/10.1016/j.conbuildmat.2024.139173.

[29] J. Cai, X. Li, Thermoelectric properties of geopolymers with the addition of nano-silicon carbide (SiC) powder, Ceram. Int. 47 (2021) 19752–19759. https://doi.org/10.1016/j.ceramint.2021.03.313.

[30] J. Wei, Y. Wang, X. Li, Z. Jia, S. Qiao, Y. Jiang, Y. Zhou, Z. Miao, D. Gao, H. Zhang, Dramatically Improved Thermoelectric Properties by Defect Engineering in Cement-Based Composites, ACS Appl. Mater. Interfaces 13 (2021) 3919–3929. https://doi.org/10.1021/acsami.0c18863.

[31] N. Asim, M. Badiei, N.A. Samsudin, M. Mohammad, H. Razali, D. Hui, Clean technology option development for smart and multifunctional construction materials: Sustainable geopolymer composites, Journal of Building Engineering 94 (2024). https://doi.org/10.1016/j.jobe.2024.109932.

[32] A. Santos, S. Andrejkovičová, F. Almeida, F. Rocha, Thermoelectric properties of geopolymers with iron ore mine waste: A case study for energy management, Ceram. Int. 50 (2024) 36112–36125. https://doi.org/10.1016/j.ceramint.2024.06.424.

[33] J. Cai, J. Tan, X. Li, Thermoelectric behaviors of fly ash and metakaolin based geopolymer, Constr. Build. Mater. 237 (2020). https://doi.org/10.1016/j.conbuildmat.2019.117757.

[34] M. Sun, Z. Li, Q. Mao, D. Shen, Study on the hole conduction phenomenon in carbon fiber-reinforced concrete, Cem. Concr. Res. 28 (1998) 549–554.

[35] S. Wen, D.D.L. Chung, Seebeck effect in carbon fiber-reinforced cement, Cem. Concr. Res. 29 (1999) 1989–1993.

[36] S. Wen, D.D.L. Chung, Enhancing the Seebeck effect in carbon fiber-reinforced cement by using intercalated carbon fibers, Cem. Concr. Res. 30 (2000) 1295–1298.

[37] J. Wei, Y. Wang, X. Li, Z. Jia, S. Qiao, Q. Zhang, J. Du, Effect of porosity and crack on the thermoelectric properties of expanded graphite/carbon fiber reinforced cement-based composites, Int. J. Energy Res. 44 (2020) 6885–6893. https://doi.org/10.1002/er.5437.

[38] J. Wei, Q. Zhang, L. Zhao, L. Hao, C. Yang, Enhanced thermoelectric properties of carbon fiber reinforced cement composites, Ceram. Int. 42 (2016) 11568–11573. https://doi.org/10.1016/j.ceramint.2016.04.014.

[39] I. Vareli, L. Tzounis, K. Tsirka, I.E. Kavvadias, K. Tsongas, M. Liebscher, A. Elenas, L.N. Gergidis, N.M. Barkoula, A.S. Paipetis, High-performance cement/SWCNT thermoelectric nanocomposites and a structural thermoelectric generator device towards large-scale thermal energy harvesting, J. Mater. Chem. C Mater. 9 (2021) 14421–14438. https://doi.org/10.1039/d1tc03495b.

[40] M. Davoodabadi, I. Vareli, M. Liebscher, L. Tzounis, M. Sgarzi, A.S. Paipetis, J. Yang, G. Cuniberti, V. Mechtcherine, Thermoelectric energy harvesting from single-walled carbon nanotube alkali-activated nanocomposites produced from industrial waste materials, Nanomaterials 11 (2021). https://doi.org/10.3390/nano11051095.

[41] I. Vareli, A. Gkaravela, S. Polyviou, N.M. Barkoula, A.S. Paipetis, Structural Carbon-Enhanced Cementitious Thermoelectric Generators (TEGs): Optimal Energy Filtering and TEG Design for Outstanding Energy Harvesting, ACS Appl. Electron. Mater. 6 (2024) 2851–2861. https://doi.org/10.1021/acsaelm.3c00465.

[42] W. Pichór, M. Frąc, Thermoelectric properties of expanded graphite as filler of multifunctional cement composites, Composites Theory and Practice 12 (2012) 205–209.

[43] S. Ghosh, S. Harish, M. Ohtaki, B.B. Saha, Enhanced figure of merit of cement composites with graphene and ZnO nanoinclusions for efficient energy harvesting in buildings, Energy 198 (2020). https://doi.org/10.1016/j.energy.2020.117396.

[44] Y. Wang, J. Wei, Y. Zhou, Z. Miao, Y. Guo, X. Li, H. Zhang, W. Huang, Defect engineering treatment of indium tin oxide significantly enhances the thermoelectric properties of cement-based composites for large-scale energy harvesting, Journal of Building Engineering 68 (2023). https://doi.org/10.1016/j.jobe.2023.106082.

[45] X. Liu, M. Qu, A.P.T. Nguyen, N.R. Dilley, K. Yazawa, Characteristics of new cement-based thermoelectric composites for low-temperature applications, Constr. Build. Mater. 304 (2021). https://doi.org/10.1016/j.conbuildmat.2021.124635.

[46] S. Ghosh, S. Harish, M. Ohtaki, B.B. Saha, Thermoelectric figure of merit enhancement in cement composites with graphene and transition metal oxides, Mater. Today Energy 18 (2020). https://doi.org/10.1016/j.mtener.2020.100492.

[47] S. Wen, D.D.L. Chung, Seebeck effect in steel fiber reinforced cement, Cem. Concr. Res. 30 (2000) 661–664.

[48] S. Wen, D.D.L. Chung, Cement-based thermocouples, Cem. Concr. Res. 30 (2001) 507–510.

[49] S. Wen, D.D.L. Chung, Rectifying and thermocouple junctions based on Portland cement, J. Mater. Res. 16 (2001) 1989–1993.

[50] S. Wen, D.D.L. Chung, Electrical behavior of cement-based junctions including the pn-junction, Cem. Concr. Res. 31 (2001) 129–133.

[51] T. Ji, X. Zhang, X. Zhang, Y. Zhang, W. Li, Effect of Manganese Dioxide Nanorods on the Thermoelectric Properties of Cement Composites, Journal of Materials in Civil Engineering 30 (2018) 04018224. https://doi.org/10.1061/(ASCE)MT.1943-5533.0002401.

[52] T. Ji, S. Zhang, Y. He, X. Zhang, X. Zhang, W. Li, Enhanced thermoelectric property of cement-based materials with the synthesized MnO2/carbon fiber composite, Journal of Building Engineering 43 (2021). https://doi.org/10.1016/j.jobe.2021.103190.

[53] D. Wu, X. Xiong, J. Ma, L. Lv, J. Huang, Enhanced thermoelectric and compressive performance of MnO2 coated carbon fiber/cement composites by microwave electrodeposition/microwave alkali treatment, Ceram. Int. 49 (2023) 37535–37548. https://doi.org/10.1016/j.ceramint.2023.09.080.

[54] S.A. Ghahari, E. Ghafari, N. Lu, Effect of ZnO nanoparticles on thermoelectric properties of cement composite for waste heat harvesting, Constr. Build. Mater. 146 (2017) 755–763. https://doi.org/10.1016/j.conbuildmat.2017.04.165.

[55] Y. Wan, S. Tan, L. Li, H. Zhou, L. Zhao, H. Li, Z. Han, Fabrication and thermoelectric property of the nano Fe2O3/carbon fiber/cement-based composites for potential energy harvesting application, Constr. Build. Mater. 365 (2023). https://doi.org/10.1016/j.conbuildmat.2022.130021.

[56] T. Ji, X. Zhang, W. Li, Enhanced thermoelectric effect of cement composite by addition of metallic oxide nanopowders for energy harvesting in buildings, Constr. Build. Mater. 115 (2016) 576–581. https://doi.org/10.1016/j.conbuildmat.2016.04.035.

[57] T. Ji, S. Zhang, Y. He, X. Zhang, W. Li, Enhanced Thermoelectric Efficiency of Cement-Based Materials with Cuprous Oxide for Sustainable Buildings, Advances in Materials Science and Engineering 2022 (2022) 1–11. https://doi.org/10.1155/2022/6403756.

[58] J. Wei, L. Hao, G.P. He, C.L. Yang, Thermoelectric power of carbon fiber reinforced cement composites enhanced by Ca3Co4O9, Applied Mechanics and Materials 320 (2013) 354–357. https://doi.org/10.4028/www.scientific.net/AMM.320.354.

[59] G. Karalis, J. Zhao, T. Köberle, V. Mechtcherine, M. Liebscher, Temperature sensing performance of doped continuous carbon nanofiber filament-based thermocouples integrated in geopolymer-based mortar, Mater. Today Commun. 47 (2025). https://doi.org/10.1016/j.mtcomm.2025.113235.

[60] C. Forman, I.K. Muritala, R. Pardemann, B. Meyer, Estimating the global waste heat potential, (2016). https://doi.org/10.1016/j.rser.2015.12.192.

[61] J. Wei, Z. Nie, G. He, L. Hao, L. Zhao, Q. Zhang, Energy harvesting from solar irradiation in cities using the thermoelectric behavior of carbon fiber reinforced cement composites, RSC Adv. 4 (2014) 48128–48134. https://doi.org/10.1039/c4ra07864k.

[62] C. Xin, Z. Hu, Z. Fang, M. Chaudhary, H. Xiang, X. Xu, L. Aigouy, Z. Chen, Flexible and wearable plasmonic-enabled organic/inorganic hybrid photothermoelectric generators, Mater. Today Energy 22 (2021). https://doi.org/10.1016/j.mtener.2021.100859.

[63] J. Cao, D.D.L. Chung, Role of moisture in the Seebeck effect in cement-based materials, Cem. Concr. Res. 35 (2005) 810–812. https://doi.org/10.1016/j.cemconres.2004.05.036.

[64] H. Ran, M. Elchalakani, M. Ali Sadakkathulla, S. Yehia, J. Cai, T. Xie, Thermoelectric engineered cementitious composites with low thermal conductivity for efficiency improvement of buildings, Energy Build. 317 (2024). https://doi.org/10.1016/j.enbuild.2024.114390.

[65] M. Yossef, J. Kuva, S. Mousavihashemi, A. Ward, M. Perry, T. Kallio, J. Puttonen, Ionic thermoelectric performance of cement and its modifications, Case Studies in Construction Materials 22 (2025). https://doi.org/10.1016/j.cscm.2024.e04186.

[66] P. Martauz, I. Janotka, J. Strigáč, M. Bačuvčík, Fundamental properties of industrial hybrid cement: Utilization in ready-mixed concretes and shrinkage-reducing applications, Materiales de Construccion 66 (2016). https://doi.org/10.3989/mc.2016.04615.

[67] C. Shi, C. Meyer, A. Behnood, Utilization of copper slag in cement and concrete, Resour. Conserv. Recycl. 52 (2008) 1115–1120. https://doi.org/10.1016/j.resconrec.2008.06.008.

[68] R. Wang, Q. Shi, Y. Li, Z. Cao, Z. Si, A critical review on the use of copper slag (CS) as a substitute constituent in concrete, Constr. Build. Mater. 292 (2021). https://doi.org/10.1016/j.conbuildmat.2021.123371.

[69] L. Alarcon-Ruiz, G. Platret, E. Massieu, A. Ehrlacher, The use of thermal analysis in assessing the effect of temperature on a cement paste, Cem. Concr. Res. 35 (2005) 609–613. https://doi.org/10.1016/j.cemconres.2004.06.015.

[70] V. Musumeci, A supercritical water-based technology for calcium silicate hydrate nanoparticles production, PhD thesis, Universite de Bordeaux & Universidad del Pais Vasco, 2021.

[71] V. Rathanasalam, J. Perumalsami, K. Jayakumar, Mechanical and microstructural properties of copper slag based blended geopolymer concrete, Medziagotyra 27 (2021) 302–307. https://doi.org/10.5755/j02.ms.26521.

[72] S. Arora, P. Jangra, Y.Y. Lim, T.M. Pham, Strength, durability, and microstructure of self-compacting geopolymer concrete produced with copper slag aggregates, Environmental Science and Pollution Research 30 (2023) 666–684. https://doi.org/10.1007/s11356-022-22170-1.

[73] N. Arunachelam, J. Maheswaran, M. Chellapandian, T. Ozbakkaloglu, Effective Utilization of Copper Slag for the Production of Geopolymer Concrete with Different NaOH Molarity under Ambient Curing Conditions, Sustainability (Switzerland) 14 (2022). https://doi.org/10.3390/su142316300.

[74] M. Sivasakthi, R. Jeyalakshmi, N.P. Rajamane, Fly ash geopolymer mortar: Impact of the substitution of river sand by copper slag as a fine aggregate on its thermal resistance properties, J. Clean. Prod. 279 (2021). https://doi.org/10.1016/j.jclepro.2020.123766.

[75] R. Panchapakesan, Electret Effect in Cement, Master of Science, State University of New York at Buffalo, 2007.

[76] A. Caggiano, I. Peralta, V.D. Fachinotti, G. Goracci, J.S. Dolado, Atomistic simulations, meso-scale analyses and experimental validation of thermal properties in ordinary Portland cement and geopolymer pastes, Comput. Struct. 285 (2023). https://doi.org/10.1016/j.compstruc.2023.107068.

[77] S. Mindess (Ed.), Developments in the Formulation and Reinforcement of Concrete, Woodhead Publishing, 2019.

[78] O. Sengul, Use of electrical resistivity as an indicator for durability, Constr. Build. Mater. 73 (2014) 434–441. https://doi.org/10.1016/j.conbuildmat.2014.09.077.

[79] T. Honorio, F. Benboudjema, T. Bore, M. Ferhat, E. Vourc'H, The pore solution of cement-based materials: Structure and dynamics of water and ions from molecular simulations, Physical Chemistry Chemical Physics 21 (2019) 11111–11121. https://doi.org/10.1039/c9cp01577a.

[80] D. Vigolo, S. Buzzaccaro, R. Piazza, Thermophoresis and thermoelectricity in surfactant solutions, Langmuir 26 (2010) 7792–7801. https://doi.org/10.1021/la904588s.

[81] M.B. Ogundiran, S. Kumar, Synthesis and characterisation of geopolymer from Nigerian Clay, Appl. Clay Sci. 108 (2015) 173–181. https://doi.org/10.1016/j.clay.2015.02.022.

[82] F.I. Adeniyi, M.B. Ogundiran, T. Hemalatha, B.B. Hanumantrai, Characterization of raw and thermally treated Nigerian kaolinite-containing clays using instrumental techniques, SN Appl. Sci. 2 (2020). https://doi.org/10.1007/s42452-020-2610-x.

[83] X. Yao, Z. Zhang, H. Zhu, Y. Chen, Geopolymerization process of alkali-metakaolinite characterized by isothermal calorimetry, Thermochim. Acta 493 (2009) 49–54. https://doi.org/10.1016/j.tca.2009.04.002.

[84] C.A. Rosas-Casarez, S.P. Arredondo-Rea, J.M. Gómez-Soberón, J.L. Alamaral-Sánchez, R. Corral-Higuera, M.J. Chinchillas-Chinchillas, O.H. Acuña-Agüero, Experimental study of XRD, FTIR and TGA techniques in geopolymeric materials, International Journal of Advances in Computer Science & Its Applications-IJCSIA 4 (2014).

[85] P. Duxson, G.C. Lukey, J.S.J. Van Deventer, Physical evolution of Na-geopolymer derived from metakaolin up to 1000 °c, J. Mater. Sci. 42 (2007) 3044–3054. https://doi.org/10.1007/s10853-006-0535-4.

[86] H.K. Tchakouté, C.H. Rüscher, S. Kong, E. Kamseu, C. Leonelli, Comparison of metakaolin-based geopolymer cements from commercial sodium waterglass and sodium waterglass from rice husk ash, J. Solgel Sci. Technol. 78 (2016) 492–506. https://doi.org/10.1007/s10971-016-3983-6.

[87] H.K. Tchakouté, C.H. Rüscher, S. Kong, E. Kamseu, C. Leonelli, Thermal Behavior of Metakaolin-Based Geopolymer Cements Using Sodium Waterglass from Rice Husk Ash and Waste Glass as Alternative Activators, Waste Biomass Valorization 8 (2017) 573–584. https://doi.org/10.1007/s12649-016-9653-7.

[88] B. Roling, C. Martiny, S. Murugavel, Ionic conduction in glass: New information on the interrelation between the “jonscher behavior” and the “nearly constant-loss behavior” from broadband conductivity spectra, Phys. Rev. Lett. 87 (2001) 085901/1-085901/4. https://doi.org/10.1103/PhysRevLett.87.085901.

[89] D.L. Sidebottom, B. Roling, K. Funke, Ionic conduction in solids: Comparing conductivity and modulus representations with regard to scaling properties, Phys. Rev. B Condens. Matter Mater. Phys. 63 (2001). https://doi.org/10.1103/PhysRevB.63.024301.

[90] A.S. Nowick, A. V Vaysleyb, W. Liu, Identification of distinctive regimes of behaviour in the ac electrical response of glasses, Solid State Ion. 105 (1998) 121–128. https://doi.org/10.1016/S0167-2738(97)00457-8.

[91] X. Chen, E. Kim, P. Suraneni, L. Struble, Quantitative correlation between the degree of reaction and compressive strength of metakaolin-based geopolymers, Materials 13 (2020) 1–13. https://doi.org/10.3390/ma13245784.

[92] Y. Zuo, G. Ye, Preliminary interpretation of the induction period in hydration of sodium hydroxide/silicate activated slag, Materials 13 (2020) 1–19. https://doi.org/10.3390/ma13214796.

[93] S. Alonso, A. Palomo, Alkaline activation of metakaolin and calcium hydroxide mixtures: influence of temperature, activator concentration and solids ratio, Mater. Lett. 47 (2001) 55–62. https://doi.org/10.1016/S0167-577X(00)00212-3.

[94] F. Puertas, M. Palacios, H. Manzano, J.S. Dolado, A. Rico, J. Rodríguez, A model for the C-A-S-H gel formed in alkali-activated slag cements, J. Eur. Ceram. Soc. 31 (2011) 2043–2056. https://doi.org/10.1016/j.jeurceramsoc.2011.04.036.

[95] R. González-Teresa, J.S. Dolado, A. Ayuela, J.C. Gimel, Nanoscale texture development of C-S-H gel: A computational model for nucleation and growth, Appl. Phys. Lett. 103 (2013). https://doi.org/10.1063/1.4838396.

[96] E.L. Hseumou, A.M.N. Moudio, H.K. Tchakouté, C.H. Rüscher, Investigation of the Compressive Strength, Ultrasonic Pulse Velocity, Calorimetric, Microstructural and Rheological Properties of the Calcined Laterite-Based Geopolymer Materials, J. Inorg. Organomet. Polym. Mater. 34 (2024) 979–998. https://doi.org/10.1007/s10904-023-02869-5.

[97] J.L. Provis, P. Duxson, J.S.J. van Deventer, G.C. Lukey, The role of mathematical modelling and gel chemistry in advancing geopolymer technology, Chemical Engineering Research and Design 83 (2005) 853–860. https://doi.org/10.1205/cherd.04329.

[98] C. Chen, S. Shenoy, K. Sasaki, H. Zhang, Q. Tian, Influence of liquid-to-solid ratios on properties and microstructure of coal gasification slag-based one-part geopolymer, Case Studies in Construction Materials 20 (2024). https://doi.org/10.1016/j.cscm.2024.e02924.

[99] R. Ghosh, S.P. Sagar, A. Kumar, S.K. Gupta, S. Kumar, Estimation of geopolymer concrete strength from ultrasonic pulse velocity (UPV) using high power pulser, Journal of Building Engineering 16 (2018) 39–44. https://doi.org/10.1016/j.jobe.2017.12.009.

[100] A. Tutal, S. Partschefeld, J. Schneider, A. Osburg, EFFECTS OF BIO-BASED PLASTICIZERS, MADE FROM STARCH, ON THE PROPERTIES OF FRESH AND HARDENED METAKAOLIN-GEOPOLYMER MORTAR:

BASIC INVESTIGATIONS, Clays Clay Miner. 68 (2020) 413–427. https://doi.org/10.1007/s42860-020-00084-8.

[101] A. Alhamoud, H.T. Riahi, A. Ataei, Mechanical properties and stress-strain relationship of slag-based one-part geopolymer concrete: A comparative study, Results in Engineering 24 (2024). https://doi.org/10.1016/j.rineng.2024.102952.

[102] A. Lopes, S. Lopes, M. Fernandes, Time Evolution of the Modulus of Elasticity of Metakaolin-Based Geopolymer, Applied Sciences (Switzerland) 13 (2023). https://doi.org/10.3390/app13042179.

[103] M.A. Boulebnane, A.A. Belkadi, K. Boudeghdegh, T. Chiker, A. Berkouche, L. Benaddache, A. Cousture, S. Aggoun, Optimizing mix design methods for using slag, ceramic, and glass waste powders in eco-friendly geopolymer mortars, Archives of Civil and Mechanical Engineering 25 (2025). https://doi.org/10.1007/s43452-024-01077-3.

[104] O.G. Rivera, W.R. Long, C.A. Weiss, R.D. Moser, B.A. Williams, K. Torres-Cancel, E.R. Gore, P.G. Allison, Effect of elevated temperature on alkali-activated geopolymeric binders compared to portland cement-based binders, Cem. Concr. Res. 90 (2016) 43–51. https://doi.org/10.1016/j.cemconres.2016.09.013.

[105] D.M. Degefu, Z. Liao, U. Berardi, G. Labbé, The effect of activator ratio on the thermal and hygric properties of aerated geopolymers, Journal of Building Engineering 45 (2022). https://doi.org/10.1016/j.jobe.2021.103414.

[106] M.C. Bignozzi, S. Manzi, M.E. Natali, W.D.A. Rickard, A. Van Riessen, Room temperature alkali activation of fly ash: The effect of Na 2O/SiO2 ratio, Constr. Build. Mater. 69 (2014) 262–270. https://doi.org/10.1016/j.conbuildmat.2014.07.062.

[107] W. Van De Walle, S. Claes, H. Janssen, Implementation and validation of a 3D image-based prediction model for the thermal conductivity of cellular and granular porous building blocks, Constr. Build. Mater. 182 (2018) 427–440. https://doi.org/10.1016/j.conbuildmat.2018.06.105.

[108] Y. Xiong, Z. Shen, S. Yuan, Y. Liu, T. Jin, Y. Liang, R. Masrour, G. Niu, L. Xu, Ion migration mediated high Seebeck effect in halide perovskites and application in infrared detection, Chemical Engineering Journal 477 (2023). https://doi.org/10.1016/j.cej.2023.147168.

[109] H. Cheng, X. He, Z. Fan, J. Ouyang, Flexible Quasi-Solid State Ionogels with Remarkable Seebeck Coefficient and High Thermoelectric Properties, Adv. Energy Mater. 9 (2019). https://doi.org/10.1002/aenm.201901085.

[110] H. Wang, U. Ail, R. Gabrielsson, M. Berggren, X. Crispin, Ionic Seebeck effect in conducting polymers, Adv. Energy Mater. 5 (2015). https://doi.org/10.1002/aenm.201500044.

[111] W.J. Mccarter, G. Starrs, T.M. Chrisp, Immittance spectra for Portland cement/fly ash-based binders during early hydration, Cem. Concr. Res. 29 (1999) 377–387. https://doi.org/10.1016/S0008-8846(98)00209-9.

[112] S. Wansom, N.J. Kidner, L.Y. Woo, T.O. Mason, AC-impedance response of multi-walled carbon nanotube/cement composites, Cem. Concr. Compos. 28 (2006) 509–519. https://doi.org/10.1016/j.cemconcomp.2006.01.014.

[113] Y. Zhu, H. Zhang, Z. Zhang, Y. Yao, Electrochemical impedance spectroscopy (EIS) of hydration process and drying shrinkage for cement paste with W/C of 0.25 affected by high range water reducer, Constr. Build. Mater. 131 (2017) 536–541. https://doi.org/10.1016/j.conbuildmat.2016.08.099.

[114] X. Hu, C. Shi, X. Liu, J. Zhang, G. de Schutter, A review on microstructural characterization of cement-based materials by AC impedance spectroscopy, Cem. Concr. Compos. 100 (2019) 1–14. https://doi.org/10.1016/j.cemconcomp.2019.03.018.

[115] Q. Jiang, H. Sun, D. Zhao, F. Zhang, D. Hu, F. Jiao, L. Qin, V. Linseis, S. Fabiano, X. Crispin, Y. Ma, Y. Cao, High Thermoelectric Performance in n-Type Perylene Bisimide Induced by the Soret Effect, Advanced Materials 32 (2020). https://doi.org/10.1002/adma.202002752.

[116] S. Sun, X.L. Shi, W. Lyu, M. Hong, W. Chen, M. Li, T. Cao, B. Hu, Q. Liu, Z.G. Chen, Stable, Self-Adhesive, and High-Performance Graphene-Oxide-Modified Flexible Ionogel Thermoelectric Films, Adv. Funct. Mater. 34 (2024) 2402823. https://doi.org/10.1002/adfm.202402823.